

Detection of Bright Spots in Seismic Signal Using Pattern Recognition Techniques

Kou-Yuan Huang
K. S. Fu

TR-EE 83-35
September 1983

School of Electrical Engineering
Purdue University
West Lafayette, Indiana 47907

AD-A136210

This work was supported by NSF Grant ECS 81-19886 and ONR Contract N00014-79-C-0574

DETECTION OF BRIGHT SPOTS IN SEISMIC SIGNAL USING
PATTERN RECOGNITION TECHNIQUES

Kou-Yuan Huang
and
K. S. Fu

School of Electrical Engineering
Purdue University
West Lafayette, Indiana 47907

TR-EE 83-35
September

This work was supported by NSF Grant ECS 81-19886 and
ONR Contract N00014-79-C-0574.

BIBLIOGRAPHIC DATA SHEET	1. Report No. TR-EE 83-35	2.	3. Recipient's Accession No.
4. Title and Subtitle DETECTION OF BRIGHT SPOTS IN SEISMIC SIGNAL USING PATTERN RECOGNITION TECHNIQUES		5. Report Date September 1983	
		6.	
7. Author(s) Kou-Yuan Huang and K. S. Fu		8. Performing Organization Rept. No. TR-EE 83-35	
9. Performing Organization Name and Address Purdue University School of Electrical Engineering West Lafayette, IN 47907		10. Project/Task/Work Unit No.	
		11. Contract/Grant No. NSF Grant ECS 81-19886 ONR N00014-79-C-0574	
12. Sponsoring Organization Name and Address National Science Foundation Washington, D.C. 20550 and Office of Naval Research Arlington, VA 22217		13. Type of Report & Period Covered Technical	
		14.	
15. Supplementary Notes			
16. Abstracts Bright spot is one of the pattern classes in a seismic section and the indicators of gas (hydrocarbon) accumulation. In the past, detection of bright spots depended primarily upon visual examination and the experience of a geophysicist. It is the authors' contention that bright spot detection could be made more confidently by computer-aided analysis. This study concerns with two computer-aided methods. One is the decision-theoretic pattern recognition, the other is the syntactic or structural pattern recognition. Using these two methods, a seismogram is classified into two classes, i.e., bright spot and non-bright spot. In the decision-theoretic pattern recognition, three features from seismic traces extracted, envelope, instantaneous frequency, and polarity. Hilbert transform theorem plays an important role in the analytic signal analysis. Linear and tree classification techniques are applied. The classification result provides candidate bright spots. The second approach to detect candidate bright spots is the utilization of the			
17. Key Words and Document Analysis. 17a. Descriptors syntactic pattern recognition technique. Tree classification is used to extract the pattern wavelets of bright spot. Structural information of the pattern wavelets of a bright spot is used, as are Levenshtein distance computation and nearest-neighbor decision rule. A threshold is determined from error probability calculation and is used to detect candidate bright spots. Another factor affecting the detection of bright spot is frequency attenuation. A "partitioning-method" is presented. A seismogram is partitioned into small sections and the tree classification is performed in each section to detect the candidate bright spot. After the candidate bright spots are determined, syntactic pattern recognition technique is used again to recognize the string representation of a bright spot in a 17b. Identifiers, Open-Ended Terms two dimensional seismogram. The final result will indicate a bright spot or non-bright spot. It is common in seismic signal analysis to use the zero-phase Ricker wavelets. This study also utilizes these patterns in the simulation to test the proposed techniques as they are applied to the relative-amplitude real seismogram. The classification results obtained from these computer-aided methods can be used to improve seismic interpretation. 17c. COSATI Field/Group			
18. Availability Statement		19. Security Class (This Report) UNCLASSIFIED	21. No. of Pages
		20. Security Class (This Page) UNCLASSIFIED	22. Price

TABLE OF CONTENTS

	Page
LIST OF TABLE.....	viii
LIST OF FIGURES.....	ix
ABSTRACT	xvii
CHAPTER I - INTRODUCTION.....	1
1.1 Statement of the Problem	1
1.2 Literature Survey.....	8
1.2.1 Pattern Recognition in Classification of Seismic Signals	8
1.2.2 Analytic Signal Analysis.....	10
1.3 Organization of Thesis	10
1.4 Summary of Contributions.....	12
CHAPTER II - ANALYTIC SIGNAL ANALYSIS: FEATURE EXTRACTION	14
2.1 Introduction.....	14
2.2 Hilbert Transfer Function and Hilbert Transform Theorem.....	16
2.3 Analytic Signal and Its Representations.....	17
2.4 Analytic Signal Analysis in Sinucoidal Singals.....	18
2.5 Implementation in Discrete Calculations and Minimum Number of Truncated Hilbert Operators Required for a Finite Discrete Signal with Length N.....	20
2.6 Instantaneous Frequency in AM Waveforms	24
2.7 Instantaneous Frequency of Sinusoidal Waveforms with AM Applications.....	25
2.8 Rayleigh and Uniform Distributions	27
2.9 Sinusoidal Signal and Gaussian Noise in Analytic Signal Analysis	27

2.10 Rayleigh Distribution of the Envelope of Gaussian Noise in Discrete Time Case	35
2.11 Instantaneous Phase of Gaussian Noise.....	43
2.12 FM Demodulation Using Instantaneous Frequency.....	44
2.13 Envelope Application to Classification of Signal and Gaussian Noise	53
2.14 Resolution and Analytic Signal Analysis in Ricker Wavelets	60
2.15 Conclusions	66
CHAPTER III - DECISION-THEORETIC PATTERN RECOGNITION FOR DETECTION OF CANDIDATE BRIGHT SPOT.....	
3.1 Introduction.....	68
3.2 Linear Classification of Ricker Wavelets for the Detection of Candidate Bright Spot.....	69
3.2.1 Linear Classification of Ricker Wavelets	70
3.2.2 Linear Classification for the Detection of Candidate Bright Spot	75
3.3 Thin-Bed Effect.....	84
3.4 Tree Classification of Ricker Wavelets for the Detection of Candidate Bright Spot	84
3.4.1 Introduction	84
3.4.2 Definition of Polarity	92
3.4.3 Design of Tree Classifier	93
3.4.4 The First Hypothesis and Its Corresponding Tree Classifier	97
3.4.5 The Second Hypothesis and Its Corresponding Tree Classifier	102
3.4.6 The Third Hypothesis and Its Corresponding Tree Classifier	106
3.4.7 Real-Data Experiment	106
3.5 Conclusions	110
CHAPTER IV - DETECTION OF CANDIDATE BRIGHT SPOT IN FREQUENCY ATTENUATED SEISMOGRAMS USING A PARTITIONING-METHOD AND TREE CLASSIFICATION.....	
4.1 Introduction.....	117
4.2 Procedure of Partitioning-Method and Tree Classification.....	118
4.3 Boundary Determination in Seismogram Partition.....	120
4.4 Results of Boundary Determination	124
4.5 Results of Partitioning-Method and Tree Classification for the Detection of Candidate Bright Spot	133

4.6 Discussions.....	133
CHAPTER V - USE OF SYNTACTIC PATTERN RECOGNITION FOR THE DETECTION OF CANDITATE BRIGHT SPOT.....	
5.1 Introduction.....	137
5.2 Syntactic Pattern Recognition for the Classification of Ricker Wavelets in the Simulated Seismic Trace	142
5.2.1 Optimal Quantization Encoding	142
5.2.2 Likelihood Ratio Test (LRT)	148
5.2.3 Global Detection.....	149
5.2.4 Levenshtein Distance	151
5.2.5 Local Detection.....	151
5.2.6 Classification Rules and Results	153
5.3 Syntactic Pattern Recognition for the Detection of Canditate Bright Spot in a Simulated Seismogram	156
5.4 Syntactic Pattern Recognition for the Detection of Canditate Bright Spot in the Real Data Experiment	167
5.5 Conclusions	179
CHAPTER VI - SYNTACTIC PATTERN RECOGNITION FOR THE RECOGNITION OF BRIGHT SPOT.....	
6.1 Introduction.....	181
6.2 Local Pattern Testing	182
6.3 Global Pattern Testing	192
6.4 Syntactic Pattern Recognition for the Recognition of Bright Spot	194
6.4.1 Preprocessing	194
6.4.2 Generation of Training Patterns of Bright spot.....	198
6.4.3 String Distance Computation	199
6.4.4 Thresholding for the Recognition of Bright Spot String	221
6.5 Experimental Results	221
6.6 Discussions.....	235
CHAPTER VII - SUMMARY AND RECOMMENDATIONS.....	
7.1 Summary	236
7.2 Recommendation	238
LIST OF REFERENCES.....	239

LIST OF TABLES

Table	Page
2.1 Hilbert transform.....	19
2.2 Output of Hilbert operator.....	22
2.3 Instantaneous Frequency of the Sinusoidal Waveforms	26
3.1 Clustering Results	98
5.1 String of Ricker wavelets	147
5.2 The Encoded String of the Extracted Pattern.....	164

LIST OF FIGURES

Figure		Page
1.1	Record section processed to bring out relative amplitudes. Bright spot at center shows known gas accumulation. (Western Geophysical Co. of America.) (After Dobrin, 1976)	3
1.2	Horizontal reflections (at 1.2 and 2.0 s) indicative of gas-oil water contacts. Note arched reflections above each flat event, presumably from top of gas sand. (Teledyne Exploration Co.) (After Dobrin, 1976)	4
1.3	Depression of deep reflectors under multiple gas zones caused by reduction of velocity in gas-bearing sands. Note attenuation of reflections below well at times greater than 1.1 s. (Continental Oil Co.) (After Dobrin, 1976)	5
2.1	Feature distribution of two cosine signals	19
2.2A	Weak signal ($f_1=35\text{Hz}$) plus Gaussian noise, its envelope and instantaneous frequency	31
2.2B	Envelope distribution of Figure 2.2A	32
2.2C	Instantaneous frequency distribution of Figure 2.2A (Instantaneous frequency centered at $f_c=35\text{Hz}$)	33
2.3A	Strong signal ($f_1=10\text{Hz}$) plus Gaussian noise, its envelope and instantaneous frequency	36
2.3B	Envelope distribution of Figure 2.3A (S/N is high)	37
2.3C	Instantaneous frequency distribution of Figure 2.3A (S/N is high)	38
2.4A	Weak signal ($f_1=10\text{Hz}$) plus Gaussian noise, its envelope and instantaneous frequency	39
2.4B	Envelope distribution of Figure 2.4A (S/N is low)	40

2.4C	Instantaneous frequency distribution of Figure 2.4A (S/N is low)	41
2.5A	Gaussian noise, $N(0,0.024^2)$ sampling interval = 0.004 seconds	45
2.5B	Envelope distribution of Figure 2.5A.....	46
2.5C	Instantaneous phase distribution of Figure 2.5A by shifting $\frac{\pi}{2}$	47
2.5D	Instantaneous frequency distribution of Figure 2.5A.....	48
2.6A	Instantaneous frequency of FM without noise, baseband signal is a step function	51
2.6B	Instantaneous frequency of FM without noise, baseband signal is a cosine waveform.....	51
2.7	Instantaneous frequency of FM with high S/N, baseband signal is a step function	54
2.8	Instantaneous frequency of FM with high S/N, baseband signal is a cosine waveform.....	55
2.9A	Signal + Noise	56
2.9B	Envelope of Figure 2.9A	57
2.9C	Instantaneous frequency of Figure 2.9A	58
2.9D	Classification result using envelope=0.122	59
2.10	Instantaneous frequency of 25 Hz Ricker wavelet (Sampling interval 0.001 second)	62
2.11	Instantaneous frequency of 25 Hz Ricker wavelet (Sampling interval 0.004 seconds)	63
2.12A	Instantaneous frequency and envelope of mixed 20 Hz and 30 Hz Ricker wavelets (Phase reversal and 4 point peak-to-peak distance).....	64
2.12B	Instantaneous frequency and envelope distribution of 2.12A	65
3.1	Block diagram of a decision-theoretical pattern recognition system	71
3.2	Signal,its instantaneous frequency and envelope	72
3.3	Linear Classifier.....	73
3.4	Linear classification result of Ricker wavelets	73
3.5A	Geological structure	76

3.5B	Synthetic seismogram of bright spot	78
3.5C	Power value along receiving station	81
3.5D	Histrgom of Figure 3.5C.....	81
3.6A	Feature distribution of training samples and linear classfier	82
3.6B	Linear classification result of bright spot.....	83
3.7	Synthetic seismogram of bright spot (Thickness of gas sand zone is quarter wavelength)	85
3.8	Tree classification result of bright spot (Quarter wavelength at gas sand zone).....	86
3.9A	Geological structure	87
3.9B	Synthetic seismogram of bright spot (Thickness of gas sand zone is 2/3 quarter wavelength)	88
3.10	Linear classification result of bright spots(2/3 quarter wavelength at gas sand zone)	89
3.11	Block diagram of a tree classification system	91
3.12A	30 and 20 Hz Ricker wavelets and its analytic signal representations	94
3.12B	Feature distribution of a seismic trace	95
3.13	Tree classifier of the first hypothesis	99
3.14A	Signal, its instantaneous frequency & envelope	99
3.14B	Result of tree classification (The first hypothesis)	99
3.15A	The first hypothesis synthetic seismogram of bright spots	100
3.15B	Feature distribution of testing traces	100
3.15C	Tree classification result of bright spots	101
3.16	Tree classifier of the second hypothesis	103
3.17A	Signal, its instantaneous frequency & envelope.....	103
3.17B	Result of tree classification (The second hypothesis).....	103
3.18A	The second hypothesis synthetic seismogram of bright spots..	104
3.18B	Feature distribution of testing traces	104
3.18C	Tree classification result of bright spot.....	105
3.19	Tree classifier of the third hypothesis	107
3.20A	Signal, its instantaneous freuency and envelope	107

3.20B	Result of tree classification (The third hypothesis)	107
3.21A	The third hypothesis synthetic seismogram of bright spots.....	108
3.21B	Feature distribution of testing traces	108
3.21C	Tree classification result of bright spots	109
3.22A	Relative amplitude seismogram at Mississippi Canyon (Negative on the right)	111
3.22B	Feature distribution of testing traces	111
3.22C	Tree classification result of bright spots	112
3.23A	Relative amplitude seismogram at High Island (Negative on the right)	113
3.23B	Feature distribution of testing traces	113
3.23C	Tree classification result of bright spots	114
4.1	Block diagram of partitioning-method and tree classifier system	119
4.2	Relative amplitude seismogram at Mississippi Canyon and partitioning boundaries (5 sections).....	125
4.3	Power distribution	125
4.4	Distribution of signal distance k_i	126
4.5A	Feature distribution of training traces (The first section)	127
4.5B	Feature distribution of training traces (The second section)...	128
4.5C	Feature distribution of training traces (The third section).....	129
4.5D	Feature distribution of training traces (The fourth section)....	130
4.5E	Feature distribution of training traces (The fifth section)	131
4.6	Feature distribution of training traces.....	132
4.7	Tree classification result of bright spot (Partitioning-method and tree classification)	134
4.8	Tree classification result of bright spot (Tree classification without partition).....	135
5.1A	Signal, its instantaneous frequency, and envelope	138
5.1B	Feature distribution of a seismic trace	138
5.2A	A block diagram of a syntactic pattern recognition system (For classification of Ricker wavelets in a seismic trace).....	140

5.2B	A block diagram of syntactic pattern recognition system (For the detection of candidate bright spot in a seismogram) .	141
5.3	20 Hz and 17 Hz Ricker wavelets without noise	143
5.4	20 Hz and 17 Hz Ricker wavelets with Gaussian noise.....	144
5.5	Classification result of two classes (for the amplitude- independent encoding and minimum distance classification rule)	144
5.6	Classification result of two classes (for the amplitude-independent encoding and the NN decision rule)	144
5.7	Classification result of three classes (for the amplitude-dependent encoding and minimum distance classification rule)	144
5.8A	8-level optimal quantization encoding for d_i of 17 Hz Ricker wavelet	150
5.8B	Probability of detection for d_i of 17 Hz Ricker wavelet with amplitude-dependent encoding	150
5.9A	3 levels for d_i of 17 Hz Ricker wavelet	154
5.9B	Probability of detection for d_i of 17Hz Ricker wavelet with amplitude-independent encoding	154
5.10A	Synthetic seismogram of bright spots	157
5.10B	Testing traces	158
5.10C	Feature distribution of testing traces	159
5.10D	Tree classification result of bright spots	160
5.10E	Classification result of bright spot (Threshold=1)	161
5.10F	Classification result of bright spot (Threshold=2)	162
5.11A	8-level optimal quantization encoding for d_i of bright spot pattern in simulated seismogram	165
5.11B	Probability of detection using the conditional mean of each interval in bright spot pattern.....	165
5.12A	Real seismogram at Mississippi Canyon (Negative on the right)	168
5.12B	Tree classification result of bright spots	169
5.12C	Classification result of bright spots	170

5.13A	8-level optimal quantization encoding for d_i of bright spot pattern in Mississippi Canyon	172
5.13B	Probability of detection using the conditional mean of each interval in bright spot pattern.....	172
5.14A	Real seismogram at High Island (Negative on the right)	174
5.14B	Tree classification result of bright spots	175
5.14C	Classification result of bright spots	176
5.15A	8-level optimal quantization encoding for d_i of bright spot pattern in High Island.....	173
5.15B	Probability of detection using the conditional mean of each interval in bright spot pattern	178
6.1	1-D Classification result of the simulated seismogram.....	186
6.2	2-D Local pattern testing result of the simulated seismogram.....	187
6.3	1-D Classification result at High Island	188
6.4	2-D Local pattern testing result at High Island.....	189
6.5	1-D Classification result at Mississippi Canyon	190
6.6	2-D Local pattern testing result at Mississippi Canyon.....	191
6.7	2-D Local and global pattern testing result at Mississippi Canyon	195
6.8	A block diagram of syntactic pattern recognition system (For the recognition of bright spot in 2-D seismogram of candidate bright spot)	196
6.9	Simulated peak seismogram of bright spot for flat shape, training string o^{19}	200
6.10	Simulated peak seismogram of bright spot for arched shape, training string $oao^{15}Ao$	201
6.11	Simulated peak seismogram of bright spot for arched shape, training string $a^4o^{11}A^4$	202
6.12	Simulated peak seismogram of bright spot for arched shape, training string $a^4oao^7AoA^4$	203
6.13	Simulated peak seismogram of bright spot for arched shape, training string $ba^5o^7A^5B$	204

6.14	Simulated peak seismogram of bright spot for arched shape, training string $b^2a^5o^5A^5B^2$	205
6.15	Simulated peak seismogram of bright spot for arched shape, training string $b^3aba^2o^5A^2BAB^3$	206
6.16	Simulated peak seismogram of bright spot for arched shape, training string $cb^4a^3o^3A^3B^4C$	207
6.17	Simulated peak seismogram of bright spot for arched shape, training string $c^3b^3a^2o^3A^2B^3C^3$	208
6.18	Simulated peak seismogram of bright spot for arched shape, training string, $c^3b^2a^3o^3A^3B^2C^3$	209
6.19	Simulated peak seismogram of bright spot for concave shape, training string $oAo^{15}ao$	210
6.20	Simulated peak seismogram of bright spot for concave shape, training string $A^4o^{11}a^4$	211
6.21	Simulated peak seismogram of bright spot for concave shape, training string $A^5o^9a^5$	212
6.22	Simulated peak seismogram of bright spot for concave shape, training string $BA^5o^7a^5b$	213
6.23	Simulated peak seismogram of bright spot for concave shape, training string $B^2ABA^3o^5a^3bab^2$	214
6.24	Simulated peak seismogram of bright spot for concave shape, training string $B^4A^3o^5a^3b^4$	215
6.25	Simulated peak seismogram of bright spot for concave shape, training string $CB^3A^4o^3a^4b^3c$	216
6.26	Simulated peak seismogram of bright spot for concave shape, training string $C^3B^3A^2o^3a^2b^3c^3$	217
6.27	Simulated peak seismogram of bright spot for concave shape, training string $C^3B^2A^3o^3a^2b^3c^3$	218
6.28	Flow chart of method (I)	222
6.29	Flow chart of method (II)	223
6.30	Flow chart of method (III).....	224
6.31	Peak seismogram of Figure 6.1.....	225
6.32	Extracted string, $a^4xao^7A^2xA^3$, from simulated seismogram ..	226
6.33	Peak seismogram of Figure 6.5.....	228

6.34	Four extracted strings, $oxo, o^2xo\tau^2o^5xo^4, o^3, o^6xo,$ from the data at Mississippi Canyon	229
6.35	Peak seismogram of Figure 6.3.....	233
6.36	Extracted string, o^2xo^8 , from the data at High Island.....	234

ABSTRACT

Bright spot is one of the pattern classes in a seismic section and the indicators of gas (hydrocarbon) accumulation. In the past, detection of bright spots depended primarily upon visual examination and the experience of a geophysicist. It is the authors' contention that bright spot detection could be made more confidently by computer-aided analysis. This study concerns with two computer-aided methods. One is the decision-theoretic pattern recognition, the other is the syntactic or structural pattern recognition. Using these two methods, a seismogram is classified into two classes, i.e., bright spot and non-bright spot.

In the decision-theoretic pattern recognition, three features from seismic traces extracted, envelope, instantaneous frequency, and polarity. Hilbert transform theorem plays an important role in the analytic signal analysis. Linear and tree classification techniques are applied. The classification result provides candidate bright spots.

The second approach to detect candidate bright spots is the utilization of the syntactic pattern recognition technique. Tree classification

is used to extract the pattern wavelets of bright spot. Structural information of the pattern wavelets of a bright spot is used, as are Levenshtein distance computation and nearest-neighbor decision rule. A threshold is determined from error probability calculation and is used to detect candidate bright spots.

Another factor affecting the detection of bright spot is frequency attenuation. A "partitioning-method" is presented. A seismogram is partitioned into small sections and the tree classification is performed in each section to detect the candidate bright spot.

After the candidate bright spots are determined, syntactic pattern recognition technique is used again to recognize the string representation of a bright spot in a two dimensional seismogram. The final result will indicate a bright spot or non-bright spot.

It is common in seismic signal analysis to use the zero-phase Ricker wavelets. This study also utilizes these patterns in the simulation to test the proposed techniques as they are applied to the relative-amplitude real seismogram. The classification results obtained from these computer-aided methods can be used to improve seismic interpretation.

CHAPTER I

INTRODUCTION

1.1 Statement of the Problem

By 1972 many oil companies had become successful in predicting the occurrence of offshore gas from exploration seismic reflection data. These predictions were based on anomalies that would be expected in the high amplitudes of reflections caused by differences between the reflectivity of surfaces bounding sands containing gas and those bounding water or oil bearing portions of the sands. The amplitude of a seismic wave reflected from an interface between two layers of materials is governed by the reflection coefficient R which is expressed for normal incidence by the relation

$$R = \frac{D_2 V_2 - D_1 V_1}{D_2 V_2 + D_1 V_1}$$

where D_1 and D_2 are the respective densities on the near (incident) and far sides of the boundary and V_1 and V_2 are the respective velocities for the two sides. The product of D and V is known as the acoustic impedance, and it is evident that the reflection coefficient and hence the reflection amplitude depend on the change in acoustic impedance across the reflecting interface. A high-amplitude portion of the reflection is referred to as a bright spot [dob76a].

Some very important indicators in predicting the occurrence of gas and oil from real seismic reflection data are as follows [dob76a, pan70a, pay77a, she74a, she75a, she76a].

(1) High amplitude is related to the high reflection coefficient at the top boundary of the gas sand.

(2) Low frequency wavelets are at the reflection of the top boundary of gas sand zone because of the high frequency attenuation.

(3) Phase reversals are produced by a negative reflection coefficient at the top boundary of gas sand and again by the positive reflection coefficient at the bottom boundary of gas sand.

Three examples of relative-amplitude real seismograms of bright spot from Dobrin are shown in Fig. 1.1, 1.2, and 1.3 [dob76a]. The shape of the bright spot is a limited continuous reflection layer and may be horizontal, arched, or concave. The problem is that the interpretation is strictly by visual analysis. A seismogram is interpreted by an interpreter from his experience, geological information from both ends of the seismogram, well information, etc. Interpretation of seismic sections is a tedious and subjective task which challenges the exploration geophysicists. Furthermore, subtle changes in the nature of the reflected signal often cannot be seen by visual analysis. Successful application of automatic information extraction techniques to seismic exploration data would greatly relieve the burden of visual inspection of large quantities of seismic section plots.

Physical properties of bright spot are used in this study. The bright spot in this study is defined in the following.

Bright spot has the following three kinds of physical properties and a continuous reflection layer.

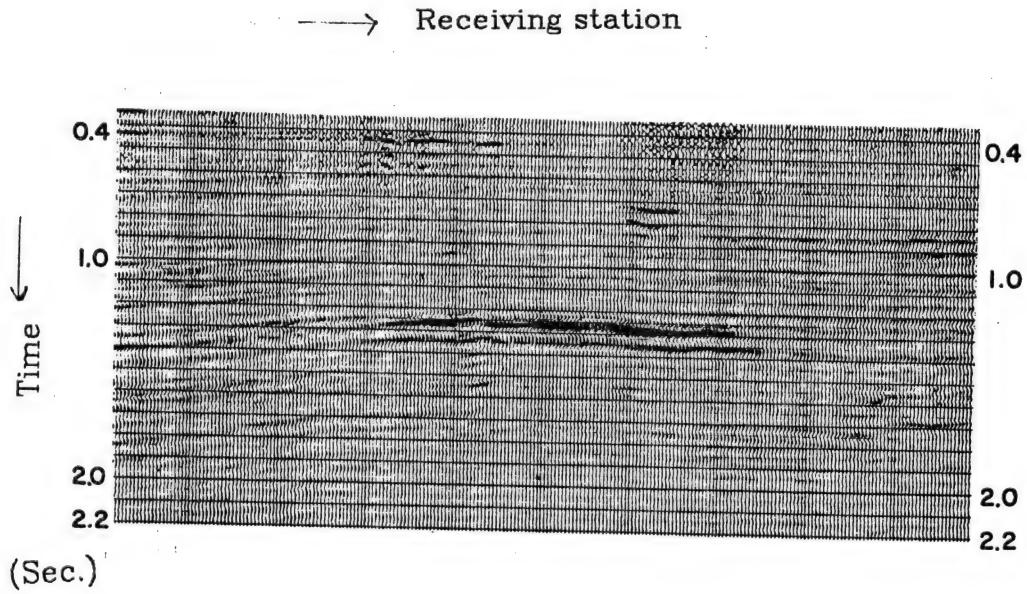


Figure 1.1 Record section processed to bring out relative amplitudes. Bright spot at center shows known gas accumulation. (Western Geophysical Co. of America.) (After Dobrin, 1976)

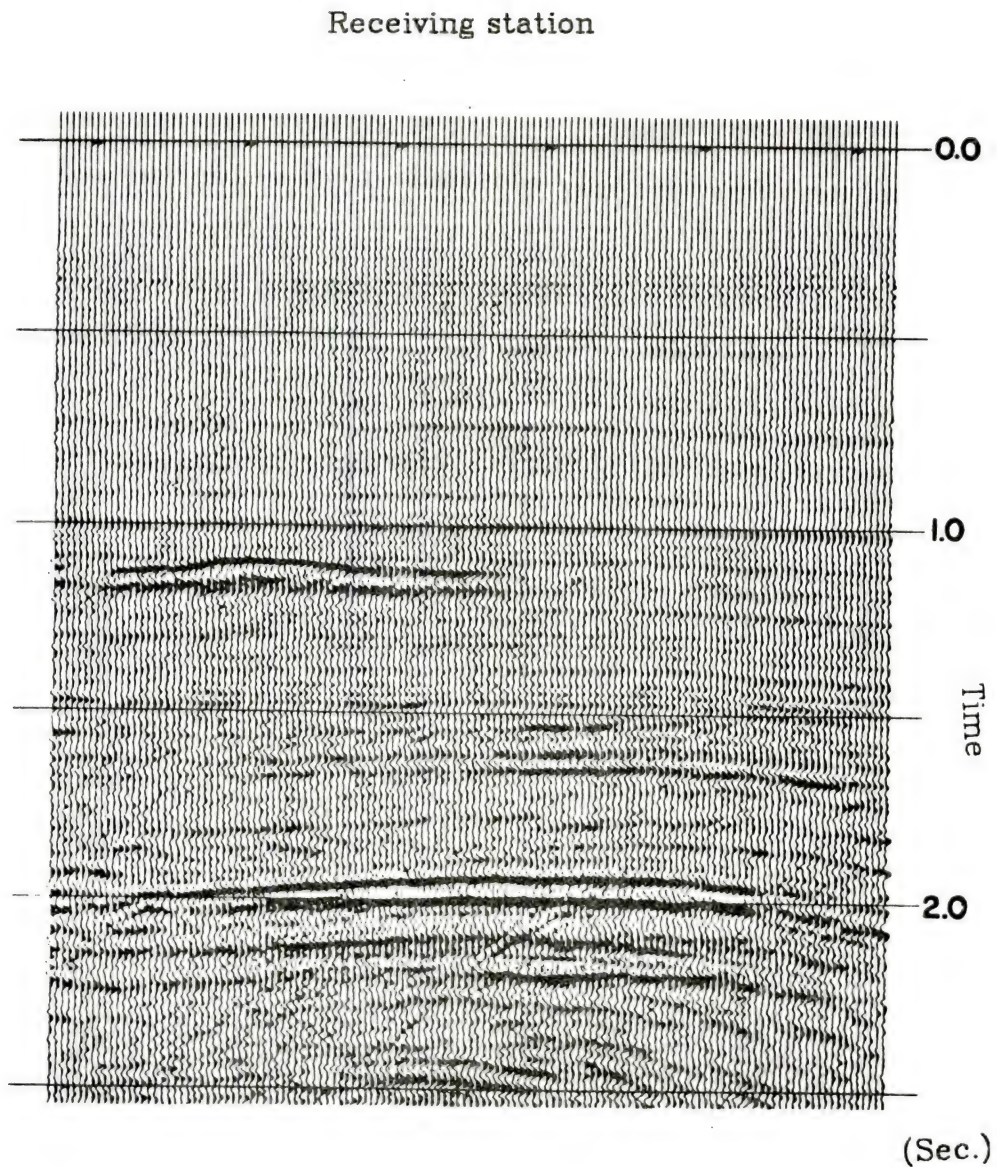


Figure 1.2 Horizontal reflections (at 1.2 and 2.0 s) indicative of gas-oil water contacts. Note arched reflections above each flat event, presumably from top of gas sand. (Teledyne Exploration Co.) (After Dobrin, 1976)

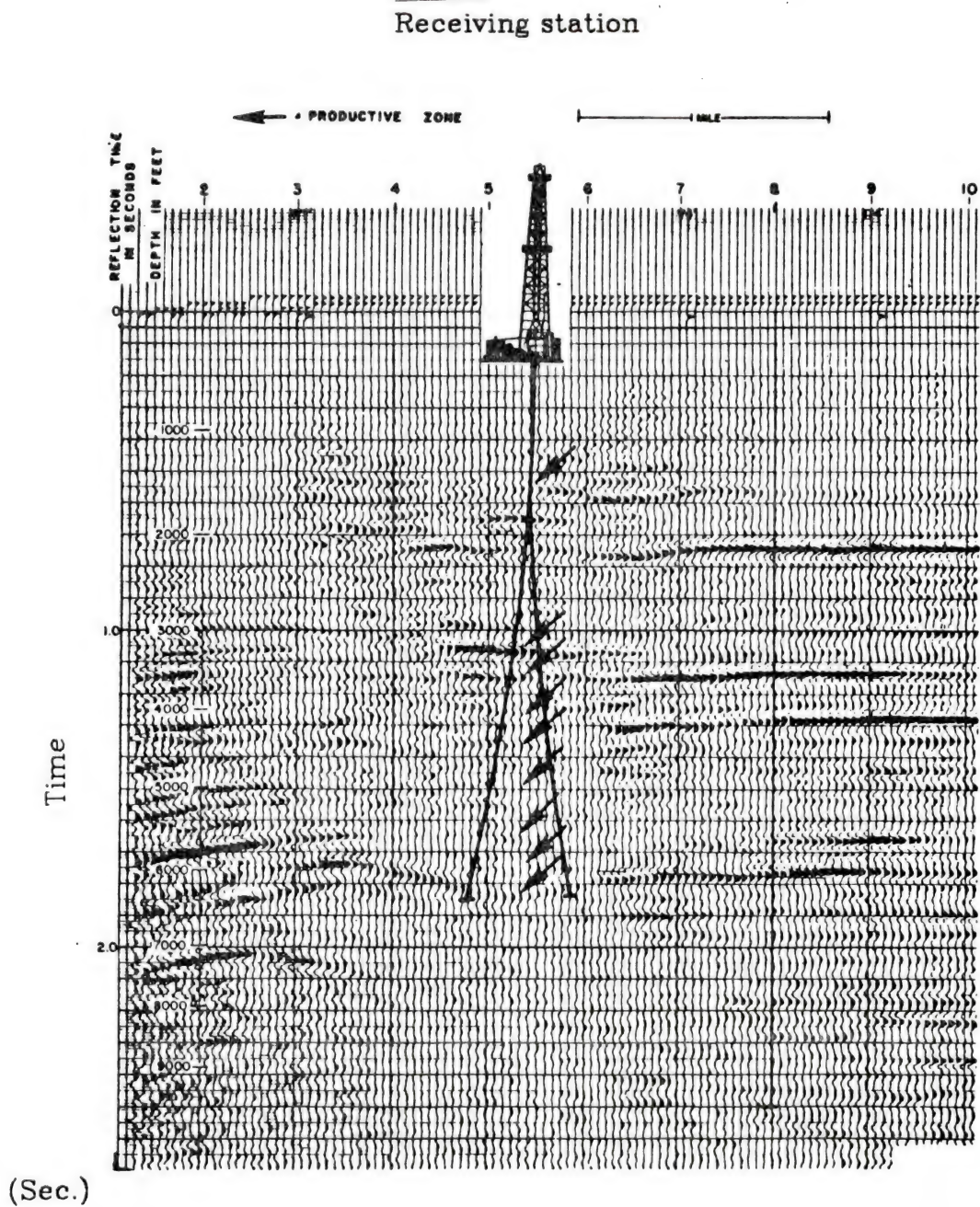


Figure 1.3 Depression of deep reflectors under multiple gas zones caused by reduction of velocity in gas-bearing sands. Note attenuation of reflections below well at times greater than 1.1 s. (Continental Oil Co.) (After Dobrin, 1976)

- (1) The first kind consists of the properties of high amplitude, low frequency, and negative polarity.
- (2) The second kind consists of the properties of high amplitude and low frequency.
- (3) The third kind consists of the properties of high amplitude and negative polarity.

Data satisfying at least one of these three kinds of properties is called a candidate bright spot. Data satisfying the properties of continuous reflection layer and one of the three kinds is called a bright spot. The second and third kinds are necessary due to the fact that low frequency content or polarity may not be significant in the seismogram.

The absolute magnitudes of the three physical properties may not be as important as their relative values because the reflection from geological structure is case by case or area by area. The dominant wavelets may be zero-phase as zero-phase Ricker wavelet [ric40a, 45a, 53a] or minimum phase [rob67a]. Comparing the dominant wavelets in the seismogram, the polarity can be determined.

Bright spot is one of the pattern classes in a seismic section and the indicators of gas (hydrocarbon) accumulation. In order to detect bright spot more confidently by computer-aided analysis, two methods are proposed. One is the decision-theoretic pattern recognition and the other is the syntactic or structural pattern recognition. Because the physical properties of a bright spot are relative, computer-geophysicist interaction is needed in this study. The seismogram is classified into two classes, i.e., bright spot and non-bright spot.

In the decision-theoretic pattern recognition, some testing traces are selected. The testing traces may be randomly selected or selected at the high-amplitude portion in the seismogram. The purpose of the testing traces is for the data reduction and to detect whether or not the candidate bright spot is in the seismogram. Three features are extracted: envelope corresponding to the amplitude, instantaneous frequency corresponding to the frequency content, and polarity testing the phase reversal. Linear and tree classification techniques are applied. The classification is point-by-point. The classification result is the candidate bright spot.

The other approach to detect a candidate bright spot is using the syntactic pattern recognition technique. Testing traces are selected from the seismogram. Tree classification is applied to detect the pattern wavelets of bright spot in the testing traces. Structural information of the bright spot wavelets is used. Levenshtein distance computation, and the nearest-neighbor decision rule are used. A threshold is determined from error probability calculation and is used to detect the candidate bright spot. The classification is trace-by-trace.

Reflection of frequency attenuation affects the detection of bright spot. A "partitioning-method" is presented. A given seismogram is partitioned into small sections. Tree classification is performed in each section to detect candidate bright spots. The major advantage of the partitioning-method is that the overlapping distribution of the envelope and instantaneous frequency can be separated.

After the candidate bright spots are determined, syntactic pattern recognition technique is used again to recognize the string of bright spot in a two dimensional seismogram. Three kinds of string distance computation are proposed to test the continuity of bright spot pattern.

The final result will indicate a bright spot or non-bright spot.

Zero-phase Ricker wavelets are usually used in the simulation of the seismic analysis [rob81a, tan79a]. From the distribution of envelope and instantaneous frequency of Ricker wavelets, tree classification is adopted. At first, obvious Ricker wavelets are classified. Then, a simulated seismogram using Ricker wavelets is classified. At last, real seismograms at Mississippi Canyon and High Island are detected to determine whether or not there is bright spot and where the bright spot is located. The relative-amplitude real seismograms in this study are provided by Mr. K. M. Barry, Vice President of the Teledyne Exploration Co.

1.2 Literature Survey

1.2.1 Pattern Recognition in Classification of Seismic Signals

Most works in the analysis of seismic signals deal with discrimination between earthquake and nuclear explosion events. Chen [che77a, 78a, 82a, 83a] proposed a statistical pattern recognition method for classification of earthquake and nuclear explosion waves. He cites a number of characteristics of seismic signals which are used as discriminants. Among these are spectral ratios for body waves and surface waves, m_b vs. M_s criterion and differences in P-wave amplitude spectra. Liu and Fu [liu82a, 82b, 83a] used syntactic approach to discriminant earthquake and nuclear explosion waves. Anderson [and78a, 82a] and Gaby [gab83a] used syntactic analysis in seismological waveforms.

Tjostheim [tjo75a, 77a, 78a, 79a] used autoregressive coefficients as features for P-wave seismic discrimination. A seismic P-wave can be represented by an autoregressive model of finite order.

Sarna and Stark [sar80a, 82a] also used autoregressive modeling for the pattern recognition of earthquake and explosion data. The results are poor.

Since 1980, several papers related to pattern recognition in seismic exploration have been published. Bois [boi80a, 81a, 81b, 82a] used autoregressive coefficients for short trace sectors between the top and the bottom boundaries of a reservoir and by this he was able to establish a decision criterion to distinguish the trace sector corresponding to layers containing oil or gas and those containing water only.

Hagen [hag81a] used principal components of instantaneous frequency for the classification of regions of a seismic section into porous and non-porous.

Huang et. al. [hua81b] decomposed a simulated seismogram into density and velocity distributions to detect bright spots. Huang et. al. [hua81c] used Z, T , likelihood ratio and Chi-squared tests and spatial relations to obtain continuous layer reflection coefficients.

Huang and Fu [hua82a] used envelope and instantaneous frequency as features and decision-theoretic pattern recognition techniques for the classification of Ricker wavelets and the detection of candidate bright spots. The classification results are displayed in the original time traces. This presentation was very important because it was very successful in real data experiment [hua83a]. Huang and Fu also proposed three hypotheses and tree classification techniques to detect candidate bright spots [hua83a, hua83e]. Huang and Fu presented a partitioning-method and tree classification in the detection of

candidate bright spots for frequency attenuated seismograms [hua83c].

Syntactic pattern recognition had been applied to character recognition, target detection, medical diagnosis, remote sensing, speech recognition, automatic inspection, and identification of human faces and fingerprints in the past decade [fu74a, 82a]. Huang and Fu presented a syntactic pattern recognition technique for the classification of Ricker wavelets [hua83d].

1.2.2 Analytic Signal Analysis

Analytic signal analysis has been applied to seismological waves and exploration seismic signal. Farnbach [far75a] used analytic signal representation for seismological waves. A recent paper by Tanner, Koehler, and Sheriff [tan77a, 79a, 80a] used complex trace (analytic signal) in exploration seismic signal. Sicking used complex trace in modeling [sic78a]. Robertson and Nogami used complex trace to thin bed stratigraphy [rob81a]. Huang et. al. used analytic signal representation for synthetic seismogram of bright spots [hua80a, 81a]. Huang and Fu presented analytic signal analysis in Gaussian noise analysis and their use in the classification of Ricker wavelets [hua83b].

1.3 Organization of Thesis

In Chapter 2, features are extracted by using analytic signal analysis. Analytic signal analysis in AM, FM, sinusoidal signal, seismic Ricker wavelets, and Gaussian noise, is discussed. Hilbert transform theorem plays an important role in the analytic signal analysis. The

usage of the non-causal Hilbert operator is also introduced.

In Chapter 3, the motivation of using tree classification in the detection of candidate bright spot is discussed. Use of linear classifier is also discussed. Three hypotheses are proposed for the constrained conditions to detect candidate bright spots similar to the constrained condition in mathematical optimization problem. Tree classifier design is discussed.

In Chapter 4, a partitioning-method and tree classification are proposed to detect candidate bright spot in order to avoid the attenuation effect. The procedures for partitioning a seismogram into small sections are discussed.

In Chapter 5, syntactic pattern recognition is used in the detection of candidate bright spot. The roles of likelihood ratio test, optimal quantization encoding, and the probability of detection involving the global, local detection and threshold setting to detect the candidate bright spots, are discussed.

For Chapter 3, 4, and 5, the results for the detection of candidate bright spots in the simulation and real data experiments are demonstrated respectively. The classification results of Ricker wavelets are also demonstrated.

In Chapter 6, syntactic pattern recognition technique is used again to recognize the string of bright spot in a two dimensional seismogram. The final result will indicate a bright spot or non-bright spot.

Finally, Chapter 7 summaries the whole study and proposes recommendation for future work.

1.4 Summary of Contributions

(1) Several lemmas are derived for the instantaneous frequency of AM and sinusoidal signals. The instantaneous frequency of Ricker wavelet is inferred from the instantaneous frequency of AM because the central part of Ricker wavelet is a cosine modulated waveform.

(2) Instantaneous frequency can be used in FM demodulation.

(3) Non-causal Hilbert operator is padded with zeros in the middle to avoid circular convolution. The minimum number of points of the Hilbert operator required for a discrete signal with length N is derived.

(4) From the analysis of zero-phase Ricker wavelet, a tree classification technique is adopted.

(5) Some lemmas for the analytic signal analysis of Gaussian noise as the ground roll motion are derived and provide the references in the tree classifier design.

(6) Three hypotheses are proposed for the constrained conditions in the tree classification to detect the candidate bright spots similar to the constrained condition of mathematical optimization problem.

(7) The major advantage of partitioning-method is that the overlapping distribution of the envelope and instantaneous frequency can be separated from different sections and attenuation effects may be avoided.

(8) In the syntactic pattern recognition for the detection of candidate bright spot, the roles of likelihood ratio test, optimal quantization encoding, and the probability of detection involving the global, local detection and threshold setting in the detection of candidate bright spots are quite important.

(9) Syntactic pattern recognition technique is used to recognize the string of bright spot in a two dimensional seismogram. Three kinds of string distance computation are proposed to test the continuity of bright spot pattern.

CHAPTER II

ANALYTIC SIGNAL ANALYSIS: FEATURE EXTRACTION

2.1 Introduction

Feature extraction is the most important part in pattern recognition. The physical meaning and separability power of features are concerned. In order to extract features from seismic signal, analytic signal analysis is applied. In this Chapter, analytic signal analyses in AM, FM, sinusoidal signal, seismic Ricker wavelet, and Gaussian noise are discussed.

Zero-phase Ricker wavelets are usually used in the simulation of seismic analysis [rob81a, tan79a]. The pattern wavelet of bright spot in real data can be compared with the central part of zero-phase Ricker wavelet. From Chapter 1, the physical properties of bright spot is relative. Here, 20Hz zero-phase Ricker wavelet is simulated as the reflection wavelet of bright spot. The 20Hz Ricker wavelet has the physical properties of high amplitude, low frequency content, and phase reversal. 30Hz zero-phase Ricker wavelet is simulated as the reflection wavelet of non-bright spot. At first, pattern recognition techniques will be applied to the classification of Ricker wavelets in a simulated seismic trace and the detection of candidate bright spot in the simulated seismogram. The one dimensional classification results can be used for two dimensional classification problem. From the classification result

of simulated seismogram, the detected portion should be a continuous reflection layer. At last, pattern recognition techniques will be applied to real seismograms. These will be described in Chapter 3. In Chapter 6, syntactic pattern recognition will be used to recognize the string of bright spot. The final result of bright spot detection will be given.

From the analysis of zero-phase Ricker wavelet, a tree classification technique is adopted. The analytic signal analysis of Gaussian noise as the ground roll motion provides the references in the tree classifier design. These will be discussed in Chapter 3. The resolution analysis of Ricker wavelet in this Chapter can be used to help the interpretation of thin-bed effect in Chapter 3.

Analytic signal [gab46a, fra69a] has usually been used in radar signal analysis, but in recent years it has become more and more important in seismic signal processing [far75a, tan77a, tan79a, hua81a, hua82a, hua83a, hua83b, rob82a, hag81a]. Envelope, instantaneous phase, and instantaneous frequency are some of the parameters in analytic signal representation. Envelope describes the shape of the signal. Instantaneous frequency extracts the internal property of the signal and is more important than the other two. Hilbert transform theorem (named here) plays an important role in the analytic signal analysis. In applications, the seismic zero-phase Ricker wavelets and sinusoidal signals can be considered as AM and the instantaneous frequency of these signals can be derived. The number of points of Hilbert operator that should be used are not discussed in [tan77a, 79a, 80a]. So the minimum number of points for the Hilbert operator in the discrete implementation will be discussed. Gaussian bandpass noise is simulated as the ground roll motion in the seismic recording system. Properties of the analytic signal in the case of Gaussian 10 - 60 Hz white

noise will be discussed here. Different definitions of envelope function and phase function are derived in [tho69a]; the distributions are Rayleigh and uniform respectively in the continuous time domain. Fortunately, the distributions of envelope and instantaneous phase using analytic signal analysis are derived here as Rayleigh and uniform respectively in both discrete and continuous time domain. Usually frequency discriminator and phase lock loop feedback tracking techniques [zie76a, gag78a] are used in FM demodulation. But the instantaneous frequency technique presented here can also treat FM demodulation. The classification of signal and noise for the case of high S/N using envelope property is also discussed. Instantaneous frequency technique treated in the time domain can also be used to detect a hidden periodic signal when its period is unknown, not using periodogram [blo76a] or harmogram [hin82a]. In [cra67a], Cramer used the cosine function as the real part and sine function as the imaginary part of the analytic signal and derived results for envelope and instantaneous frequency. It is a special case of analytic signal because the imaginary part of the analytic signal does not come from the Hilbert transform of the original signal and Hilbert transform theorem is also not used. For non-sinusoidal signal like seismic Ricker wavelets [ric40a, 45a, 53a] and teleseismic Berlage function [far75a, hua81a], the analytic signal will be calculated by using Hilbert transform [fra69a, hua81a].

2.2 Hilbert Transfer Function and Hilbert Transform Theorem

The Hilbert transfer pair [fra69a, zie76a] is

$$H(f) = -j \operatorname{sgn} f \iff h(t) = \frac{1}{\pi t}$$

Hilbert transform (H.T.) of sinusoidal signals [fra69a, zie76a] are as follows:

$$\text{H.T.}\{\cos 2\pi f_0 t\} = \sin 2\pi f_0 t \quad \text{H.T.}\{\sin 2\pi f_0 t\} = -\cos 2\pi f_0 t$$

An important theorem, Hilbert transform theorem (named here), usually used in the signal processing is stated as follows:

If $m(t)$ and $c(t)$ have bandlimited spectra that are non-overlapping and if the spectrum of $c(t)$ lies entirely above that of $m(t)$, then $\text{H.T.}\{m(t)c(t)\} = m(t)\{\text{H.T.}(c(t))\} = m(t)\bar{c}(t)$.

Ziemer and Tranter [zie76a] have proved the theorem in the time domain. This theorem can also be proved in the frequency domain.

2.3 Analytic Signal and Its Representations

The analytic signal $\psi(t)$ of a real time function $s(t)$ is a complex signal [fra69a, hua81a]:

$$\psi(t) = s(t) + j \bar{s}(t)$$

where $\bar{s}(t)$ is the Hilbert transform of $s(t)$.

The analytic signal representations are defined as follows.

Envelope:

$$\text{Env}\{s(t)\} = A(t) = |\psi(t)| = \sqrt{s^2(t) + \bar{s}^2(t)}$$

Instantaneous phase:

$$\vartheta(t) = \angle \psi(t) = \tan^{-1} \frac{\bar{s}(t)}{s(t)}$$

or for $\psi(t) = |\psi(t)| \exp\{j\vartheta(t)\}$

$$\ln \psi(t) = \ln |\psi(t)| + j \vartheta(t)$$

then $\vartheta(t) = \text{Im}[\ln \psi(t)]$

Instantaneous frequency:

$$f_i(t) = \frac{1}{2\pi} \frac{d\vartheta(t)}{dt} = \frac{1}{2\pi} \frac{d}{dt} \left\{ \tan^{-1} \frac{\bar{s}(t)}{s(t)} \right\}$$

$$= \frac{1}{2\pi} \frac{s(t) \frac{d\bar{s}(t)}{dt} - \bar{s}(t) \frac{ds(t)}{dt}}{s^2(t) + \bar{s}^2(t)}$$

$$\text{or } f_i(t) = \frac{1}{2\pi} \frac{d\vartheta(t)}{dt} = \frac{1}{2\pi} \frac{d}{dt} \text{Im}\{\ln \psi(t)\}$$

$$= \frac{1}{2\pi} \text{Im}\left\{ \frac{d}{dt} \ln \psi(t) \right\} = \frac{1}{2\pi} \text{Im}\left\{ \frac{\dot{\psi}(t)}{\psi(t)} \right\}$$

2.4 Analytic Signal Analysis in Sinusoidal Signals

Analytic signal analysis is used to extract features from original signal. In order to test the power of separability for the extracted features, the use of analytic signal analysis in sinusoidal signals is discussed. Suppose there are two sinusoidal signals as follows.

$$s_1(t) = 0.03 \cos(2\pi \cdot 20 \cdot t), \text{ then } A(t) = 0.03, f_i(t) = 20 \text{ Hz}.$$

$$s_2(t) = 0.02 \cos(2\pi \cdot 30 \cdot t), \text{ then } A(t) = 0.02, f_i(t) = 30 \text{ Hz}.$$

Envelope and instantaneous frequency of the above two sinusoidal signals are shown as above. In the physical meaning, envelope equals to the maximum absolute amplitude of the sinusoidal signal, instantaneous frequency equals to the carrier frequency of the sinusoidal signal. This is in the time domain, not in the frequency domain. The distribution of envelope and instantaneous frequency is shown in Fig. 2.1. From Fig. 2.1, the power of separability for the sinusoidal signals is good. Based on this result, analytic signal representations can be used as the features in the seismic signal analysis.

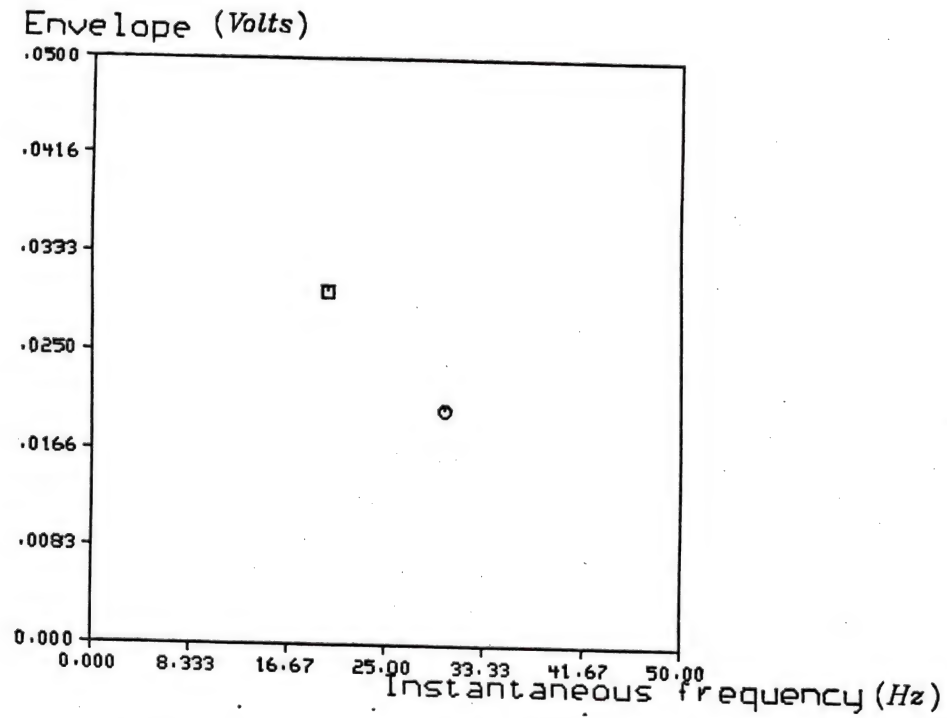


Figure 2.1 Feature distribution of two cosine signals

Table 2.1 Hilbert transform

	...	h_{-3}	h_{-2}	h_{-1}	h_0	h_1	h_2	h_3	...
a_0		$a_0 h_{-3}$	$a_0 h_{-2}$	$a_0 h_{-1}$	$a_0 h_0$	$a_0 h_1$	$a_0 h_2$	$a_0 h_3$	
a_1		$a_1 h_{-3}$	$a_1 h_{-2}$	$a_1 h_{-1}$	$a_1 h_0$	$a_1 h_1$	$a_1 h_2$	$a_1 h_3$	
a_2		$a_2 h_{-3}$	$a_2 h_{-2}$	$a_2 h_{-1}$	$a_2 h_0$	$a_2 h_1$	$a_2 h_2$	$a_2 h_3$	
a_3		$a_3 h_{-3}$	$a_3 h_{-2}$	$a_3 h_{-1}$	$a_3 h_0$	$a_3 h_1$	$a_3 h_2$	$a_3 h_3$	
	$t = 0$	$t = 1$	$t = 2$	$t = 3$					

2.5 Implementation in Discrete Calculations and Minimum Number of Truncated Hilbert Operators Required for a Finite Discrete Signal with Length N

From [gol69a, opp75a, rab75a], a Hilbert operator can be written as follows:

$$h(n) = \frac{1 - \exp[jn\pi]}{n\pi} \text{ for } n \neq 0$$

$$= 0 \quad \text{for } n = 0$$

$\bar{s}(n)$ is $s(n)$ convolving with the Hilbert operator $h(n)$. That is,

$$\bar{s}(n) = \frac{1}{\pi} \sum_{m=-\infty, m \neq n}^{\infty} s(m) \frac{[1 - \exp j\pi(n-m)]}{n-m}$$

$$= \frac{1}{\pi} \sum_{m=-\infty, m \neq 0}^{\infty} s(m-n) \frac{[1 - \exp(j\pi m)]}{m}$$

$$= \frac{2}{\pi} \sum_{m=-\infty, m \neq 0}^{\infty} s(m-n) \frac{\sin^2(\frac{m\pi}{2})}{m}$$

$$\text{or } \bar{s}(n\tau) = \tau \sum_{k=-\infty}^{\infty} h(n\tau - k\tau) s(k\tau)$$

In practice, the signal $s(k\tau)$ has only a finite extent. Suppose that $s(k\tau)$ is zero outside the index range $k=0, 1, \dots, N-1$.

$$\bar{s}(n\tau) = \tau \sum_{k=0}^{N-1} h(n\tau - k\tau) s(k\tau) \quad n=0, 1, \dots, N-1.$$

$$\text{or } \bar{s}(n\tau) = \tau \sum_{k=-(N-1)}^{N-1} h(k\tau) s(n\tau - k\tau) \quad n=0, 1, \dots, N-1.$$

The number of points needs for applying Hilbert operator is not discussed in [tan77a, 79a, 80a]. In [rab75a], the optimum design of bandpass Hilbert transformer is derived. But the effect of using N-point finite signal is not discussed. If a finite discrete signal is given as (a_0, a_1, a_2, a_3) , $N=4$, the Hilbert transform can be constructed by following Table 2.1. Summation of the slant elements equals to the output at $\dots, t=0, t=1, t=2, t=3, \dots$ etc. From Table 2.1, the effective Hilbert

operators at time $t=0$ to $t=3$ when the signal is present are $h_{-3}, h_{-2}, \dots, h_2, h_3$. Seven points of Hilbert operator are used in the four point signal. If the number of Hilbert operator is larger than 7 points, the outputs at $t=0$ to $t=3$ are the same as the outputs of using 7-point Hilbert operator, although the outputs at both ends outside the interval ($t=0$ to $t=3$) are different. So for a finite discrete signal with length N , the minimum number of the truncated Hilbert operators is $2N-1$. There is an example as follows.

Example 1:

In Table 2.2, the finite signal is given at interval $t=11$ to $t=16$, its values are 1, and its length is $N=6$ points. From the above criterion, the minimum number of points for Hilbert operator should be $2N-1 = 11$. If a 9-point (less than 11) Hilbert operator is used, the outputs at $t=11$ to $t=16$ are different from the outputs of using an 11-point Hilbert operator. If a 13- or a 15- point (larger than 11) Hilbert operator is used, the outputs at $t=11$ to $t=16$ will be the same as the outputs of using the 11-point Hilbert operator, although the tails outside the interval ($t=11$, $t=16$) are different.

It is much faster to implement $\bar{s}(n)$ in the frequency domain using the FFT algorithm. In order to avoid circular convolution, signal $s(n)$ should be padded with sufficient zeros. For non-causal Hilbert operator, $h(n)$ should be padded with sufficient zeros in the middle. Using the base 2 FFT algorithm, the sequences $s(n)$ and $h(n)$ have to be zero-padded (ZP) so that each is $(3N-2)_2$ elements long, where $(3N-2)_2$ is the smallest integer that is a power of 2 and is greater than $3N-2$. Therefore, the frequency domain implementation may be expressed as

$$\bar{s}(n\tau) = \tau * IFFT [FFT(s(n\tau) \text{ with ZP}) * FFT(h(n\tau) \text{ with ZP in middle})]$$

Table 2.2 Output of Hilbert operator

9 point Hilbert operator				11 point Hilbert operator			
	signal	output			signal	output	
1	.0000	.0	.0000	1	.0000	.0	.0000
2	.6366	.0	.0000	2	.6366	.0	.0000
3	.0000	.0	.0000	3	.0000	.0	.0000
4	.2122	.0	.0000	4	.2122	.0	.0000
5	.0000	.0	.0000	5	.0000	.0	.0000
6	.0000	.0	.0000	6	.1273	.0	-.1273
7	.0000	.0	.0000	7	.0000	.0	-.1273
8	.0000	.0	-.2122	8	.0000	.0	-.3395
9	.0000	.0	-.2122	9	.0000	.0	-.3395
10	.0000	.0	-.8488	10	.0000	.0	-.9762
11	.0000	1.0	-.8488	11	.0000	1.0	-.9762
12	.0000	1.0	-.2122	12	.0000	1.0	-.2122
13	.0000	1.0	-.2122	13	.0000	1.0	-.2122
14	.0000	1.0	.2122	14	.0000	1.0	.2122
15	.0000	1.0	.2122	15	.0000	1.0	.2122
16	.0000	1.0	.8488	16	.0000	1.0	.9762
17	.0000	.0	.8488	17	.0000	.0	.9762
18	.0000	.0	.2122	18	.0000	.0	.3395
19	.0000	.0	.2122	19	.0000	.0	.3395
20	.0000	.0	.0000	20	.0000	.0	.1273
21	.0000	.0	.0000	21	.0000	.0	.1273
22	.0000	.0	.0000	22	.0000	.0	.0000
23	.0000	.0	.0000	23	.0000	.0	.0000
24	.0000	.0	.0000	24	.0000	.0	.0000
25	.0000	.0	.0000	25	.0000	.0	.0000
26	.0000	.0	.0000	26	.0000	.0	.0000
27	.0000	.0	.0000	27	.0000	.0	.0000
28	.0000	.0	.0000	28	-.1273	.0	.0000
29	.0000	.0	.0000	29	.0000	.0	.0000
30	-.2122	.0	.0000	30	-.2122	.0	.0000
31	.0000	.0	.0000	31	.0000	.0	.0000
32	-.6366	.0	.0000	32	-.6366	.0	.0000

Table 2.2 Continued

13 point Hilbert				15 point Hilbert			
operator	signal	output		operator	signal	output	
1	.0000	.0	.0000	1	.0000	.0	.0000
2	.6366	.0	.0000	2	.6366	.0	.0000
3	.0000	.0	.0000	3	.0000	.0	.0000
4	.2122	.0	.0000	4	.2122	.0	-.0909
5	.0000	.0	.0000	5	.0000	.0	-.0909
6	.1273	.0	-.1273	6	.1273	.0	-.2183
7	.0000	.0	-.1273	7	.0000	.0	-.2183
8	.0000	.0	-.3395	8	.0909	.0	-.4305
9	.0000	.0	-.3395	9	.0000	.0	-.4305
10	.0000	.0	-.9762	10	.0000	.0	-.9762
11	.0000	1.0	-.9762	11	.0000	1.0	-.9762
12	.0000	1.0	-.2122	12	.0000	1.0	-.2122
13	.0000	1.0	-.2122	13	.0000	1.0	-.2122
14	.0000	1.0	.2122	14	.0000	1.0	.2122
15	.0000	1.0	.2122	15	.0000	1.0	.2122
16	.0000	1.0	.9762	16	.0000	1.0	.9762
17	.0000	.0	.9762	17	.0000	.0	.9762
18	.0000	.0	.3395	18	.0000	.0	.4305
19	.0000	.0	.3395	19	.0000	.0	.4305
20	.0000	.0	.1273	20	.0000	.0	.2183
21	.0000	.0	.1273	21	.0000	.0	.2183
22	.0000	.0	.0000	22	.0000	.0	.0909
23	.0000	.0	.0000	23	.0000	.0	.0909
24	.0000	.0	.0000	24	.0000	.0	.0000
25	.0000	.0	.0000	25	.0000	.0	.0000
26	.0000	.0	.0000	26	-.0909	.0	.0000
27	.0000	.0	.0000	27	.0000	.0	.0000
28	-.1273	.0	.0000	28	-.1273	.0	.0000
29	.0000	.0	.0000	29	.0000	.0	.0000
30	-.2122	.0	.0000	30	-.2122	.0	.0000
31	.0000	.0	.0000	31	.0000	.0	.0000
32	-.6366	.0	.0000	32	-.6366	.0	.0000

Since Hilbert operator is not causal, when a finite discrete signal convolves with Hilbert operator, the output always has small-value tails before and after the finite interval where the signal is zero outside the interval. From physical property, it is reasonable to assume that the instantaneous frequency is zero when the signal is zero. So if the denominator in the discrete instantaneous frequency is less than a threshold (for example 0.00001), then $f_i(n\tau)=0$. The other reason is to avoid large instantaneous frequency $f_i(n\tau)$ for small denominator. In the case of negative instantaneous frequency due to discrete calculation, they will be set to zero also. High peaks of instantaneous frequency occur at both ends of a finite interval signal because the derivative will enhance the high frequency regions.

2.6 Instantaneous Frequency in AM Waveforms

Several lemmas are presented in this section.

Lemma 1:

If $m(t)$ is a low frequency spectrum and f_0 is a high carrier frequency, both spectra are non-overlapping, then the instantaneous frequency of $m(t)\cos(2\pi f_0 t)$, $m(t)\sin(2\pi f_0 t)$, $(1+m(t))\cos(2\pi f_0 t)$, and $(1+m(t))\sin(2\pi f_0 t)$ is f_0 , that is the carrier frequency.

Proof:

Case 1. $s(t)=m(t)\cos 2\pi f_0 t$

After taking Hilbert transform,

$$\bar{s}(t)=m(t)\sin 2\pi f_0 t$$

$$\psi(t)=s(t)+js(t)=m(t)\exp[j2\pi f_0 t] \quad f_i(t)=\frac{1}{2\pi}\text{Im}\left\{\frac{\dot{\psi}(t)}{\psi(t)}\right\}=f_0.$$

The proofs of the other cases are based on the same procedure.

Lemma 2:

The instantaneous frequency of AM delayed signals in Lemma 1, $m(t)\cos(2\pi f_0(t-t_0))$ etc., is still f_0 .

These two lemmas are used to infer the instantaneous frequency of Ricker wavelets later.

2.7 Instantaneous Frequency of Sinusoidal Waveforms with AM Applications

As in Lemma 1, the sum of many sinusoidal waveforms can be derived for AM signals, then the carrier frequency of AM will be the instantaneous frequency. Several examples are shown in Table 2.3. The following two lemmas are derived.

Lemma 3:

If the frequencies of sinusoidal waveforms are $f_1, f_2, f_3, \dots, f_N$, and the sum of sinusoidal waveforms satisfies the properties of Lemma 1, then the instantaneous frequency of this signal is f_i ,

$$f_i = \frac{f_{largest} + f_{smallest}}{2}$$

Lemma 4:

From Lemma 3, if the frequencies $f_1, f_2, f_3, \dots, f_N$, of the sinusoidal waveforms form an arithmetic series and the sum of these waveforms satisfies Lemma 1, then the instantaneous frequency is

Table 2.3 Instantaneous Frequency of the Sinusoidal Waveforms

		Signal	I.F.
No baseband	1	$s(t) = \cos 2\pi f_0 t$	f_0
	2	$s(t) = \sin 2\pi f_0 t$	f_0
	3	$s(t) = \cos 2\pi f_0 t + \sin 2\pi f_0 t$	f_0
Delay case	1	$s(t) = \cos 2\pi f_0 t + \cos 2\pi f_0 (t - t_0)$	f_0
	2	$s(t) = \cos 2\pi f_0 t + \sin 2\pi f_0 (t - t_0)$	f_0
	3	$s(t) = \sin 2\pi f_0 t + \sin 2\pi f_0 (t - t_0)$	f_0
Sum of sinusoidal signal	1	$s(t) = a \cos 2\pi 4f_0 t + b \cos 2\pi 6f_0 t$ $+ b \cos 2\pi 8f_0 t + a \cos 2\pi 10f_0 t$ $= 2(a \cos 2\pi 3f_0 t + b \cos 2\pi f_0 t)$ $\cdot \cos 2\pi 7f_0 t$	$7f_0$
	2	$s(t) = a \cos 2\pi 2f_0 t - b \sin 2\pi 3f_0 t$ $+ b \sin 2\pi 9f_0 t + a \cos 2\pi 10f_0 t$ $= 2(a \cos 2\pi 4f_0 t + b \sin 2\pi 3f_0 t)$ $\cdot \cos 2\pi 6f_0 t$	$6f_0$
	3	$s(t) = \sin 2\pi 2f_0 t + \sin 2\pi 6f_0 t$ $= 2 \sin 2\pi 4f_0 t \cos 2\pi 2f_0 t$	$4f_0$

$$f_i = \frac{f_1 + f_2 + f_3 + \dots + f_N}{N}$$

$$= \frac{f_{largest} + f_{smallest}}{2}$$

2.8 Rayleigh and Uniform Distributions

Rayleigh and uniform distributions have been derived in [pap65a]. If two random variables X and Y are Gaussian, independent, with zero mean and equal variance, then the function

$$Z = \sqrt{X^2 + Y^2}$$

has a Rayleigh distribution as follows.

$$P_Z(z) = \frac{z}{\sigma^2} \exp\left[-\frac{z^2}{2\sigma^2}\right], z \geq 0$$

$$= 0, z < 0$$

$$\text{Let } W = \tan^{-1} \frac{X}{Y},$$

then random variable W is uniform in the interval $(-\frac{\pi}{2}, \frac{\pi}{2})$.

These results are used in the following analysis.

2.9 Sinusoidal Signal and Gaussian Noise in Analytic Signal Analysis

The properties of the noise in the analytic signal analysis are investigated here. In order to collect seismic reflection signal, there is a bandpass filter at the seismic receiving instrument. The ground motion noise also passes through this bandpass filter. The simulated Gaussian bandpass white noise passing through 10 - 60 Hz filter can be written as

[zie75a, gag78a]

$$n(t) = n_c(t)\cos(\omega_c t + \psi) - n_s(t)\sin(\omega_c t + \psi) \text{ where } f_c = 35\text{Hz}.$$

From Ziemer and Tranter [zie76a], $n_c(t)$ is generated by $n(t)2\cos(\omega_c t + \psi)$ passing through an ideal low-pass filter 0-25 Hz and $n_s(t)$ is generated by $n(t)[-2\sin(\omega_c t + \psi)]$ passing through the same ideal low-pass filter. If $n(t)$ is a stationary Gaussian process, then $n_c(t)$ and $n_s(t)$ must be Gaussian processes, with mean zero and variance σ^2 . If the power spectral density function of the Gaussian process $n(t)$, $S_n(f)$, is 10 - 60 Hz white, i.e. symmetric with respect to f_c , then the cross-correlation $R_{sc}(\tau) = R_{cs}(\tau) = 0$, i.e., $n_c(t)$ and $n_s(t)$ are independent Gaussian processes [zie76a, gag78a]. Gaussian white noise $n(t)$ is filtered by the 10 - 60 Hz bandpass filter. The carrier frequency of $n(t)$ is $f_c = 35\text{Hz}$. $n_c(t)$ and $n_s(t)$ are 0-25Hz low-pass so $f_c = 35\text{Hz}$ lies above the spectra of $n_c(t)$ and $n_s(t)$. Applying Hilbert transform theorem in Section 2.2, the Hilbert transform of $n(t)$, $\bar{n}(t)$, is

$$\bar{n}(t) = n_c(t)\sin(\omega_c t + \psi) + n_s(t)\cos(\omega_c t + \psi)$$

Although the same form of $n(t)$ and $\bar{n}(t)$ is given in [pap65a], the generations of $n_c(t)$ and $n_s(t)$ are different. In the following derivation, set $\psi = 0$ for convenient calculation. For signal, the sinusoidal signal is $s(t) = S\cos(\omega_1 t)$.

Case 1: Gaussian 10 - 60 Hz white noise process only.

Bracewell [bra78a] stated that " Regarding $y(t)$ as the superposition of harmonic components in unrelated phases, we see that the process of Hilbert transformation which shifts every Fourier component by a different amount, gives another but independent superposition of the same kind. Based on these assumptions it is thus found that the envelope is distributed according to a Rayleigh distribution," where

$y(t) = \bar{n}(t)$ here. But this statement lacks a mathematical proof.

Applying Hilbert transform theorem to $n(t)$, we can prove it here.

Substituting $n(t)$ and $\bar{n}(t)$ into the formula of the analytic signal representations,

$$\text{Env}\{s(t)\} = A(t) = |\psi(t)| = \sqrt{n^2(t) + \bar{n}^2(t)} = \sqrt{n_c^2(t) + n_s^2(t)}$$

where $n_c(t)$ and $n_s(t)$ are $N(0, \sigma^2)$ and independent, so $A(t)$ is a Rayleigh distribution.

$$P_{A(t)}(a) = \frac{a}{\sigma^2} \exp\left[-\frac{a^2}{2\sigma^2}\right], a \geq 0$$

Lemma 5: The envelope of Gaussian bandpass white noise is a Rayleigh distribution.

For instantaneous frequency,

$$f_{I.F.}(t) = \frac{1}{2\pi} \frac{n(t) \frac{d\bar{n}(t)}{dt} - \bar{n}(t) \frac{dn(t)}{dt}}{n^2(t) + \bar{n}^2(t)}$$

$$= \frac{1}{2\pi} \left[\omega_c + \frac{n_c(t)\dot{n}_s(t) - n_s(t)\dot{n}_c(t)}{n_c^2(t) + n_s^2(t)} \right]$$

So the instantaneous frequency is centered at the carrier frequency f_c .

The denominator, $n_c(t)$, $\dot{n}_c(t)$, $n_s(t)$, and $\dot{n}_s(t)$ are Gaussian.

$n_c^2(t) + n_s^2(t)$ is $\chi^2(2)$, Chi-square of 2 degree of freedom, but

$\frac{n_c(t)\dot{n}_s(t) - n_s(t)\dot{n}_c(t)}{n_c^2(t) + n_s^2(t)}$ is not expected to have any specific probability

distribution.

Case 2: Sinusoidal signal plus Gaussian 10 - 60 Hz white noise with the same carrier frequency f_c .

$$x(t) = s(t) + n(t) = S \cos \omega_c t + n_c(t) \cos(\omega_c t + \psi) - n_s(t) \sin(\omega_c t + \psi)$$

$$\text{Env}\{x(t)\} = A(t) = |\psi(t)| = \sqrt{x^2(t) + \bar{x}^2(t)} = \sqrt{(S + n_c(t))^2 + n_s^2(t)}$$

The distribution of $A(t)$ is a Rician density [gag78a].

$$P_{A(t)}(a) = \frac{a}{\sigma^2} \exp\left[-\frac{(a^2 + S^2)}{2\sigma^2}\right] I_0\left(\frac{aS}{\sigma^2}\right), a \geq 0$$

where $I_0\left(\frac{aS}{\sigma^2}\right)$ is the modified Bessel function of order zero.

For strong signal, $S^2 \gg \sigma^2$

then, $A(t) = S + n_c(t)$

Hence $A(t)$ is approximately normal, with mean S and variance σ^2 :

$$P_{A(t)}(a) = \frac{1}{\sqrt{2\pi}\sigma} \exp\left[-\frac{(a-S)^2}{2\sigma^2}\right]$$

For weak signal, $S^2 \ll \sigma^2$

$$A(t) = \sqrt{n_c^2(t) + n_s^2(t)}$$

which is the same as the Rayleigh distribution in Case 1.

For instantaneous frequency,

$$\begin{aligned} f_{I.F.}(t) &= \frac{1}{2\pi} \frac{x(t) \frac{d\bar{x}(t)}{dt} - \bar{x}(t) \frac{dx(t)}{dt}}{x^2(t) + \bar{x}^2(t)} \\ &= \frac{1}{2\pi} \left[\omega_c + \frac{(S + n_c(t)) \dot{n}_s(t)}{(S + n_c(t))^2 + n_s^2(t)} \right] \end{aligned}$$

So the instantaneous frequency is always centered at the carrier frequency f_c . The experimental results for weak signal are shown in Fig. 2.2.

Case 3: Sinusoidal signal plus Gaussian 10 - 60 Hz white noise with carrier frequencies f_1 and f_c respectively.

$$x(t) = s(t) + n(t) = S \cos \omega_1 t + n_c(t) \cos(\omega_c t + \psi) - n_s(t) \sin(\omega_c t + \psi)$$

$$\begin{aligned} \text{Env}\{x(t)\} &= A(t) = |\psi(t)| = \sqrt{x^2(t) + \bar{x}^2(t)} \\ &= \sqrt{(S + m_1(t))^2 + n_c^2(t) + n_s^2(t) - m_1^2(t)} \end{aligned}$$

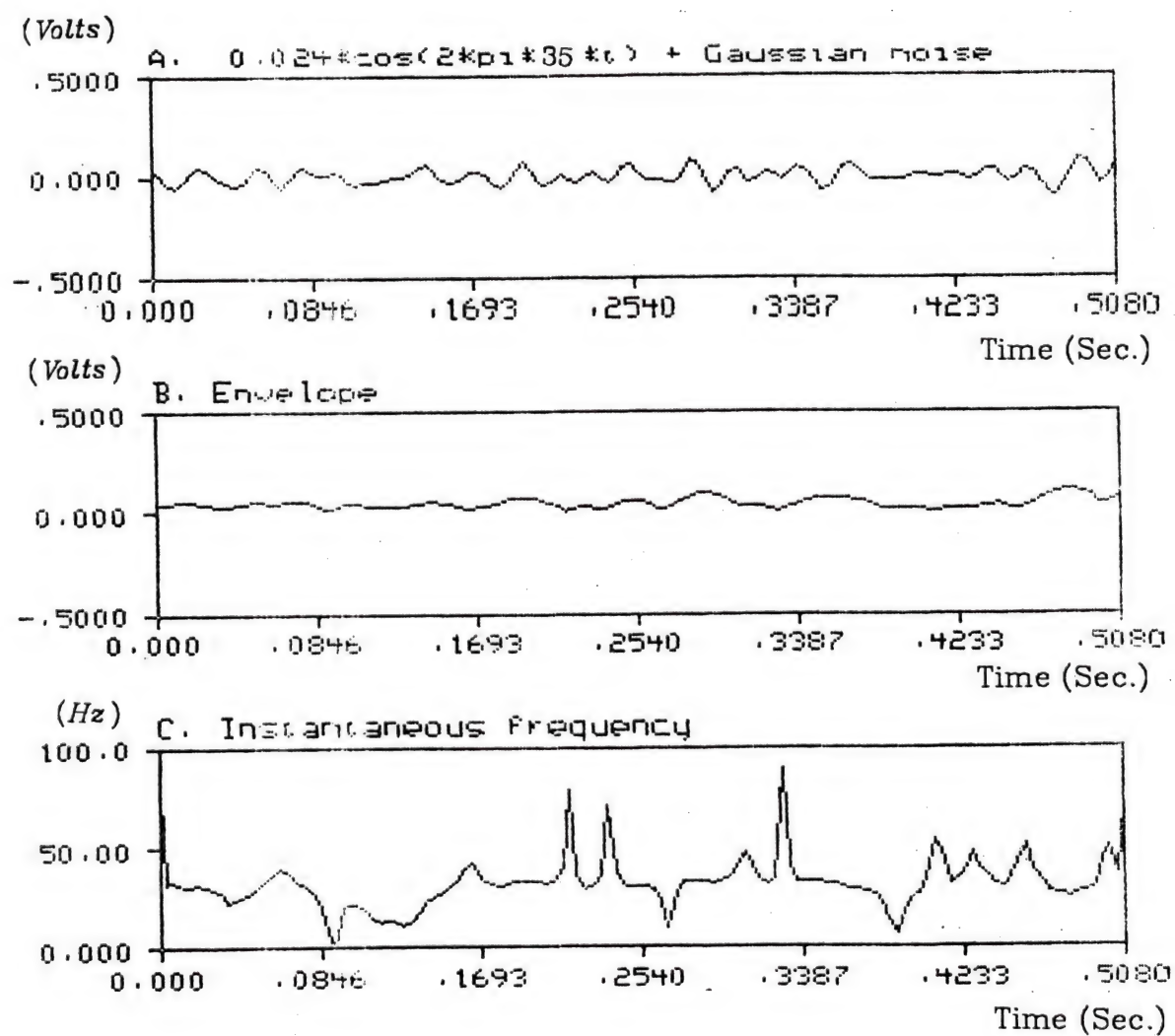


Figure 2.2A Weak signal ($f_1=35\text{Hz}$) plus Gaussian noise, its envelope and instantaneous frequency

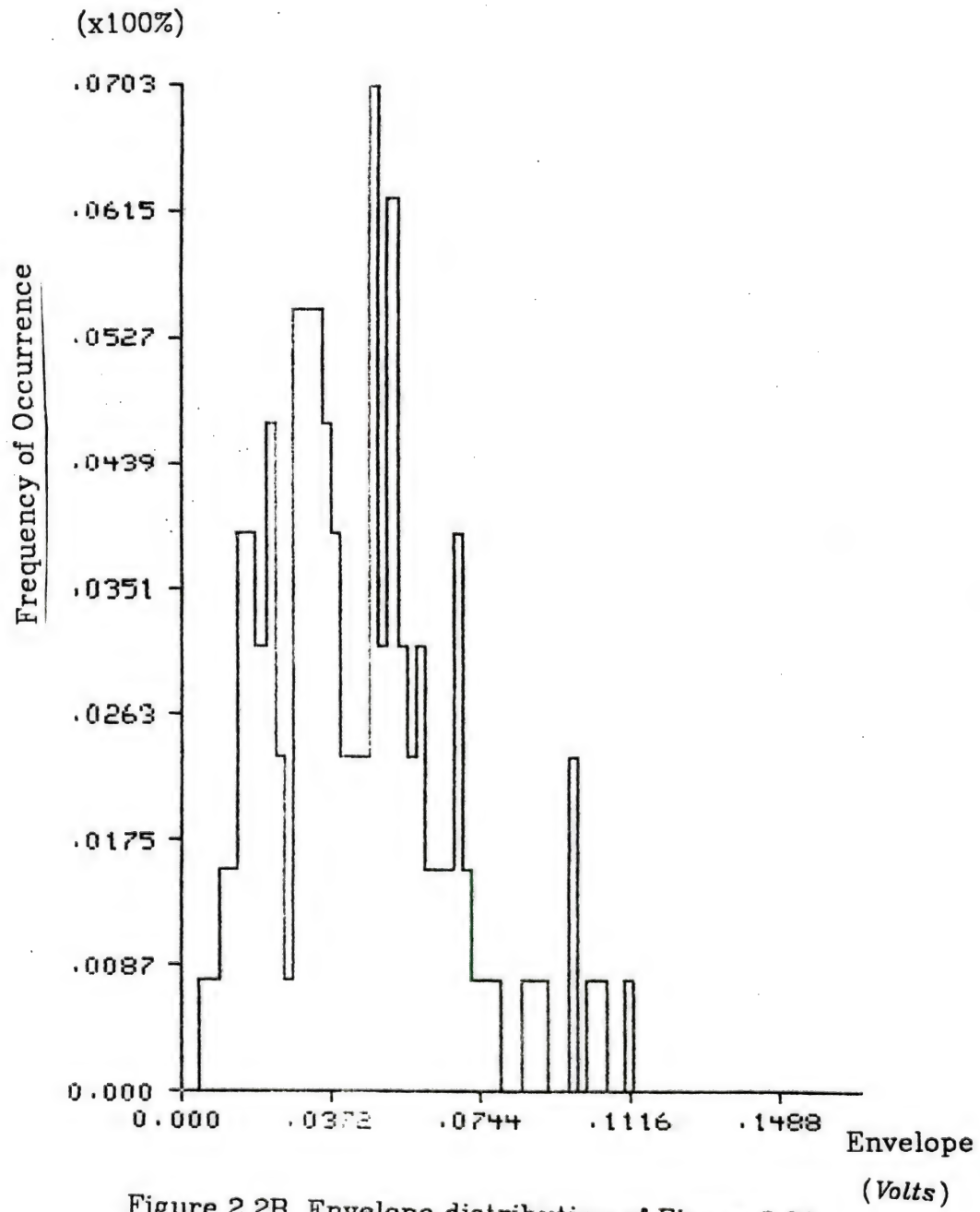


Figure 2.2B Envelope distribution of Figure 2.2A

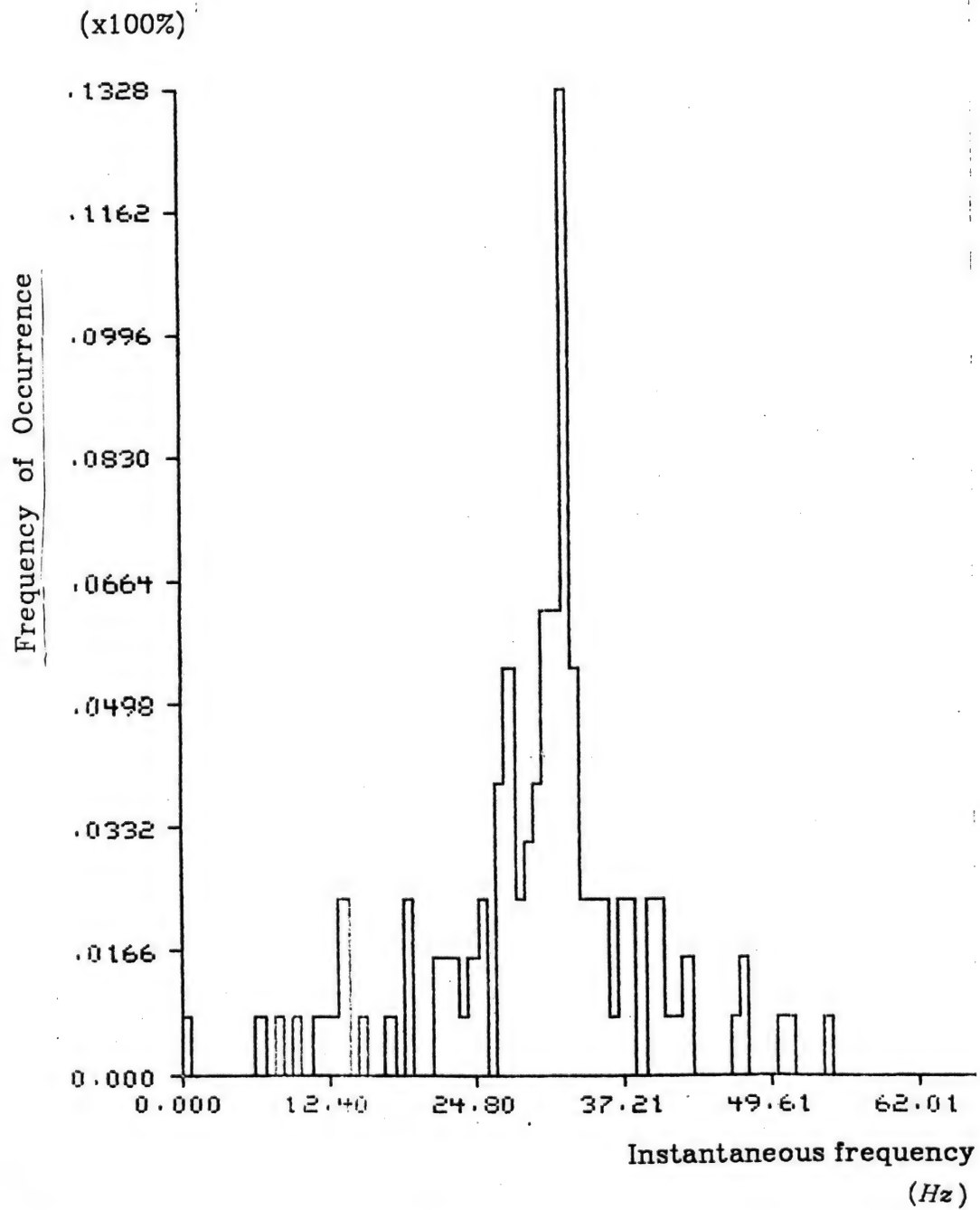


Figure 2.2C Instantaneous frequency distribution of Figure 2.2A (Instantaneous frequency centered at $f_c = 35\text{Hz}$)

where $m_1(t) = n_c(t) \cos(\omega_c - \omega_1)t - n_s(t) \sin(\omega_c - \omega_1)t$ and Gaussian $N(0, \sigma^2)$.

For strong signal, $S^2 \gg \sigma^2$

then, $A(t) = S + m_1(t)$

Hence $A(t)$ is approximately normal, with mean S and variance σ^2 :

$$P_{A(t)}(a) = \frac{1}{\sqrt{2\pi}\sigma} \exp \frac{-(a-S)^2}{2\sigma^2}$$

For weak signal, $S^2 \ll \sigma^2$

$$A(t) = \sqrt{n_c^2(t) + n_s^2(t)}$$

So $A(t)$ is a Rayleigh distribution.

For instantaneous frequency,

$$\begin{aligned} f_{I.F.}(t) &= \frac{1}{2\pi} \frac{x(t) \frac{d\bar{x}(t)}{dt} - \bar{x}(t) \frac{dx(t)}{dt}}{x^2(t) + \bar{x}^2(t)} \\ &= \frac{1}{2\pi} \frac{M_2(t)}{M_1(t)} \end{aligned}$$

where

$$M_1(t) = S^2 + n_c^2(t) + n_s^2(t) + 2Sm_1(t)$$

$$\begin{aligned} \text{and } M_2(t) &= S^2\omega_1 - S[-\dot{n}_c(t) \sin(\omega_c - \omega_1)t - \dot{n}_s(t) \cos(\omega_1 - \omega_c)t] \\ &\quad + S\omega_c m_1(t) + S\omega_1 m_1(t) + n_c^2(t)\omega_c + n_c(t)\dot{n}_s(t) - \dot{n}_c(t)n_s(t) + n_s^2(t)\omega_c \end{aligned}$$

For strong signal, $S^2 \gg \sigma^2$

$$f_{I.F.}(t) = \frac{1}{2\pi} \left[\omega_1 + \frac{M_3(t)}{M_1(t)} \right]$$

where

$$\begin{aligned} M_3(t) &= -\omega_1 n_c^2(t) - \omega_1 n_s^2(t) - S\omega_1 m_1(t) \\ &\quad - S[-\dot{n}_c(t) \sin(\omega_c - \omega_1)t - \dot{n}_s(t) \cos(\omega_1 - \omega_c)t] \\ &\quad + S\omega_c m_1(t) + n_c^2(t)\omega_c + n_c(t)\dot{n}_s(t) - \dot{n}_c(t)n_s(t) + n_s^2(t)\omega_c \end{aligned}$$

The instantaneous frequency is centered at the carrier frequency of the

signal, f_1 .

For weak signal, $S^2 \ll \sigma^2$

$$f_{L.F.}(t) = \frac{1}{2\pi} \left[\omega_c + \frac{M_4(t)}{M_1(t)} \right]$$

where

$$\begin{aligned} M_4(t) = & -\omega_c S^2 - S \omega_c m_1(t) + S^2 \omega_1 \\ & - S [-\dot{n}_c(t) \sin(\omega_c - \omega_1)t - \dot{n}_s(t) \cos(\omega_1 - \omega_c)t] \\ & + S \omega_1 m_1(t) + n_c(t) \dot{n}_s(t) - \dot{n}_c(t) n_s(t) \end{aligned}$$

So the instantaneous frequency is centered at the carrier frequency of the Gaussian noise, f_c . The experimental results of high S/N are shown in Fig. 2.3. The experimental results of low S/N are shown in Fig. 2.4.

From Case 3, for high S/N, instantaneous frequency can be used to detect a hidden periodic signal when its period is unknown. This is a different way to use periodogram [blo76a] and harmogram [hin82a].

2.10 Rayleigh Distribution of the Envelope of Gaussian Noise in Discrete Time Case

I. Discrete Envelope

$\bar{s}(n)$ is the convolution of $s(n)$ with Hilbert operator $h(n)$.

The discrete envelope is defined as

$$\begin{aligned} A(n) &= \sqrt{s^2(n) + \bar{s}^2(n)} = \sqrt{s^2(n) + \sum_{k=0}^{N-1} h(n-k)s(k)} \\ &= \sqrt{s^2(n) + \sum_{k=-(N-1)}^{N-1} h(k)s(n-k)} \quad n=0,1,2, \dots, N-1. \end{aligned}$$

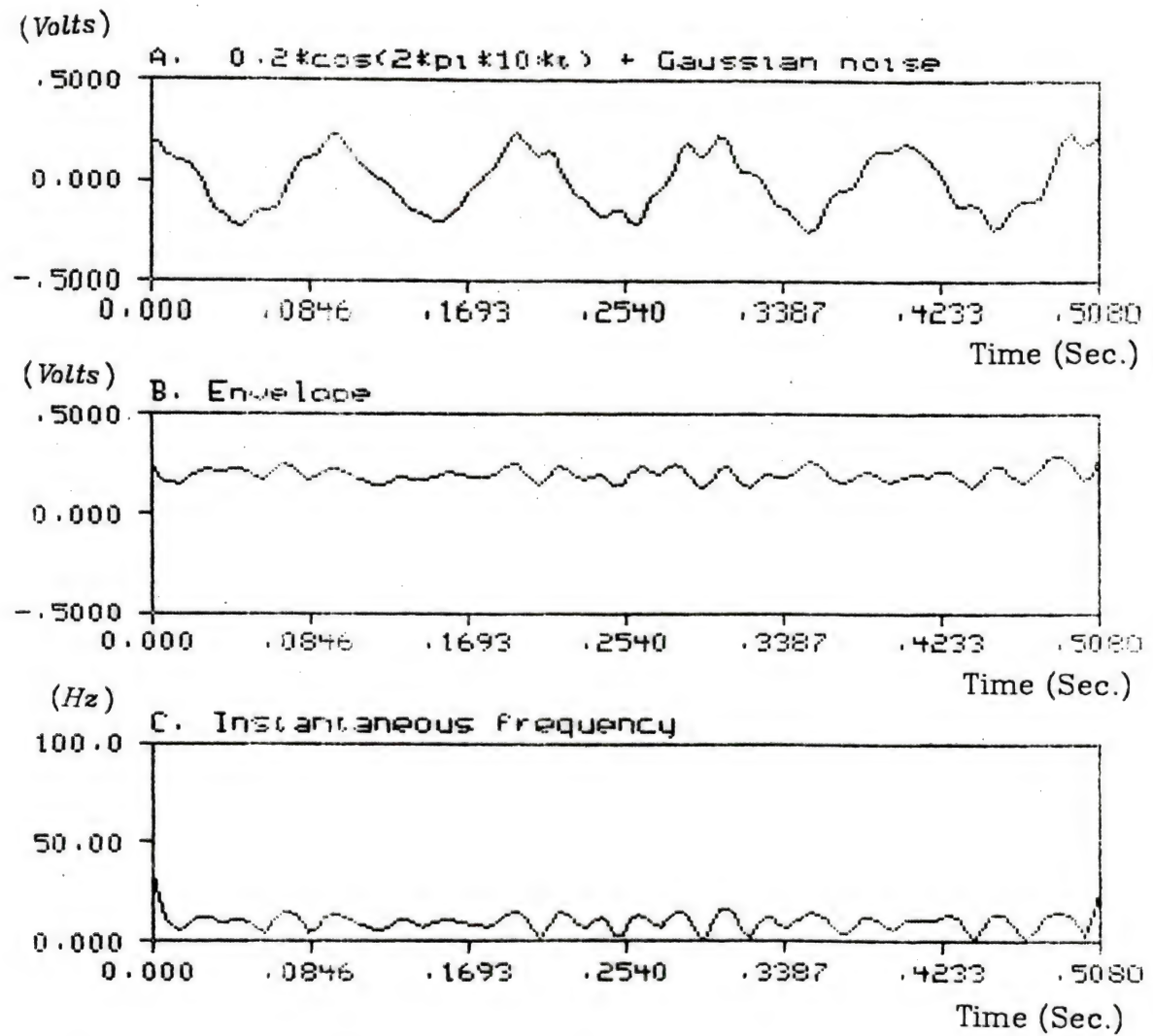


Figure 2.3A Strong signal ($f_1=10\text{Hz}$) plus Gaussian noise, its envelope and instantaneous frequency

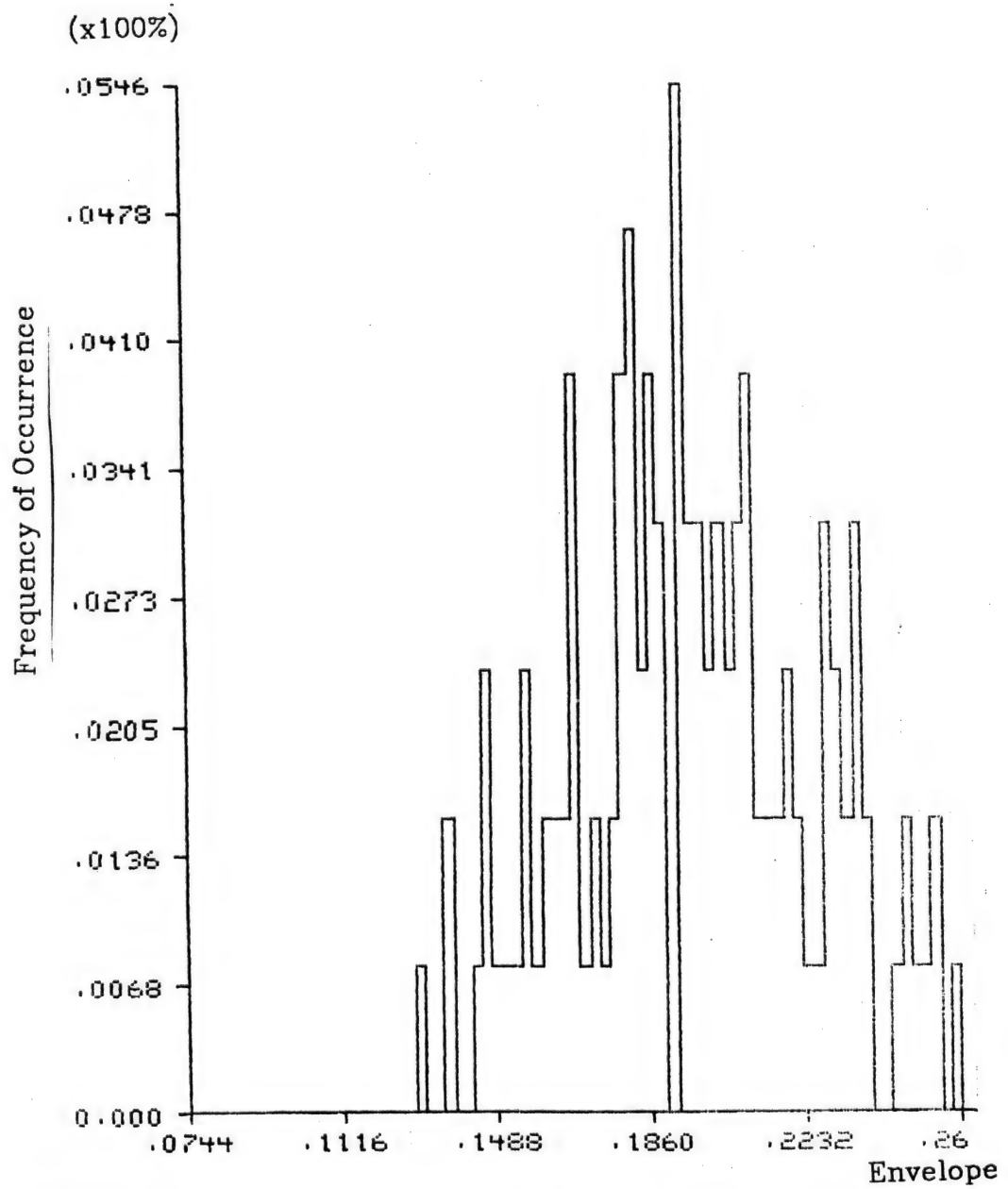


Figure 2.3B Envelope distribution of Figure 2.3A (S/N is high) (Volts)

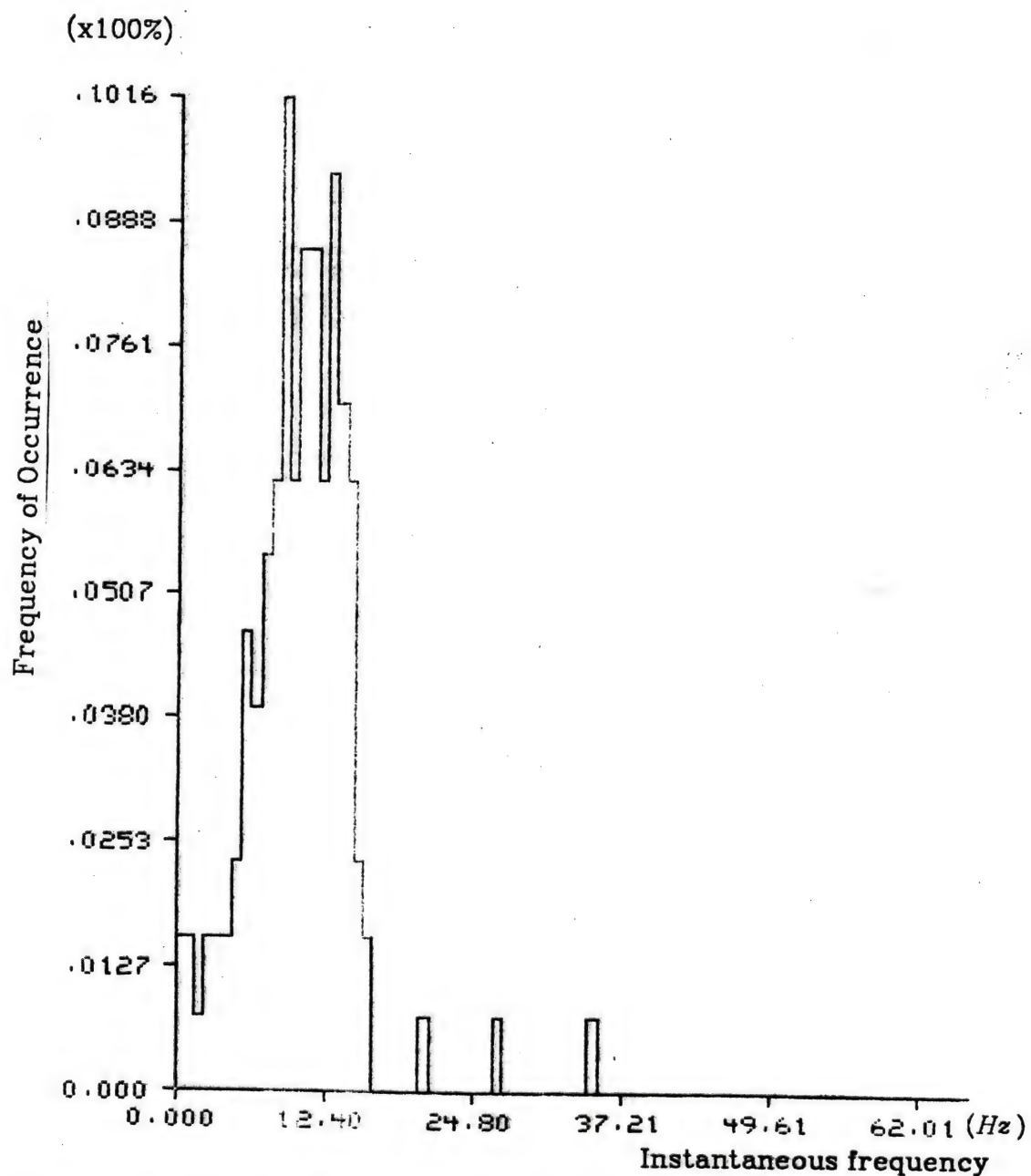


Figure 2.3C Instantaneous frequency distribution of Figure 2.3A (S/N is high)

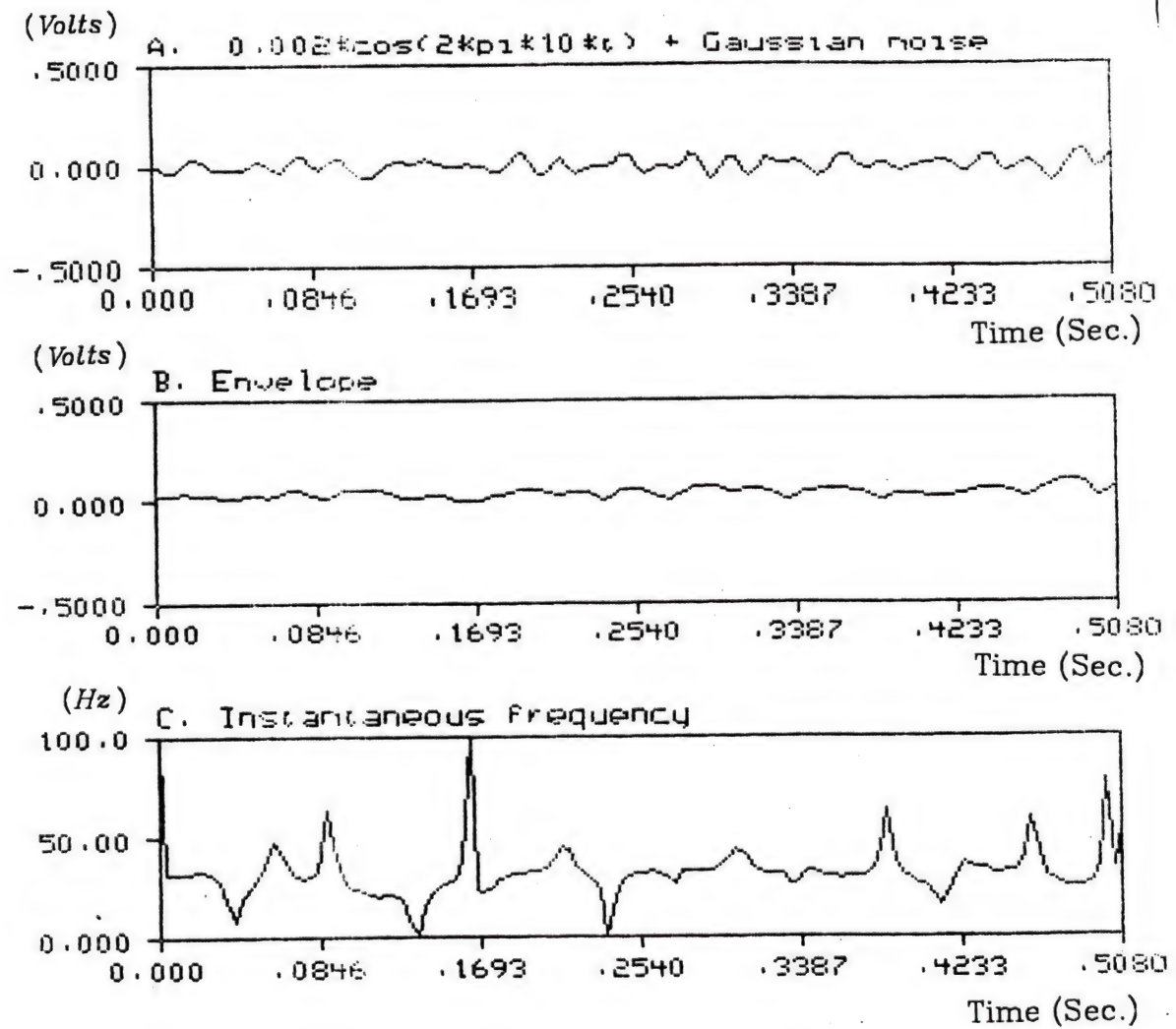


Figure 2.4A Weak signal ($f_1=10\text{Hz}$) plus Gaussian noise, its envelope and instantaneous frequency

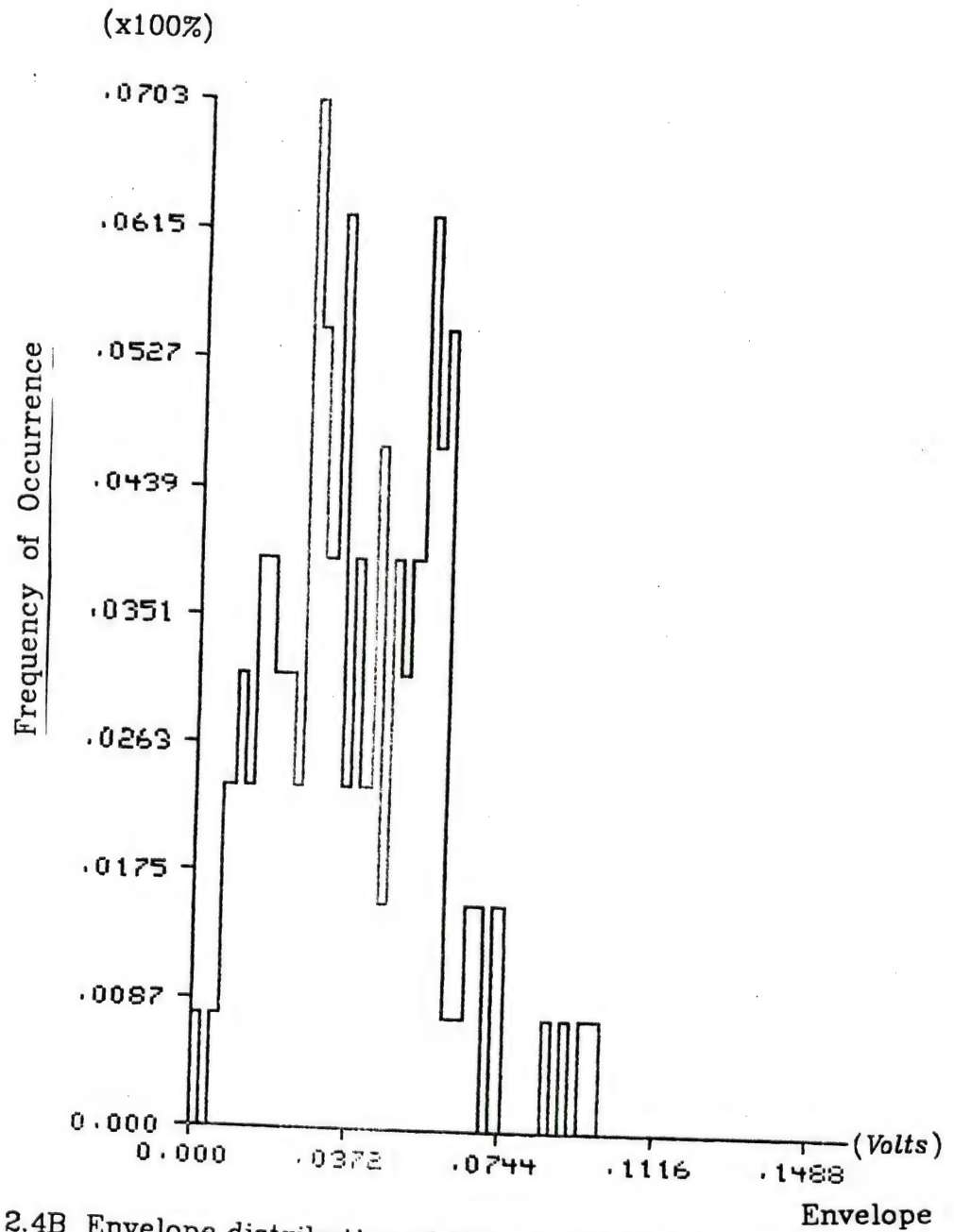


Figure 2.4B Envelope distribution of Figure 2.4A (S/N is low)

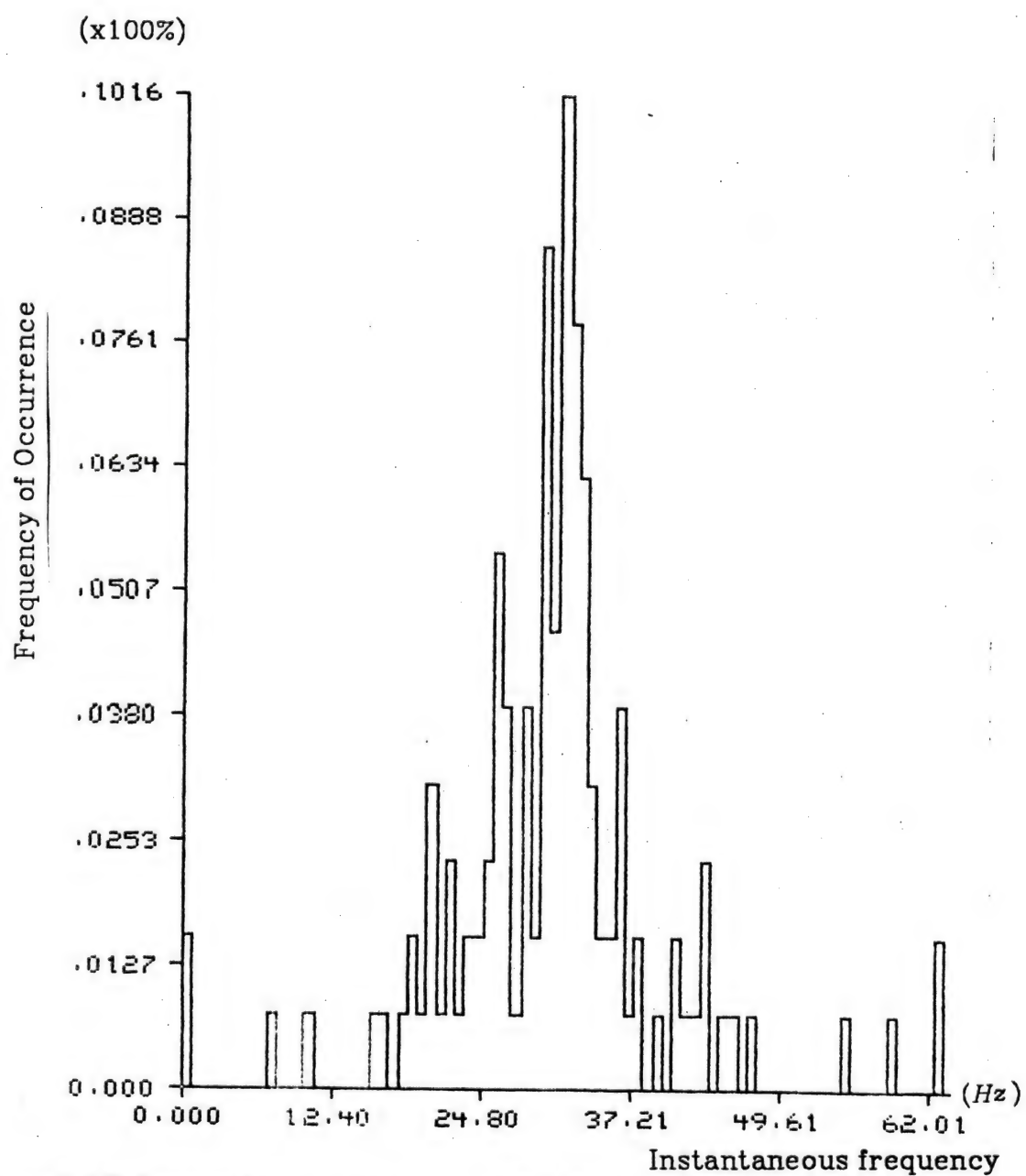


Figure 2.4C Instantaneous frequency distribution of Figure 2.4A (S/N is low)

II. Rayleigh Distribution of Discrete Envelope

Lemma 6:

Suppose that $s(n)$, $n=0, 1, 2, \dots, N-1$, where N is finite, are samples from a Gaussian independent noise, with zero mean and variance σ^2 . After Hilbert transforming, $\bar{s}(n)$ is Gaussian, independent from $s(n)$ at the time n , and the envelope distribution in the analytic signal representation is a Rayleigh density.

Proof:

$s(n)$, $n=0, 1, \dots, N-1$, are Gaussian $N(0, \sigma^2)$ and independent.

$$\bar{s}(n) = \sum_{k=-(N-1)}^{N-1} h(k) s(n-k) = \sum_{k=0}^{N-1} h(n-k) s(k)$$

$\bar{s}(n)$ is a linear combination of Gaussian $s(k)$, $k=0, 1, \dots, N-1$, and is also a Gaussian, with

$$\text{Mean of } \bar{s}(n) = E[\bar{s}(n)] = \sum_{k=0}^{N-1} h(n-k) E[s(k)] = 0, \text{ and}$$

$$\text{Variance of } \bar{s}(n) = \sum_{k=-(N-1)}^{N-1} h^2(k) \text{Var}[s(n-k)] = \sum_{k=0}^{N-1} h^2(n-k) \text{Var}[s(k)]$$

$$\text{If } N=128, \sum_{k=-128}^1 h^2(k) = 0.9037, \sum_{k=-122}^5 h^2(k) = 0.9648, \sum_{k=-118}^{11} h^2(k) = 0.9814.$$

After $n=5$, $\text{Var}[\bar{s}(n)] = \sigma^2$. So $\bar{s}(n)$ is Gaussian with $N(0, \sigma^2)$

The next step is to prove that $s(n)$ and $\bar{s}(n)$ are independent from each other at the same time $t=n$.

$$\text{Covariance}(s(n), \bar{s}(n)) = \text{COV}(s(n), \sum_{k=0}^{N-1} h(n-k) s(k))$$

$$= \text{COV}(s(n), [h(n)s(0) + h(n-1)s(1) + h(n-2)s(2) + \dots + h(0)s(n) + \dots + h(n-(N-1))s(N-1)])$$

$$= E[(s(n)-0)[h(n)s(0) + \dots + h(0)s(n) + \dots + h(n-(N-1))s(N-1)-0]]$$

$$=0+0+\dots+E[s(n)h(0)s(n)]+0+0+\dots+0$$

$$=h(0)E[s^2(n)]=0\sigma^2=0$$

(For $n \neq k$, $s(n)$ and $s(k)$ are independent.)

So $s(n)$ and $\bar{s}(n)$ are uncorrelated at the same time $t=n$. Because $s(n)$ and $\bar{s}(n)$ are Gaussian $N(0, \sigma^2)$. So they are independent at the time $t=n$.

Hence, envelope $A(n) = \sqrt{s^2(n) + \bar{s}^2(n)}$ is a Rayleigh distribution.

2.11 Instantaneous Phase of Gaussian Noise

Lemma 7:

The instantaneous phase of Gaussian white bandpass noise is a uniform distribution between $\frac{-\pi}{2}$ and $\frac{\pi}{2}$.

Proof :

(1) Continuous time case

For instantaneous phase,

$$\vartheta(t) = \tan^{-1} \frac{\bar{n}(t)}{n(t)}$$

$$n(t) = n_c(t) \cos(\omega_c t + \psi) - n_s(t) \sin(\omega_c t + \psi)$$

$$\bar{n}(t) = n_c(t) \sin(\omega_c t + \psi) + n_s(t) \cos(\omega_c t + \psi)$$

$$E[n(t)\bar{n}(t)]$$

$$= E[(n_c(t) \cos(\omega_c t + \psi) - n_s(t) \sin(\omega_c t + \psi))(n_c(t) \sin(\omega_c t + \psi) + n_s(t) \cos(\omega_c t + \psi))]$$

$$= R_{cs}(0) \cos^2(\omega_c t + \psi) - R_{sc}(0) \sin^2(\omega_c t + \psi)$$

$$= 0 \text{ (for Gaussian bandpass white noise, } R_{sc}(\tau) = R_{cs}(\tau) = 0 \text{)}$$

Because they are Gaussian, $n(t)$ and $\bar{n}(t)$ are independent at the same time t .

Thus, $\vartheta(t) = \tan^{-1} \frac{\pi(t)}{n(t)}$ is a uniform distribution between $-\frac{\pi}{2}$ and $\frac{\pi}{2}$.

(2) Discrete time case

From Lemma 6, $\pi(i)$ and $n(i)$ are Gaussian, independent with $N(0, \sigma^2)$, so the instantaneous phase is uniformly distributed in the interval $(-\frac{\pi}{2}, \frac{\pi}{2})$.

The distributions of envelope, instantaneous phase, and instantaneous frequency of Gaussian noise are shown in Fig. 2.5.

2.12 FM Demodulation Using Instantaneous Frequency

FM baseband signal can be demodulated by using instantaneous frequency.

(I) FM demodulation without noise.

Lemma 8:

A frequency modulated waveform has the form

$$s(t) = A \cos[\omega_c t + \Delta_\omega \int m(t) dt]$$

$$\text{or } s(t) = A \sin[\omega_c t + \Delta_\omega \int m(t) dt]$$

If the carrier frequency f_c is high and the frequency spectrum of $m(t)$ is low, i.e., $J_{2k}(\beta) = 0$ and $J_{2k+1}(\beta) = 0$ when $(2k+1)\omega_m \geq \omega_c$ for large positive integer k , then the instantaneous frequency of this FM signal can be derived as

$$\begin{aligned} \omega(t) &= \omega_c + \frac{d}{dt}[\Delta_\omega \int m(t) dt] \\ &= \omega_c + \Delta_\omega m(t) \end{aligned}$$

$$\text{or } f_i(t) = f_c + \frac{\Delta_\omega}{2\pi} m(t)$$

$$\text{and } m(t) = \frac{2\pi}{\Delta_\omega} (f_i(t) - f_c)$$

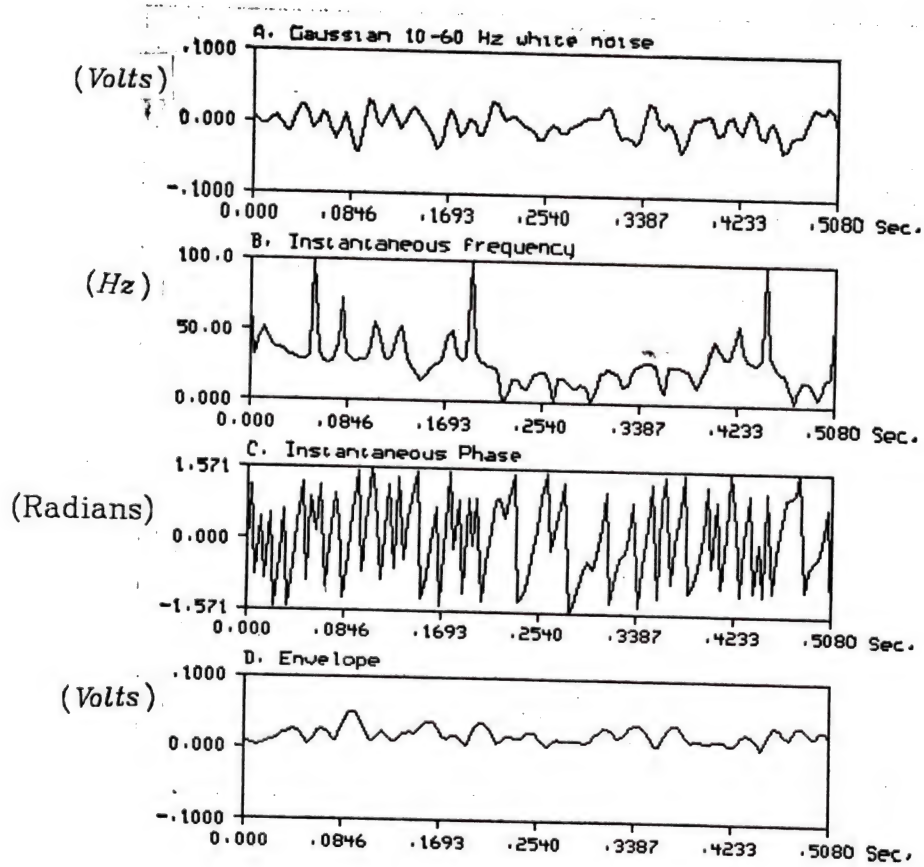


Figure 2.5A Gaussian noise, $N(0, 0.024^2)$ sampling interval = 0.004 seconds

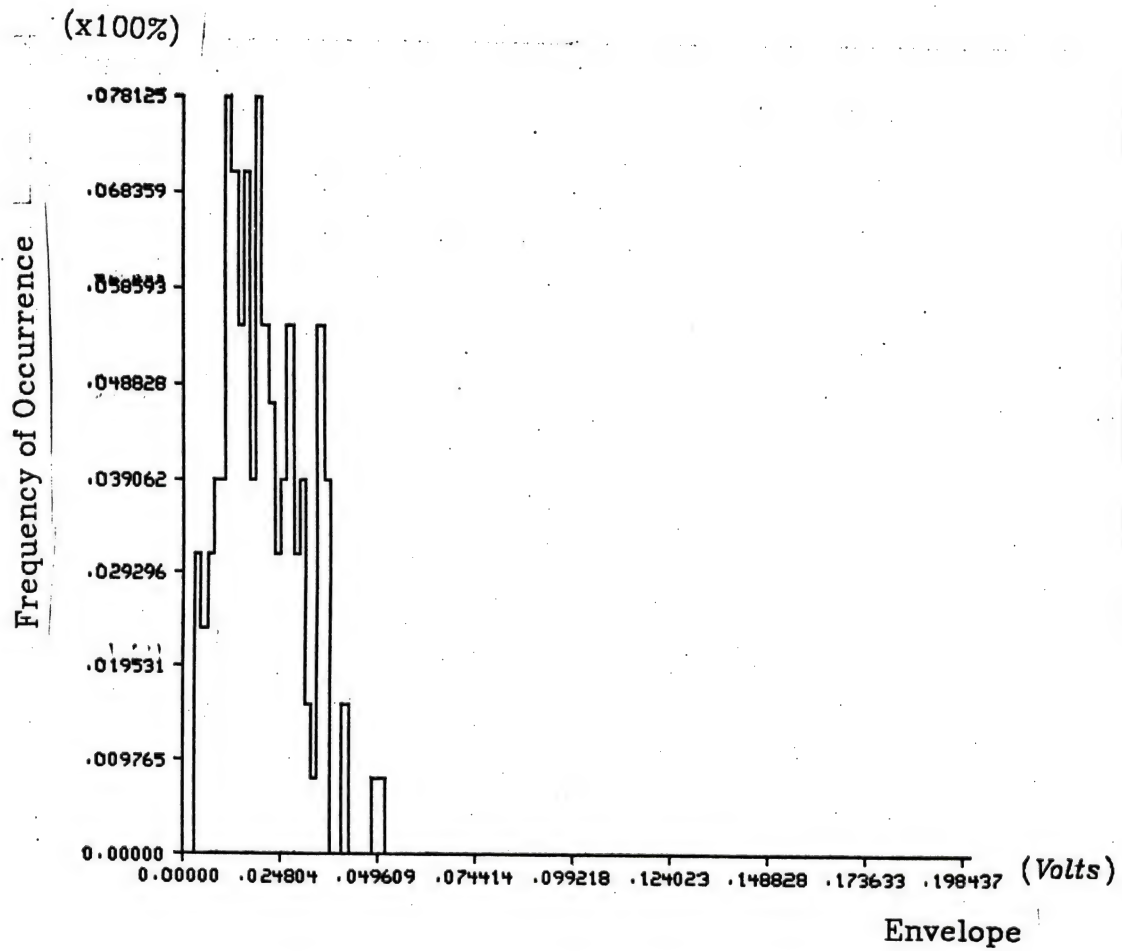


Figure 2.5B Envelope distribution of Figure 2.5A

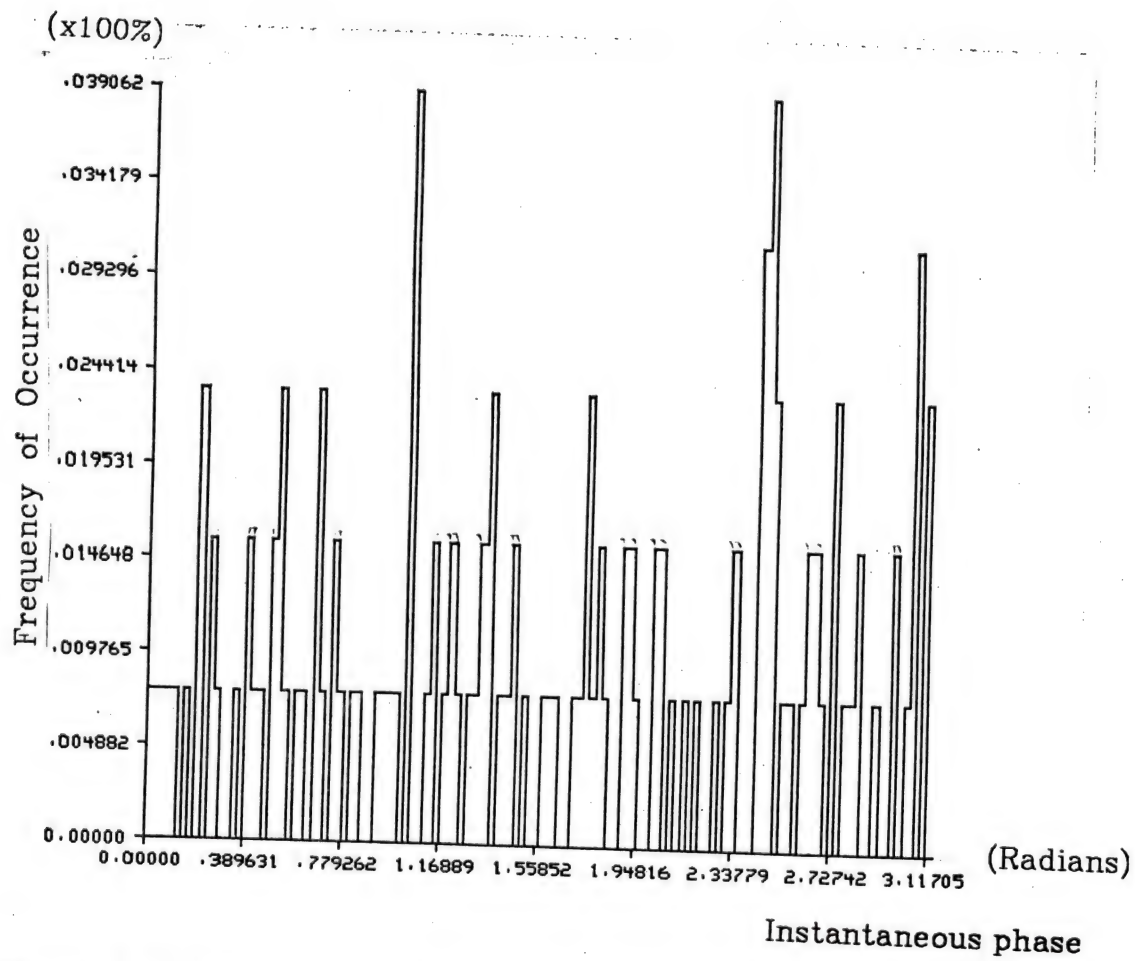


Figure 2.5C Instantaneous phase distribution of Figure 2.5A by shifting $\frac{\pi}{2}$

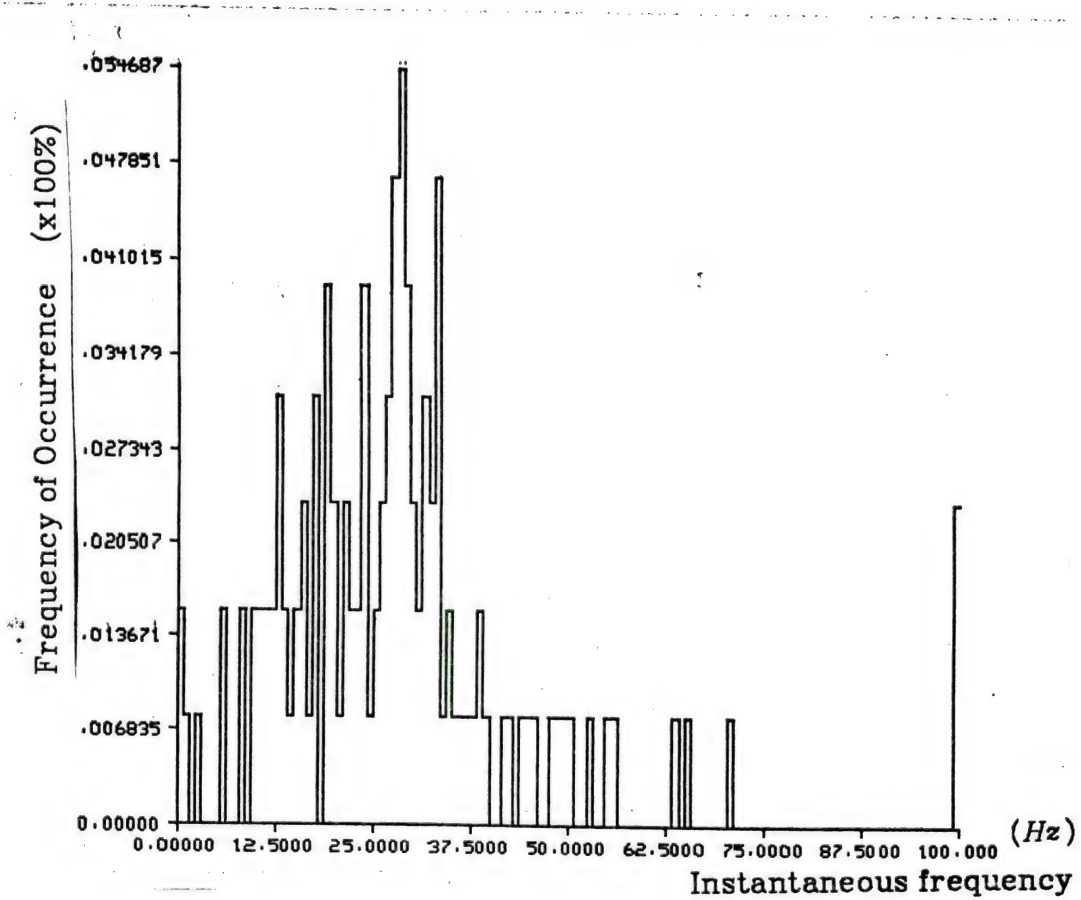


Figure 2.5D Instantaneous frequency distribution of Figure 2.5A

Proof :

Let $m(t) = \cos \omega_m t$, $A=1$

$$s(t) = A \cos [\omega_c t + \Delta_\omega \int \cos \omega_m t dt]$$

$$= \cos (\omega_c t + \beta \sin \omega_m t) \text{ where } \beta = \frac{\Delta_\omega}{\omega_m}$$

$$= \cos \omega_c t \cos (\beta \sin \omega_m t) - \sin \omega_c t \sin (\beta \sin \omega_m t)$$

$$= \cos \omega_c t [J_0(\beta) + 2 \sum_{k=1}^{\infty} J_{2k}(\beta) \cos (2k \omega_m t)]$$

$$- \sin \omega_c t [2 \sum_{k=0}^{\infty} J_{2k+1}(\beta) \sin [(2k+1) \omega_m t]]$$

where $J_{2k}(\beta)$ and $J_{2k+1}(\beta)$ are Bessel functions.

From the assumption, $J_{2k}(\beta) = 0$ and $J_{2k+1}(\beta) = 0$ when $(2k+1)\omega_m \geq \omega_c$ for large positive integer k .

Then using Hilbert transform theorem

$$\text{H.T.}\{s(t)\} = \bar{s}(t)$$

$$= \sin \omega_c t [J_0(\beta) + 2 \sum_{k=1}^{\infty} J_{2k}(\beta) \cos (2k \omega_m t)]$$

$$+ \cos \omega_c t [2 \sum_{k=0}^{\infty} J_{2k+1}(\beta) \sin [(2k+1) \omega_m t]]$$

$$= \sin \omega_c t \cos (\beta \sin \omega_m t) + \cos \omega_c t \sin (\beta \sin \omega_m t)$$

$$= \sin (\omega_c t + \beta \sin \omega_m t)$$

$$\psi(t) = s(t) + j\bar{s}(t) = \exp [j(\omega_c t + \beta \sin \omega_m t)]$$

$$f_i(t) = \frac{1}{2\pi} \text{Im} \left\{ \frac{\dot{\psi}(t)}{\psi(t)} \right\}$$

$$= f_c + \frac{\Delta_\omega}{2\pi} \cos \omega_m t = f_c + \frac{\Delta_\omega}{2\pi} m(t)$$

$$\text{then, } m(t) = \frac{2\pi}{\Delta_\omega} (f_i(t) - f_c)$$

The same procedures can be used for $s(t) = A \sin [\omega_c t + \Delta_\omega \int \cos \omega_m t dt]$

In the computer simulation, there are two examples as follows.

Example 2:

$$s(t) = \sin[2\pi f_c t + 2\pi f_d \int m(t) dt]$$

where $f_c = 25\text{Hz}$, $f_d = 25\text{Hz}$, the sampling interval is 0.001 second and $m(t)$ is a unit step function. The instantaneous frequency of this FM is a step function shown in Fig. 2.6A.

Example 3:

$$s(t) = \sin[2\pi f_c t + \Delta\omega \int \cos\omega_m t dt], \text{ where } m(t) = \cos\omega_m t$$

$$= \sin[2\pi f_c t + \frac{\Delta\omega}{\omega_m} \sin\omega_m t]$$

$$= \sin[2\pi f_c t + \sin 2\pi f_m t], \text{ let } \frac{\Delta\omega}{\omega_m} = 1$$

where $f_c = 50\text{Hz}$, $f_m = 5\text{Hz}$.

In order to satisfy the conditions in Lemma 8, i.e., the carrier frequency f_c is high and the frequency spectrum of $m(t)$ is low, $J_{2k}(\beta) = 0$ and $J_{2k+1}(\beta) = 0$ when $(2k+1)\omega_m \geq \omega_c$ for large positive integer k ,

$$\begin{aligned} f_i(t) &= f_c + \frac{\Delta\omega}{2\pi} \cos\omega_m t \\ &= f_c + f_m \cos\omega_m t \end{aligned}$$

The instantaneous frequency of this FM is a cosine waveform shown in Fig. 2.6B. The small variation of the results shown in Fig. 2.6A and 2.6B comes from the finite discrete calculation like the FIR filter [opp75a, rab75a].

(II) FM demodulation in Gaussian noise.

In the Gaussian 10 - 60 Hz white noise plus FM signal,

$$\text{Let } m(t) = \cos\omega_m t$$

$$x(t) = s(t) + n(t)$$

$$= A \cos(\omega_c t + \beta \sin\omega_m t) + n_c(t) \cos(\omega_c t + \psi) - n_s(t) \sin(\omega_c t + \psi)$$

After taking Hilbert transform, we obtain

$$\bar{x}(t) = A \sin(\omega_c t + \beta \sin\omega_m t) + n_c(t) \sin(\omega_c t + \psi) + n_s(t) \cos(\omega_c t + \psi)$$

For convenience, set $\psi = 0$.

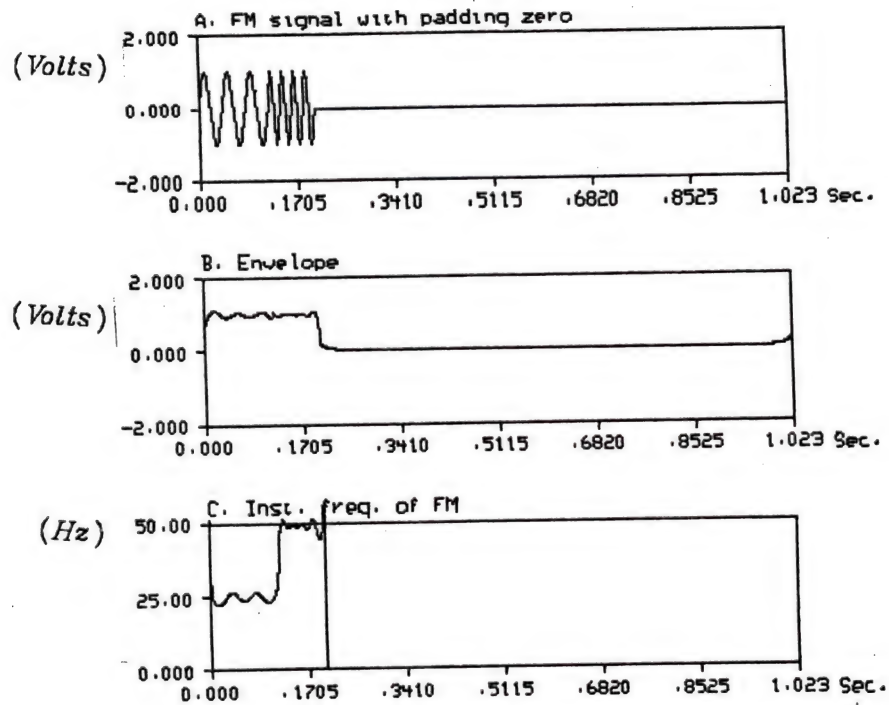


Figure 2.6A Instantaneous frequency of FM without noise, baseband signal is a step function

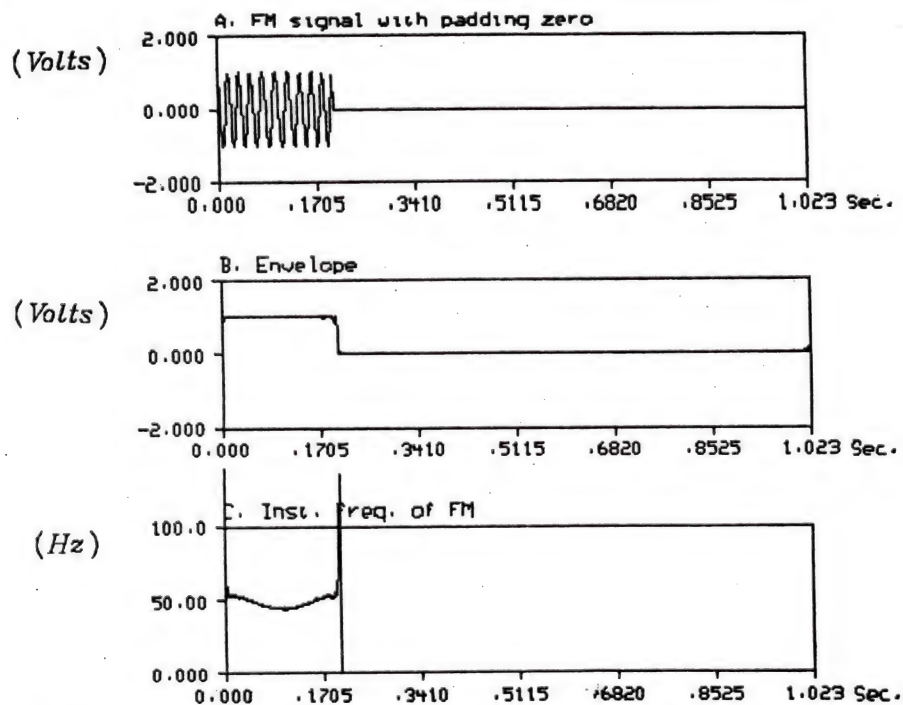


Figure 2.6B Instantaneous frequency of FM without noise, baseband signal is a cosine waveform

in which the numerator in the instantaneous frequency formula

$$\begin{aligned} x(t) \frac{d\bar{x}(t)}{dt} - \bar{x}(t) \frac{dx(t)}{dt} \\ = A^2(\omega + \beta\omega_m \cos\omega_m t) - An_2(t) + A\omega_c n_1(t) + A(\omega_c + \beta\omega_m \cos\omega_m t)n_1(t) \\ + \omega_c(n_c^2(t) + n_s^2(t)) + n_c(t)\dot{n}_s(t) - n_s(t)\dot{n}_c(t) \end{aligned}$$

$$\text{where } n_1(t) = n_c(t)\cos(\beta\sin\omega_m t) + n_s(t)\sin(\beta\sin\omega_m t)$$

$$\text{where } n_2(t) = \dot{n}_c(t)\sin(\beta\sin\omega_m t) + \dot{n}_s(t)\cos(\beta\sin\omega_m t)$$

and the denominator in the instantaneous frequency formula

$$x^2(t) + \bar{x}^2(t) = A^2 + n_c^2(t) + n_s^2(t) + 2An_1(t) = N_1(t)$$

If $A \gg \sigma^2$, i.e. for strong signal, the instantaneous frequency can be derived as

$$f_i(t) = f_c + \beta f_m \cos\omega_m t + \frac{1}{2\pi} N_2(t)$$

$$\text{then, } m(t) = \cos\omega_m t = \frac{1}{\beta f_m} [f_i(t) - f_c - \frac{N_2(t)}{2\pi}]$$

$$= [f_i(t) - f_c - \frac{N_2(t)}{2\pi}] \frac{2\pi}{\Delta\omega}$$

$$\text{where } N_2(t) = \frac{N_3(t)}{N_1(t)},$$

$$\text{and } N_3(t) = -An_2(t) + A\omega_c n_1(t) + A(\omega_c + \beta\omega_m \cos\omega_m t)n_1(t)$$

$$+ \omega_c(n_c^2(t) + n_s^2(t)) + n_c(t)\dot{n}_s(t) - n_s(t)\dot{n}_c(t)$$

$$- (\omega_c + \beta\omega_m \cos\omega_m t)(A^2 + n_c^2(t) + n_s^2(t) + 2An_1(t))$$

If $A \ll \sigma^2$, i.e. for weak signal, the instantaneous frequency can be derived as

$$f_i(t) = f_c + \frac{N_4(t)}{2\pi}$$

$$\text{where } N_4(t) = \frac{N_5(t)}{N_1(t)},$$

$$\text{and } N_5(t) = A^2(\omega_c + \beta\omega_m \cos\omega_m t) - An_2(t) + A\omega_c n_1(t)$$

$$+ A(\omega_c + \beta\omega_m \cos\omega_m t)n_1(t)$$

$$+ n_c(t)\dot{n}_s(t) - n_s(t)\dot{n}_c(t) - \omega_c(A^2 + 2An_1(t))$$

The instantaneous frequency will be centered at the carrier frequency f_c . The signal will not be demodulated.

If the signal is a sine carrier, i.e. $s(t) = A \sin[\omega_c(t) + \beta \sin \omega_m t]$, the results will be the same.

In the computer simulation, there are two examples as follows.

Example 4:

$$x(t) = s(t) + n(t) = A \sin[2\pi f_c t + 2\pi f_d \int m(t) dt] + n(t)$$

where $m(t)$ is a unit step function, $f_c = 35\text{Hz}$, $f_d = 25\text{Hz}$.

For strong signal, $A \gg \sigma^2$, ($A=1, \sigma^2=0.05^2$), the result is shown in Fig. 2.7, a step function.

Example 5:

$$x(t) = s(t) + n(t) = A \sin[2\pi f_c t + \Delta\omega \int m(t) dt] + n(t),$$

where $m(t) = \cos \omega_m t$, $f_c = 35\text{Hz}$, $f_m = 5\text{Hz}$.

For strong signal, $A \gg \sigma^2$, ($A=1, \sigma^2=0.05^2$), the result is a cosine waveform and shown in Fig. 2.8.

2.13 Envelope Application to Classification of Signal and Gaussian Noise

In Fig. 2.9, there are two hypotheses:

$$H_0: x(t) = n(t)$$

$$H_1: x(t) = s(t) + n(t)$$

where signal $s(t) = S \cos \omega_1 t$ and Gaussian noise $n(t) = n_c(t) \cos(\omega_c t + \psi) - n_s(t) \sin(\omega_c t + \psi)$

Consider $H_0: x(t) = n(t)$ then its envelope $A(t)$ as the above property is a Rayleigh distribution.

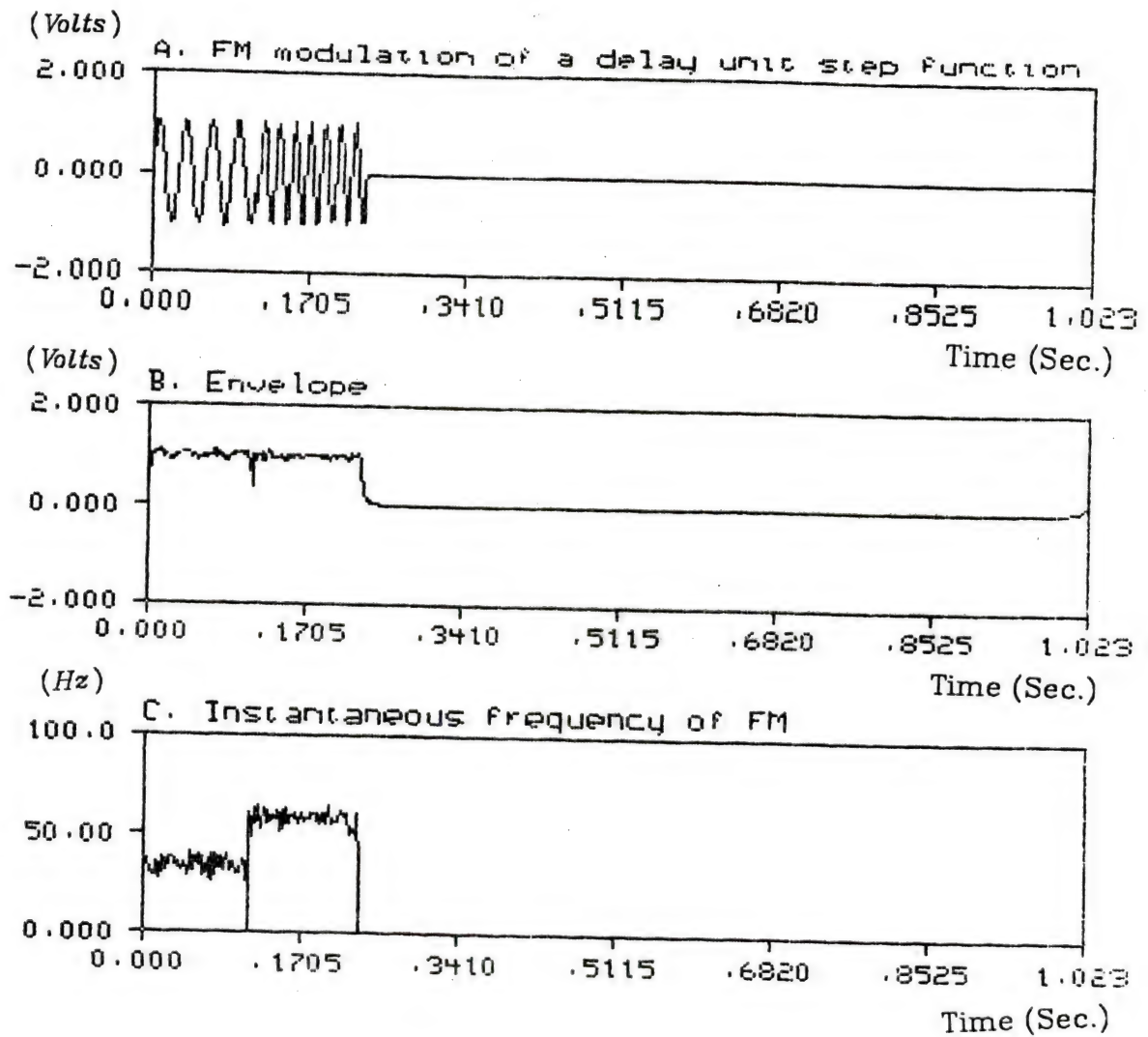


Figure 2.7 Instantaneous frequency of FM with high S/N, baseband signal is a step function

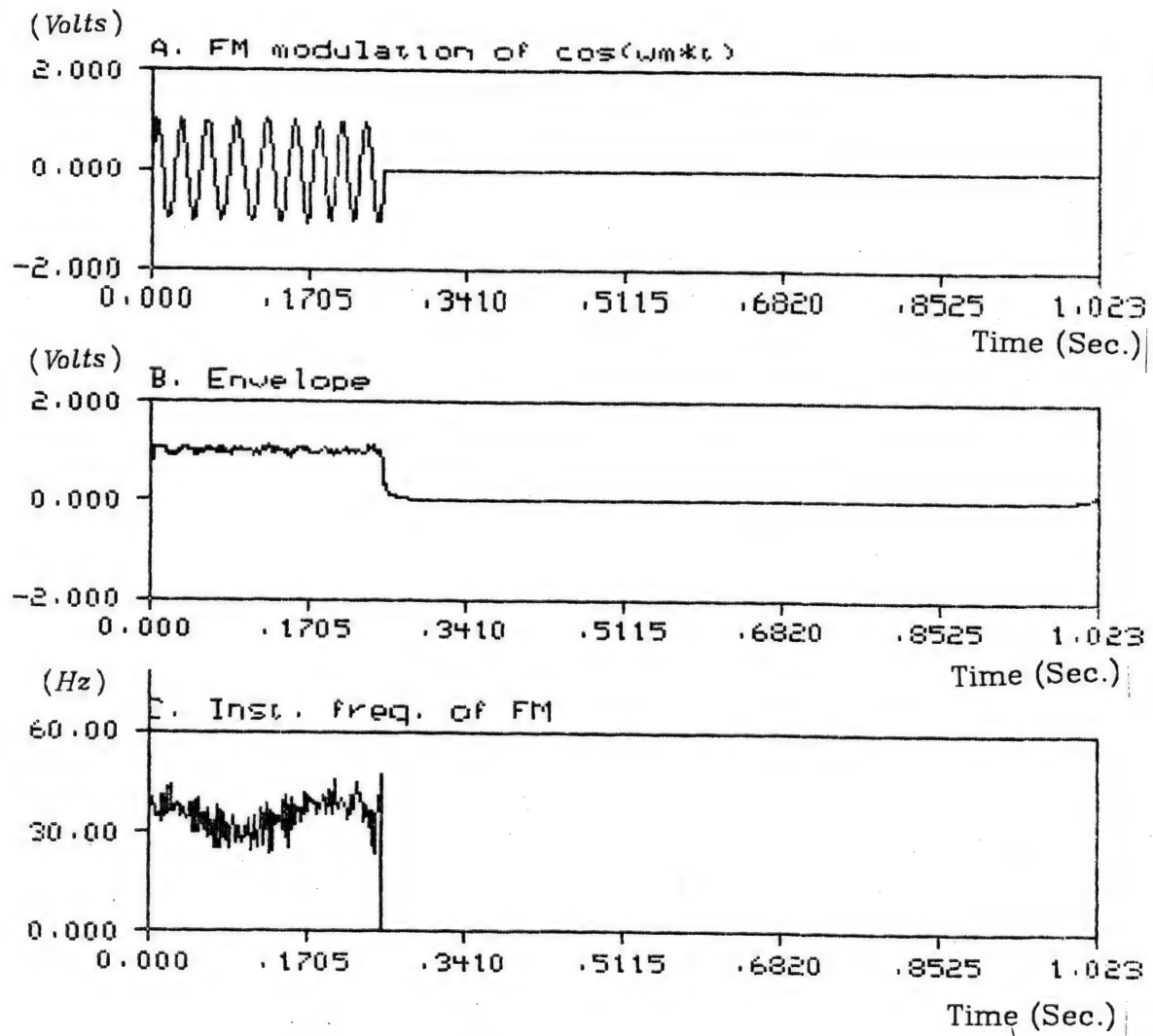


Figure 2.8 Instantaneous frequency of FM with high S/N, baseband signal is a cosine waveform

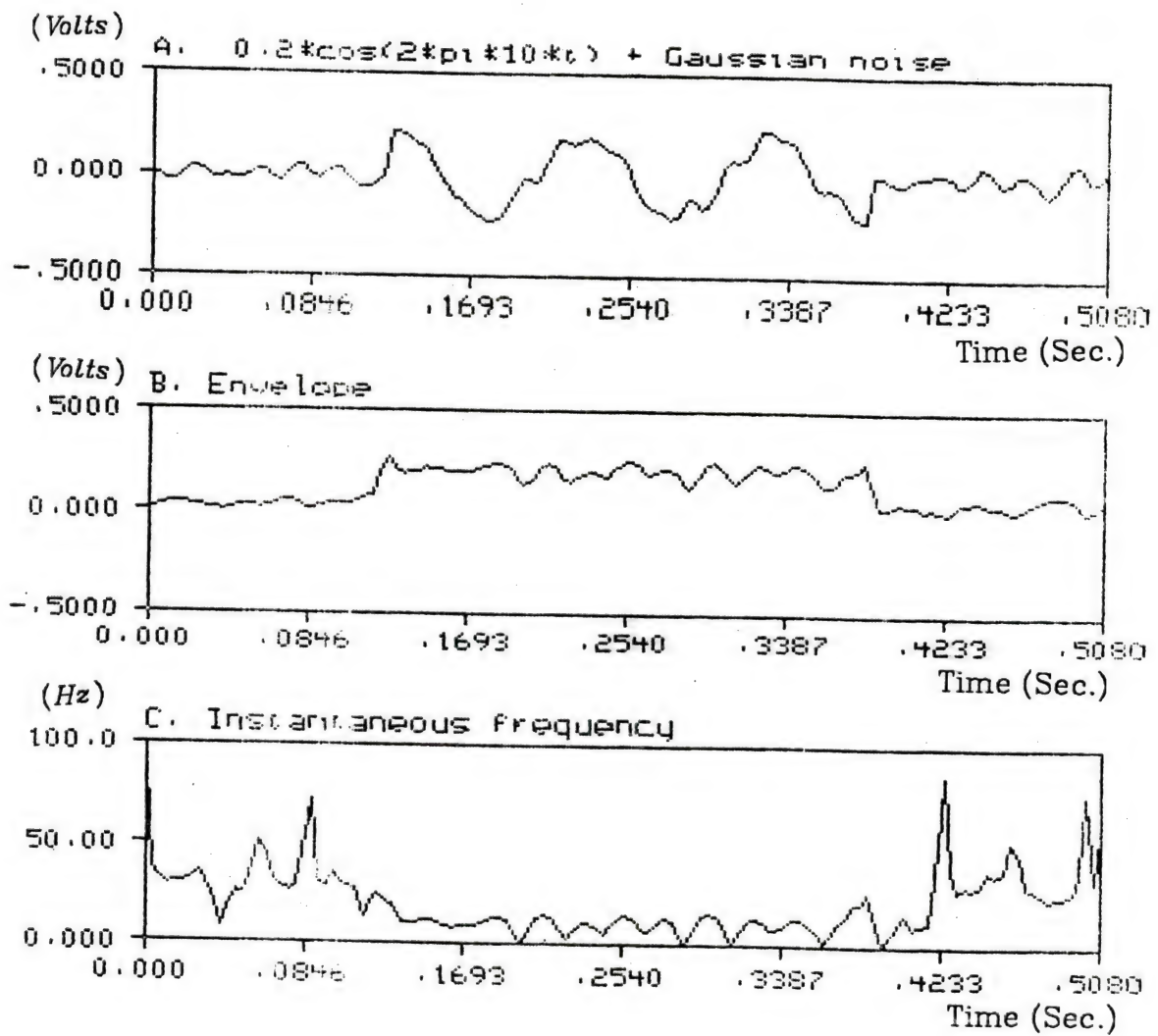
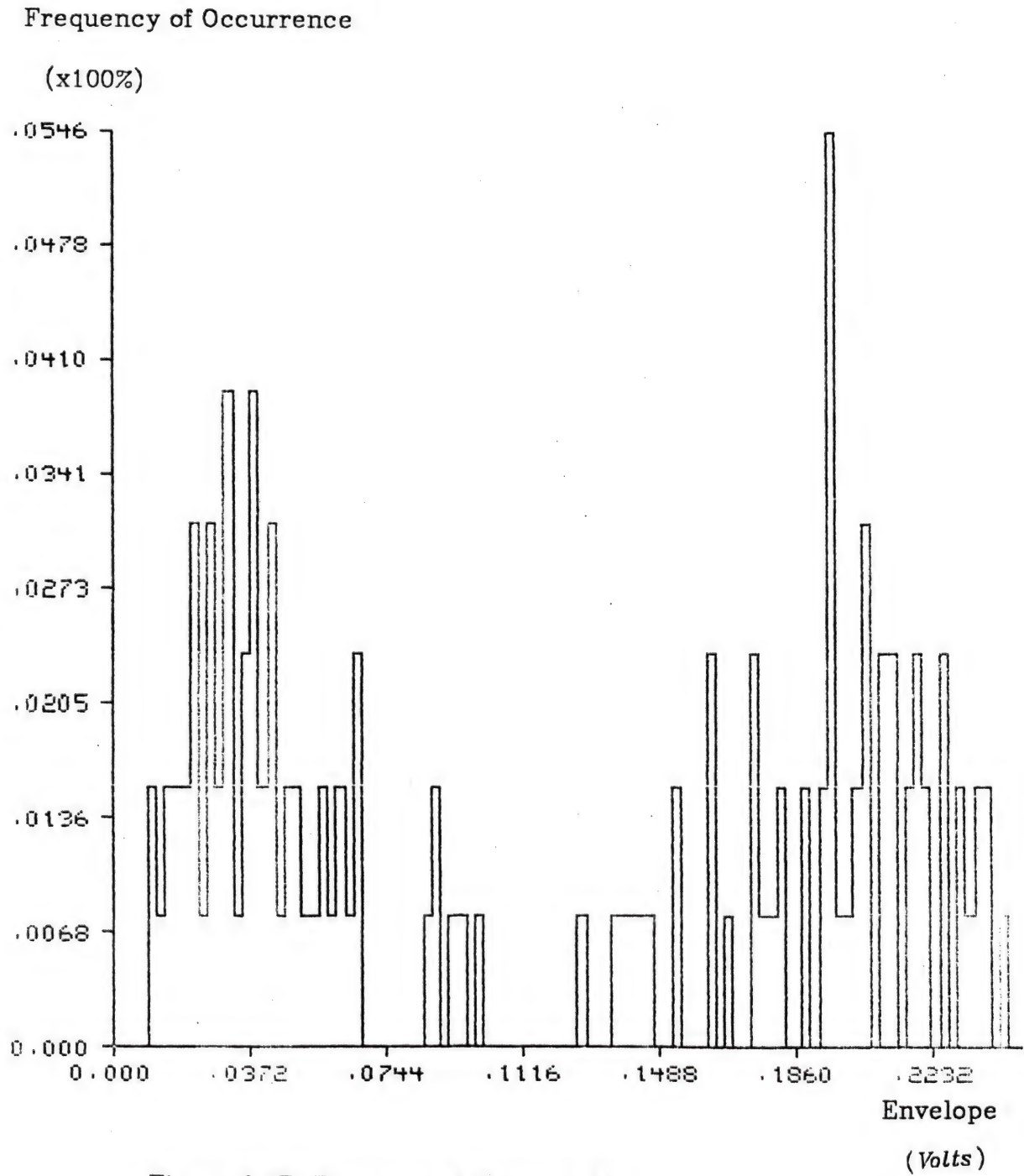


Figure 2.9A Signal + Noise



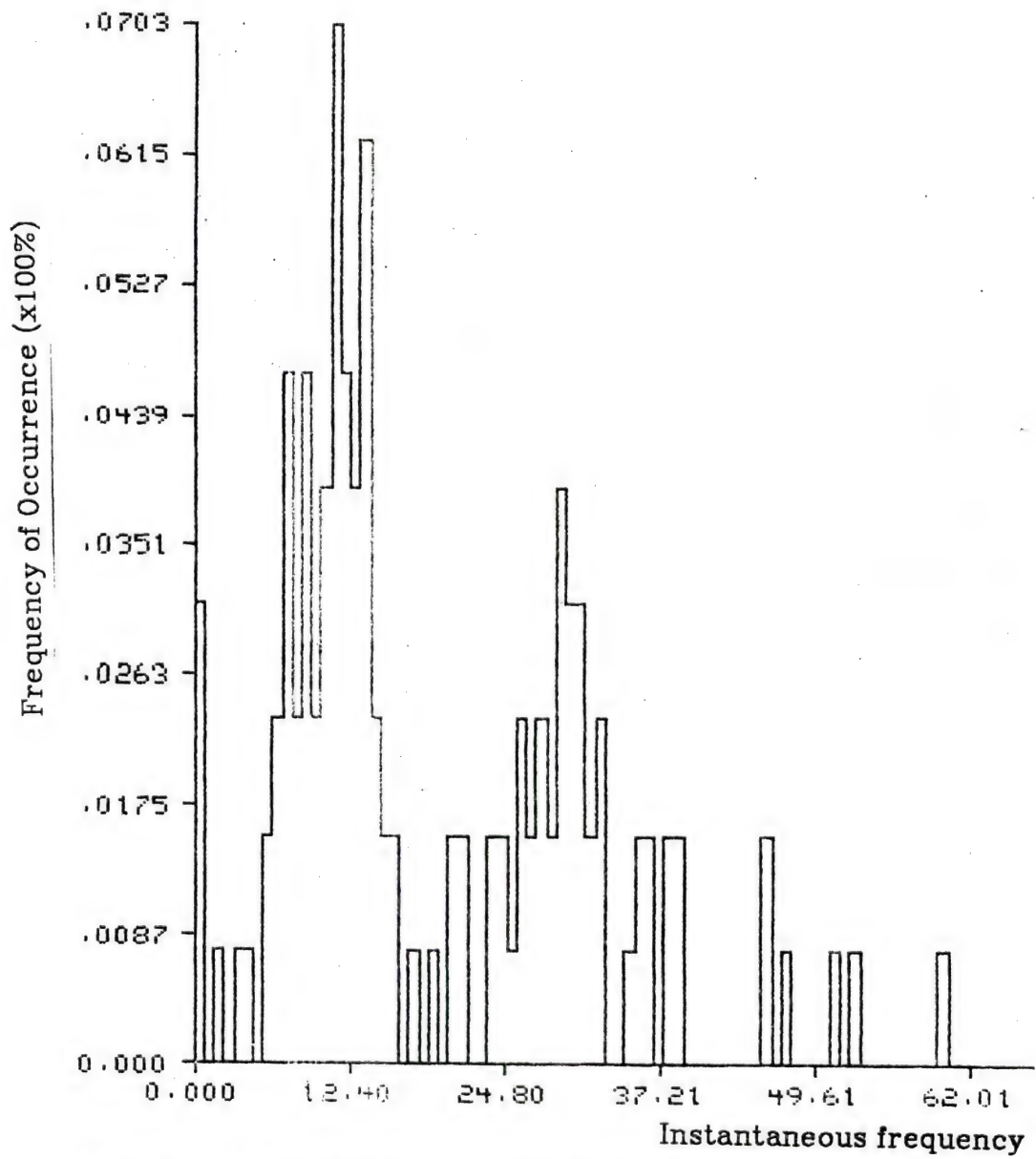


Figure 2.9C Instantaneous frequency of Figure 2.9A (Hz)

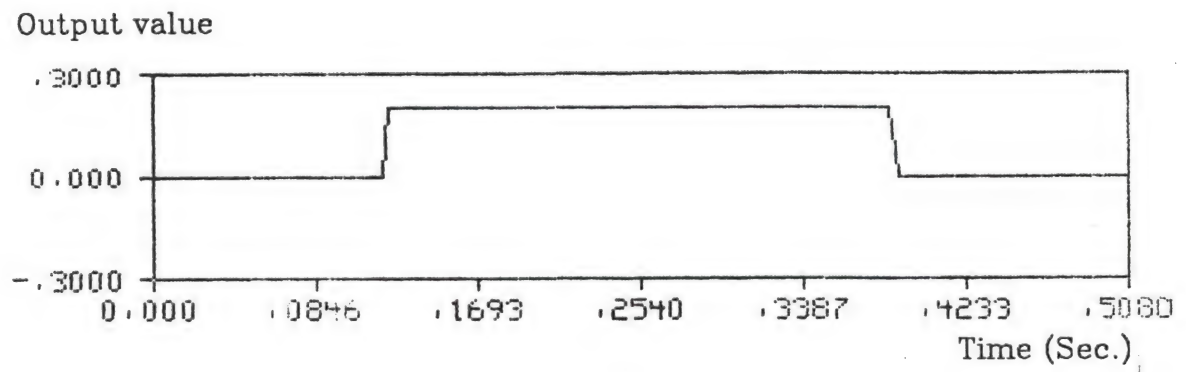


Figure 2.9D Classification result using envelope=0.122

$$A(t) = \sqrt{n_c^2(t) + n_s^2(t)}$$

$$P_{A(t)}(a) = \frac{a}{\sigma^2} \exp\left[-\frac{(a^2)}{2\sigma^2}\right], a \geq 0$$

Consider $H_1: x(t) = s(t) + n(t)$, then for strong signal, i.e. high S/N, its envelope $A(t)$ is approximately Gaussian.

$$P_{A(t)}(a) = \frac{1}{\sqrt{2\pi}\sigma} \exp\left[-\frac{(a-S)^2}{2\sigma^2}\right]$$

Using Bayes decision rule,

$P(H_0)p(X/H_0) > P(H_1)p(X/H_1)$, then X belongs to H_0 .

$P(H_0)p(X/H_0) < P(H_1)p(X/H_1)$, then X belongs to H_1 .

For half region is signal and half region is noise, so selecting $P(H_0) = P(H_1) = 1/2$, the Bayes classifier is

$$\log_e \frac{a\sqrt{2\pi}}{\sigma} = \frac{S}{2\sigma^2}(2a - S)$$

For noise, $\sigma = 0.05$, signal $S = 0.2$, then the Bayes classifier is $a = 0.122$. The classification result is shown in Fig. 2.9D. Compared with the original signal plus noise in Fig. 2.9A, the result in Fig. 2.9D is quite good.

Envelope in the signal $s(t) = S \cos \omega_1 t$ plus noise and noise have Gaussian and Rayleigh distributions respectively. So the Bayes classifier can be determined easily. But instantaneous frequency distributions in the signal plus noise and noise are centered at f_1 and f_c respectively. No model distribution can be used and the classifier may be designed from histogram distribution. So using envelope as the feature for the classification of signal and noise is better than using the instantaneous frequency for high S/N.

2.14 Resolution and Analytic Signal Analysis in Ricker Wavelets

The central part of a f -Hz zero-phase Ricker wavelet [ric40a, 45a, 53a] can be considered as a double-sideband modulated waveform with carrier frequency f . The carrier frequency f is higher than the baseband signal and satisfies the Hilbert transform theorem. So the instantaneous frequency will be approximately f Hz. The instantaneous frequency of 25 Hz Ricker wavelets is shown in Fig. 2.10 for sampling interval 0.001 second and in Fig. 2.11 for sampling interval 0.004 seconds. Although the maximum of the instantaneous frequency of 25 Hz Ricker wavelets are different for different sampling intervals, they are approximately equal to f Hz of f -Hz Ricker wavelets.

For the resolution problem, from Robertson and Nogami [rob81a], the limit of resolution between two seismic wavelets is the sand thickness thinning to a quarter period of the dominant seismic wavelet, i.e., the distance between the peaks of the two seismic wavelets should be larger than half period of the dominant wavelet. The situation needs to be investigated here is when the peak-to-peak distance of two seismic wavelets is less than the half period of the dominant wavelet.

Example 6:

For 20 Hz Ricker wavelet, $f = 20$, $T = \frac{1}{20} = 0.05 \text{ sec.}$

then $\frac{T}{2} = 0.025 \text{ sec.}$ (half period)

Sampling interval = 0.004 sec./per interval

$\frac{0.025}{0.004} = 6.25 = 6 \text{ or } 7 \text{ points}$ (for resolution limit)

In Fig. 2.12, results of the 4-point peak-to-peak distance of two Ricker wavelets are shown, where the dominant 20 Hz zero-phase Ricker wavelet is related to the reflection of high amplitude, low frequency, and phase reversal; the other is 30 Hz Ricker wavelet. Some experiments are conducted when the distances between two peaks of zero-

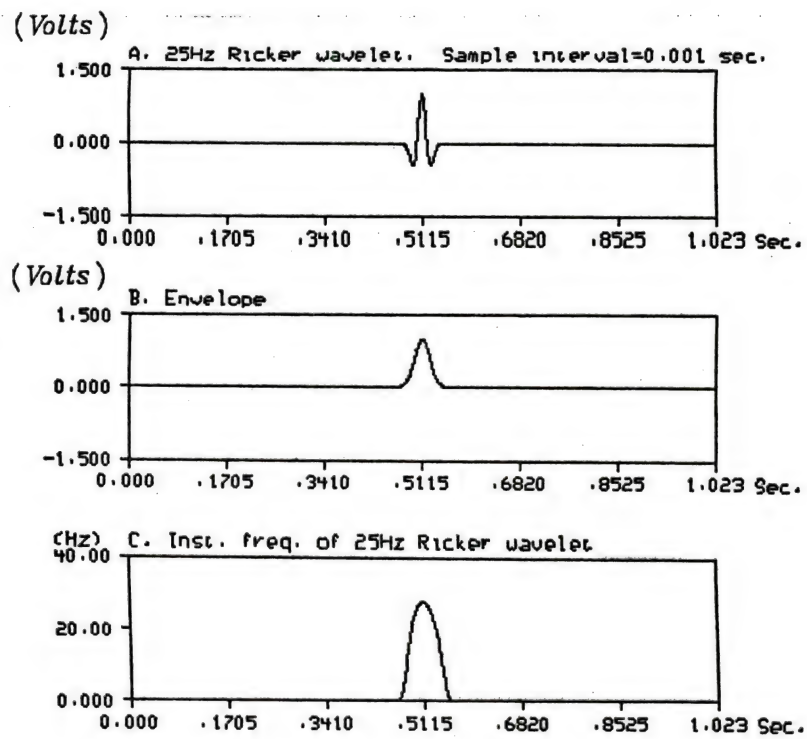


Figure 2.10 Instantaneous frequency of 25 Hz Ricker wavelet (Sampling interval 0.001 second)

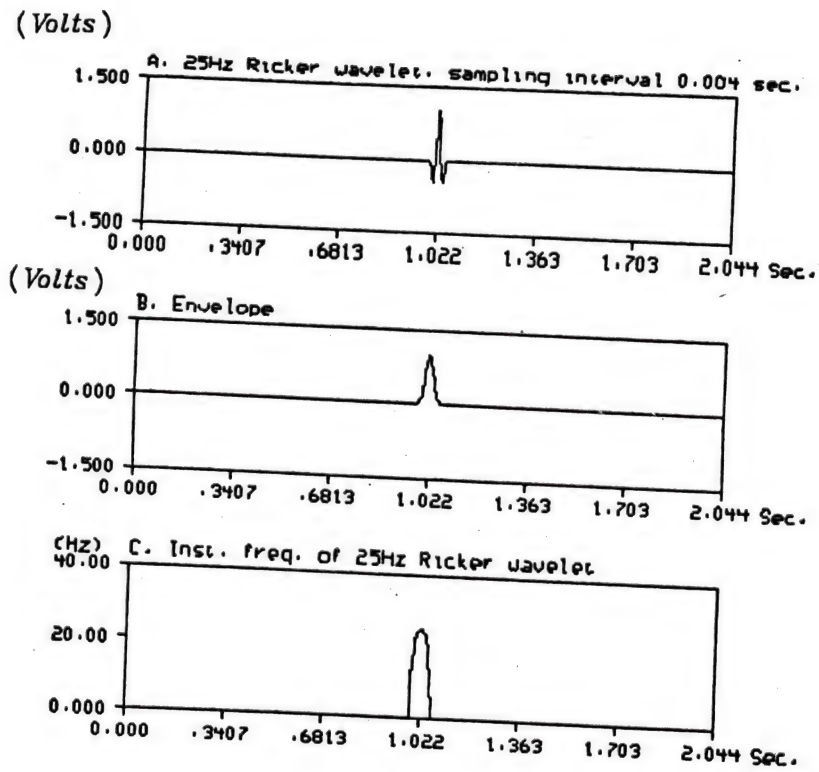


Figure 2.11 Instantaneous frequency of 25 Hz Ricker wavelet (Sampling interval 0.004 seconds)

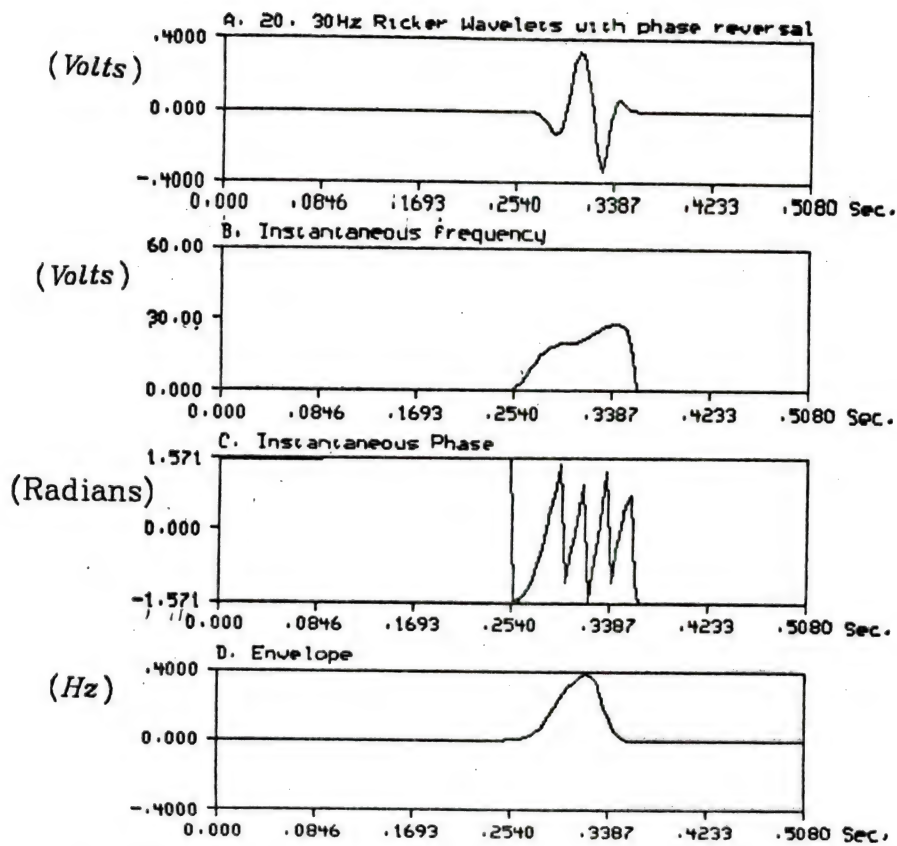


Figure 2.12A Instantaneous frequency and envelope of mixed 20 Hz and 30 Hz Ricker wavelets (Phase reversal and 4 point peak-to-peak distance)

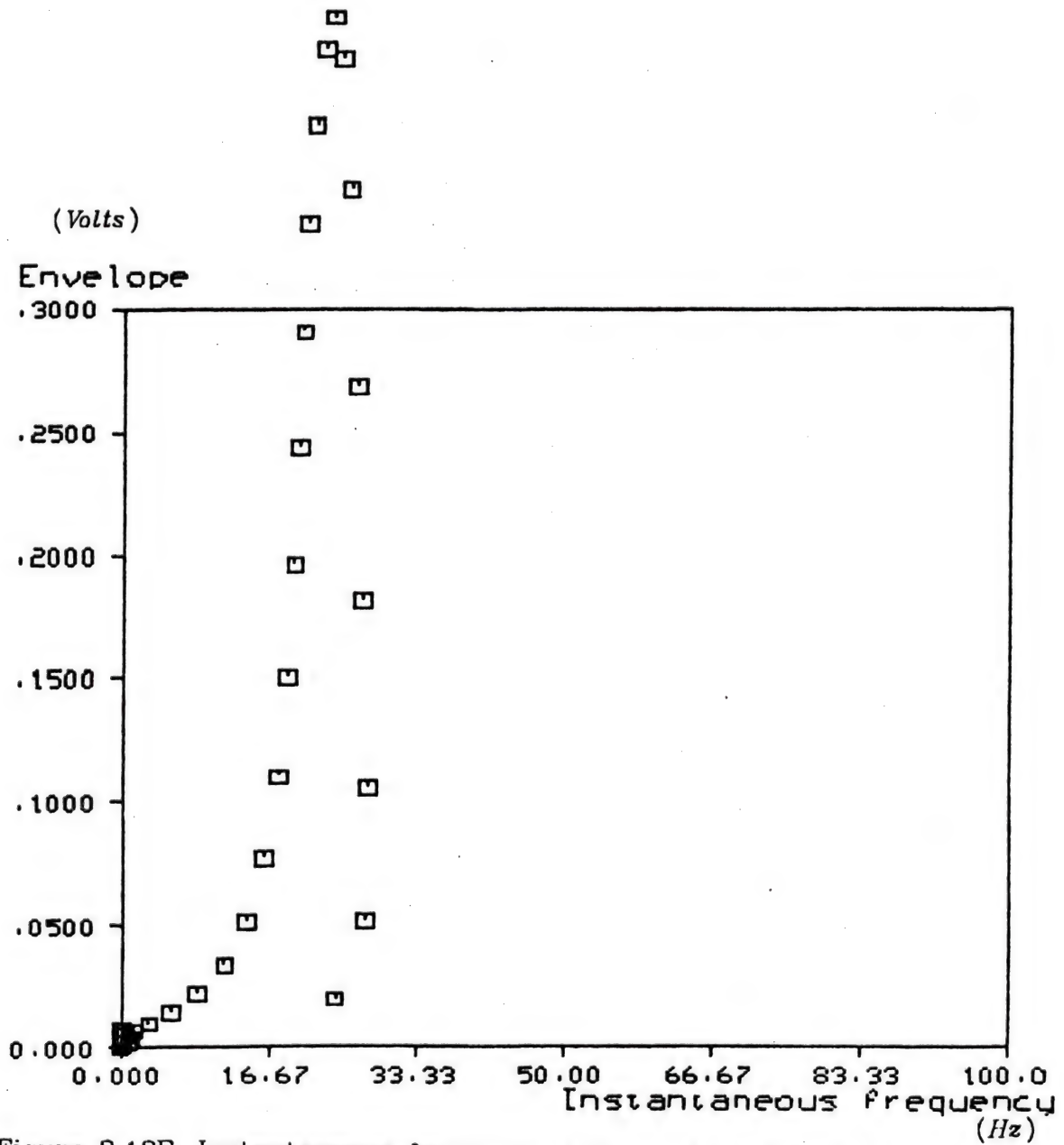


Figure 2.12B Instantaneous frequency and envelope distribution of Figure 2.12A

phase 20 and 30 Hz Ricker wavelets are 26, 15, 8, 7, 6, 5, 4, 3, 2, and 1 points. The separability of two Ricker wavelets are quite good until the peak-to-peak distance reduces to 6 or 7 points (half period). When the peak-to-peak distance is less than 6 points, for the dominant 20 Hz Ricker wavelet, its instantaneous frequency is not affected too much, but the peak of its envelope is shifted and higher than that of the original 20 Hz Ricker wavelet because of the interference from low amplitude 17Hz Ricker wavelet.

2.15 Conclusions

The conclusions of this investigation are summarized as follows.

(1) Hilbert transform theorem plays the most important role in the analytic signal analysis.

(2) The minimum number of points of Hilbert operator required for a finite discrete signal with length N is $2N-1$. In order to implement $\bar{s}(n)$ in the frequency domain using FFT algorithm and avoid circular convolution, the minimum number of points of signal $s(n)$ and Hilbert operator $h(n)$ is $(3N-2)_2$, where $(3N-2)_2$ is the smallest integer that is a power of 2 and is greater than $3N-2$. For non-causal Hilbert operator, $h(n)$ should be padded with sufficient zeros in the middle.

(3) Instantaneous frequencies of AM and sinusoidal waveform are equal to their carrier frequencies.

(4) The results of signal and Gaussian bandpass white noise in the analytic signal analysis are as follows.

Case 1: Gaussian 10 - 60 Hz white noise only.

The envelope is a Rayleigh distribution, the instantaneous phase is a

uniform distribution between $-\pi/2$ and $\pi/2$. Both properties can be proved in the continuous and discrete time domains. The instantaneous frequency is centered at the carrier frequency f_c .

Case 2: Sinusoidal signal plus Gaussian 10 - 60 Hz white noise with the same carrier frequency f_c .

The envelope is a Rician density [gag78a]. For strong signal, the envelope is a Gaussian distribution. For weak signal, the envelope is a Rayleigh distribution. For both strong and weak signal cases, the instantaneous frequency is centered at the carrier frequency f_c .

Case 3: Sinusoidal signal plus Gaussian 10 - 60 Hz white noise with carrier frequencies f_1 and f_c respectively.

For strong signal, the envelope is also a Gaussian distribution and the instantaneous frequency is centered at the signal carrier frequency f_1 . So using instantaneous frequency analysis can detect a hidden periodic signal for high S/N when its period is unknown. For weak signal, the envelope is also a Rayleigh distribution and the instantaneous frequency is centered at the noise carrier frequency f_c .

(5) FM demodulation using instantaneous frequency is quite satisfactory for high S/N.

(6) For high S/N, using envelope as the feature for classification of signal and noise is better than using the instantaneous frequency.

(7) The central part of a f -Hz zero-phase Ricker wavelet can be considered as an approximately sinusoidal signal with carrier frequency f . So the instantaneous frequency will be approximately f Hz. If the peak-to-peak distance of two Ricker wavelets is less than the half period of the dominant one, then its instantaneous frequency is not affected too much, but its envelope is shifted and higher than the original one.

CHAPTER III

DECISION-THEORETIC PATTERN RECOGNITION FOR DETECTION OF CANDIDATE BRIGHT SPOT

3.1 Introduction

Feature extraction in seismic signal has been discussed in Chapter 2. In this Chapter, decision-theoretic pattern recognition will be used to detect candidate bright spot.

As mentioned in Chapter 2, zero-phase Ricker wavelets are usually used in the simulation of seismic analysis [rob81a, tan79a]. The pattern wavelet of the bright spot in real data can be compared with the central part of the zero-phase Ricker wavelet. From Chapter 1, the physical properties of bright spot is known to be relative. Here, 20Hz zero-phase Ricker wavelet is simulated as the reflection wavelet of bright spot. The 20Hz Ricker wavelet has the physical properties of high amplitude, low frequency content, and phase reversal. 30Hz zero-phase Ricker wavelet is simulated as the reflection wavelet of non-bright spot.

At first, Ricker wavelets are classified by using linear and tree classification techniques. Then a simulated seismogram using Ricker wavelets is classified. The usage of Ricker wavelets in the simulation is to test the proposed techniques as they are applied to the real seismogram. At last, pattern recognition is used for the detection of

candidate bright spot in the real seismogram.

The classification result in this chapter also gives the candidate bright spots. The use of spatial relation to test the consistency of reflection layer of bright spot is discussed in Chapter 6.

In this chapter, as in [hua82a], envelope and instantaneous frequency are again used as the features in the classification of Ricker wavelets and an important feature, polarity, is used to check the phase reversal property of gas reflection. In the analysis of zero-phase Ricker wavelet, the envelope is uniformly distributed between one-third of the maximum envelope and the maximum envelope, and the instantaneous frequency is almost constant within this interval. So the use of tree classification appears to be a good choice. Besides, the tree classifiers in this case are easy to design and computationally efficient, and tree classification has been used in remote sensing data [swa77a, 78a, wu75a, you76a]. Three hypotheses are proposed in the tree classification for detection of candidate bright spot. The first hypothesis is that the candidate bright spot has high amplitude, low frequency content, and phase reversal. The second hypothesis is that the candidate bright spot has high amplitude and low frequency content. The third hypothesis is that the candidate bright spot has high amplitude and phase reversal. Linear classification is also discussed in the following.

3.2 Linear Classification of Ricker Wavelets for the Detection of Candidate Bright Spot

A seismic section always contains several pattern classes. In order to analyze the patterns in a seismic section, a decision-theoretic

pattern recognition system is presented in Fig. 3.1. One-dimensional simulated seismic trace and two-dimensional simulated seismogram are investigated here. The purpose of the classification of Ricker wavelets is to determine how to classify the pattern wavelets in a seismic trace. The one dimensional classification can be directly applied to two dimensional classification problem. In a two-dimensional seismogram, training traces are randomly selected or selected from the high amplitude traces. Classifiers are derived from the features distribution of the training traces. So the classifiers are determined from the physical properties of training traces. From the classification of simulated seismogram, the results are the candidate bright spots.

3.2.1 Linear Classification of Ricker Wavelets

In a simulated seismic trace (Fig.3.2), three classes of data are generated. The 20Hz, 30Hz Ricker wavelets and Gaussian white band 10 Hz - 60 Hz random noise are generated. The three pattern classes can be defined as

$$H1 : r(t)=n(t)$$

$$H2 : r(t)=20\text{Hz Ricker wavelet} + n(t)$$

$$H3 : r(t)=30\text{Hz Ricker wavelet} + n(t)$$

Using analytic signal analysis, envelope and instantaneous frequency are extracted from the signal itself and used as the two features in the decision-theoretic pattern recognition system. The envelope value is multiplied by 200.0 such that the magnitudes of both envelope and instantaneous frequency are in the same order of magnitude. From the scattering diagram of the data distribution of the two features in Fig. 3.3, the three pattern classes can be separated.

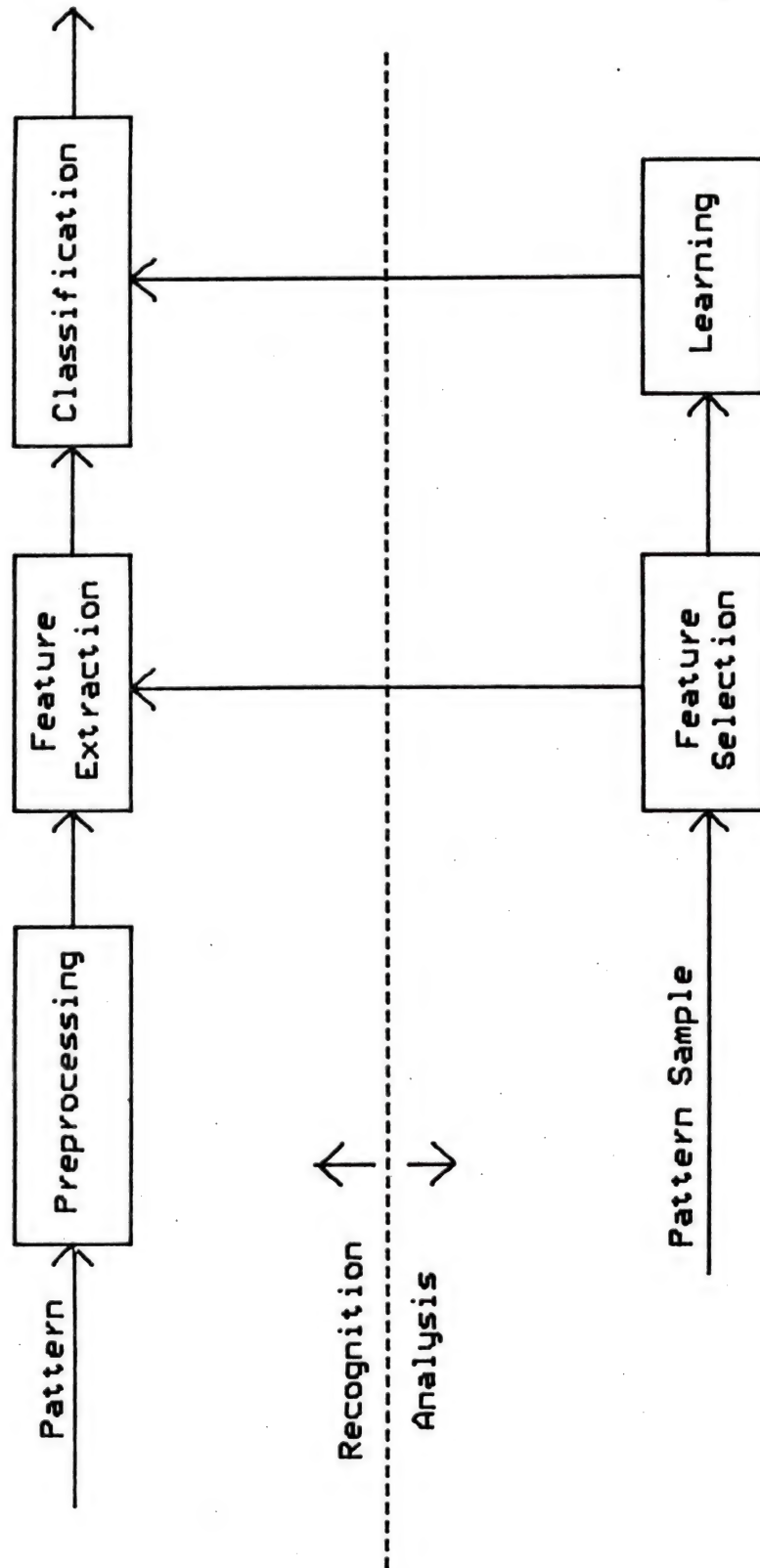


Figure 3.1 Block diagram of a decision-theoretical pattern recognition system

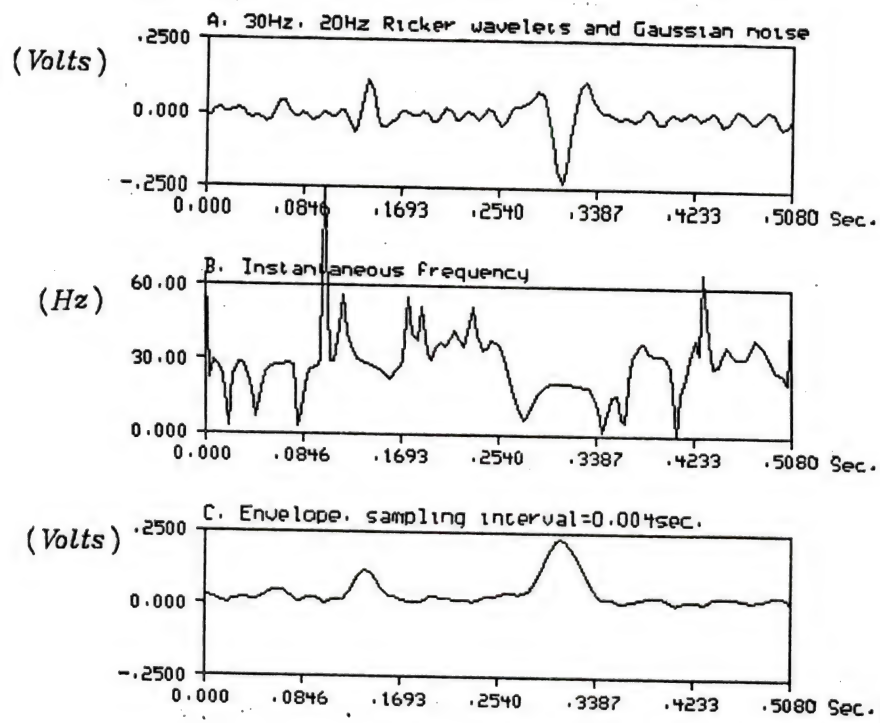


Figure 3.2 Signal, its instantaneous frequency and envelope

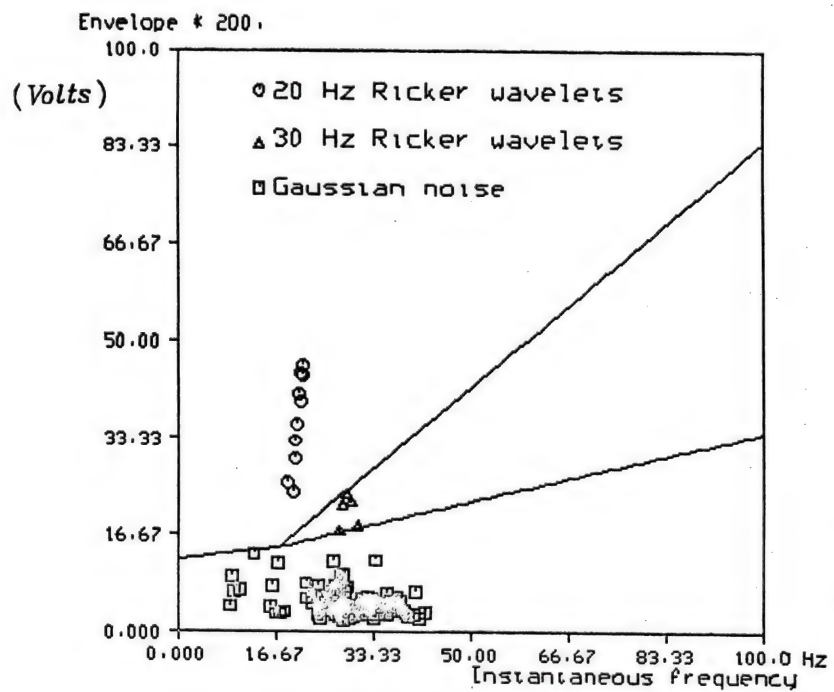


Figure 3.3 Linear Classifier

Output value



Figure 3.4 Linear classification result of Ricker wavelets

Linear classification technique is used. A modified fixed-increment training procedure is presented in the following which is different from the fixed increment training procedure [fuk72a].

In a two-dimensional feature space, suppose Y is a training sample. The training sample belongs to one of the two classes, C_1 and C_2 . The linear equation of decision boundary has weight vector W . Suppose that the linear equation passes through a given point (a, b) . This given point (a, b) is given by a subjective selection or the intersection point from the two equations of decision boundary which are solved by using fixed increment training procedure [fuk72a, fu82a].

$$Y = \begin{bmatrix} y(1) \\ y(2) \\ 1 \end{bmatrix} = \begin{bmatrix} f_i(t) \\ A(t) \\ 1 \end{bmatrix} \quad \text{Weight vector } W = \begin{bmatrix} w(1) \\ w(2) \\ w(3) \end{bmatrix}$$

$$\text{Set } \alpha=1, \quad \text{Initially set } W = \begin{bmatrix} 0 \\ 0 \\ 0 \end{bmatrix}$$

If $Y \in C_1$, $Y^T W > 0$, W not change

If $Y \in C_1$, $Y^T W \leq 0$,

$$\begin{bmatrix} w'(1) \\ w'(2) \end{bmatrix} = \begin{bmatrix} w(1) \\ w(2) \end{bmatrix} + \alpha \begin{bmatrix} y(1) \\ y(2) \end{bmatrix} \quad \text{and } w'(3) = -(w'(1)a + w'(2)b)$$

If $Y \in C_2$, $Y^T W < 0$, W not change

If $Y \in C_2$, $Y^T W \geq 0$,

$$\begin{bmatrix} w'(1) \\ w'(2) \end{bmatrix} = \begin{bmatrix} w(1) \\ w(2) \end{bmatrix} - \alpha \begin{bmatrix} y(1) \\ y(2) \end{bmatrix} \quad \text{and } w'(3) = -(w'(1)a + w'(2)b)$$

In Fig. 3.3, using the fixed-increment and the modified fixed-increment training procedures, the equations of decision boundary are determined as follows.

Here, $g_{23}(x, y) = 0$ is the equation of decision boundary between the feature distributions of 20Hz and 30Hz Ricker wavelets, $g_{13}(x, y) = 0$ is the equation of decision boundary between the feature distributions of

30Hz and Gaussian noise, $g_{12}(x,y)=0$ is the equation of decision boundary between the feature distributions of 20Hz and Gaussian noise. Using the fixed-increment training procedure, two equations of decision boundary $g_{13}(x,y)=0$, $g_{23}(x,y)=0$, can be found and have intersection point (a,b) . Then the third equation of decision boundary $g_{12}(x,y)=0$ is determined by using the modified fixed-increment training procedure, i.e. the last element of the weighting vector will be changed by $w'(3) = -(w'(1)a + w'(2)b)$. The three equations of decision boundary will intersect at one point (a,b) (Fig.3.3).

The other method is that a point (a,b) is given first and the three equations of decision boundary will pass this point (a,b) after training procedure. It is possible to give this point at two dimensional space. The convergence of this modified fixed-increment training procedure is very fast. In this seismic trace, the linear classification result is shown in Fig. 3.4. The central parts of 20Hz and 30Hz Ricker wavelets are classified, so the classification result in Fig. 3.4 is quite good.

3.2.2 Linear Classification for the Detection of Candidate Bright Spot

The one-trace pattern recognition techniques can be directly applied to 2-D reflection seismogram to classify the candidate bright spot because the processing is trace-by-trace. A typical geological model of gas accumulation from Dobrin [dob76a] is shown in Fig. 3.5A. The gas sand zone has density $D=2.025gm/cm^3$, velocity $V=1.737km/sec$. The oil sand zone has density $D=2.27gm/cm^3$, velocity $V=2.225km/sec$. Above the gas and oil sand zone is the shale layer. The primary reflection synthetic seismogram is generated in Fig.

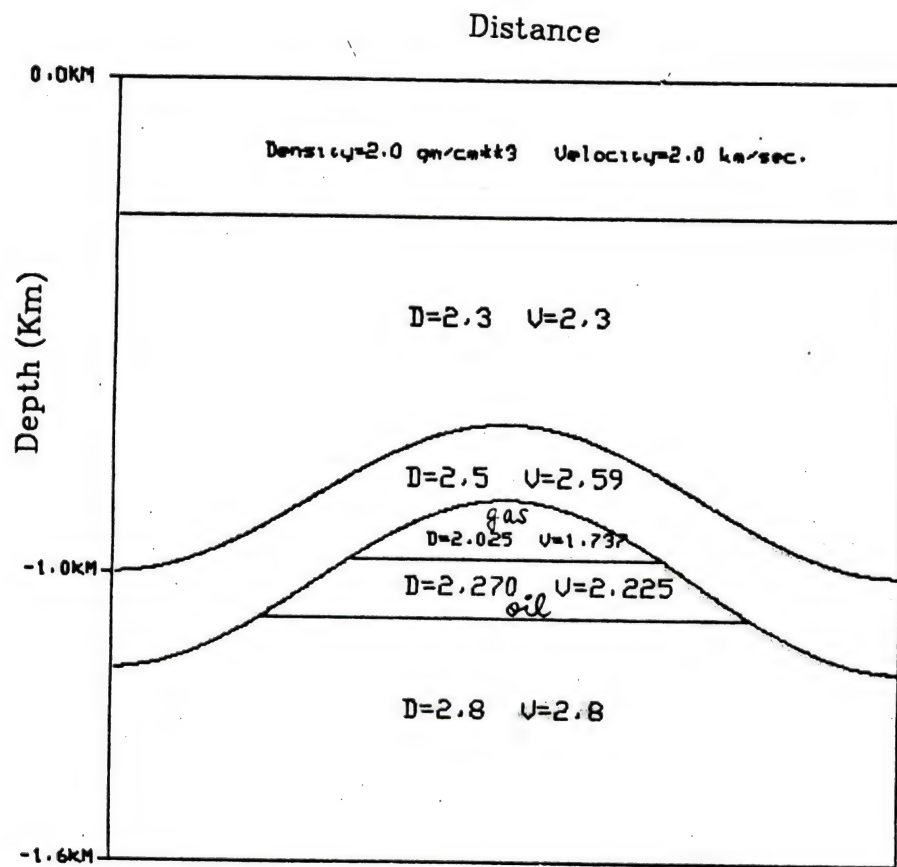


Figure 3.5A Geological structure

3.5B. The 20 Hz and 30 Hz zero-phase Ricker wavelets are used in Fig. 3.5B [ric40a, ric45a, ric53a]. There are 64 traces in the seismogram. Every trace has 512 points. The sampling interval is 0.004 seconds. Gaussian 10 - 60 Hz white noise is a simulation of recording of earth ground roll motion. Of course there are some sophisticated modeling techniques to generate more complex seismograms, but the primary reflection seismogram is the most efficient and the easiest one corresponding to the geological structures.

The thickness of the gas sand zone is large because the time to pass this gas sand zone is longer than one cycle of 20Hz Ricker wavelet. The thickness of the gas sand zone considered in the simulated seismogram is related to the resolution problem for the 20Hz Ricker wavelet passing through the gas sand zone without interference with the reflection from the bottom layer.

Two pattern classes are considered in the simulated seismogram. One is the 20Hz Ricker wavelet at the boundary of shale and gas sand zones (bright spot). The 20Hz Ricker wavelet has high amplitude proportional to the high reflection coefficient, phase reversal and low frequency content due to high frequency attenuation in the gas sand zone. The other is the non-bright spot, the 30Hz Ricker wavelet at the other layer boundary reflection and Gaussian white band 10 Hz - 60 Hz random noise corresponding to the random noise collected in the field. The envelope (multiplied by 200.0) and instantaneous frequency are selected as two features.

Two methods for the automatical selection of training traces are presented in the following.

(I) The training traces are equally selected from the seismogram to cover the reflection characteristics of every kind of layers. Suppose

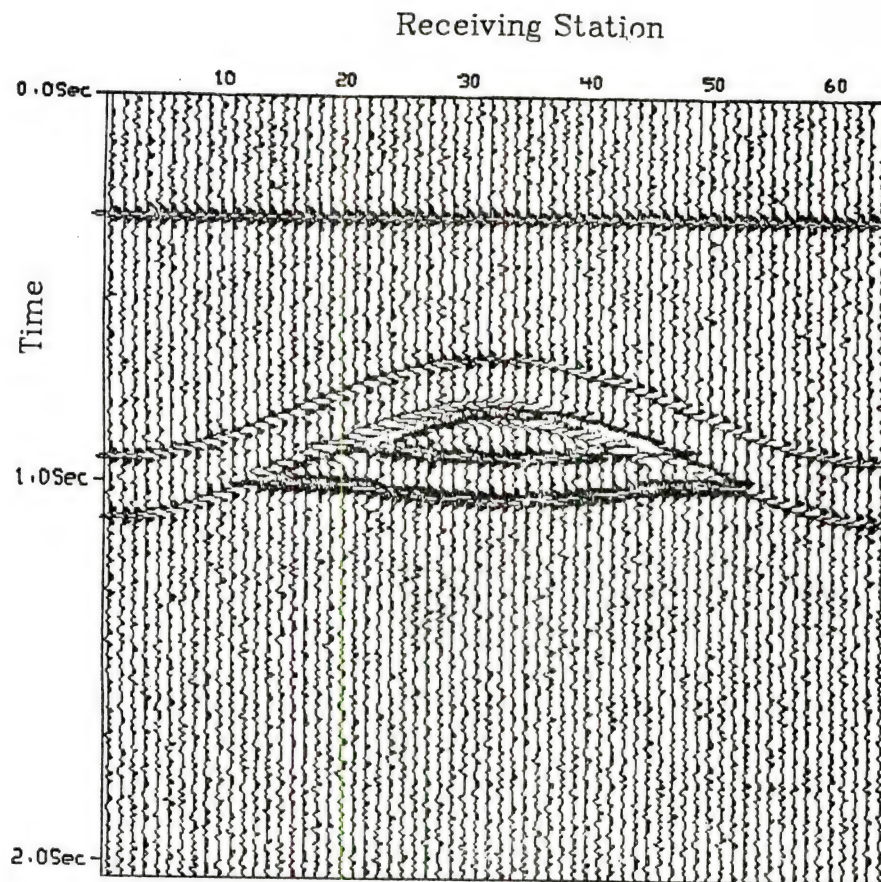


Figure 3.5B Synthetic seismogram of bright spot

that the number of traces in the seismogram is N , then the number of training traces is $\frac{N}{8}$.

(II) The training traces are selected from high amplitude traces.

Algorithm 3.1: Selection of training traces from the high amplitude portion

Input: $a(i,j)$ values of seismic data, N traces of seismogram with m points per trace.

Output: Location of training traces

Method:

- (1) Let the number of training traces equal to $N/8$.
- (2) Calculate the power distribution $p(j)$ along every trace. The power of each trace is calculated by

$$\frac{1}{m} \sum_{i=1}^m a^2(i,j) = p(j) \quad j=1,2,\dots,N$$

- (3) Use K-means algorithm for $K=2$ to find the cluster centers of two classes, m_1 , and m_2 , and let the threshold = $\frac{(m_1+m_2)}{2}$.

(4) Thresholding $p(j)$ to segment the whole trace into several zones. Determine the first and last points of each zone and calculate the length of each zone.

- (5) Set weight 2 for the power value above the threshold and weight 1 for the value below and equal to the threshold. Distribute the $N/8$ training traces to these zones equally.

Discussion of K-means clustering analysis can be found in [lin80a, swa78a, tou74a]. Two classes are in the analysis, they are high amplitude traces and low amplitude traces. In Step (3), using K-means algorithm for $K=2$ can separate the two classes.

Using Algorithm 3.1 in simulated seismogram of Fig. 3.5B, the power values along time axis is shown in Fig. 3.5C, the threshold is 0.0017. Three zones are segmented. From the 1st to 19th traces are the first zone, from the 20th to 45th traces are the high amplitude zone, from the 46th to 64th traces are the third zone. The location of the training traces are the 10th, 23rd, 28th, 32nd, 36th, 40th, 55th and shown in Fig. 3.5C. Training traces are concentrated on the high amplitude traces. At the first zone and third zone, only one testing trace is at each zone because there is round off error. The total number of training traces selected is 7 in this experiment. The histogram of the power data is shown in Fig. 3.5D. From visual inspection, the threshold is 0.0017 which is the same as the output of Algorithm 3.1.

In the experimental study, method (I) is used. Training traces are equally selected from the seismogram for easy selection and convenience. The training traces are the 4th, 12th, 20th, 28th, 36th, 44th, 52nd, and 60th traces. Training samples are selected for the values of envelope larger than 0.15 in Fig. 3.6A. A linear classifier is used. The modified fixed-increment training procedure is applied. In the scattering diagram of two features, a point (a, b) is given first, the classification boundary will pass through this point (a, b) after the solution weight vector is found. Classification result using linear classifier is shown in Fig. 3.6B. Compared with original seismogram in Fig. 3.5B, it appears to be quite good in the detection of candidate bright spot.

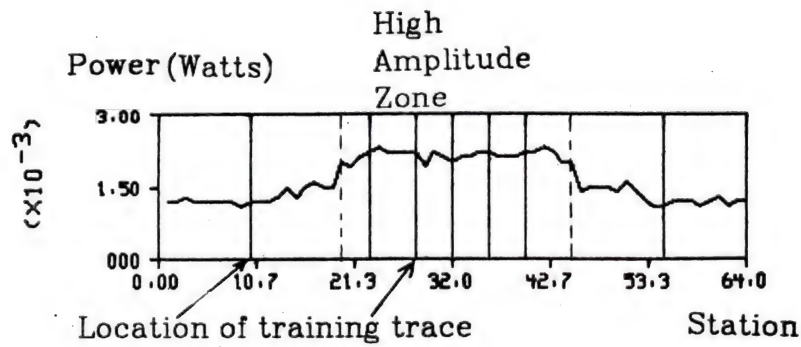


Figure 3.5C Power value along receiving station

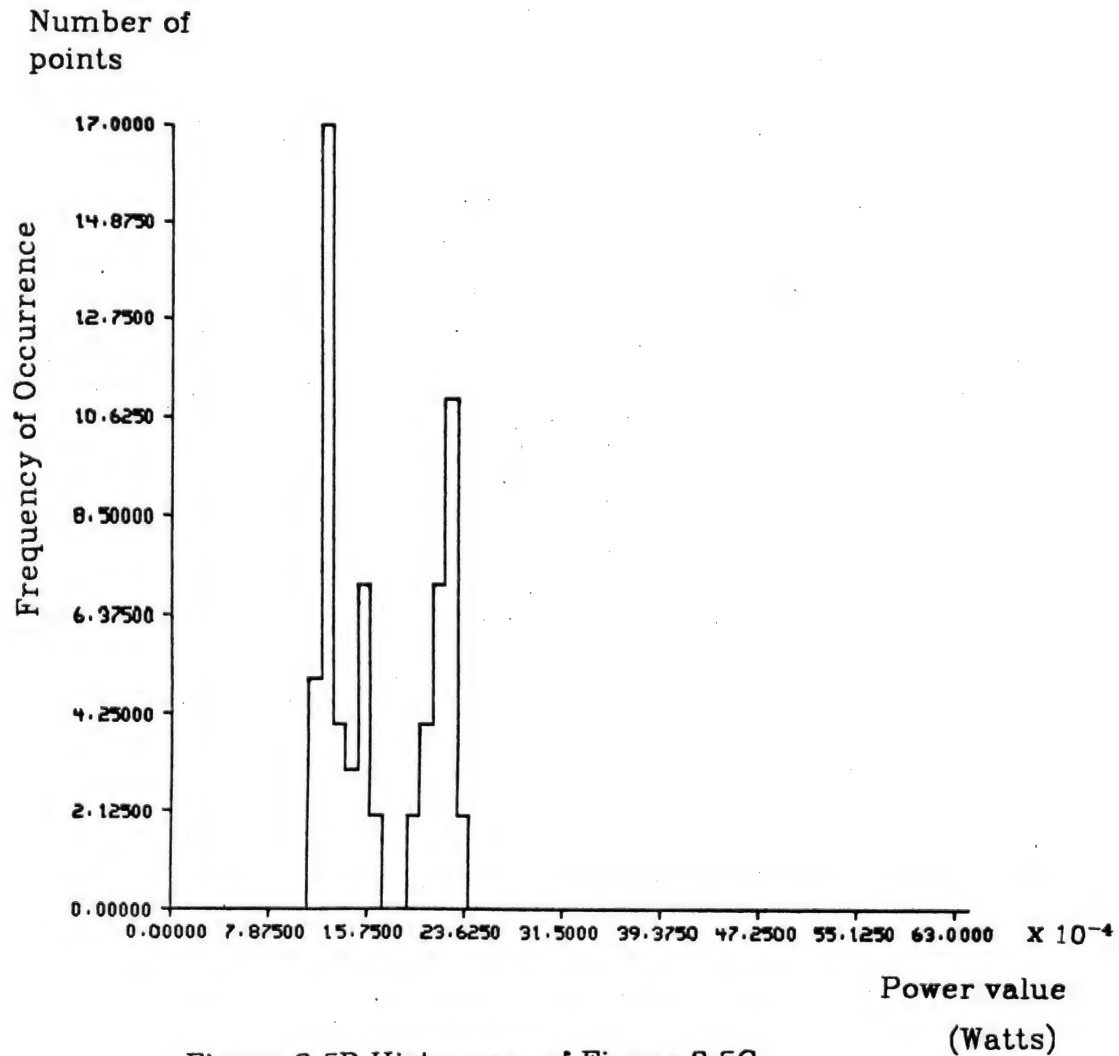


Figure 3.5D Histogram of Figure 3.5C

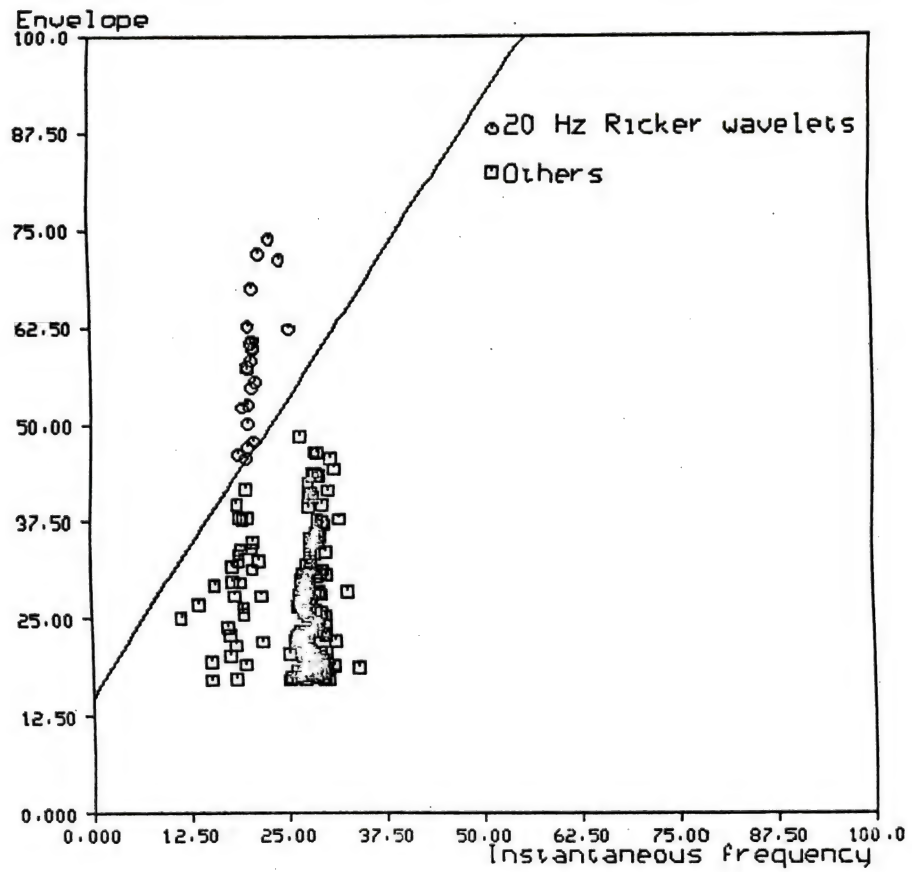


Figure 3.6A Feature distribution of training samples and linear classifier

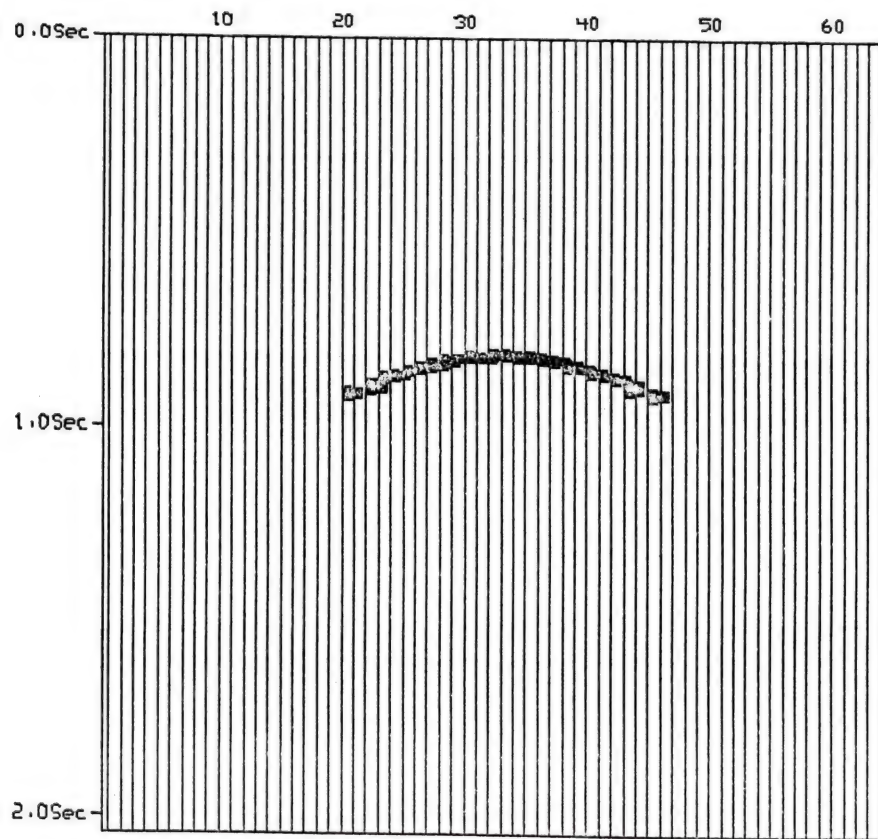


Figure 3.6B Linear classification result of bright spot

3.3 Thin-Bed Effect

In Fig. 3.9A, the time to pass through the gas sand zone is less than the half cycle of 20Hz Ricker wavelet, the gas sand zone is called "thin-bed". Using the results from Section 2.13, the experiments of thin bed for the detection of candidate bright spot are discussed. Two simulated seismograms of the second hypothesis for thin bed of gas sand zone are generated, i.e., high amplitude and low frequency at the gas reflection. The simulated seismogram for the quarter wavelength thickness of gas sand zone is shown in Fig. 3.7. The simulated seismogram for the thickness of the 2/3 quarter wavelength in gas sand zone is shown in Fig. 3.9B. From both Fig. 3.7 and Fig. 3.9B, although the 20 Hz Ricker wavelet at the top of the gas sand zone is mixed with the 30 Hz Ricker wavelet at the bottom of the gas sand zone, the 20 Hz Ricker wavelet is dominant and can overcome the interference, i.e., the physical properties are preserved. Compared with the original simulated seismograms in Fig. 3.7 and 3.9B, the classification results shown in Fig. 3.8 and Fig. 3.10 respectively seem to be still good.

3.4 Tree Classification of Ricker Wavelets for the Detection of Candidate Bright Spot

3.4.1 Introduction

In the decision-theoretic approach, another way of detecting bright spot is using tree classification. Three kinds to detect the hypotheses of candidate bright spot in the simulated seismic traces and

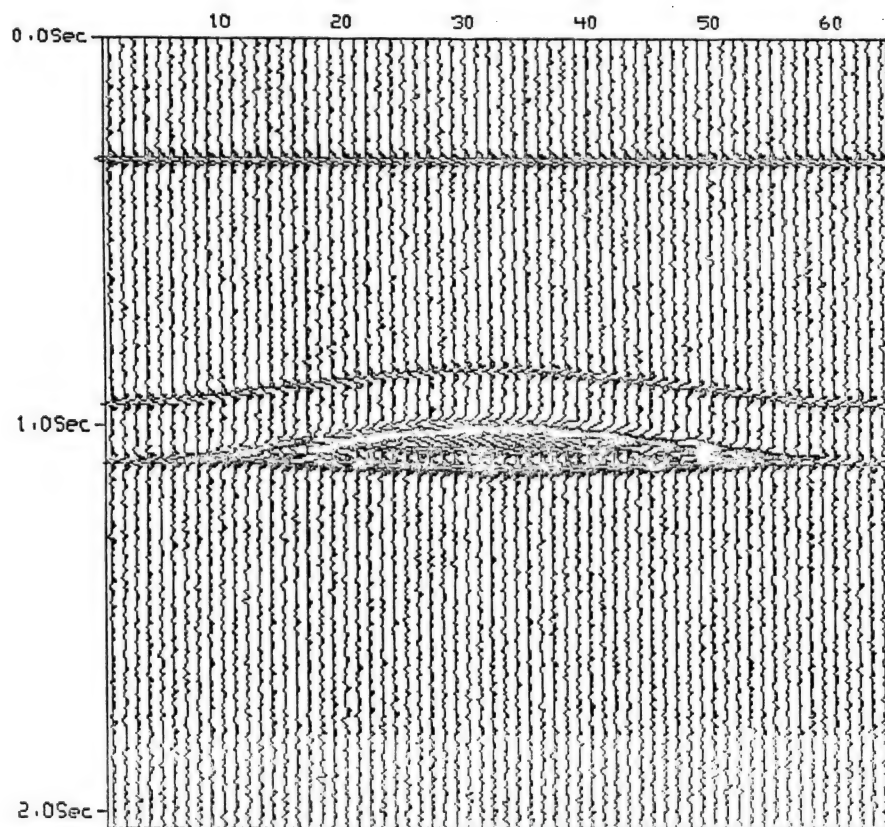


Figure 3.7 Synthetic seismogram of bright spot (Thickness of gas sand zone is quarter wavelength)

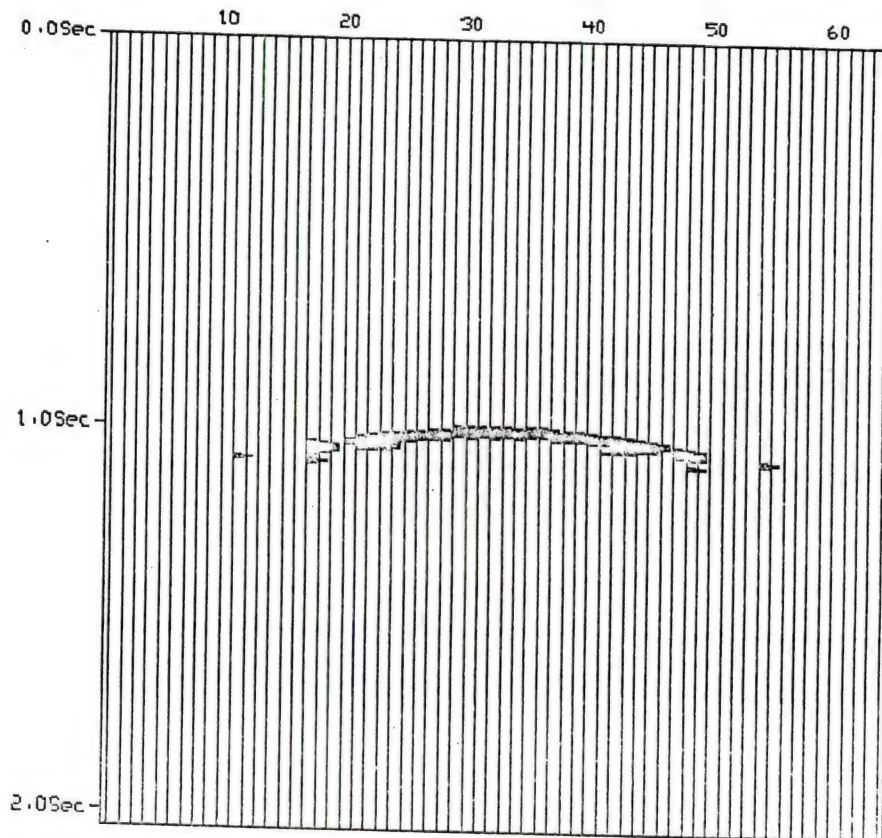


Figure 3.8 Tree classification result of bright spot (Quarter wavelength at gas sand zone)

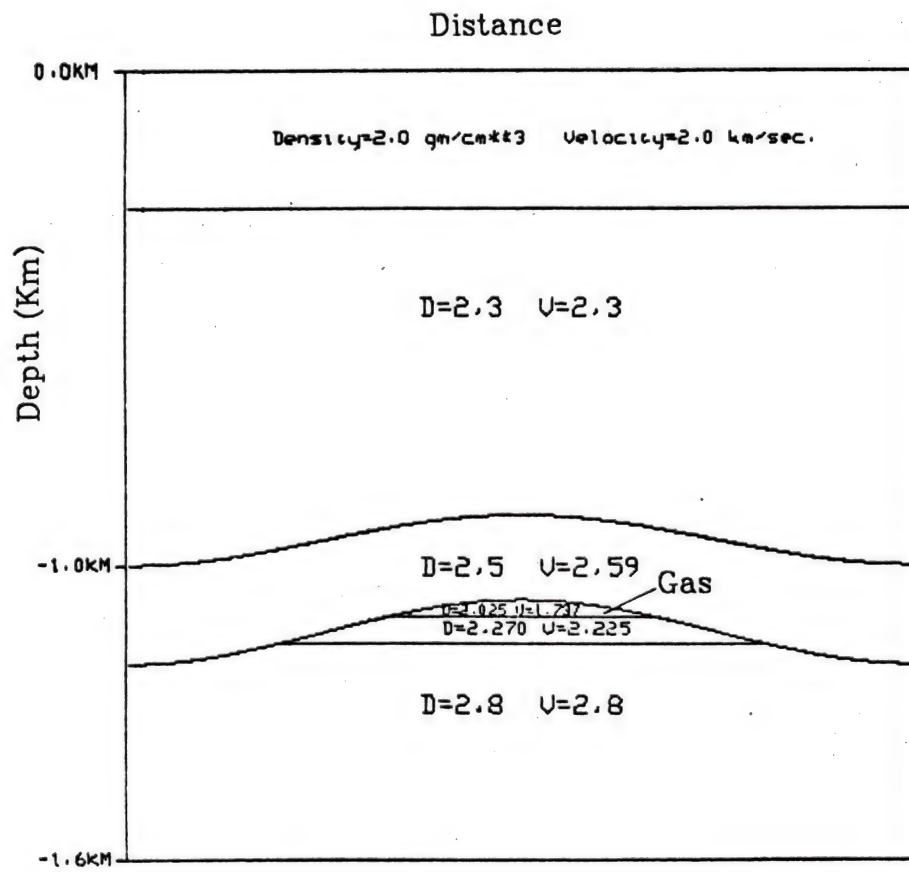


Figure 3.9A Geological structure

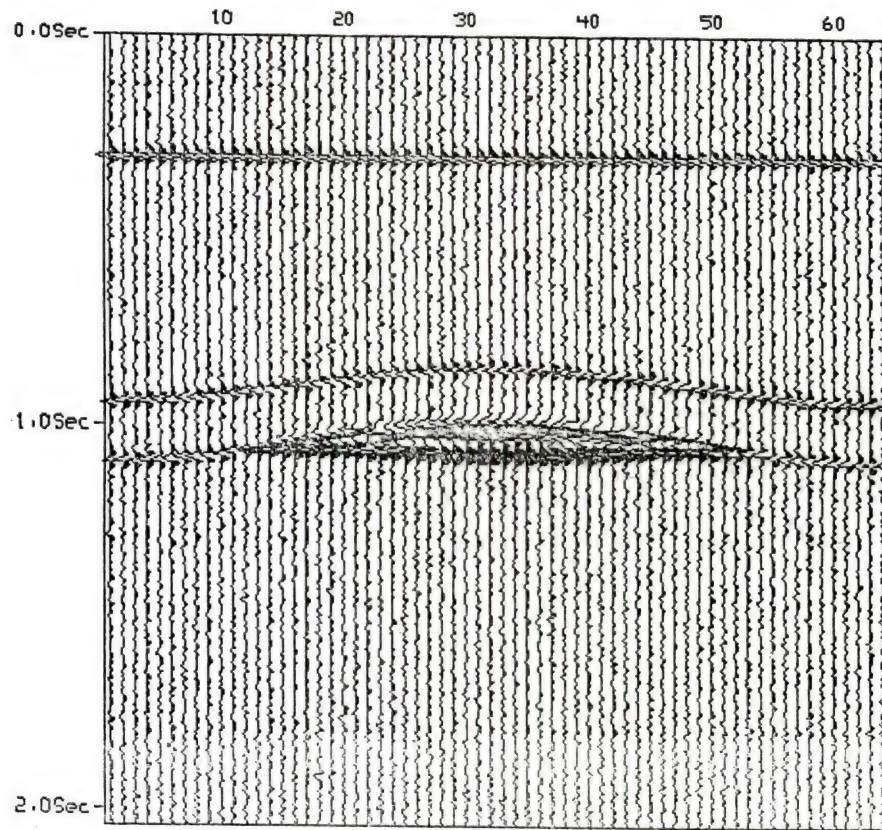


Figure 3.9B Synthetic seismogram of bright spot (Thickness of gas sand zone is $2/3$ quarter wavelength)

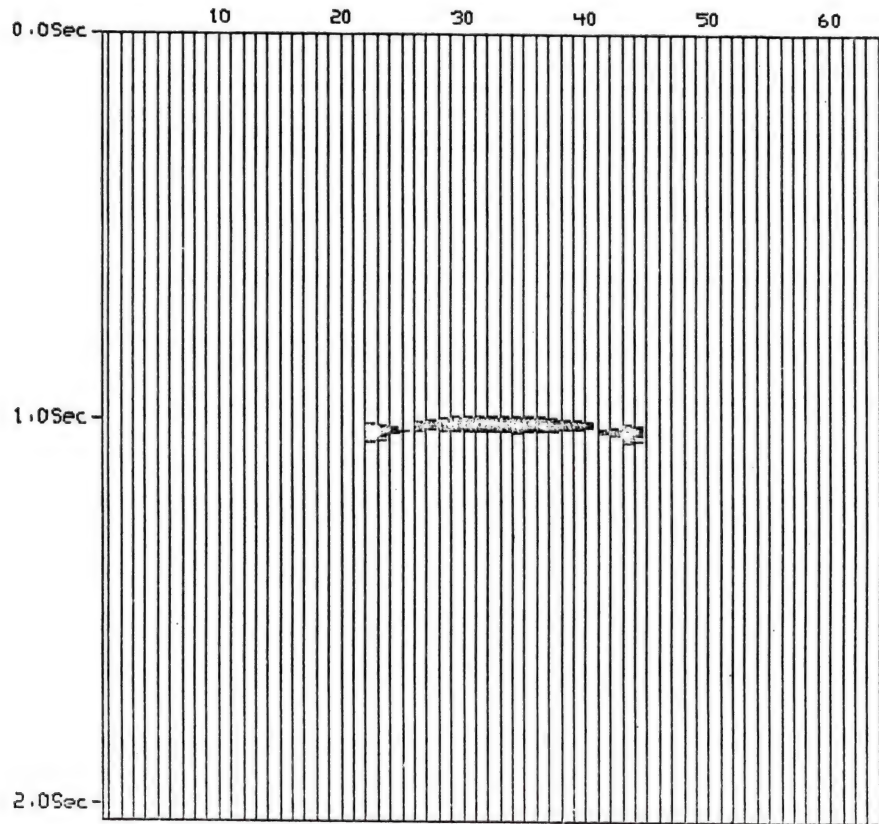


Figure 3.10 Linear classification result of bright spots ($2/3$ quarter wavelength at gas sand zone)

seismograms are presented in the following.

(1) The first hypothesis is that the bright spot has high amplitude, low frequency content and polarity reversal. Envelope, instantaneous frequency and polarity are used in the tree classifier.

(2) The second hypothesis is that the bright spot has high amplitude and low frequency content. Envelope and instantaneous frequency are used in the tree classifier.

(3) The third hypothesis is that the bright spot has high amplitude and polarity reversal. Envelope and polarity are used in the tree classifier.

The first hypothesis of candidate bright spot is the most restrictive one.

In the simulation, zero-phase Ricker wavelets are used. The same procedures can be used for minimum-phase wavelets. The purpose of one-dimensional classification of Ricker wavelets is to determine how to classify the pattern wavelets in a seismic trace. The block diagram of a tree classification system is shown in Fig. 3.11. From Fig. 3.11, for the second hypothesis, the polarity classification is not used. For the third hypothesis, the instantaneous frequency is not used.

For an input seismogram, the data are initially not known as candidate bright spot or non-candidate bright spot. Some testing traces are equally selected from the seismograms, the 4th, 12th, 20th, 28th, 36th, 44th, 52nd, and 60th traces; three hypotheses and an unsupervised clustering analysis are used to detect whether or not the testing traces have candidate bright spot. The candidate bright spot is detected if one of the three hypotheses is satisfied. Thresholds are determined by inspection for a good separability in the scattering diagram of envelope and instantaneous frequency. After designing the

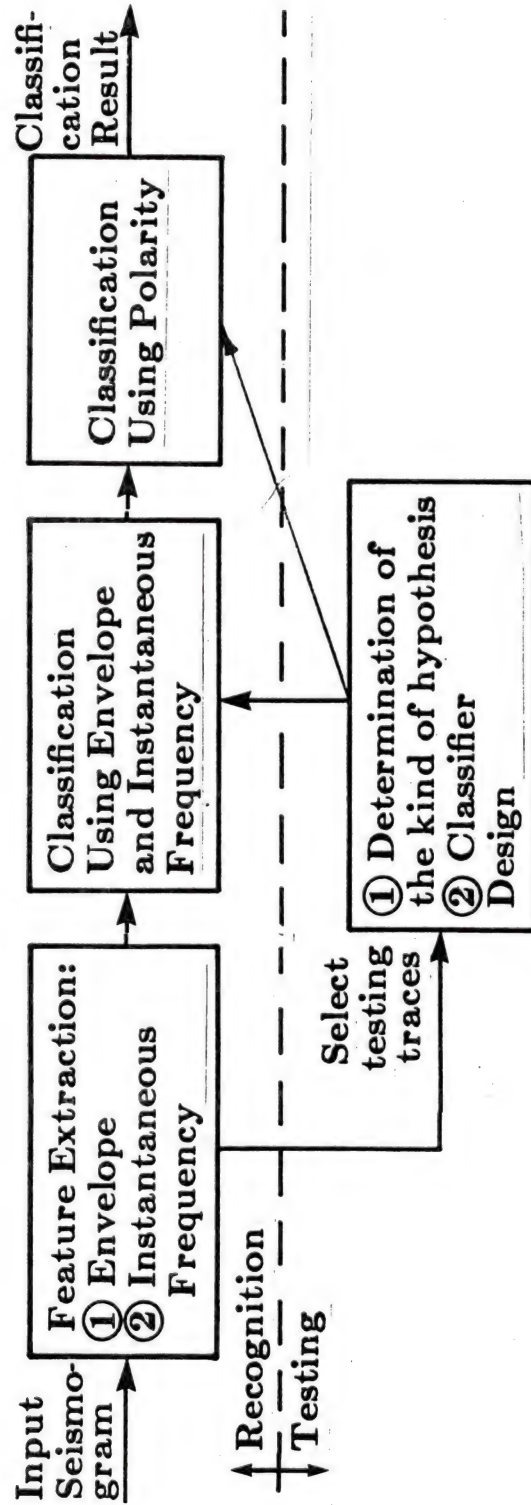


Figure 3.11 Block diagram of a tree classification system

tree classifier in terms of envelope and instantaneous frequency from the testing traces, a classification experiment is performed. Polarity classification is performed after the classification in terms of envelope and instantaneous frequency. In real data experiment, the seismograms at Mississippi Canyon and High Island are the relative-amplitude recording with bandpass 10 - 50 Hz.

3.4.2 Definition of Polarity

Envelope and instantaneous frequency are defined in Chapter 2. Polarity of zero-phase Ricker wavelets and minimum-phase wavelets are defined as follows:

(I) Suppose that a truncated symmetric zero-phase Ricker wavelet has the duration of N points, a_0, a_1, \dots, a_{N-1} . Select $N_0 < N$, where N_0 points pass through the center (extremum) of the Ricker wavelet.

If
$$\sum_{i=j}^{i=j+N_0-1} a_i < 0, \text{ then the polarity is positive.}$$

If
$$\sum_{i=j}^{i=j+N_0-1} a_i > 0, \text{ then the polarity is negative.}$$

(II) Suppose that a truncated minimum-phase wavelet [rob67a] has the duration of N points, a_0, a_1, \dots, a_{N-1} . Select $N_0 < N$, where N_0 points pass through the extremum of the minimum-phase wavelet.

If
$$\sum_{i=j}^{i=j+N_0-1} a_i > 0, \text{ then the polarity is positive.}$$

If $\sum_{i=j}^{i=j+N_0-1} a_i < 0$, then the polarity is negative.

N_0 and j are determined from the tree classification result using envelope and instantaneous frequency or from the tree classification result using envelope only.

3.4.3 Design of Tree Classifier

From the scattering diagram of the experimental results shown in Fig. 3.3 and Fig. 3.12, the envelope of a zero-phase Ricker wavelet is uniformly distributed between one-third of the maximum envelope and the maximum envelope, and the instantaneous frequency is approximately constant within this interval. Inside this interval, the data are corresponding to the central part of the Ricker wavelet. Without using these two simple properties in the tree classifier design, the detection of candidate bright spot will be a complex process. Analytic signal analysis in Gaussian noise has been discussed in Chapter 2. In Fig. 2.5, the envelope of Gaussian noise is a Rayleigh distribution. In Fig. 3.3 and 3.12, the distribution of envelope for Ricker wavelet is uniformly distributed. So in the classification of Ricker wavelets plus Gaussian bandpass noise $N(0, \sigma^2)$, the threshold of envelope is determined between Rayleigh (Gaussian noise) and uniform (Ricker wavelets) distributions. Usually the Bayes decision rule is used. For high signal to noise ratio, the threshold of envelope is determined by selecting the maximum between $\frac{1}{3}$ maximum envelope of Ricker wavelet and 3σ of Gaussian noise. For the data in the scattering diagram above the envelope threshold, the threshold of instantaneous frequency is

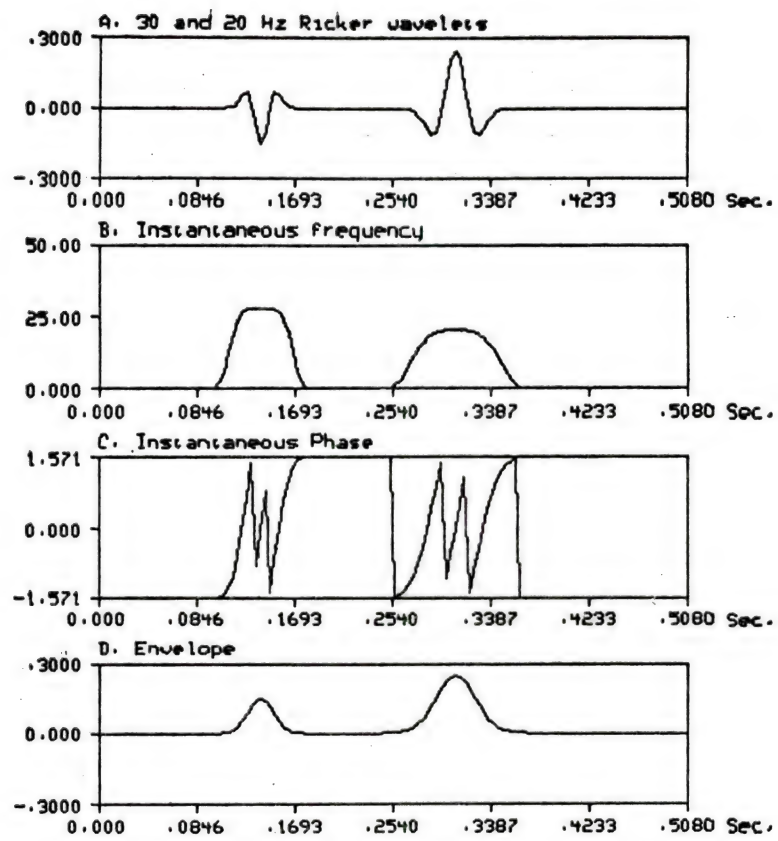


Figure 3.12A 30 and 20 Hz Ricker wavelets and its analytic signal representations

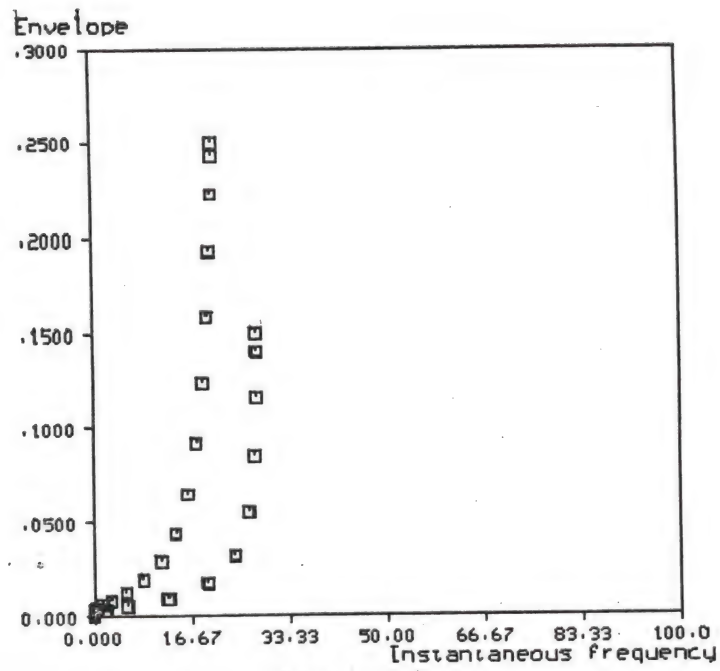


Figure 3.12B Feature distribution of a seismic trace

determined by inspection if data are separable, or by a K-means clustering analysis and maximum PFS (pseudo F-statistics) value [vog78a].

To design a classifier in terms of instantaneous frequency only, the unsupervised clustering analysis is reduced to one-dimensional analysis. K-means clustering algorithm is used for the clustering analysis. In the first step, setting $k=2$, using K-means clustering algorithm, the centers of two classes are found. If $|m_1 - m_2|$ is less than 3.0 Hz of instantaneous frequency, then the number of class is one, otherwise the number of class is two or more. In the second step, if the number of class is two or more, then for different k ($k \geq 2$), the PFS value [vog78a] is calculated to determine the optimum clustering number.

$$PFS = \frac{tr S_b (n - k)}{tr S_w (k - 1)}$$

where S_b is the between-cluster scatter matrix and S_w is the within-cluster scatter matrix [vog78a, fuk74a, liu82a].

The maximum PFS value corresponds to the optimal cluster number. After the PFS analysis, the classification threshold on instantaneous frequency is determined by $\frac{m_1 + m_2}{2}$, where m_1 and m_2 are the centers of the leftmost two classes.

In the scattering diagram of envelope and instantaneous frequency, for the case of one class above envelope threshold, the bright spot is detected by the third hypothesis. For the case of two or more classes, the bright spot is detected by the first or second hypothesis.

Three examples are presented. The first example is the simulation of 20 and 30 Hz Ricker wavelets in a seismic trace in Fig. 3.2 or 3.17.

The second example is the simulation of 20 and 30 Hz Ricker wavelets in the seismogram in Fig. 3.5 or 3.18. The third example is the real seismogram analysis at Mississippi Canyon in Fig. 3.22. Table 3.1 shows the clustering analysis of these three examples. For good separability of features, the threshold is determined by visual inspection.

For detection of candidate bright spot in two-dimensional seismograms, the testing traces are equally selected from a seismogram to cover the reflection characteristics of every kind of layers. The testing traces are the 4th, 12th, 20th, 28th, 36th, 44th, 52nd, and 60th traces. Eight testing traces are selected from a 64-trace seismogram. One testing trace is selected from every eight traces. This kind of selection of testing traces is easy and convenient. Three hypotheses and an unsupervised clustering analysis are used to detect whether or not the testing traces have candidate bright spot. The tree classifier design is the same as that for one-dimensional case. After determining the tree classifiers from the testing traces, the whole seismogram will be processed.

3.4.4 The First Hypothesis and Its Corresponding Tree Classifier

There are four classes in the simulated seismic trace (Fig. 3.14A) and seismogram (Fig. 3.15A):

C1: $r(t)=n(t)+20$ Hz Ricker wavelet at top of gas sand zone with polarity reversal.

C2: $r(t)=n(t)+20$ Hz Ricker wavelet at top of oil sand zone.

C3: $r(t)=n(t)+30$ Hz Ricker wavelet from other boundaries.

C4: $r(t)=n(t)$ Gaussian 10-60 Hz white noise.

where C1 and C2 are related to the high amplitude, low frequency

Table 3.1 Clustering Results

(1) In Fig.3.2. 20 Hz and 30 Hz Ricker wavelets in a simulated seismic trace

	trSb	trSw	PFS	
$k = 2$	179.44	3.28	710.67	← optimal
$k = 3$	0.75	1.975	549.15	
$k = 4$	0.75	1.975	335.59	

I.F. threshold = 23.66

(2) In Fig.3.5. 20 Hz and 30 Hz Ricker wavelets in synthetic seismogram

	trSb	trSw	PFS	
$k = 2$	879.44	77.75	542.93	← optimal
$k = 3$	914.33	42.86	501.35	
$k = 4$	922.70	34.49	410.24	

I.F. threshold = 24.73

(3) In Fig.3.22. Real seismogram at Mississippi Canyon

	trSb	trSw	PFS	
$k = 2$	228.80	108.23	71.87	no significant optimal
$k = 3$	275.27	61.76	73.54	
$k = 4$	300.82	36.21	88.63	

I.F. threshold = 26.69

Select $k=2$, one is bright spot, the other is none.

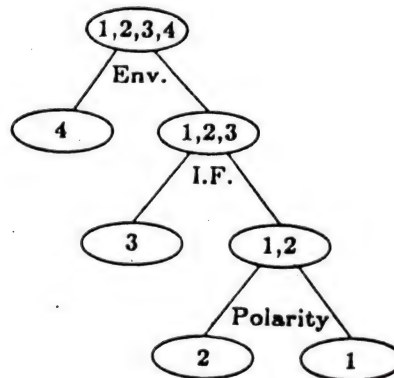


Figure 3.13 Tree classifier of the first hypothesis

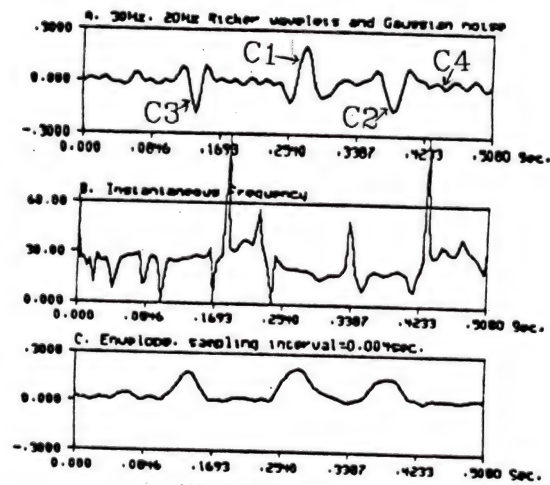


Figure 3.14A Signal, its instantaneous frequency & envelope

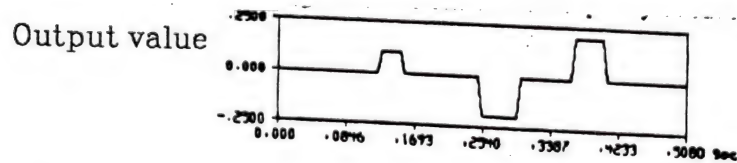


Figure 3.14B Result of tree classification (The first hypothesis)

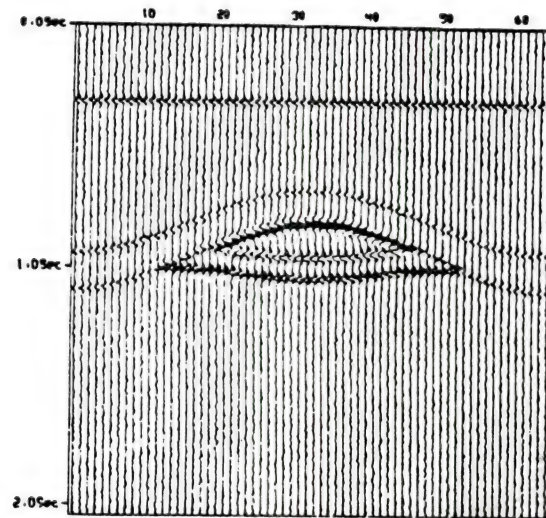


Figure 3.15A The first hypothesis synthetic seismogram of bright spots

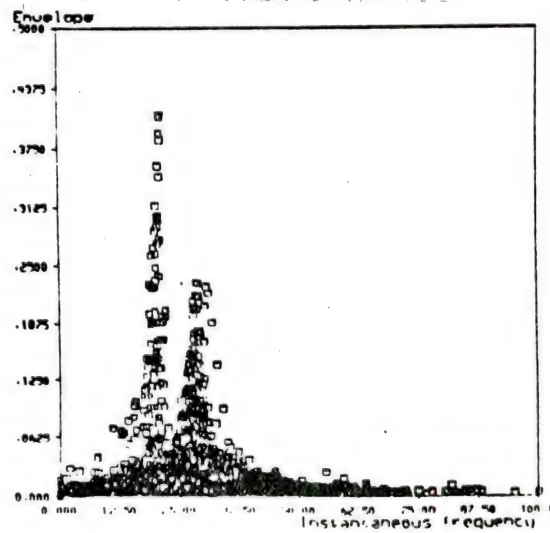


Figure 3.15B Feature distribution of testing traces

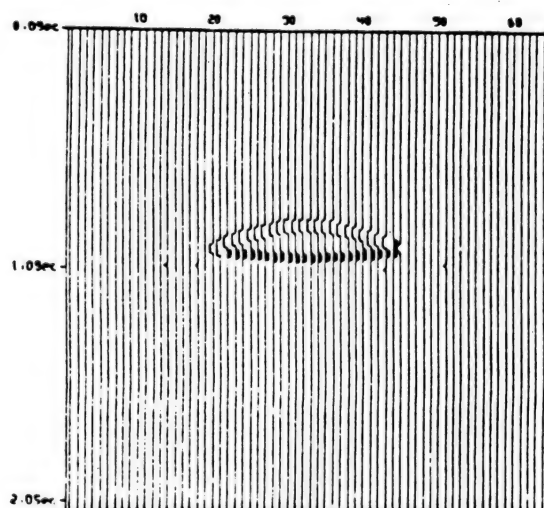


Figure 3.15C Tree classification result of bright spots

content and polarity reversal in gas and oil sand zones. Envelope, instantaneous frequency and polarity are selected as the features in the tree classification. The binary tree classifier designed is shown in Fig. 3.13. Both classification results of Ricker wavelets and the detection of candidate bright spot are shown in Fig. 3.14B and 3.15C. Compared with the original simulated seismic trace in Fig. 3.14A and seismogram in Fig. 3.15A, the results are quite good. In Fig. 3.14B, four classes are classified by using envelope, instantaneous frequency, and polarity. Using polarity as a feature can detect the reflections in gas and oil.

3.4.5 The Second Hypothesis and Its Corresponding Tree Classifier

There are three classes in the simulated seismic trace (Fig. 3.17A) and seismogram (Fig. 3.18A) :

C1: $r(t)=n(t)+20$ Hz Ricker wavelet at top of gas sand zone with polarity reversal.

C2: $r(t)=n(t)+30$ Hz Ricker wavelet from other boundaries.

C3: $r(t)=n(t)$ Gaussian 10-60 Hz white noise.

where C1 is related to the high amplitude, low frequency content and polarity reversal in gas sand zone. Envelope and instantaneous frequency are selected as the features in the tree classification. The binary tree classifier designed is shown in Fig. 3.16. Classification results of Ricker wavelets and the detection of candidate bright spot are shown in Fig. 3.17B and 3.18C respectively. Compared with the original simulated seismic trace in Fig. 3.17A and seismogram in Fig. 3.18A, the results are quite good. In Fig. 3.17B, three classes are classified by using envelope and instantaneous frequency. Envelope and

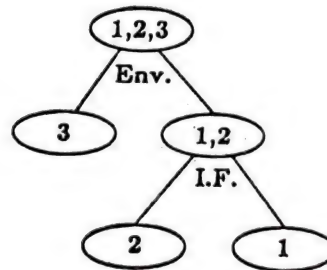


Figure 3.16 Tree classifier of the second hypothesis

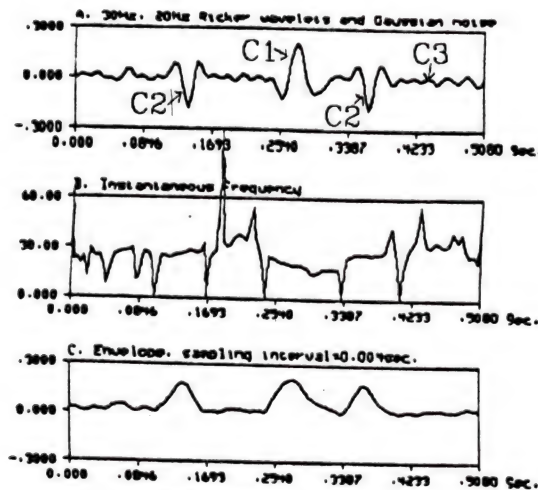


Figure 3.17A Signal, its instantaneous frequency & envelope

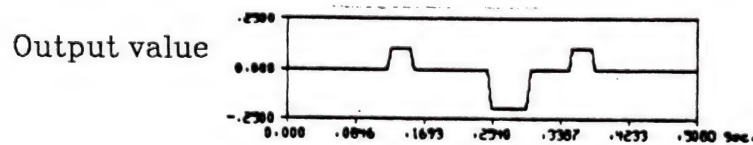


Figure 3.17B Result of tree classification (The second hypothesis)

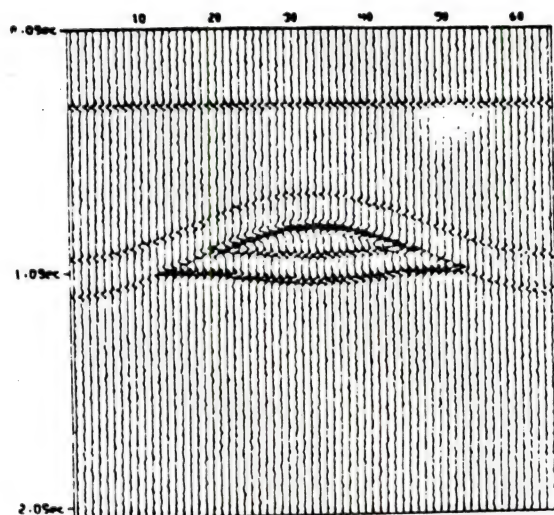


Figure 3.18A The second hypothesis synthetic seismogram of bright spots

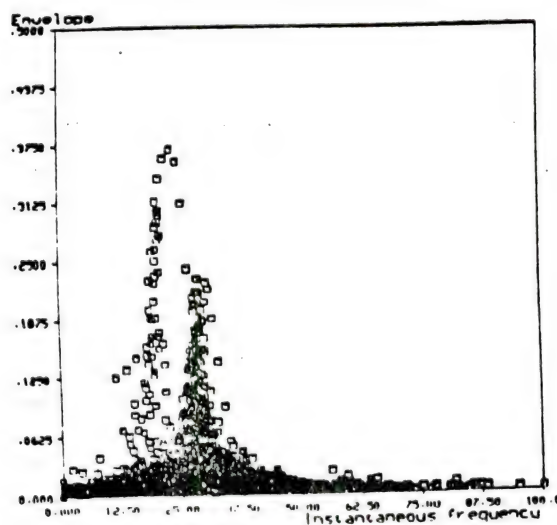


Figure 3.18B Feature distribution of testing traces

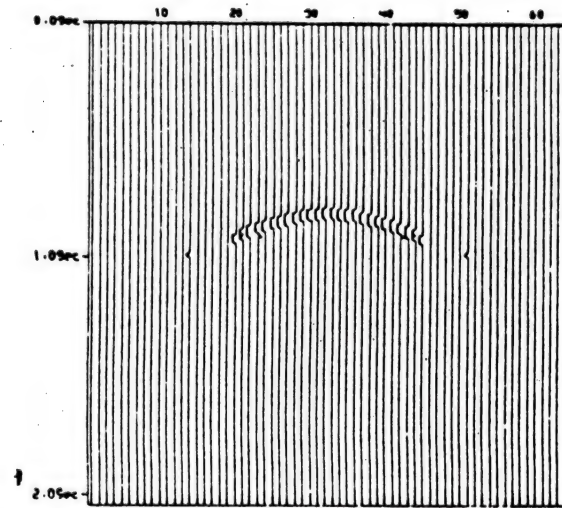


Figure 3.18C Tree classification result of bright spot

polarity can also be selected as the features for this kind of hypothesis.

3.4.6 The Third Hypothesis and Its Corresponding Tree Classifier

There are three classes in the simulated seismic trace (Fig. 3.20A) and seismogram (Fig. 3.21A):

C1: $r(t)=n(t)+25$ Hz Ricker wavelet at top of gas sand zone with polarity reversal.

C2: $r(t)=n(t)+25$ Hz Ricker wavelet from other boundaries.

C3: $r(t)=n(t)$ Gaussian 10-60 Hz white noise.

where C1 is related to the high amplitude and polarity reversal, but no low frequency content in the gas sand zone. Envelope and polarity are selected as the features in the tree classification. The tree classifier designed is shown in Fig. 3.19. Classification results of Ricker wavelets and the detection of candidate bright spot are shown in Fig. 3.20B and 3.21C respectively. Compared with the original simulated seismic trace in Fig. 3.20A and seismogram in Fig. 3.21A, the results are quite good. In Fig. 3.20B, three classes are classified by using envelope and polarity. Using polarity as the feature can detect the polarity reversal in the Ricker wavelet of a seismic trace and the candidate bright spot of the seismogram.

3.4.7 Real-Data Experiment

Two relative amplitude seismograms are processed.

(I) Data from Mississippi Canyon

In Fig. 3.22, at 0.2 and 1.4 seconds, the dominant wavelets are the

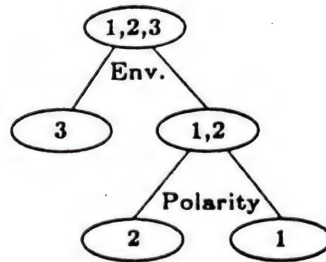


Figure 3.19 Tree classifier of the third hypothesis

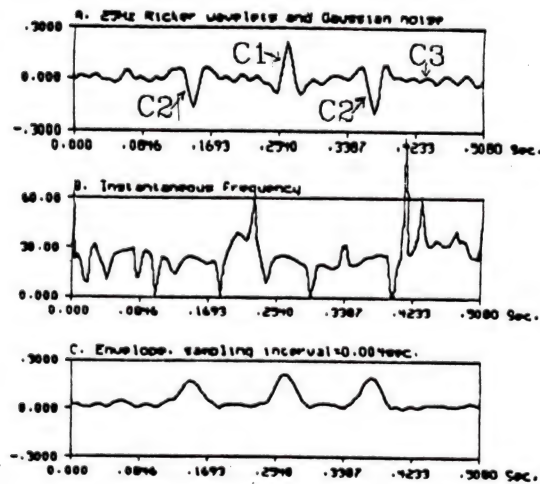


Figure 3.20A Signal, its instantaneous frequency and envelope

Output value

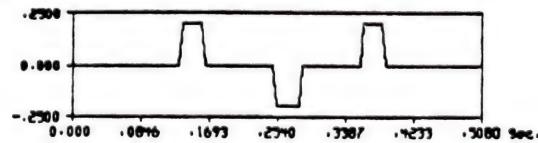


Figure 3.20B Result of tree classification (The third hypothesis)

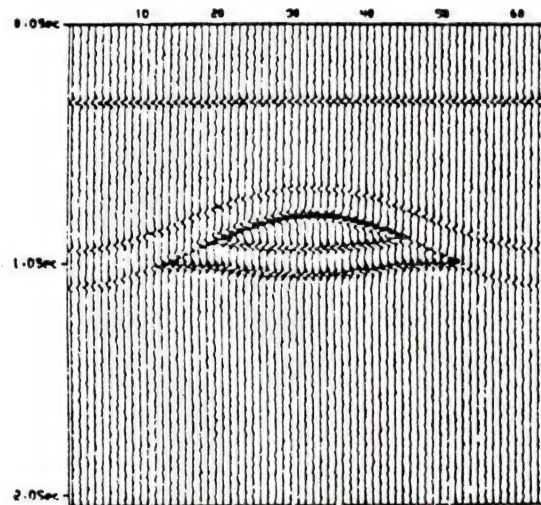


Figure 3.21A The third hypothesis synthetic seismogram of bright spots

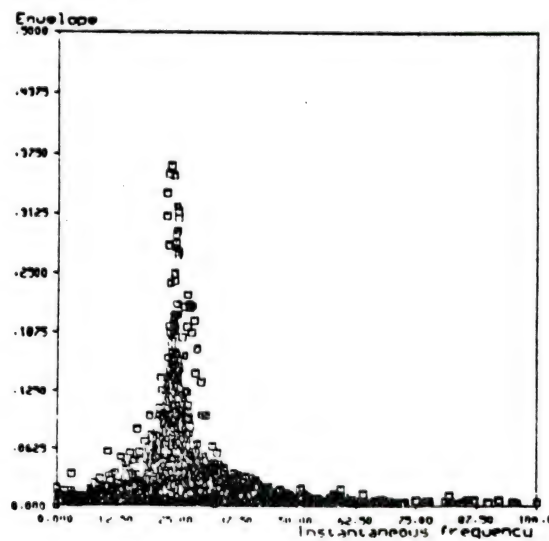


Figure 3.21B Feature distribution of testing traces

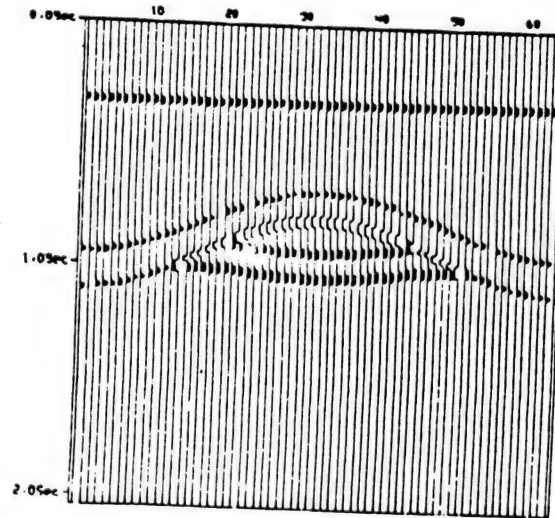


Figure 3.21C Tree classification result of bright spots

minimum-phase wavelets. The tree classifier designed is the same as that in Fig. 3.13 for the first hypothesis. The classification result is shown in Fig. 3.22C. Compared with the real data in Fig. 3.22, the result is easy to be interpreted. The candidate bright spot is at 1.4 seconds which is the most probable to accumulate gas. The left-hand side of 1.4 seconds with positive polarity comes from the interference effect of thin bed. The high frequency contents at 1.3 seconds and the neighbors of the 20th trace have been eliminated using the instantaneous frequency threshold.

(II) Data from High Island

In Fig. 3.23, at 1.7 seconds, the dominant wavelets are the zero-phase wavelets. From the scattering diagram of envelope and instantaneous frequency in the testing traces, the low frequency content is found to be not significant. The tree classifier designed is the same as that in Fig. 3.19 for the third hypothesis. Envelope and polarity are selected as the features in the tree classification. The classification result is shown in Fig. 3.23C. The candidate bright spot is at 1.7 seconds which is the most probable to accumulate gas. At the middle part of the layer of 1.7 seconds, the reflection of the positive polarity is the most probable to accumulate oil/water. Without using the classification technique, the candidate bright spot may be interpreted at the middle part of the layer of 1.7 seconds by using visual inspection.

3.5 Conclusions

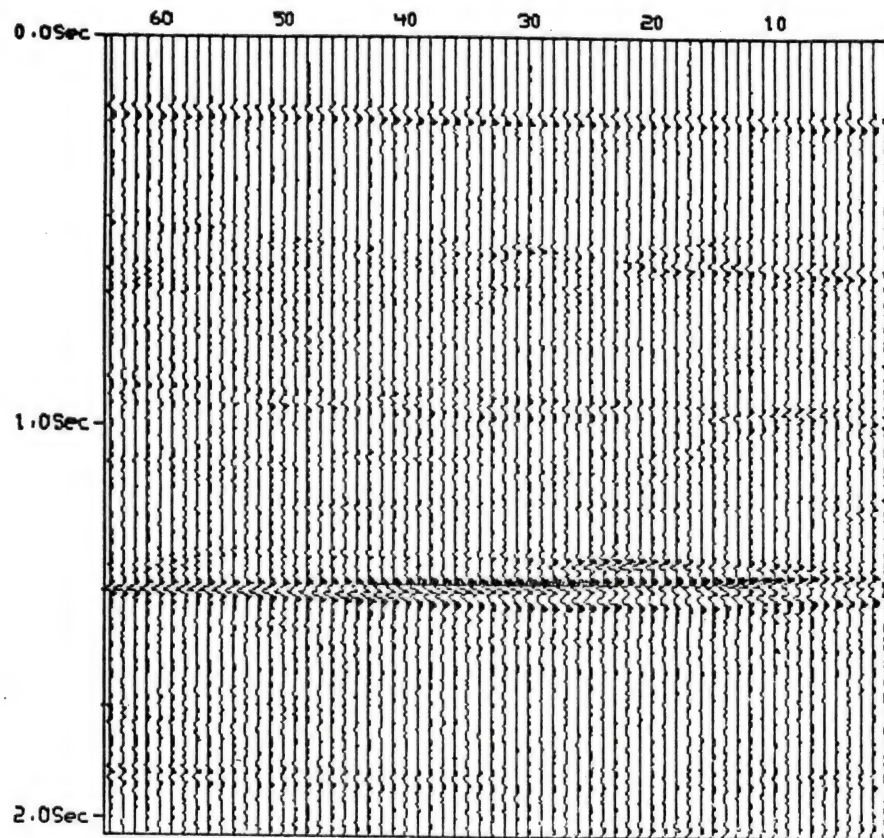


Figure 3.22A Relative amplitude seismogram at Mississippi Canyon (Negative on the Right)

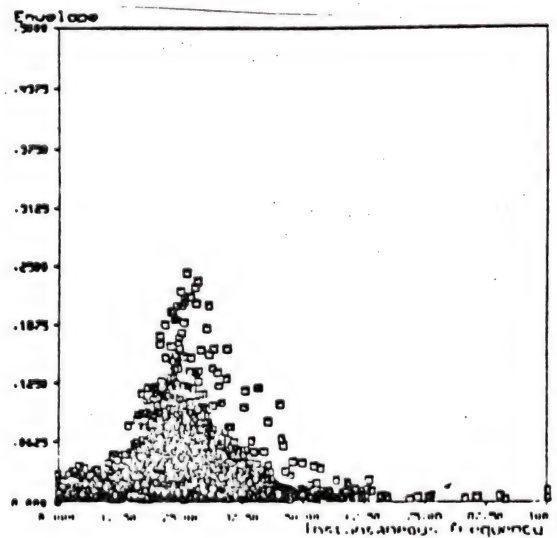


Figure 3.22B Feature distribution of testing traces

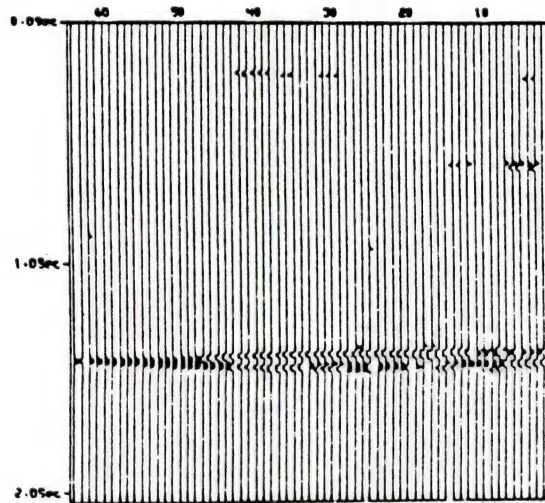


Figure 3.22C Tree classification result of bright spots

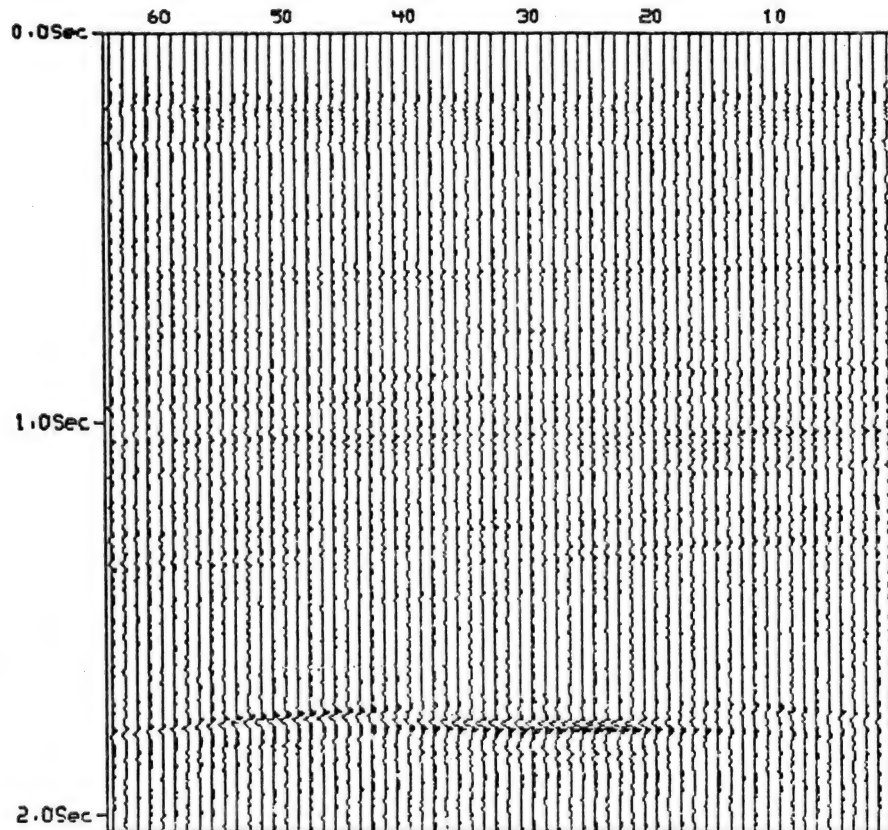


Figure 3.23A Relative amplitude seismogram at High Island (Negative on the right)

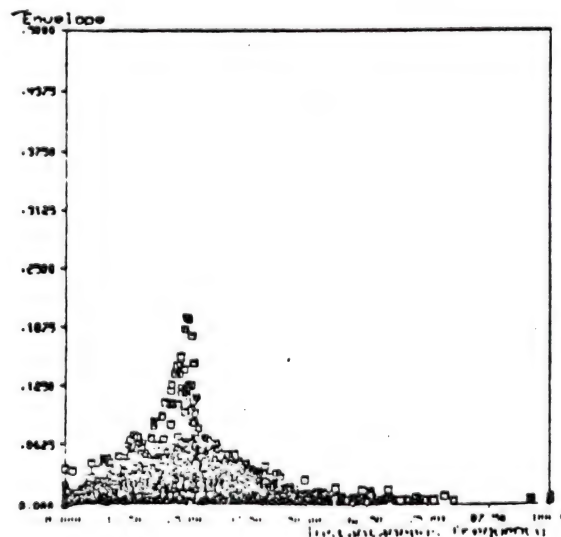


Figure 3.23B Feature distribution of testing traces

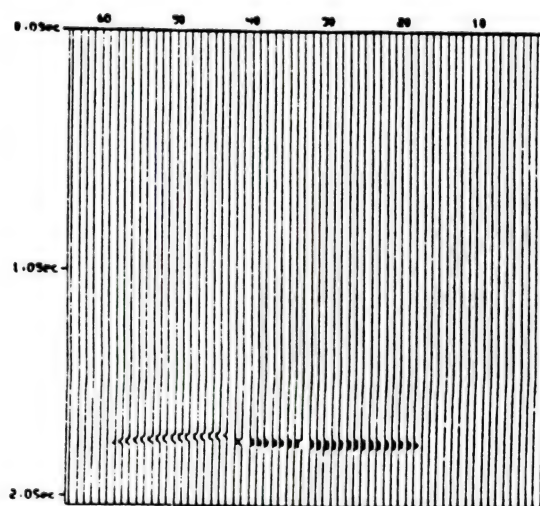


Figure 3.23C Tree classification result of bright spots

(1) The advantages of the modified fixed-increment training procedure are that the convergence is very fast and the decision boundaries are intersected at one point.

(2) From the analysis of zero-phase Ricker wavelets, the use of tree classification is proposed. The advantages of the tree classification are easy to design and computationally efficient. As a matter of fact, the design of the tree classifier is easier than that of the linear classifier.

(3) The envelope threshold is determined from the uniform distribution of wavelets and Rayleigh distribution of Gaussian noise. The threshold of the instantaneous frequency is determined by visual inspection if data are visually separable or by an unsupervised clustering analysis.

(4) For high signal to noise ratio, using envelope is easy to separate signal plus noise (Ricker wavelets plus noise, seismic data) and noise alone. So envelope is selected as the feature for the first-level tree classification. Instantaneous frequency is selected as the feature for the second-level tree classification. Polarity is used after the classifications in terms of envelope and instantaneous frequency.

(5) In real data, the wavelet is not exactly the minimum-phase or zero-phase wavelet. Since a major part of the wavelet is close to the central part of Ricker wavelet, so a tree classifier can be used.

(6) Envelope, instantaneous frequency and polarity have been used as the features for tree classification in the simulated and real relative-amplitude seismograms. The detected candidate bright spot satisfies one of the three hypotheses. The classification results are quite good and can be used to improve seismic interpretation. The detected candidate bright spot (gas reflection) is clearly shown.

(7) For the linear classification of simulated seismogram in this Chapter, training samples have good separability and linear classifier can be determined. But tree classifiers of envelope and instantaneous frequency can even be designed by visual inspection. In the real data, the testing samples are not known as bright spot or non-bright spot. Linear classifier can not be used. For the real data, the pattern of reflection wavelet approximately to the central part of zero-phase Ricker wavelet. From the analysis of Ricker wavelet, tree classification is proposed. Envelope can be used to classify high amplitude and low amplitude portion. Instantaneous frequency can be used to classify low frequency and high frequency contents. So a tree classifier is easy to design and efficient.

CHAPTER IV

DETECTION OF CANDIDATE BRIGHT SPOT IN FREQUENCY ATTENUATED SEISMOGRAM USING A PARTITIONING-METHOD AND TREE CLASSIFICATION

4.1 Introduction

There are many attenuation effects in a seismogram, quality factor Q being the dominant one [car81a, fut62a, gar64a, gar74a, ham72a, joh81a, kja79a, obr61a, sch78a, str70a, tro62a, wyl62a]. The most commonly used measures of attenuation found in the literature are the attenuation coefficient α which is the exponential decay constant of the amplitude of a plane wave traveling in a homogeneous medium; the quality factor Q and its inverse Q^{-1} , sometimes called internal friction or dissipation factor [tok81a]. The quantities are related as follows:

$$\frac{1}{Q} = \frac{\alpha v}{\pi f}$$

where v is the velocity and f is the frequency.

Frequency attenuation effect may appear in a seismogram. A bright spot has important indicators of high amplitude, low frequency content, and phase reversal. But reflections from other layers in a seismogram probably also contain some of these indicators, especially the low frequency content. Consequently, the decision-theoretic pattern recognition techniques proposed in Chapter 3 to classify the whole seismogram often may not be effective enough. A "partitioning-method" is proposed in this Chapter. The basic idea is that bright spots

having low frequency content is only absolutely true in a small section of a seismogram. Block diagram of the partitioning-method and tree classification system is shown in Fig. 4.1. A seismogram is first partitioned into small sections. For each section, three hypotheses and their corresponding tree classification techniques (described in Chapter 3) are used to detect the candidate bright spot. The major advantage of the partitioning-method is that the overlapping distributions of the envelope and instantaneous frequency in different sections can be separated, i.e., the distribution of envelope and instantaneous frequency from one seismic section is not disturbed by those of other seismic sections. The design of the tree classifier in one seismic section is therefore easier than that for the whole seismogram. The computer time for processing a small section is also shorter than that for processing the whole seismogram. The experiment on a real seismogram in Mississippi Canyon is presented.

4.2 Procedure of Partitioning-Method and Tree Classification

From the block diagram of the partitioning-method and tree classification system in Fig. 4.1, five steps are described as follows.

(1) Envelope and instantaneous frequency are extracted as the features from the input seismogram.

(2) The seismogram is partitioned into small sections by using a boundary determination procedure, of which the detailed steps are discussed in Section 4.3.

(3) Testing traces are selected according to the method (I) or (II) described in Section 3.2.2. Testing traces are equally selected or

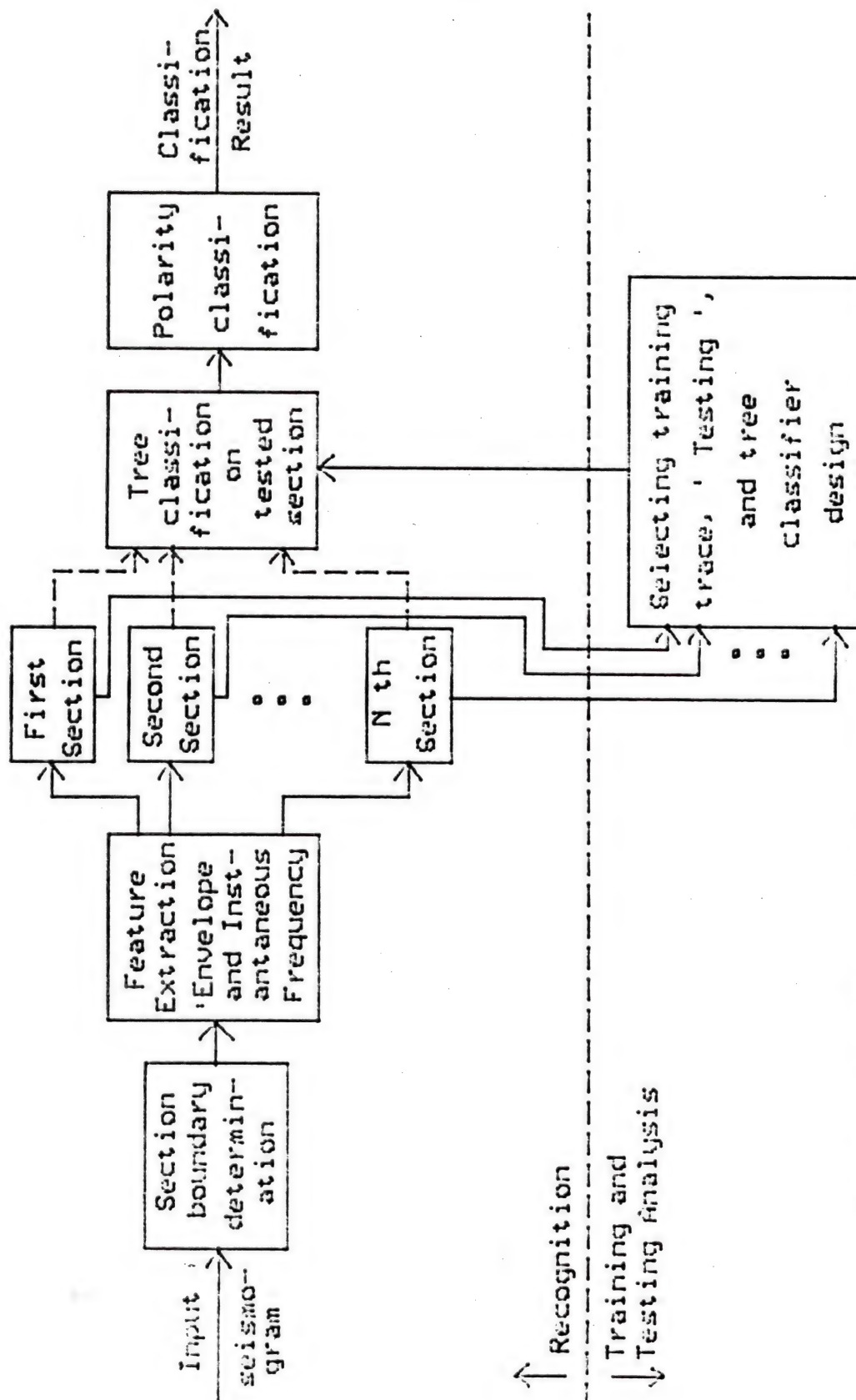


Figure 4.1 Block diagram of partitioning-method and tree classifier system

selected at high amplitude traces from each section. The three hypotheses and tree classification techniques in Chapter 3 are used to detect which sections contain candidate bright spot.

(4) Combine the classification results from each section and output the complete classification results.

4.3 Boundary Determination in Seismogram Partition

In Huang and Fu [hua83c], boundaries are determined by visual inspection to partition a seismogram into small sections to avoid frequency and/or amplitude attenuation effect in the detection of candidate bright spot. The rule of boundary determination is that each section covers some entity reflections, i.e., two or three more reflection layers close together. The boundary may pass through the reflection wavelets, but such a boundary should be avoided. The problem is that boundary determination is not unique and is only subjective by visual inspection. Now, a new method is proposed for the determination of boundaries and a more objective analysis may be entailed. The boundary will pass the middle point between two signals. The real seismogram of Mississippi Canyon is used in the analysis. There are 64 traces and 512 points for every trace.

Steps of processing are given as follows.

Step 1: Find the power distribution along time axis.

Suppose that $a(i,j), i=1,2,\dots,512, j=1,2,\dots,64$, are the data values in the seismogram, where i is the index of time, and j is the index of seismic trace. For every time i , summation of the 64

horizontal squared data values represents the energy of reflection at time i . (The summation looks like a projection). Then the summation divided by 64 represents the power at time i .

$$\frac{1}{64} \sum_{j=1}^{64} a^2(i, j) = s(i), \quad i = 1, 2, \dots, 512$$

From $s(i), i = 1, 2, \dots, 512$, we can see the reflection distribution with respect to time i . This also has the meaning of probability of reflection at time i or the depth of the earth.

The high amplitude wavelets are called "signal plus noise." The data with low values are called "noise." At time i , if only noise is present for $j, j = 1, 2, \dots, 64$, and assumed Gaussian zero-mean, then $s(i)$ represents the variance of the noise. At horizontal and vertical directions, Gaussian noise is assumed. If signal plus noise is present at high amplitude wavelet, then $s(i)$ approximately represents the power of the signal.

For the reflection of horizontal layer, the distribution of $s(i)$ is more concentrated and has a sharp peak. For non-horizontal reflection, i.e., slope (dip) reflection or complex reflection (example of simulated seimogram in Fig. 3.5B), the distribution of $s(i)$ is widely spread.

Step 2: Threshold to separate signal plus noise and noise only

Two methods are considered in the following:

(1) Set a threshold which is equal to 5 times of variance of the noise, then classify signal plus noise and noise.

In order to calculate the distance between two successive signals, a threshold must be determined to separate the signal plus noise and noise. The method presented in this Chapter is to calculate the

variance σ^2 of the noise in the 1st trace of the seismogram at Mississippi Canyon. The threshold is set to $5\sigma^2$. The square root of threshold value equals to $\sqrt{5}\sigma$. The probability of noise value that is beyond $\pm\sqrt{5}\sigma$ is small. Above the threshold the signal is present.

(2) If we do not know the noise, then measure the maximum of the power value at each wavelet, find the average of those maximum values and set a threshold which is equal to the half of this average.

Step 3: Find the distance between two successive signals.

If the first point ($i=1$) is noise, then the first point is a starting point. From the starting point of i , scan and test the next signal location (left edge of signal plus noise), then calculate the distance as d_1 . Scan the right edge point of the signal plus noise (above threshold) as the starting point and repeat the same procedure to calculate the successive signal distances as d_2, d_3, \dots, d_n .

Step 4: Find the threshold for successive signal distances.

Display the distribution of d_i and determine the threshold D by inspection from histogram or by K-means clustering algorithm for $K=2$ [lin80a, swa78a, tou74a]. The reason for $K=2$ is that the signal distances are two classes, i.e., the class of long signal distance and the class of short signal distance. From clustering result, the two class centers are determined. Threshold D is the average of two class centers.

Step 5: Determine the boundary location.

After determining the threshold D from Step 4, compare d_i with D . If $d_i > D$, then a boundary is set in the middle of the two signals, i.e., the boundary is determined by the position of starting point plus $\frac{d_i}{2}$. If

$d_i < D$, then no boundary is found. Accumulate the distance without boundary. Continue to compare d_i with D . A constant is set if the scanned distance is larger than this constant, for example 0.5 seconds, then the boundary is automatically set at the middle of the next interval. This can avoid no boundary. Boundary distance of 0.5 seconds is good from [str70a]. If boundary distance is large, for example 1.0 seconds, the Q effect is large [str70a].

According to the analysis above, the threshold can be set by using the method (1) or (2) in Step 2. An algorithm is presented as in the followings.

Algorithm 4.1: Determination of partitioning boundary in a seismogram

Input: An m points seismogram with N traces, constant c and t , where c is 5 times of noisy variance, $t=0.5$ seconds

Output: Location of the partitioning boundary

Method:

- (1) Find the power distribution along time axis.
- (2) Set a threshold c to classify signal plus noise and noise only.
- (3) Find the distance between two successive signals. The distances are d_1, d_2, \dots , and d_n .
- (4) Find the threshold D of the signal distances by using K-means clustering algorithm for $K=2$. The threshold is the average of two class centers.
- (5) Determine the boundary location.

Compare d_i with D . If $d_i > D$, then a boundary is set at the middle point of the two signals. If $d_i < D$, then no boundary is found. Accumulate the distance without boundary. Continue to compare d_i with D .

(6) If the scanned distance is larger than the constant $t=0.5$ seconds, then the boundary is automatically set at the middle of the next interval. Go to (5), until the end of the data is reached.

4.4 Results of Boundary Determination

The results of applying Algorithm 4.1 to the real seismogram at Mississippi Canyon Fig. 4.2 are as follows.

Fig. 4.3 is the result of Step (1) to find the power distribution along time i , $i=1,2,\dots,512$. The variance of the noise in the 1st trace of Mississippi Canyon is $0.0001972 = \sigma^2$. $5\sigma^2=0.000986=0.001$. In Step (2), the threshold for classifying signal plus noise and noise is 0.001. Fig. 4.4 is the result of the Step (3) and (4). Signal distance d_i is displayed and the threshold D is calculated as $D=52$ by K-means clustering analysis for $K=2$. From Step (5), the boundaries are determined at time=0.408 seconds, 0.776, 1.164, and 1.724 seconds. Five sections are generated. The resulting boundaries are shown in Fig. 4.2.

Fig. 4.5A, 4.5B, 4.5C, 4.5D, 4.5E are the feature distribution of the testing traces for the first, second, third, fourth, and fifth sections respectively. Fig. 4.6 is the feature distribution of the testing traces for the whole trace. Fig. 4.5D is compared with Fig. 4.6. The overlapping distribution of the envelope and instantaneous frequency has been separated in Fig. 4.5D. The distribution of envelope and instantaneous frequency in the 4th section (Fig. 4.5D) is not influenced by those from other sections. The tree classifier design in Fig. 4.5D is easier than that in Fig. 4.6.

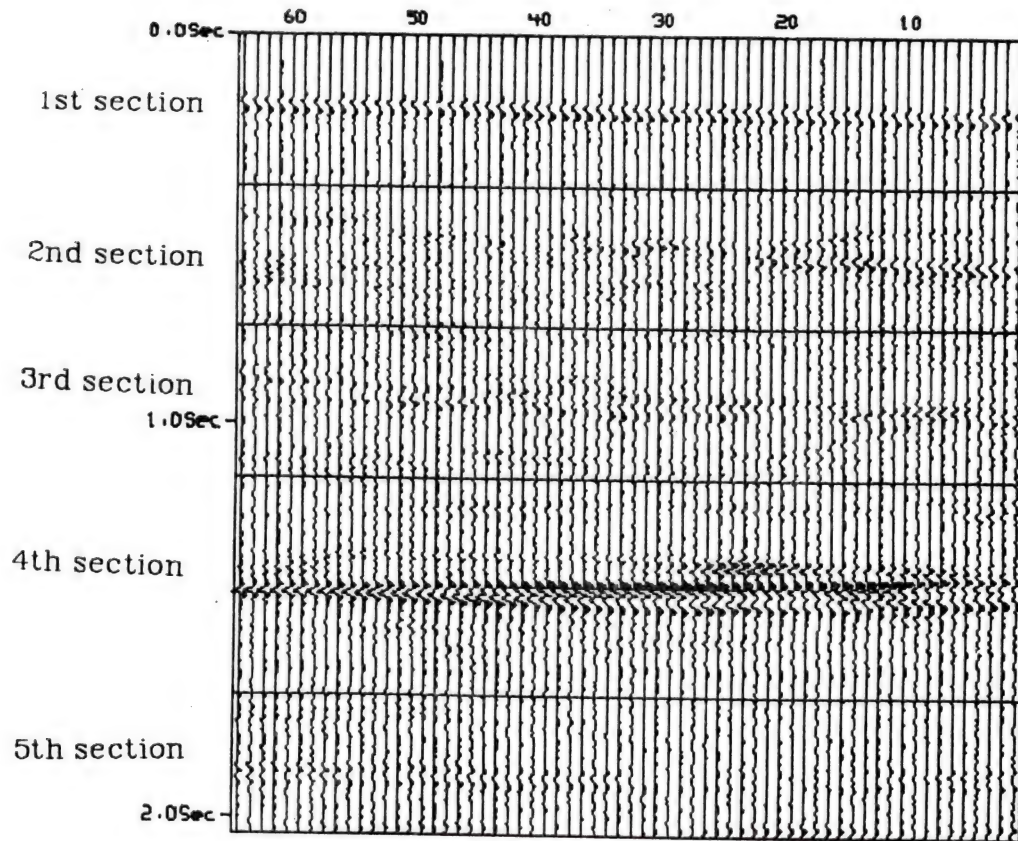


Figure 4.2 Relative amplitude seismogram at Mississippi Canyon and partitioning boundaries (5 sections)

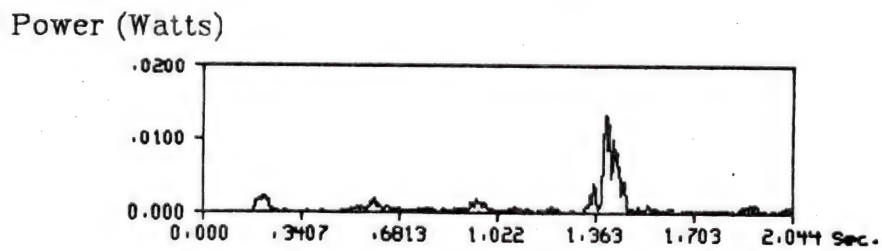
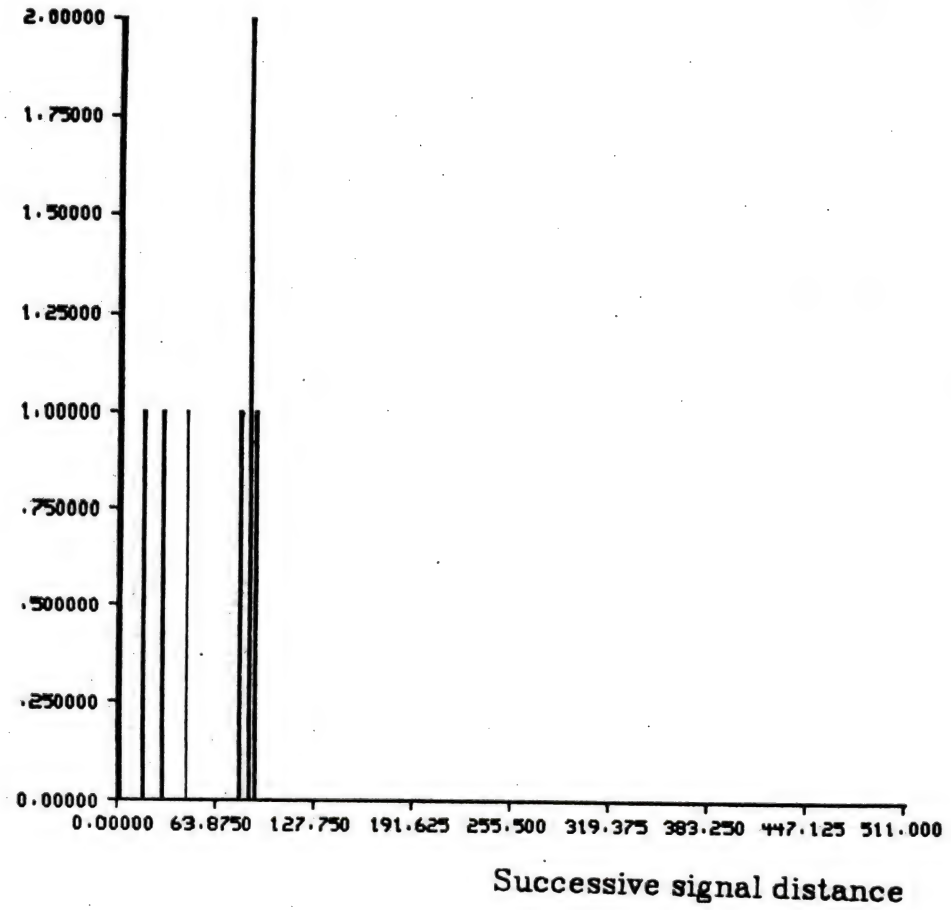


Figure 4.3 Power distribution

Number of Points

Figure 4.4 Distribution of signal distance k_i

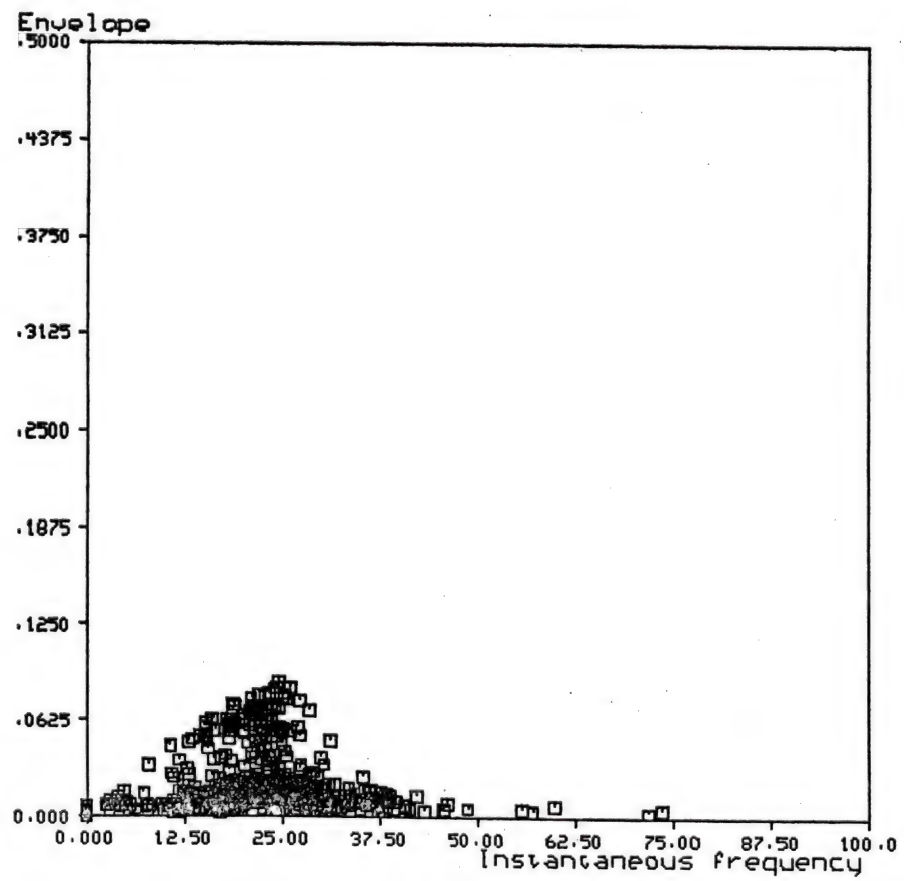


Figure 4.5A Feature distribution of training traces (The first section)

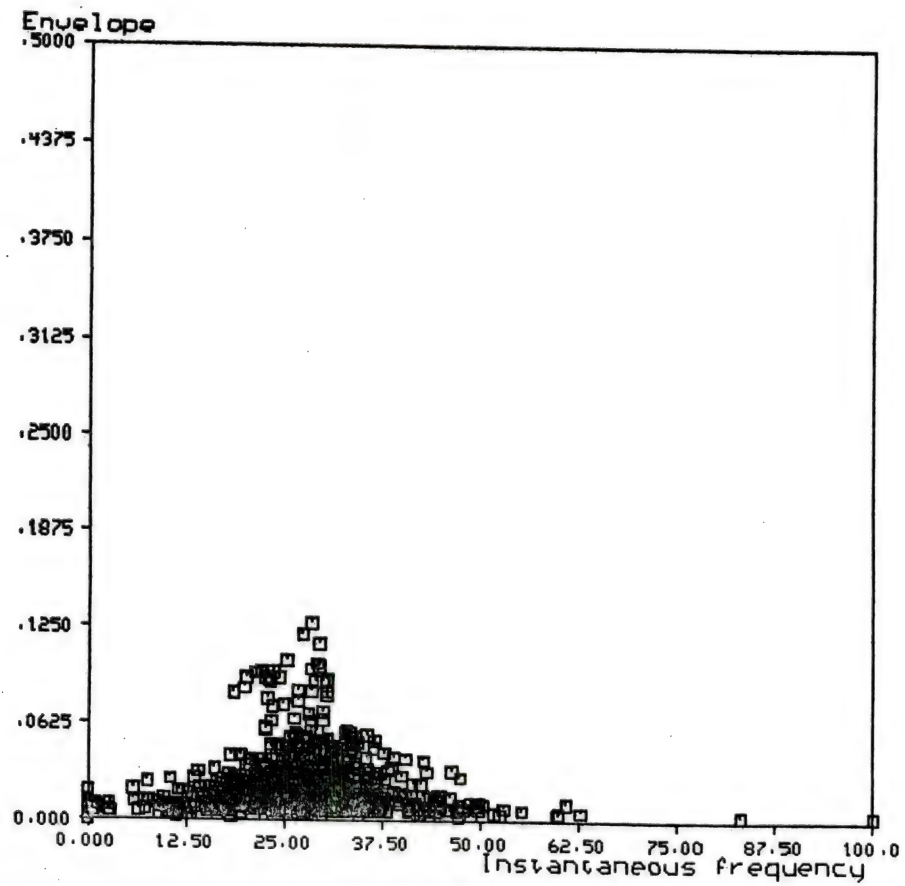


Figure 4.5B Feature distribution of training traces (The second section)

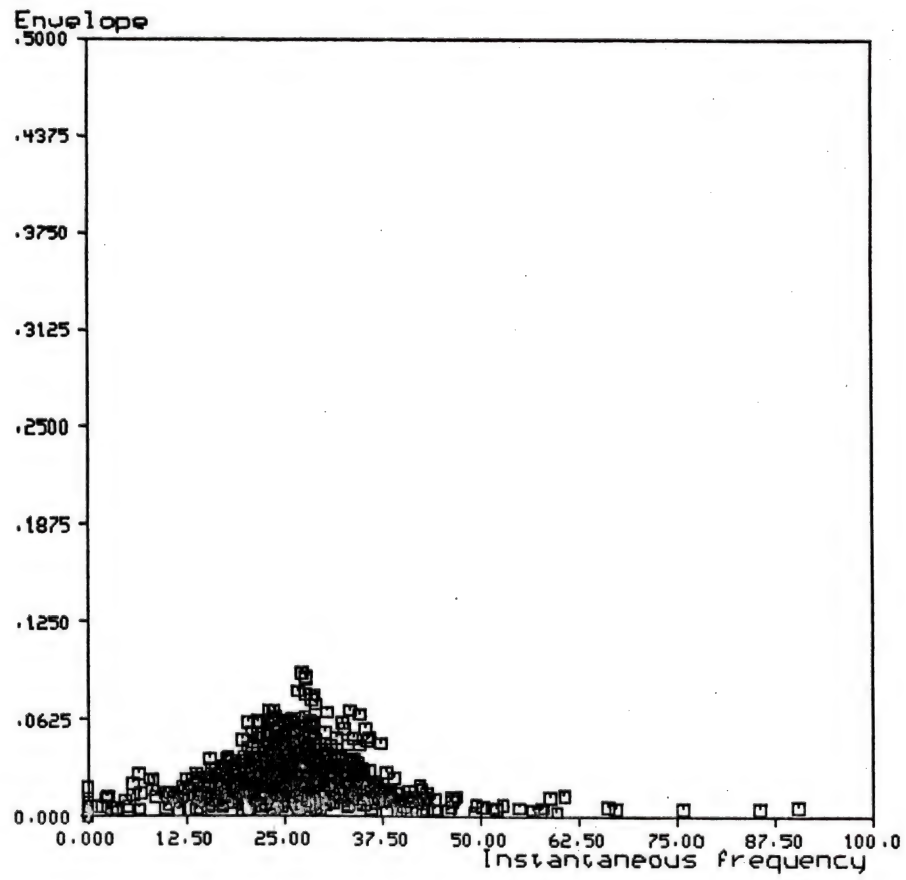


Figure 4.5C Feature distribution of training traces (The third section)

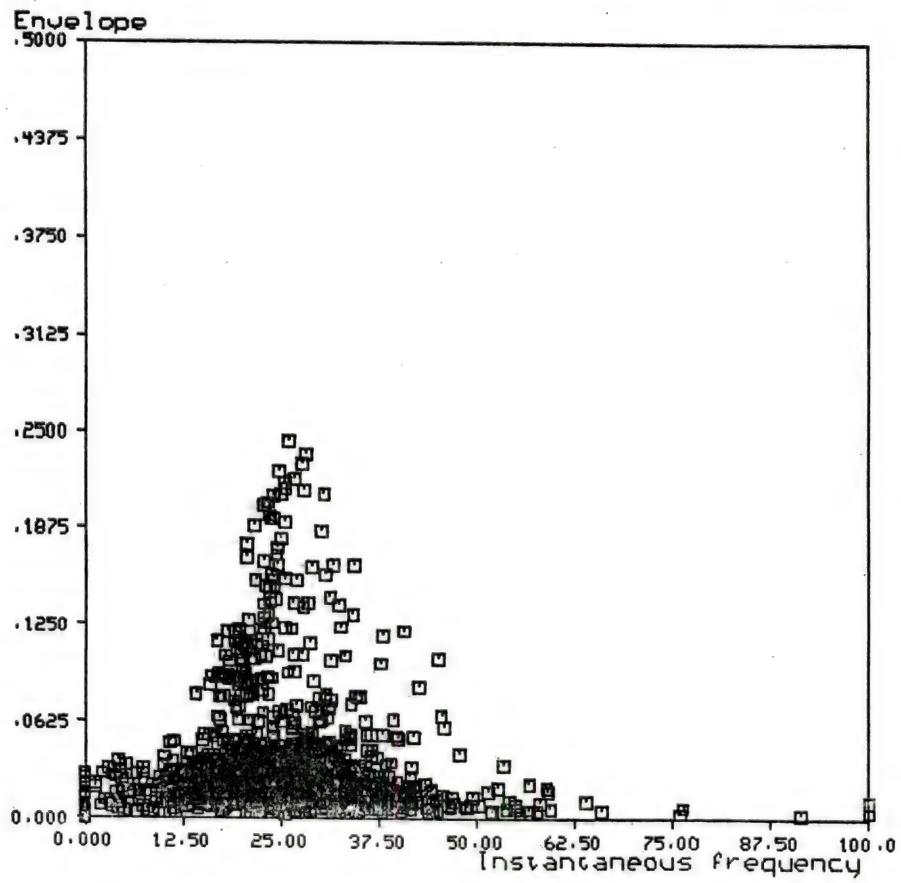


Figure 4.5D Feature distribution of training traces (The fourth section)

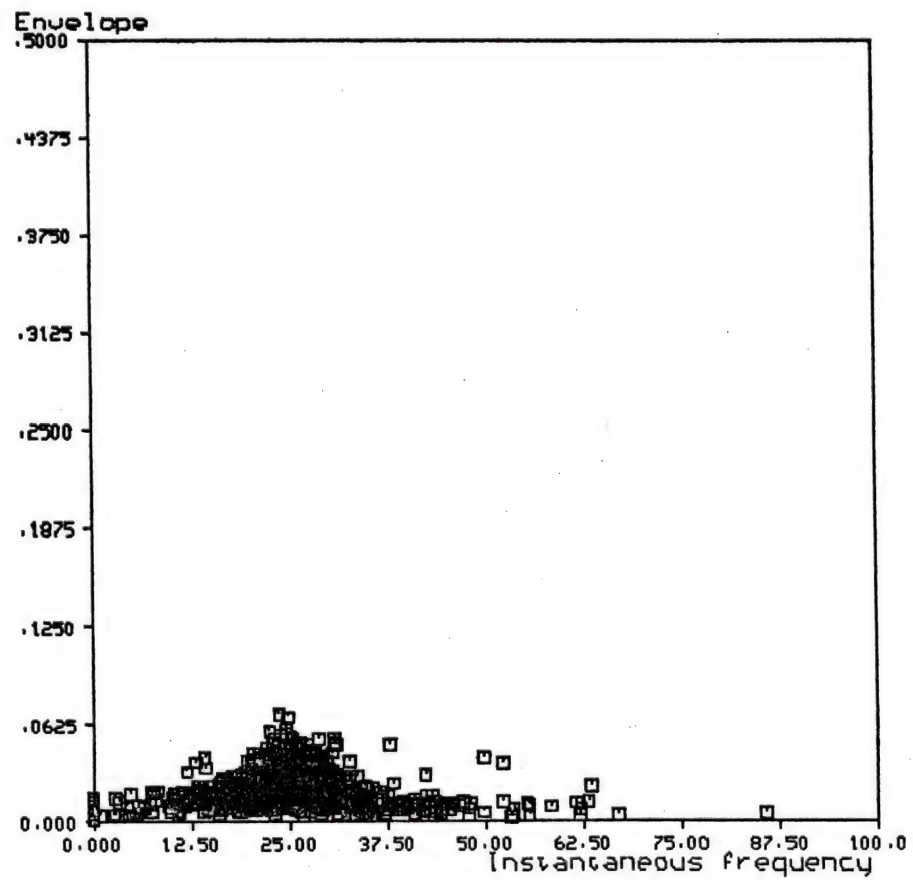


Figure 4.5E Feature distribution of training traces (The fifth section)

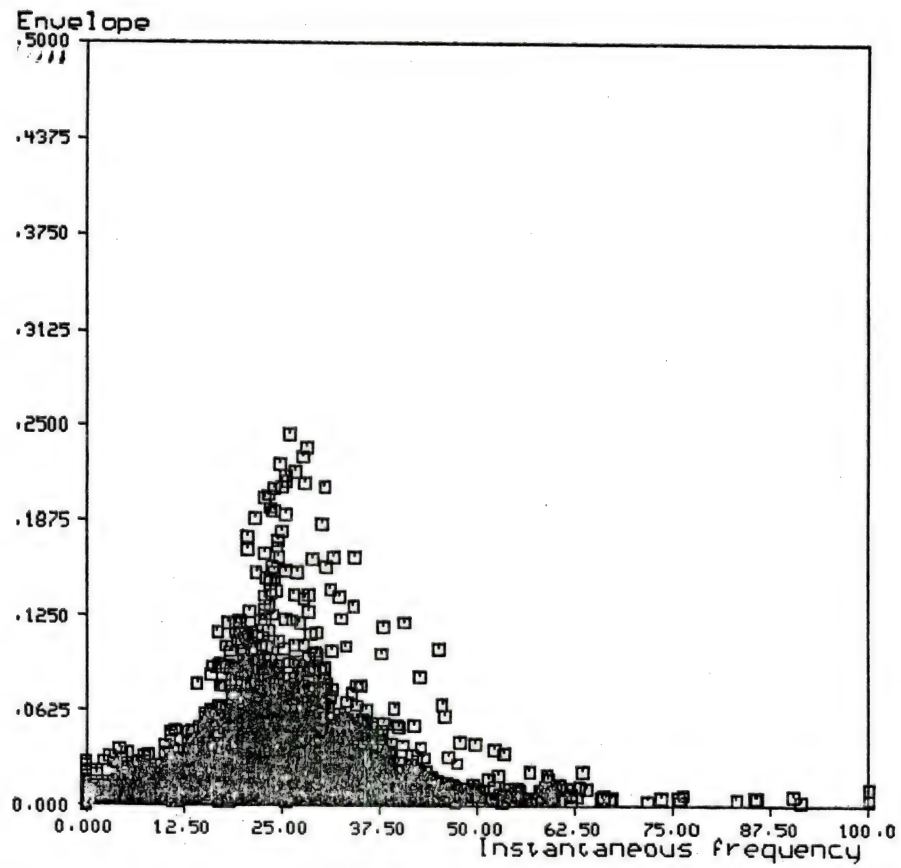


Figure 4.6 Feature distribution of training traces

4.5 Results of Partitioning-Method and Tree Classification for the Detection of Candidate Bright Spot

The 5 sections are tested using 3 hypotheses and their corresponding tree classification techniques. Testing traces are the 4th, 12th, 20th, 28th, 36th, 44th, 52th, and 60th traces. From the feature distribution of envelope and instantaneous frequency in the testing traces of each section, only the 4th section returns the candidate bright spot information and satisfies the first hypothesis in Chapter 3, i.e., high amplitude, low frequency, and negative polarity. After classifying the 64 traces in the 4th section, the complete classification result is shown in Fig. 4.7. The classification result using tree classification without partition (Chapter 3) is shown in Fig. 4.8. Fig. 4.7 is compared with Fig. 4.8. In Fig. 4.7, using the partitioning method, the candidate bright spot is located at 1.4 seconds. Compared with Fig. 4.2, Fig. 4.7 has a significant improvement on the classification result that is quite important in seismic interpretation.

4.6 Discussions

(1) The major advantage of the proposed partitioning-method is that the overlapping distributions of the envelope and instantaneous frequency in different sections can be separated, i.e., the distribution of envelope and instantaneous frequency at one section is not affected by those from other sections. The classifier is easy to design.

(2) The threshold in Step 2 to classify the noise and signal plus noise is equal to 5 times of the variance of noise in the seismogram.

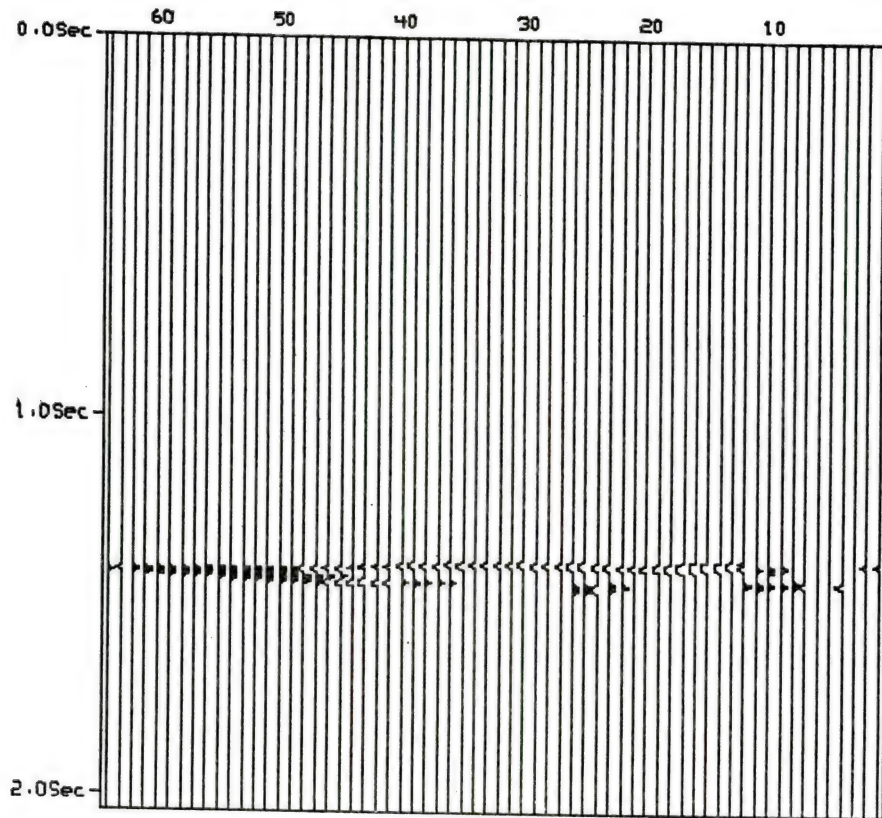


Figure 4.7 Tree classification result of bright spot
(Partitioning-method and tree classification)

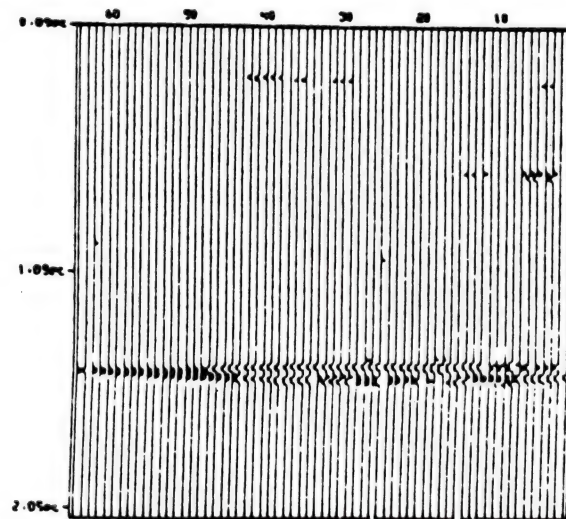


Figure 4.8 Tree classification result of bright spot
(Tree classification without partition)

(3) The determination of partitioning boundary along the horizontal direction can also be used along the vertical direction or other directions. In a long seismogram, partitioning a seismogram along the vertical direction is needed. If the reflection layer is slanted, then it will be necessary to partition the seismogram in that direction. The direction of the boundary determination is dependent upon the direction of the reflection layers.

(4) Computer time for the processing of small sections is shorter than that for the whole seismogram.

(5) The proposed method for boundary determination is more objective than visual inspection [hua83c]. This proposed method can be applied to long and wide seismograms as well.

CHAPTER V

USE OF SYNTACTIC PATTERN RECOGNITION FOR THE DETECTION OF CANDIDATE BRIGHT SPOT

5.1 Introduction

In Chapter 3, decision-theoretic pattern recognition techniques have been applied to the classification of Ricker wavelets and the detection of candidate bright spot [hua82a, 83a]. The classifier design is based on the good separability among different classes. When the inter-class separability is poor, classifier design in decision-theoretic pattern recognition is not easy. In Fig. 5.1A (sampling interval=0.004 seconds), there are three kinds of zero-phase Ricker wavelet (without noise), two 20 *Hz* Ricker wavelets with reflection coefficient -0.25 and -0.12 respectively, and one 17 *Hz* Ricker wavelet with reflection coefficient -0.12. From the scatter diagram of envelope and instantaneous frequency in Fig. 5.1B, it is not easy to design a classifier to classify these three Ricker wavelets. So the approach of syntactic pattern recognition is proposed. The structural information of Ricker wavelets is used. Also in a seismogram, the wavelets of a bright spot have some specific structure. So syntactic pattern recognition approach is proposed for the classification of Ricker wavelets and the detection of candidate bright spot.

(Amplitude)

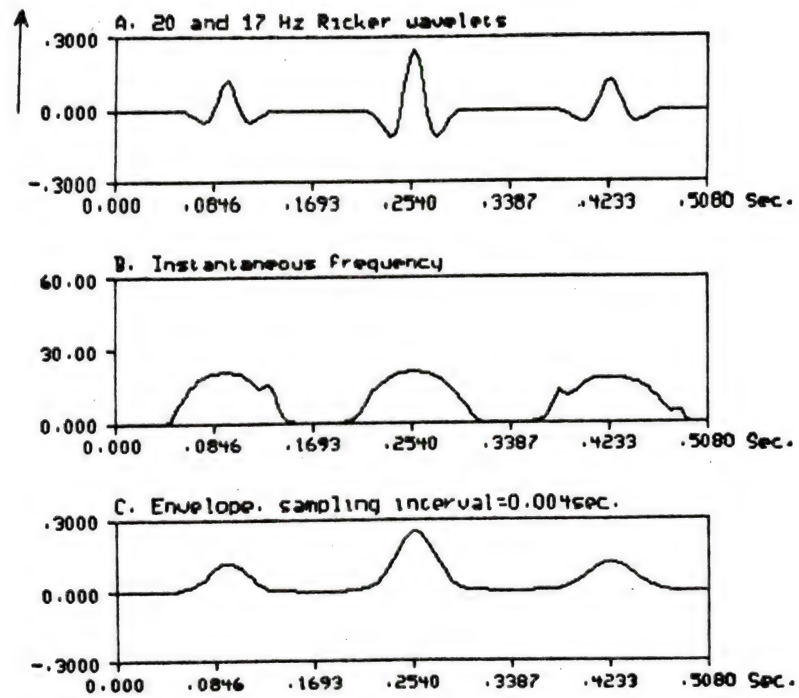


Figure 5.1A Signal, its instantaneous frequency, and envelope

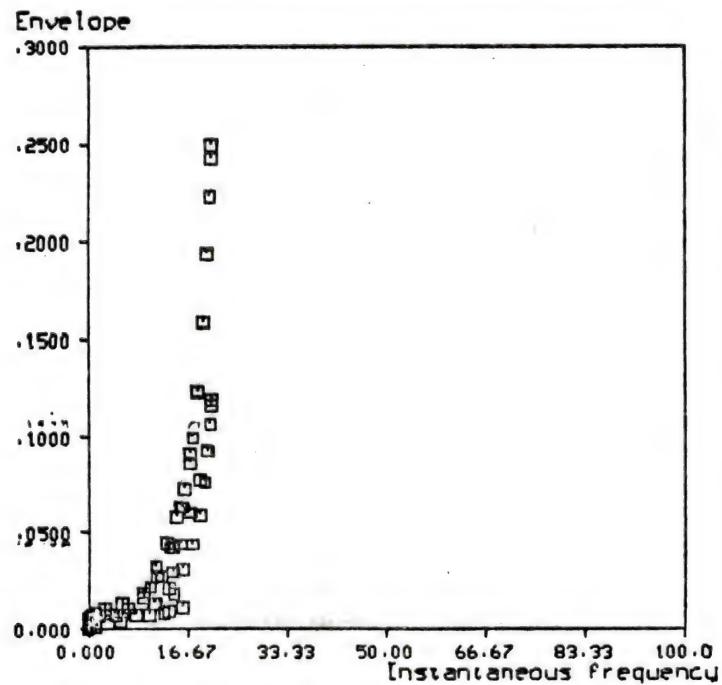


Figure 5.1B Feature distribution of a seismic trace

A syntactic pattern recognition technique is first used for the classification of Ricker wavelets in a simulated seismic trace. Then, a syntactic pattern recognition technique is used to detect the candidate bright spot in a simulated seismogram as well as real seismograms of Mississippi Canyon and High Island.

A block diagram of syntactic pattern recognition system for the classification of Ricker wavelets in a simulated seismic trace is shown in Fig. 5.2A. In the classification of Ricker wavelets, amplitude-independent and amplitude-dependent encodings of optimal quantization are used. Many techniques of peak recognition and waveform analysis can be found in [hor75a, 77a, pav71a, 73a, san79a, shl82a]. In this study, Ricker wavelets is represented by the optimal quantization encoding. The global detection is to detect the possible wavelets. Levenshtein distance is computed between the possible wavelet string and the reference strings of Ricker wavelets. The local detection is to extract the candidate wavelet. Minimum distance and nearest-neighbor classification rules are used.

A block diagram of syntactic pattern recognition system for the detection of candidate bright spot is shown in Fig. 5.2B. In the detection of candidate bright spot, testing traces are selected from the input seismogram and tree classification techniques are used in the detection of candidate bright spot. From the detected candidate bright spot, the sample patterns of the wavelets are extracted. Amplitude-dependent encoding with optimal quantization is also used. Using the probability of detection, a threshold is set to detect the candidate bright spot.

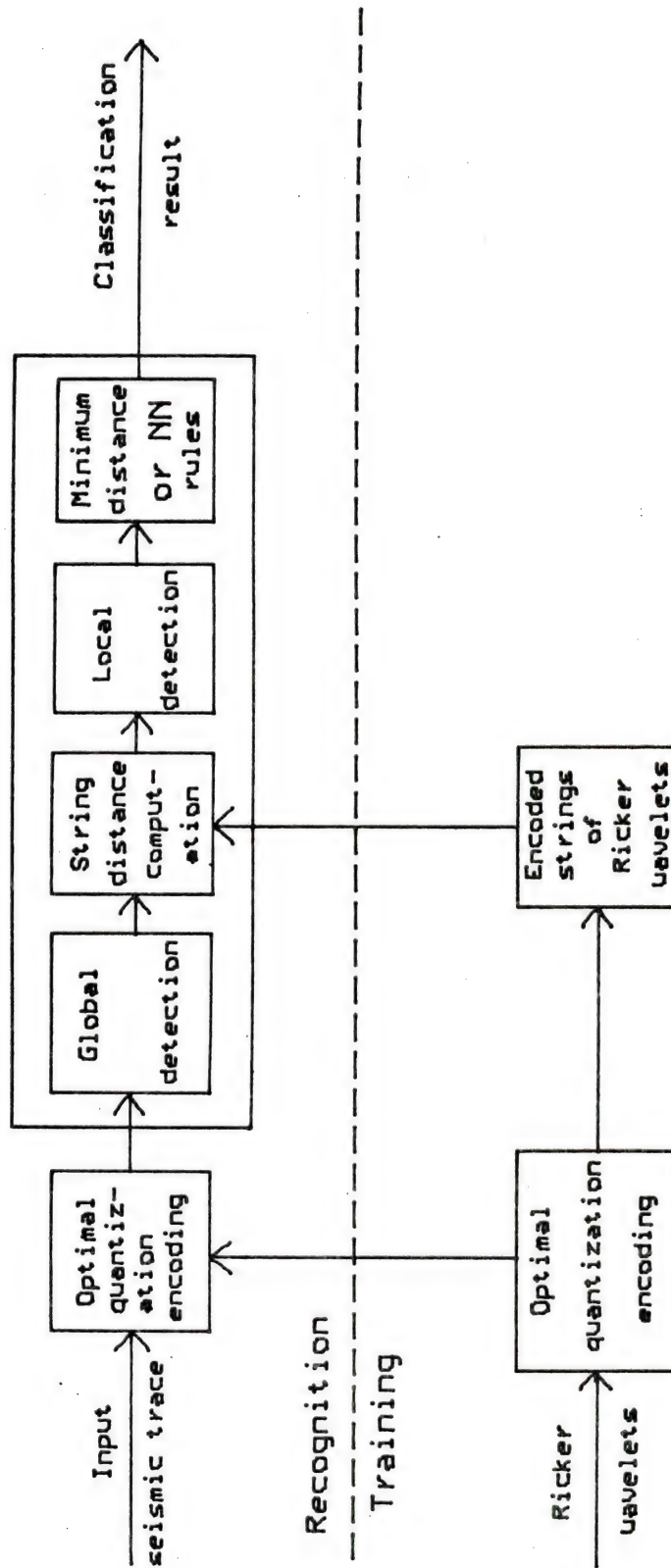


Figure 5.2A A block diagram of syntactic pattern recognition system
(For classification of Ricker wavelets in a seismic trace)

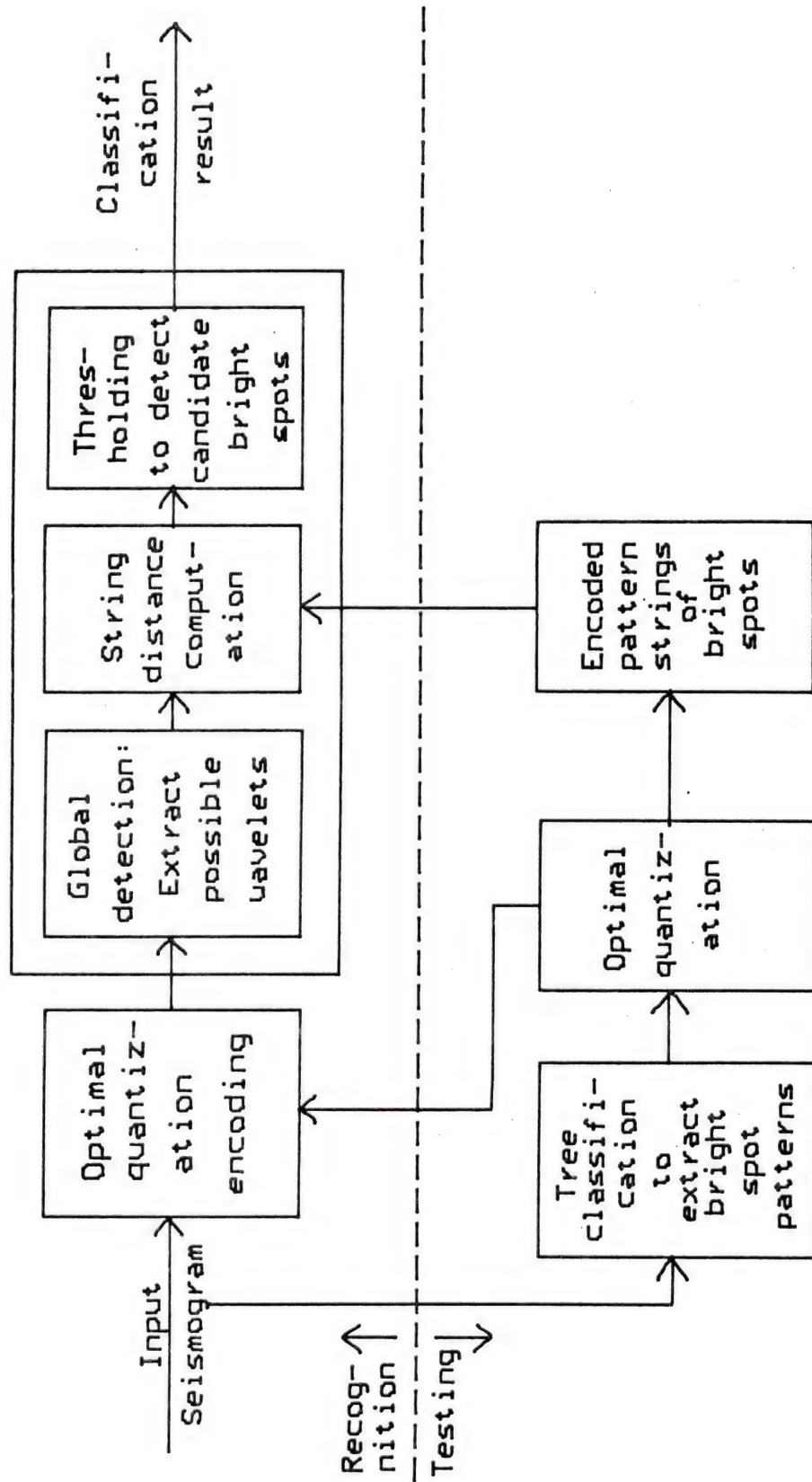


Figure 5.2B A block diagram of syntactic pattern recognition system
(For the detection of candidate bright spot in a seismogram)

5.2 Syntactic Pattern Recognition for the Classification of Ricker Wavelets in the Simulated Seismic Trace

5.2.1 Optimal Quantization Encoding

In Fig. 5.4, there are four classes in the simulated seismic trace.

- C1: $r(t)=n(t)+20$ Hz Ricker wavelet with reflection coefficient -0.18
- C2: $r(t)=n(t)+20$ Hz Ricker wavelet with reflection coefficient -0.2960
- C3: $r(t)=n(t)+17$ Hz Ricker wavelet with reflection coefficient -0.18
- C4: $r(t)=n(t)$ Gaussian 10-60 Hz noise with $N(0,0.024^2)$

Initially, the seismic trace is encoded by amplitude-independent encoding and amplitude-dependent encoding of the optimal quantization encoding. Assign the i th pair of waveform points $[(x_i, y_i), (x_{i+1}, y_{i+1})]$ to the symbol ω_i connoting the slope characteristic of the line segment joining the two points. Setting $d_i = y_{i+1} - y_i$. There are two kinds of string encoding by using the optimal quantization encoding.

(1) Amplitude-independent encoding

The primitives are as follows.

$$\omega_i = p, \text{ if } d_i \geq 0.002$$

$$\omega_i = o, \text{ if } -0.002 < d_i < 0.002$$

$$\omega_i = n, \text{ if } d_i \leq -0.002$$

The constant 0.002 is a slope tolerance to provide a zero-like slope attribute. This kind of encoding pattern can not be used for the classification of 20Hz Ricker wavelets with different amplitudes, because the encoded strings are all the same. Using these primitives, only two kinds of Ricker wavelets can be classified, i.e., 20 and 17 Hz Ricker wavelets.

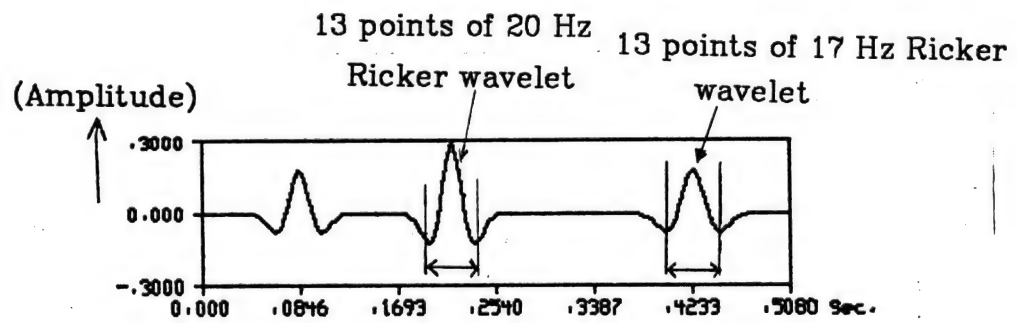


Figure 5.3 20 Hz and 17 Hz Ricker wavelets without noise

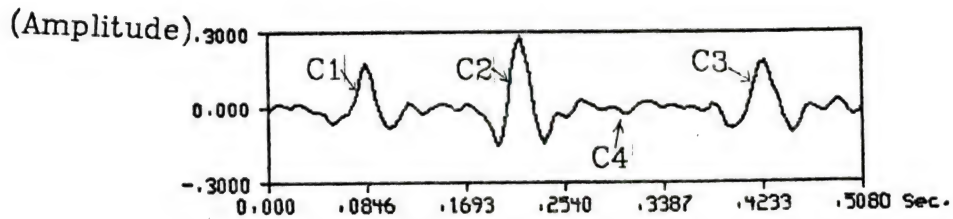


Figure 5.4 20 Hz and 17 Hz Ricker wavelets with Gaussian noise

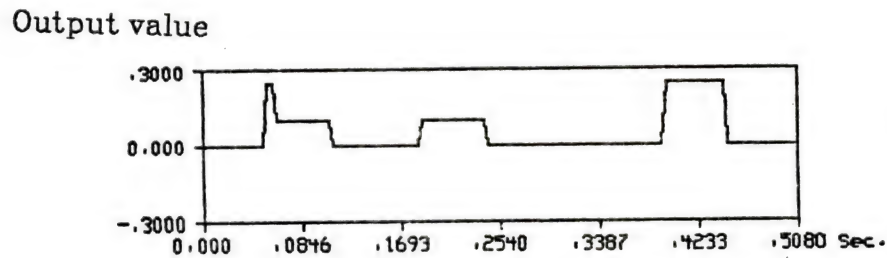


Figure 5.5 Classification result of two classes (for the amplitude-independent encoding and the minimum distance classification rule)

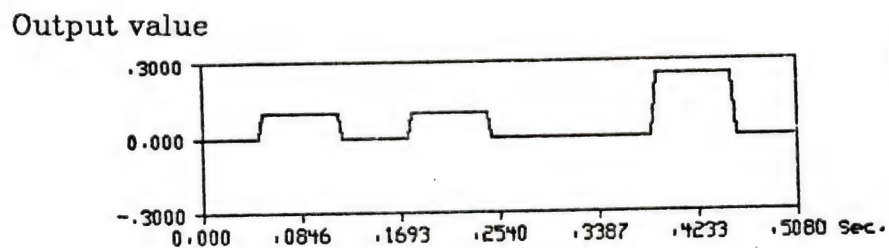


Figure 5.6 Classification result of two classes (for the amplitude-independent encoding and the NN decision rule)

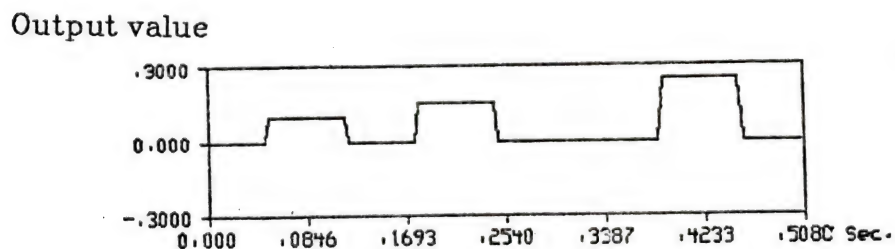


Figure 5.7 Classification result of three classes (for the amplitude-dependent encoding and the minimum distance classification rule)

(2) Amplitude-dependent encoding

For the amplitude-dependent encoding, the assignment of $d_i = y_{i+1} - y_i$ to a symbol is a quantization problem. From the analysis of the central part of 17Hz Ricker wavelet, the amplitudes of the 13 data points, $y_i, i=1,2, \dots, 13$ are

-0.0796, -0.0737, -0.0399, .0213, .0952, .1563, .1800, .1563,
.0952, .0213, -0.0399, -0.0737, -0.0796.

The 13 data points are indicated in Fig. 5.3. The distribution of the differences $d_i = y_{i+1} - y_i, i=1,2, \dots, 12$, is a Gaussian distribution which can be proved by a χ^2 - test [net82a]. From the analysis of the central part of 20Hz Ricker wavelet, the amplitudes of the same 13 data points, $y_i, i=1,2, \dots, 13$ are

-0.1317, -0.1100, -0.0230, .1137, .2428, .2960, .2428, .2960,
.2428, .1137, -0.0230, -0.1100, -0.1317.

The 13 data points are indicated in Fig. 5.3. The distribution of the differences $d_i = y_{i+1} - y_i, i=1,2, \dots, 12$, is a Gaussian distribution which can be proved by a χ^2 - test [net82a]. The number of selected data points is not fixed, since it depends on the shape of the represented wavelet.

The optimal quantization of 8 levels for the Gaussian samples is used [gag78a]. From the experiments in this chapter, if the standard deviation σ_s of the d_i of the signal is larger than $1.5\sigma_n$ of the d_i of the noise, then 8-level optimal quantization is good. For the number of quantization levels is larger than 8, for example 16, the interval of quantization is smaller and the representation of the signal without noise is more accurate than the representation of using 8-level quantization. For large noise, the quantization will be very sensitive. For the number of quantization levels is less than 8, for example 4 or 2, the

interval of quantization is large, different signal may be quantized as the same representation. It is enough to use 8-level quantization for high S/N in the later analysis. The primitives are as follows.

$\omega_i = d$ for $d_i > 1.76\sigma$	$c_8 = 2.15\sigma$
$\omega_i = c$ for $1.05\sigma < d_i \leq 1.76\sigma$	$c_7 = 1.34\sigma$
$\omega_i = b$ for $0.5\sigma < d_i \leq 1.05\sigma$	$c_6 = 0.75\sigma$
$\omega_i = a$ for $0.0\sigma < d_i \leq 0.5\sigma$	$c_5 = 0.24\sigma$
$\omega_i = A$ for $-0.5\sigma < d_i \leq 0.0\sigma$	$c_4 = -0.24\sigma$
$\omega_i = B$ for $-1.05\sigma < d_i \leq -0.5\sigma$	$c_3 = -0.75\sigma$
$\omega_i = C$ for $-1.76\sigma < d_i \leq -1.05\sigma$	$c_2 = -1.34\sigma$
$\omega_i = D$ for $d_i \leq -1.76\sigma$	$c_1 = -2.15\sigma$

where σ is the standard deviation of $d_i = y_{i+1} - y_i$ distribution for the wavelet and $c_i, i=1,2, \dots, 8$ are the conditional sample mean value of each interval. Using these primitives, three kinds of Ricker wavelet can be classified. $\sigma=0.051661$ of d_i distribution is selected from the smallest σ for 17 Hz Ricker wavelet and the 8-level optimal quantization is determined.

The amplitude-independent and amplitude-dependent encoded strings for the central part of Ricker wavelets without noise are listed in Table 5.1. These strings are used as the reference strings of the three kinds of Ricker wavelet and represented by $x^i, i=1,2,3$. x^1 represents the string of 20Hz Ricker wavelet with reflection coefficient -0.18. x^2 represents the string of 20Hz Ricker wavelet with reflection coefficient -0.2960. x^3 represents the string of 17Hz Ricker wavelet with reflection coefficient -0.18. Their lengths are equal in the computation of Levenshtein distance.

Table 5.1 String of Ricker wavelets

	Amplitude-Independent	Amplitude-Dependent
20 Hz Ricker wavelet with reflection coefficient - 0.18	np^5n^5p	$AabccbBCCBAa$
20 Hz Ricker wavelet with reflection coefficient - 0.2960	np^5n^5p	$AacddbBDDCAa$
17 Hz Ricker wavelet with reflection coefficient - 0.18	p^6n^6	$abcccaACCCBA$

5.2.2 Likelihood Ratio Test (LRT)

Suppose that an independent, identical Gaussian noise $n_i, i=1,2, \dots, N$ with zero mean and variance σ^2 is added to the 17 Hz Ricker wavelet, $y_i, i=1,2, \dots, N$, then, $d_i = y_{i+1} + n_{i+1} - (y_i + n_i) = y_{i+1} - y_i + n_{i+1} - n_i$. So d_i is a Gaussian noise with mean $y_{i+1} - y_i$, and variance $2\sigma^2$. If only a Gaussian noise is present, then $d_i = n_{i+1} - n_i$ is also Gaussian with $N(0, 2\sigma^2)$.

From Section 5.2.1, the distribution of the differences $d_i = y_{i+1} - y_i, i=1,2, \dots, N$, of 17 Hz Ricker wavelet is a Gaussian distribution with $N(0, \sigma_s^2)$.

Suppose that the signal and the noise are independent Gaussian. In the detection problem, there are two hypotheses. One is the signal plus noise, $N(0, \sigma_s^2 + \sigma_n^2)$, the other is the noise only, $N(0, \sigma_n^2)$. Then the likelihood ratio test [van68a] is shown in the following.

$$H_0: \text{Gaussian noise } P(r) = \frac{1}{\sqrt{2\pi}\sigma_n} \exp\left[-\frac{r^2}{2\sigma_n^2}\right]$$

$$H_1: \text{Signal + noise } P(r) = \frac{1}{\sqrt{2\pi}\sigma_1} \exp\left[-\frac{r^2}{2\sigma_1^2}\right], \text{ where } \sigma_1^2 = \sigma_n^2 + \sigma_s^2$$

The Likelihood Ratio Test is that

$$\Lambda(r) = \frac{p(r/H_1)}{p(r/H_0)} = \frac{\sigma_n}{\sigma_1} \exp\left[-\frac{r^2}{2}\left(\frac{1}{\sigma_1^2} - \frac{1}{\sigma_n^2}\right)\right]$$

If $\Lambda(r) > \eta$, then H_1 is true.

If $\Lambda(r) < \eta$, then H_0 is true.

Taking ln on both sides and rearranging the terms, we obtain the following result.

$$\text{Let } \frac{\ln \eta - \ln\left(\frac{\sigma_n}{\sigma_1}\right)}{\frac{1}{2}\left(\frac{1}{\sigma_n^2} - \frac{1}{\sigma_1^2}\right)} = \beta^2$$

If $r^2 > \beta^2$, then H_1 is true.

If $r^2 < \beta^2$, then H_0 is true.

i.e.,

If $|r| > \beta$, then H_1 is true.

If $|r| < \beta$, then H_0 is true.

Suppose that H_0 and H_1 are equal probable, then $\eta=1$ is used in the experiments of this chapter.

For the 17 Hz Ricker wavelet, $\sigma_s=0.051661$, $\sigma_n=0.033941$ and $\sigma_1=0.061813$. Substituting σ_n and σ_1 into LRT formula above, then a signal is present, if $r \geq 0.0444542$, or $r \leq -0.0444542$.

In the following, global and local detections are for the amplitude-dependent encoding.

5.2.3 Global Detection

For an input seismic string, the wavelets must be detected and extracted. So a global detection is proposed to detect the possible wavelets. Combining the likelihood ratio test (LRT) and the 8-level optimal quantization of 17 Hz Ricker wavelet, a signal is detected if $r \geq 0.054244 = 1.05\sigma_s$, or $r \leq -0.054244 = -1.05\sigma_s$, i.e. the region of the symbols 'c', 'd', 'C', and 'D' in Fig. 5.8A. The probability of detecting signal is 0.2938. For every input string of 12 symbols, $12 \times 0.2938 = 3.5256$. Truncated $3.5256 = 3$. The approximated number of detected symbol is 3. So a threshold is set, if the number of symbols,

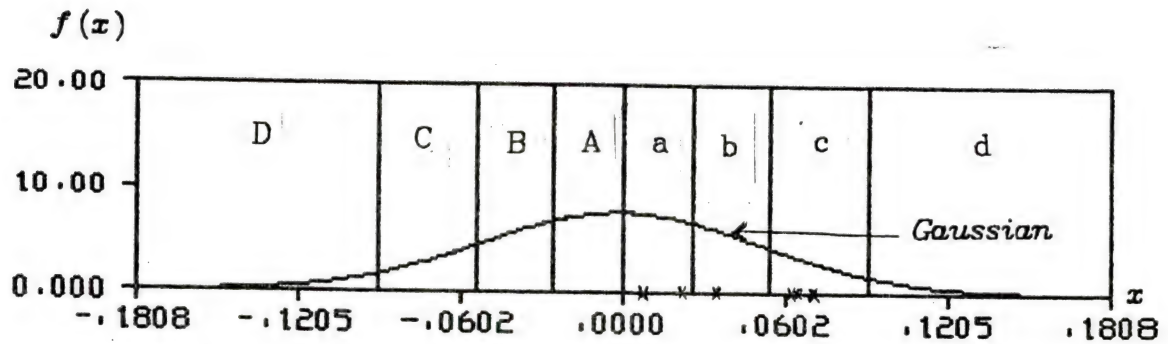


Figure 5.8A 8-level optimal quantization encoding for d_i of

17 Hz Ricker wavelet

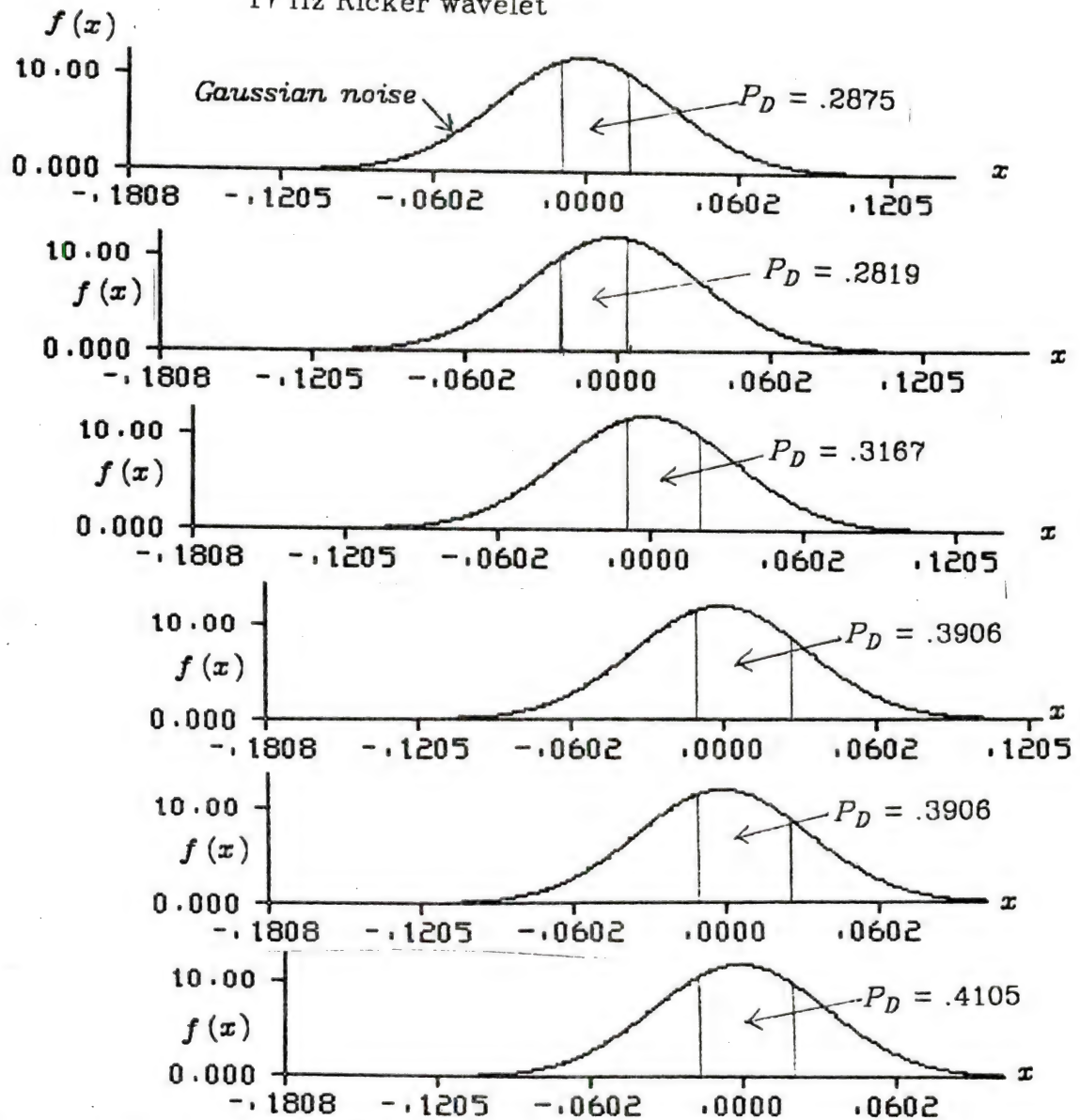


Figure 5.8B Probability of detection for d_i of 17 Hz Ricker wavelet with amplitude-dependent encoding

'c', 'd', 'C', or 'D', is equal to or larger than 3, then a possible wavelet is detected. Otherwise, input the next string. The purpose of this global detection is to extract the possible wavelet and to reduce the string distance computation time.

5.2.4 Levenshtein Distance

Levenshtein distance between two strings [lev66a] is defined as the minimum number of symbol insertions, deletions, and substitutions required to transform one string into the other string. The Levenshtein distance between x and y denoted as $d^L(x, y)$ is

$$d^L(x, y) = \min_j [k_j + m_j + n_j]$$

where k_j, m_j , and n_j are the number of substitution, deletion, and insertion transformations respectively. This distance can be computed using a string-to-string correction algorithm [wag74a].

5.2.5 Local Detection

The local detection for amplitude-dependent and amplitude-independent encoding is discussed in the following.

(I) Amplitude-dependent encoding

Levenshtein distance between the possible wavelet string and the reference strings of Ricker wavelets is computed, a threshold is set to detect whether or not the possible wavelet is a candidate wavelet. The threshold is calculated from the probability of detecting every encoded symbol. From the analysis of 17Hz Ricker wavelet (the smallest

variance), $d_i = y_{i+1} - y_i$ falls into one quantization interval of 8 intervals and corrupted by Gaussian noise $N(0, 2\sigma_n^2)$. So the probability of detection in this quantization interval can be calculated from Figure 5.8. For 12 d_i of 17 Hz Ricker wavelet, the probability of detecting every d_i can be calculated by using the statistical table of normal distribution. The sum of these 12 detection probabilities is 4.1556.

$$(2 * (.2875 + .2819 + .3167 + .3906 + .3906 + .4105)) = 4.1556$$

Truncated 4.1556 = 4.

The approximated number of detection symbols is 4. The number of missing and false symbols is $12 - 4 = 8$, i.e., error or un-detected symbols. From the definition of Levenshtein distance, if Levenshtein distance between an input string of 17 Hz Ricker wavelet corrupted by Gaussian noise and a reference string of 17 Hz Ricker wavelet without noise is computed, then the input string belongs to the reference string if Levenshtein distance is less than 8 symbols. So 8 is selected as a threshold. The threshold is set 7 in the experiment. The same calculations are for the 20 Hz Ricker wavelets. For an input string y , if the distance $d^L(x^1, y) \leq 7$, or $d^L(x^2, y) \leq 7$, or $d^L(x^3, y) \leq 7$, then the minimum distance and the nearest-neighbor classification rules are used. Otherwise, input the next interval string and repeat the process. The purpose in setting this threshold is to extract true wavelets for the classification. The number of the detected symbols is dependent on the location of $d_i = y_{i+1} - y_i$ and the variance of Gaussian noise.

(II) Amplitude-independent encoding

For the amplitude-independent encoding experiment, Levenshtein distance between every input string and the reference strings of Ricker wavelets is computed. From Section 5.2.1, three intervals are for

symbols 'n', 'o', and 'p'. The difference d_i of 17 Hz Ricker wavelet falls into 'p' or 'n'. Then, this d_i is corrupted by the Gaussian noise $N(0, 2\sigma_n^2)$, $d_i = (y_{i+1} - y_i) + (n_{i+1} - n_i)$, where n_i , $i=1, 2, \dots, N$ are Gaussian independent with $N(0, \sigma_n^2)$. Then the probability of detecting this d_i can be calculated. For the 12 d_i of the 17 Hz Ricker wavelet, the probability of detecting every d_i can be calculated by using the statistical table of normal distribution. (Fig 5.9). The sum of these 12 detection probabilities is 10.0692.

$$(2 * (.545 + .789 + .8264 + .9706 + .9706 + .9830)) = 10.0692$$

Truncated 10.0692 = 10.

The approximated number of detection symbols is 10. The number of missing and false symbols is $12 - 10 = 2$, i.e., error or un-detected symbols. The input string belongs to the reference string if Levenshtein distance is less than 2 symbols. So 2 is selected as a threshold. The same calculations are for the 20Hz Ricker wavelets. The threshold is set to 2 to extract the Ricker wavelets in this experiment. The central parts of the 20Hz Ricker wavelets with reflection coefficient -0.18 and -0.2960 respectively are encoded as the same string. $x^1 = x^2$. If the distance $d^L(x^1, y) \leq 2$, or $d^L(x^3, y) \leq 2$, then the candidate wavelet is extracted and the minimum distance classification rule is used. Otherwise, input the next 12-symbol string.

5.2.6 Classification Rules and Results

The classification methods presented here are the minimum-distance and the nearest-neighbor(NN) classification rules. The advantage of these rules is the fast computation.

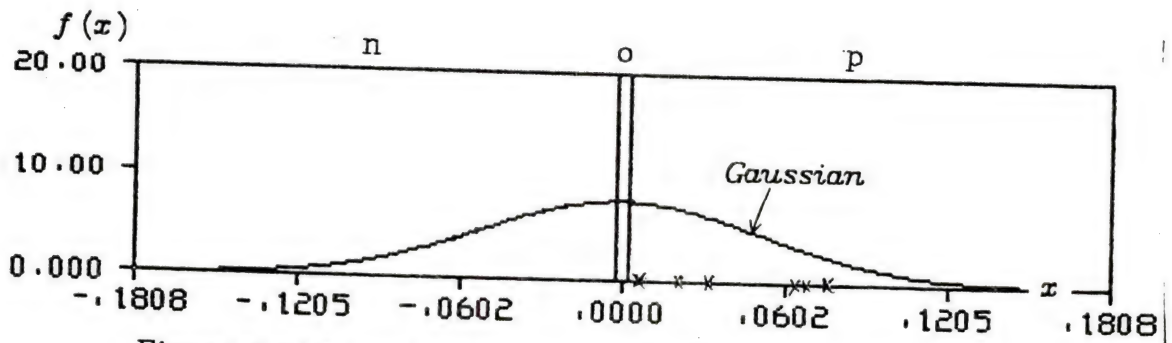


Figure 5.9A 3 levels for d_i of 17Hz Ricker wavelet

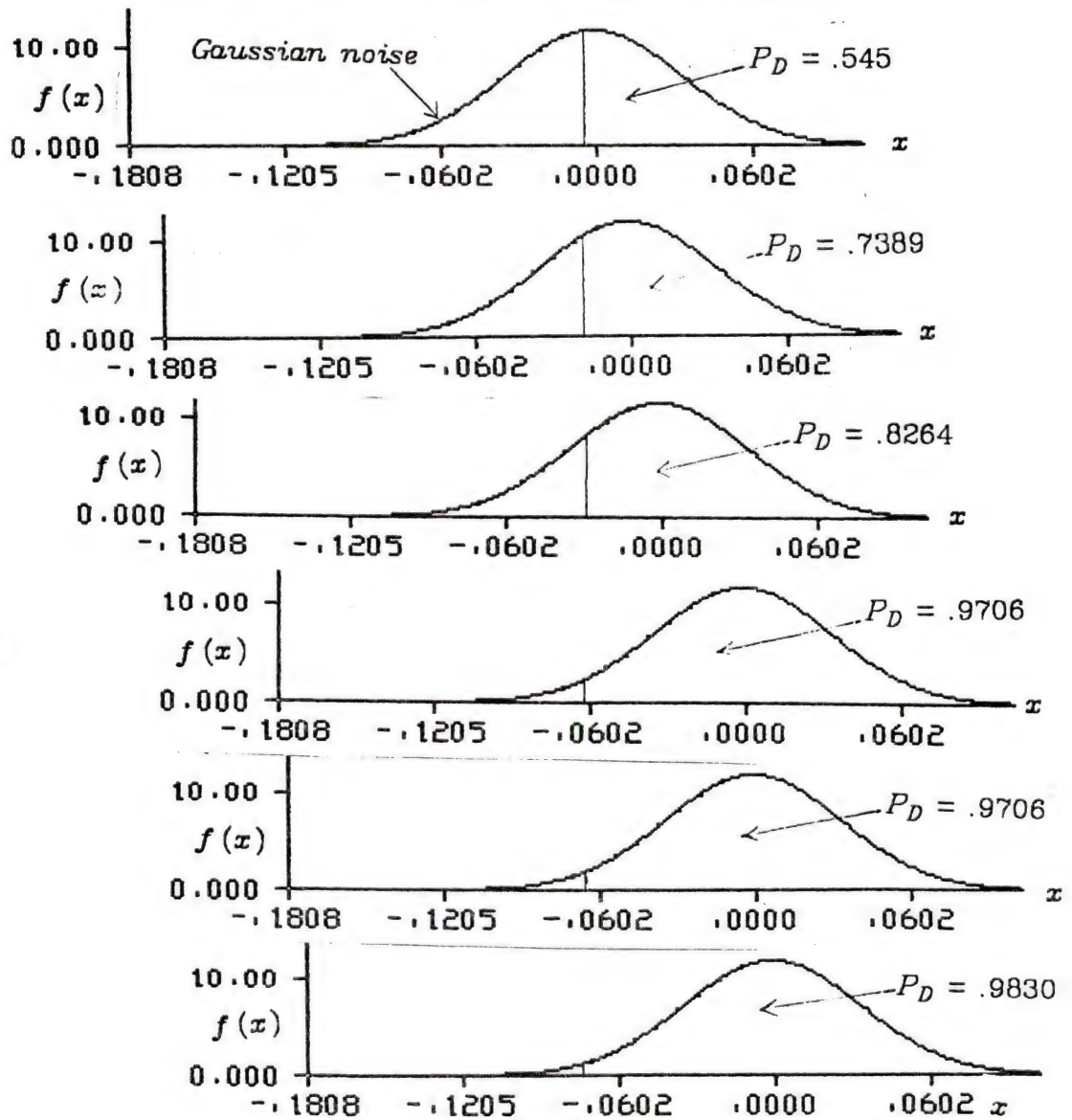


Figure 5.9B Probability of detection for d_i of 17Hz Ricker wavelet with amplitude-independent encoding

The definition of the minimum distance and the NN classification rules are as follows.

a) Minimum-distance classification rule

There are 3 reference strings of Ricker wavelets, x^1, x^2 , and x^3 . y belongs to ω_j , if $d^L(x^j, y) = \min_i [d^L(x^i, y)]$

b) NN classification rule

There are two classes of Ricker wavelet, i.e., 20 and 17 Hz only, ω_1 and ω_2 . X^1 and X^2 are the reference string sets for 20 and 17 Hz Ricker wavelets,

where $X^1 = [x_1^1, x_2^1]$, $X^2 = [x_1^2]$. $d^L(X^i, y) = \min_k [d^L(x_k^i, y)]$.

y belongs to ω_j , if $d^L(x^j, y) = \min_i [d^L(X^i, y)]$

The two- and three- class classification problems are stated in the following.

(I) Two-class classification: If the amplitude-independent encoding is used in the primitive recognition, then the central parts of the 20Hz Ricker wavelets with reflection coefficient -0.18 and -0.2960 respectively are encoded as the same string. $x^1 = x^2$. So there are two classes in the seismic trace, i.e., 20 and 17 Hz Ricker wavelets and the minimum-distance classification rule is used. The classification result is shown in Fig. 5.5. Two classes are in Fig. 5.5, one is the 20Hz Ricker wavelet, the other is the 17Hz Ricker wavelet. If the amplitude-dependent encoding is used in the primitive recognition, x^1 and x^2 are considered as one class set. There are two classes and the NN-classification rule is applied. The classification result is shown in Fig. 5.6. Two classes are in Fig. 5.6, one is the 20Hz Ricker wavelet, the other is the 17Hz Ricker wavelet. Compared with the original seismic

trace in Fig. 5.4, the result of using the amplitude-dependent encoding is better than that of using the amplitude-independent encoding. Because in Fig. 5.5, the result at the 20Hz Ricker wavelet with reflection coefficient -0.18 has two class results.

(II) Three-class classification: The amplitude-dependent optimal quantization encoding is used and the minimum-distance classification rule is applied. Compared with the original seismic trace in Fig. 5.4, the classification result shown in Fig. 5.7 is quite good. The classification result in Fig. 5.7 is the 17Hz Ricker wavelet and the 20Hz Ricker wavelets with amplitude -0.18 and -0.2960 respectively.

5.3 Syntactic Pattern Recognition for the Detection of Candidate Bright Spot in a Simulated Seismogram

In Fig. 5.10A, there are three classes in the simulated seismogram.

C1: $r(t)=n(t)+20$ Hz Ricker wavelet with reflection coefficient -0.29598 at top of gas sand zone with polarity reversal.

C2: $r(t)=n(t)+30$ Hz Ricker wavelet from other boundaries.

C3: $r(t)=n(t)$ Gaussian 10-60 Hz white noise

This is the second hypothesis of the three hypotheses described in Chapter 3. The candidate bright spot is the one with high amplitude and low frequency content. In processing this simulated seismogram, the data are not known as candidate bright spot or non-candidate bright spot. Testing traces are randomly selected from the input seismogram. Tree classification techniques [hua83a] are used in the detection of candidate bright spot. Envelope, instantaneous frequency, and polarity are used as the features. Three hypotheses (Chapter 3) are the constrained conditions for the detection of candidate bright

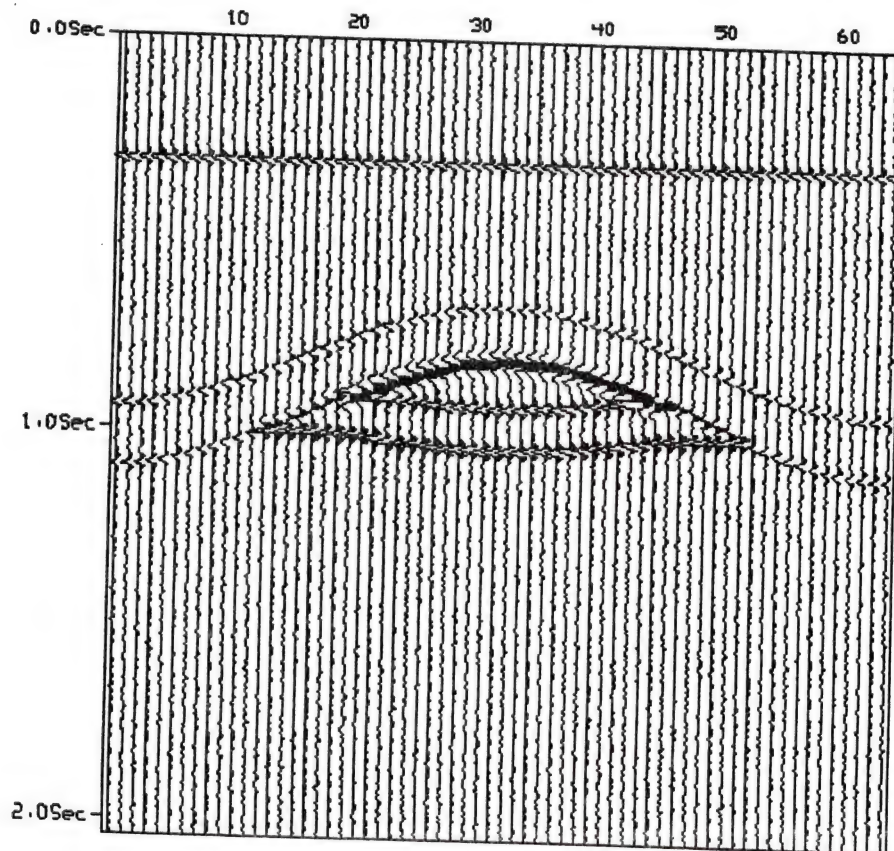


Figure 5.10A Synthetic seismogram of bright spots

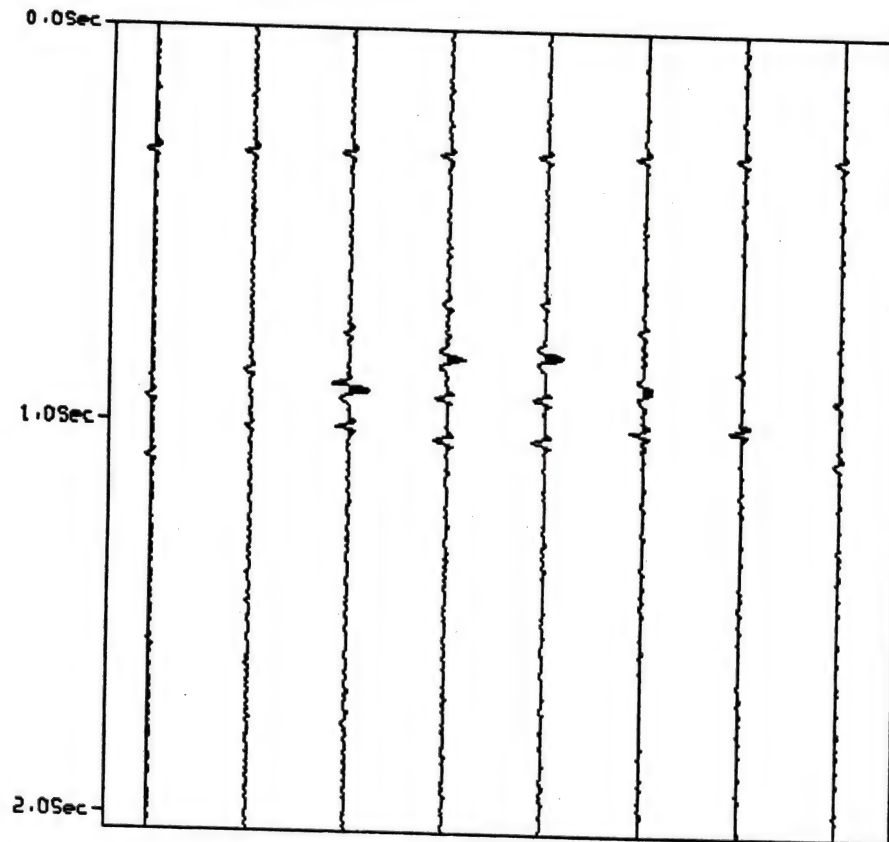


Figure 5.10B Testing traces

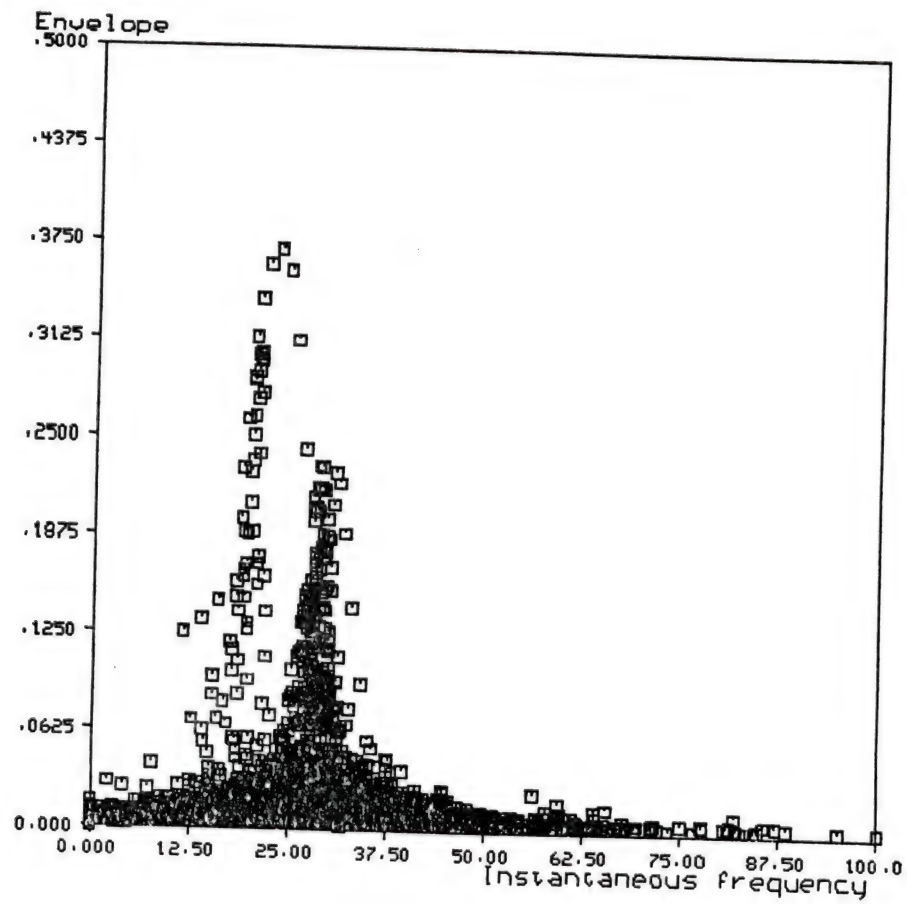


Figure 5.10C Feature distribution of testing traces

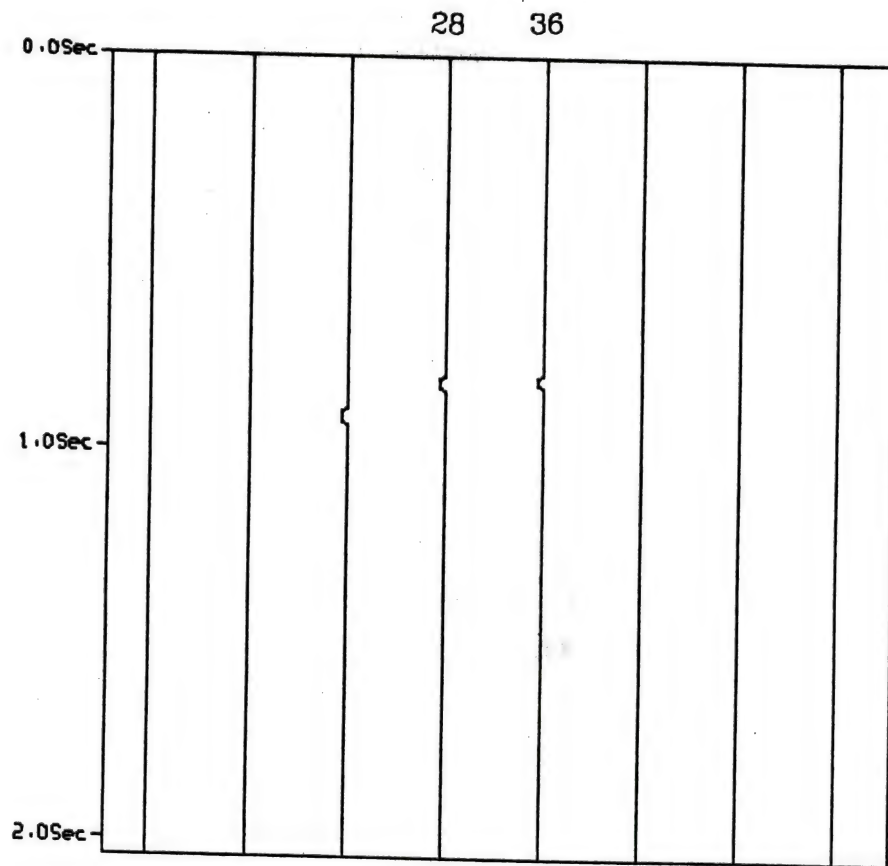


Figure 5.10D Tree classification result of bright spots

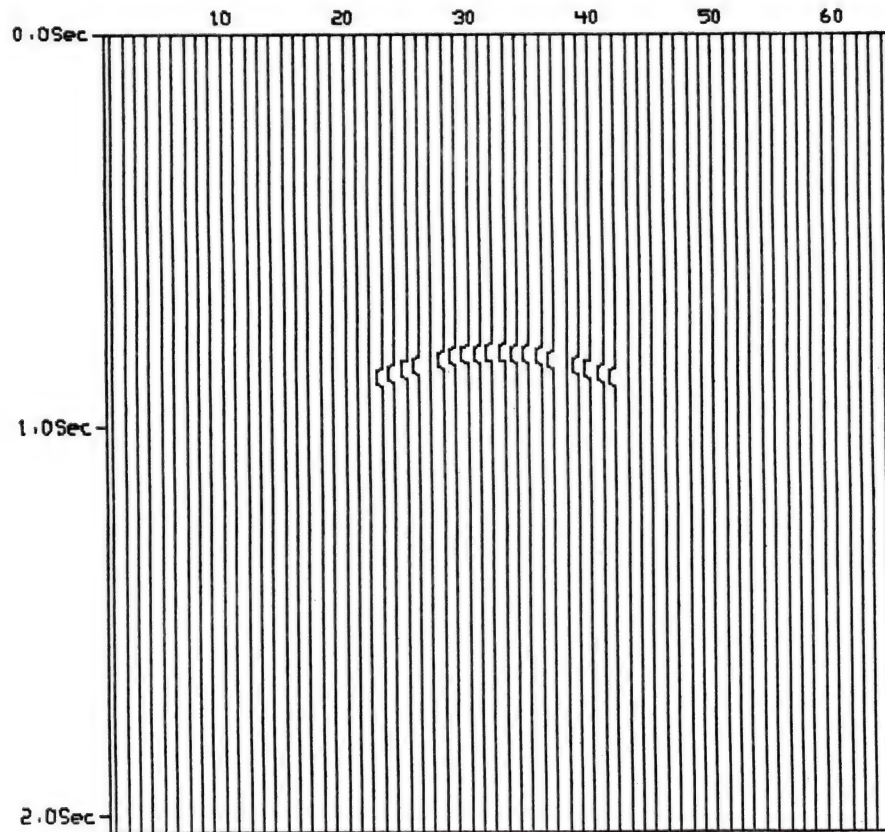


Figure 5.10E Classification result of bright spot (Threshold = 1)

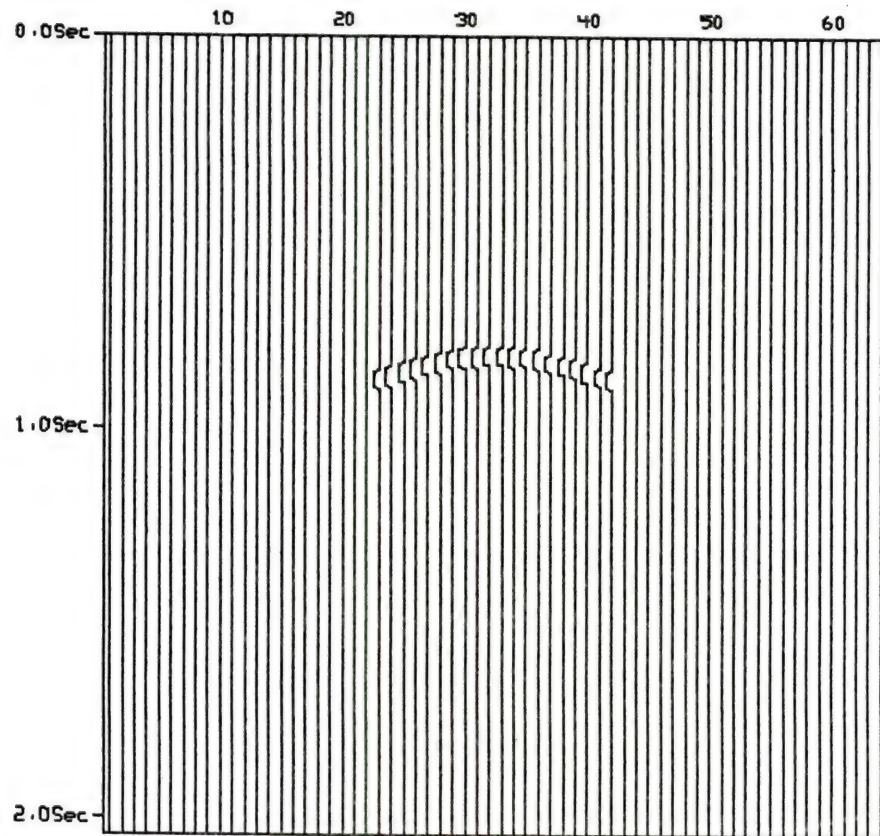


Figure 5.10F Classification result of bright spot (Threshold = 2)

spot. From the detected candidate bright spot on the 28th and 36th traces, two sample patterns of the Ricker wavelet with noise are extracted. The distribution of d_i on the extracted samples (signal plus noise) is a Gaussian $N(0, \sigma_1^2)$, $\sigma_1 = 0.100853$. The distribution of d_i for noise only on the 32th trace is a Gaussian $N(0, \sigma_n^2)$, $\sigma_n = 0.012$. Suppose that both signal and noise are independent Gaussian, then $\sigma_1^2 = \sigma_n^2 + \sigma_s^2$. $\sigma_s = 0.0998646$. The 8-level optimal quantization encoding is determined by using σ_s . So two extracted pattern samples can be encoded as strings of candidate bright spot patterns and have 10 symbols respectively here (Table 5.2). The input seismogram is encoded also.

(1) Likelihood Ratio Test (LRT)

From the likelihood ratio test, the threshold for signal and noise is determined. A signal of 20Hz Ricker wavelet is present if $r \geq 0.0249224$ or $r \leq -0.0249224$.

(2) Threshold for global detection

Comparing the 8-level optimal quantization with likelihood ratio test, the closest levels to $\beta = \pm 0.0208826$ are the end points at $\pm 0.0249277 = \pm 0.5\sigma_s$. (Fig. 5.11). Then, $\pm 0.0249277 = \pm 0.5\sigma_s$ are selected as the new threshold. The areas above 0.0249277 and below -0.0249277 are the detected areas of signal, i.e., the intervals of 'b', 'c', 'd', 'B', 'C', and 'D'. The probability of detecting 'b', 'c', 'd', 'B', 'C', and 'D' is 0.617. $10 \times 0.617 = 6.17$. Truncated 6.17 = 6. The approximated number of detected symbols at 'b', 'c', 'd', 'B', 'C', and 'D', is 6 symbols. So a threshold is set, if the number of symbol, 'b', 'c', 'd', 'B', 'C', or 'D', is equal to or larger than 6, then a possible wavelet is detected. Otherwise, input the next 10 symbol string.

Table 5.2 The Encoded String of the Extracted Patterns

	String Representation
[1] For Simulated Seismogram	
(1) Pattern from the 28th trace	<i>abccbBCCBA</i>
(2) Pattern from the 36th trace	<i>abccbACCBA</i>
[2] For Mississippi Canyon	
(1) Pattern from the 13th trace	<i>BDCbcddB</i>
(2) Pattern from the 21st trace	<i>ABBAAbdc</i>
(3) Pattern from the 29th trace	<i>BDCaddbc</i>
(4) Pattern from the 37th trace	<i>ACCAcddc</i>
[3] For High Island	
(1) Pattern from the 45th trace	<i>BBAbccaBBA</i>
(2) Pattern from the 50th trace	<i>BBBacdbBCB</i>
(3) Pattern from the 51st trace	<i>BBAbdcaCCB</i>
(4) Pattern from the 53rd trace	<i>BBAbdcaBBA</i>

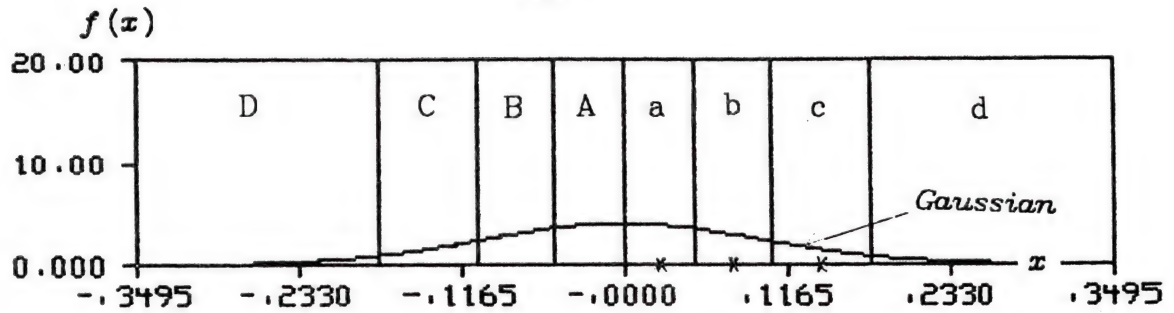


Figure 5.11A 8-level optimal quantization encoding for d_i of bright spot pattern in simulated seismogram

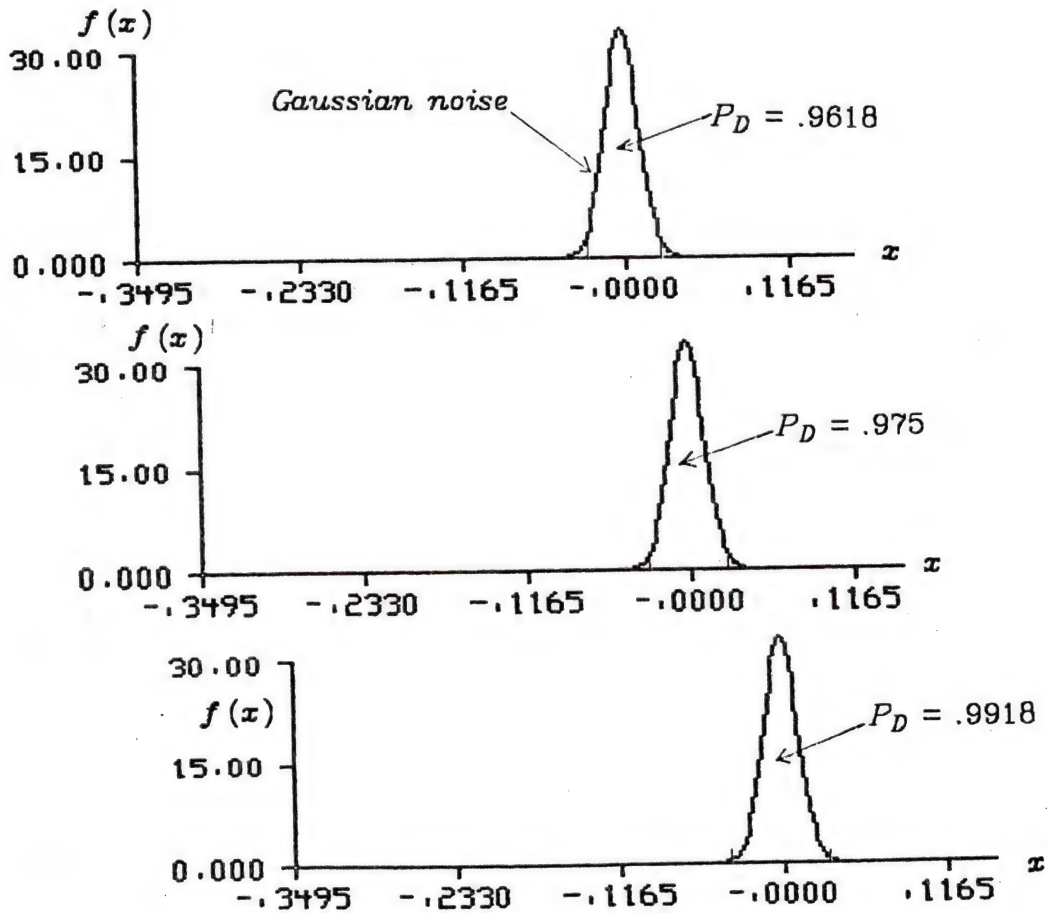


Figure 5.11B Probability of detection using the conditional mean of each interval in bright spot pattern

(3) Threshold for the detection of candidate bright spot

For the detection of candidate bright spot in simulated seismogram and real data experiment, there are no non-candidate bright spot strings. After the Levenshtein distance between a possible wavelet string and the extracted string of candidate bright spot patterns is computed, a threshold k is set to detect whether or not the possible wavelet is a candidate bright spot wavelet. The process is similar to the local detection in the classification of Ricker wavelets described above. Suppose that x is a candidate bright spot string, if $d^L(x, y) \leq k$, then y is the detected candidate bright spot string.

The exact amplitude of the signal is not known because the signal is corrupted by noise. The probability of detection can not be calculated as that for the 17 Hz Ricker wavelet described in Section 5.2.5. An alternative method is proposed. Using the 8-level optimal quantization, the d_i value is quantized to the quantized value c_i , the conditional mean of each quantization interval. Assume that Gaussian noise is added to the quantized value c_i , then the probability of detection in the quantized interval can be calculated. For 20 c_i of the quantized value of the candidate bright spot, the probability of detecting every c_i can be calculated by using the statistical table of normal distribution. The sum of these 20 detection probabilities is 19.5684.

(There are 5 'a' or 'A', 7 'b' or 'B', and 8 'c' or 'C'.
 $5 \cdot .9618 + 7 \cdot .975 + 8 \cdot .9918 = 19.5684$)

For string of 10 symbols, $19.5684/2 = 9.7842$. Truncated $9.7842 = 9$.

The approximated number of detected symbols is 9. The number of missing and false symbols is $10 - 9 = 1$, i.e., error or un-detected symbols. The input string represents a candidate bright spot if the Levenshtein distance is less than 1 symbol. So 1 is selected as a threshold. The

threshold is set 1 or 2 to detect the candidate bright spot in the experiment. A typical classification result of using threshold 1 is shown in Fig. 5.10E and a typical classification result of using threshold 2 is shown in Fig. 5.10F.

5.4 Syntactic Pattern Recognition for the Detection of Candidate Bright Spot in the Real Data Experiment

Two relative amplitude real-data seismograms are processed.

(I) Experiment at Mississippi Canyon

In Fig. 5.12A, at 0.2 and 1.4 seconds, the dominant wavelets are the minimum-phase wavelets. Testing traces are randomly selected and tree classification techniques are used [hua83a]. The selected samples of detected candidate bright spot are on the 13th, 21st, 29th, and 37th traces (Fig. 5.12B). The smallest variance of d_i distribution on the 21th trace is used in the analysis of signal and noise. The distribution of d_i at the extracted samples (signal plus noise) of the 21st trace is Gaussian with $N(0, \sigma_1^2)$ and $\sigma_1 = 0.055478$. The distribution of d_i for noise only on the 1st trace is Gaussian with $N(0, \sigma_n^2)$ and $\sigma_n = 0.014043$. Suppose that both signal and noise are independent Gaussian, then $\sigma_1^2 = \sigma_n^2 + \sigma_s^2$ and $\sigma_s = 0.053673$. The 8-level optimal quantization encoding is determined by using σ_s . So four extracted pattern samples can be encoded as strings of candidate bright spot patterns and each string has 8 symbols (Table 5.2). The pattern string of the candidate bright spot in the 21th trace is *ABBAAbdc*. The input seismogram is encoded also.

(1) Likelihood Ratio Test (LRT)

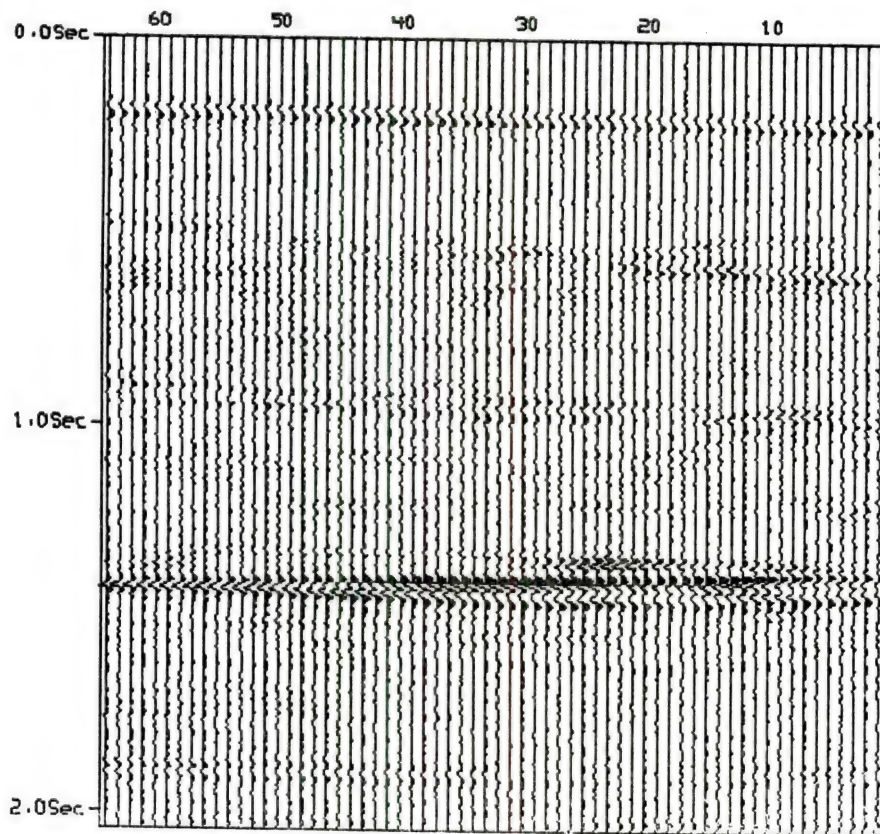


Figure 5.12A Real seismogram at Mississippi Canyon (Negative on the right)

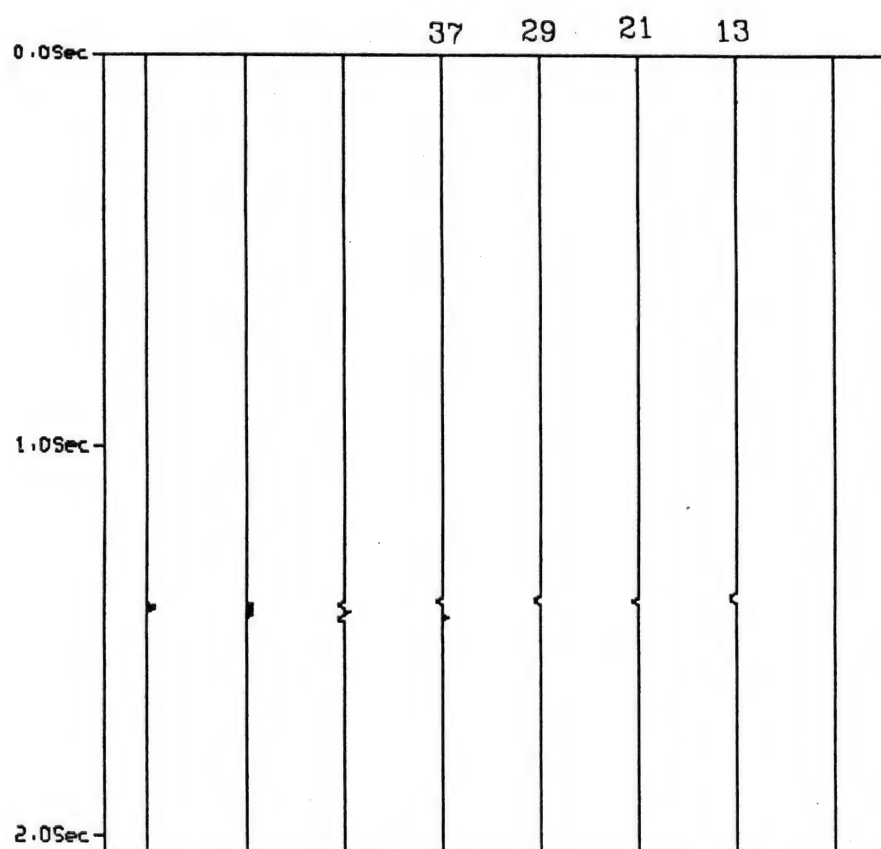


Figure 5.12B Tree classification result of bright spots

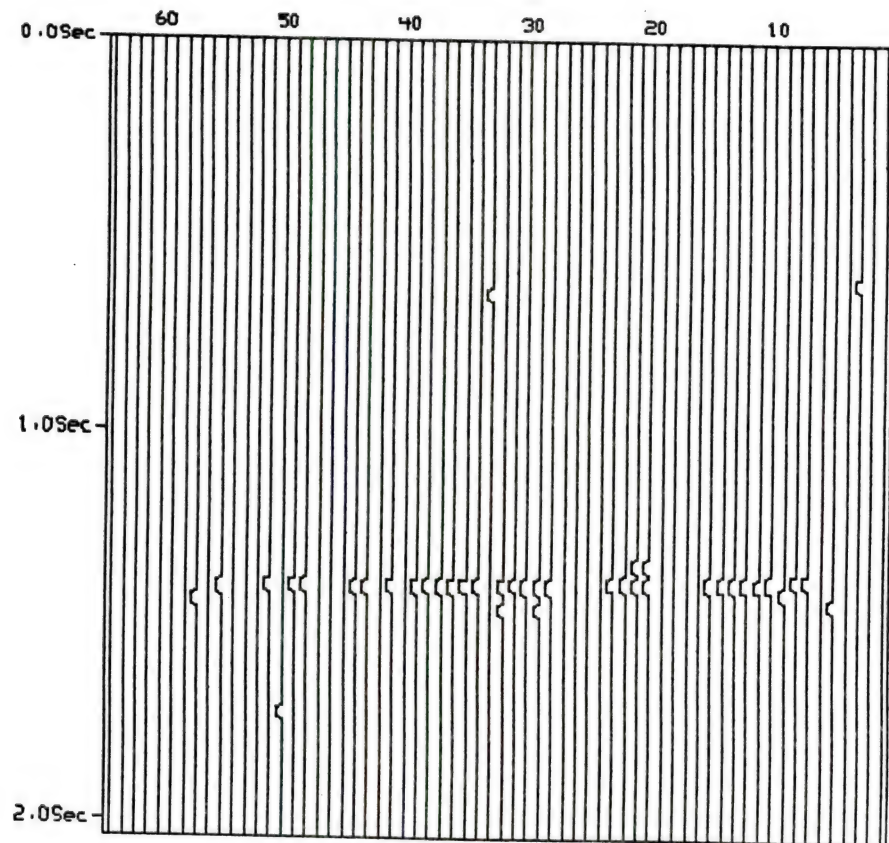


Figure 5.12C Classification result of bright spots

From the likelihood ratio test, the threshold for signal and noise is determined. Signal is present, if $r \geq 0.0240482$, or $r \leq -0.0240482$.

(2) Threshold for global detection

Comparing the 8-level optimal quantization with LRT, the closest levels to $\beta = \pm 0.0240482$ are the end points at $\pm 0.0268365 = \pm 0.5\sigma_s$. (Fig. 5.13). Then, $\pm 0.0268365 = \pm 0.5\sigma_s$ are selected as the new threshold. The areas above 0.0268365 and below -0.0268365 are the detected areas of the signal, i.e., the intervals of 'b', 'c', 'd', 'B', 'C', and 'D'. The probability of detecting 'b', 'c', 'd', 'B', 'C', and 'D' is 0.617. $8 \times 0.617 = 4.936$. Truncated $4.936 = 4$. The approximated number of detected symbols at 'b', 'c', 'd', 'B', 'C', and 'D', is 4 symbols. Here a threshold is set, if the number of symbol, 'b', 'c', 'd', 'B', 'C', or 'D', is equal to or larger than 5, then the possible wavelet is detected. Otherwise, input the next 8 symbol string.

(3) Threshold for the detection of candidate bright spot

The exact amplitude of the signal is not known because the signal is corrupted by noise. The probability of detection can not be calculated as that for the 17 Hz Ricker wavelet described in Section 5.2.5. An alternative method is proposed. Using the 8-level optimal quantization, the d_i value is quantized to the quantized value c_i , the conditional mean of each quantization interval. Assume that Gaussian noise is added to the quantized value c_i , then the probability of detection in the quantized interval can be calculated. For 8 c_i of the quantized value of the candidate bright spot, the probability of detecting every c_i can be calculated by using the statistical table of normal distribution. The sum of these 8 detection probabilities is 5.7354.

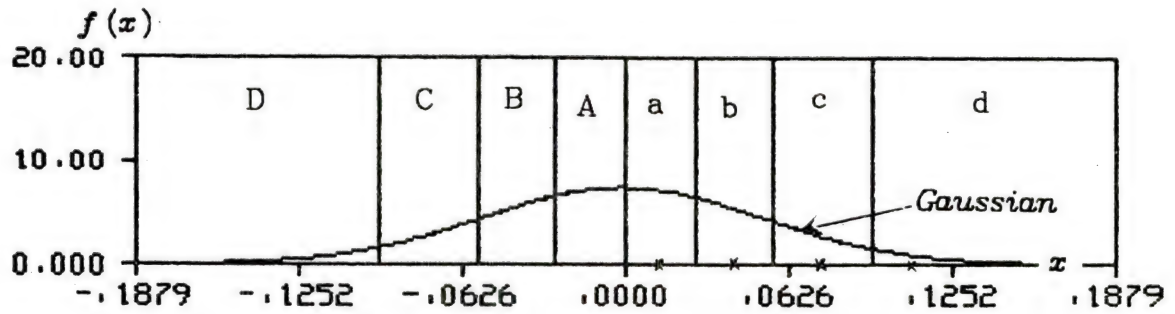


Figure 5.13A 8-level optimal quantization encoding for d_i of
bright spot pattern in Mississippi Canyon

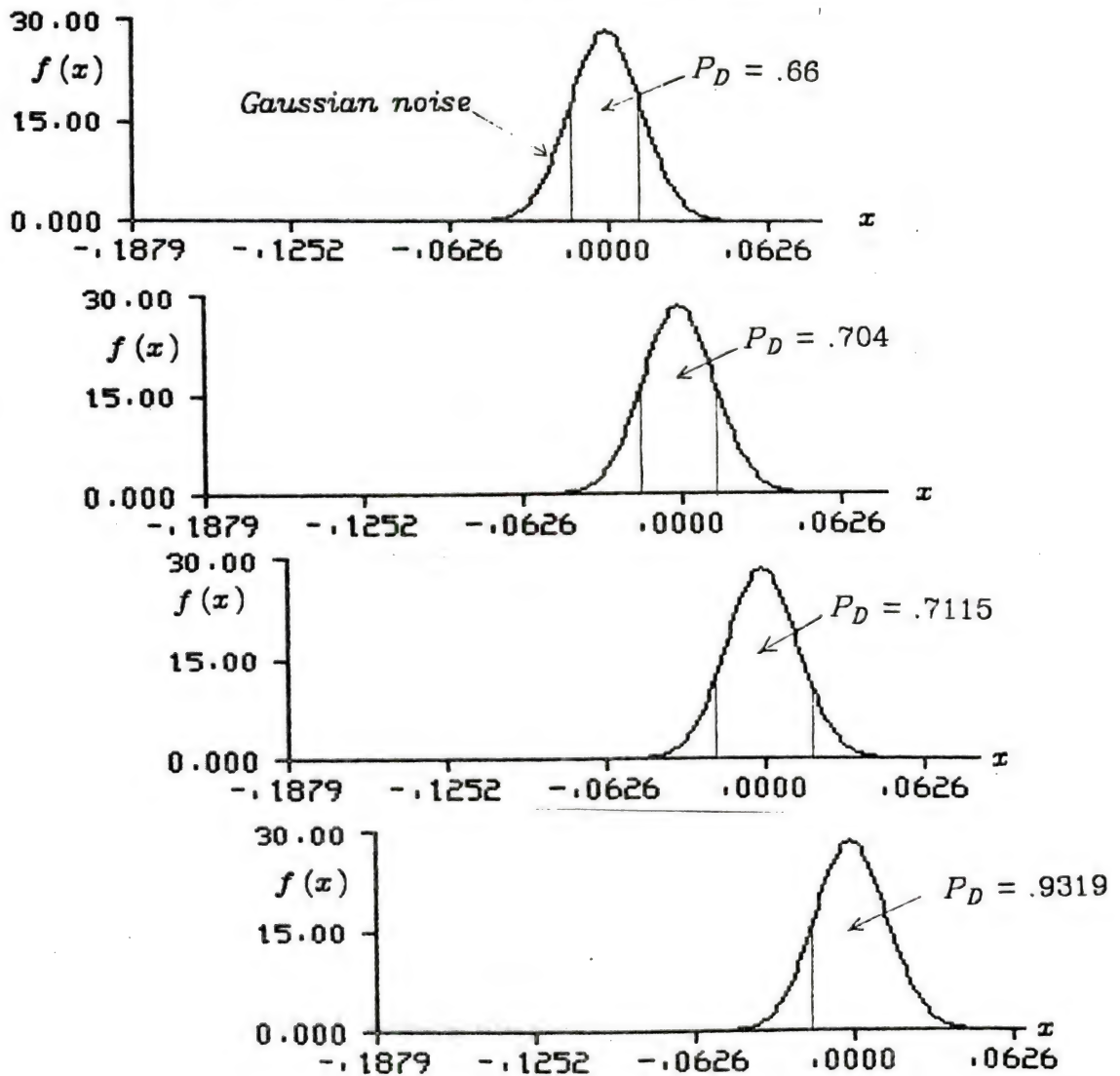


Figure 5.13B Probability of detection using the conditional mean
of each interval in bright spot pattern

There are 3 'A', 3 'b' or 'B', 1 'c', and 1 'd'.

$3*0.66+3*.704+1*.7115+1*.9319=5.7354$. Truncated 5.7354 = 5.

The approximated number of detected symbols is 5. The number of missing and false symbols is $8-5=3$, i.e., error or un-detected symbols. The input string belongs to the string of candidate bright spot if Levenshtein distance is less than 3 symbols. So 3 is selected as a threshold. Suppose that x^1, x^2, x^3 , and x^4 are candidate bright spot strings, if $d^L(x^1, y) \leq k_1$, or $d^L(x^2, y) \leq k_2$, or $d^L(x^3, y) \leq k_3$, or $d^L(x^4, y) \leq k_4$, then y is the detected candidate bright spot string. The threshold values of k_1, k_2, k_3 , and k_4 are 3 in this experiment. The typical classification result is shown in Fig. 5.12C. Compared with the original seismogram in Fig. 5.12A, Fig. 5.12C is good.

(II) Experiment at High Island

In Fig. 5.14A, at 1.7 seconds, the dominant wavelets are the zero-phase wavelets. Testing traces are randomly selected and tree classification techniques are used. The detected candidate bright spot of testing traces, the 45th and 53rd, are at both ends of the major reflection layer. So the 50th and 51st traces in the middle of the major reflection layer are also selected as the testing traces (Fig. 5.14B). The standard deviations of d_i from 4 extracted patterns are very close. The distribution of d_i in the extracted samples (signal plus noise) is Gaussian with $N(0, \sigma_1^2)$ and $\sigma_1=0.05125$. The distribution of d_i for noise only on the 1st trace is Gaussian with $N(0, \sigma_n^2)$ and $\sigma_n=0.011862$. Suppose that both signal and noise are independent Gaussian, then $\sigma_1^2 = \sigma_n^2 + \sigma_s^2$ and $\sigma_s=0.0498554$. The 8-level optimal quantization encoding is determined by using σ_s . So four extracted pattern samples can be encoded as strings of candidate bright spot patterns and each string has 10

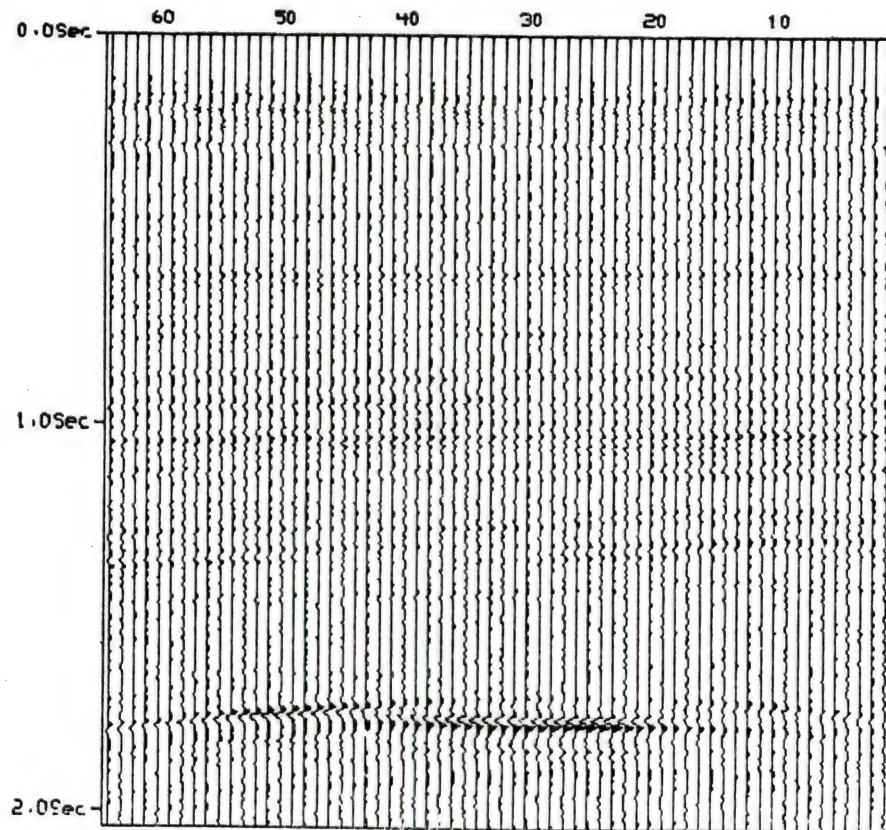


Figure 5.14A Real seismogram at High Island (Negative on the right)

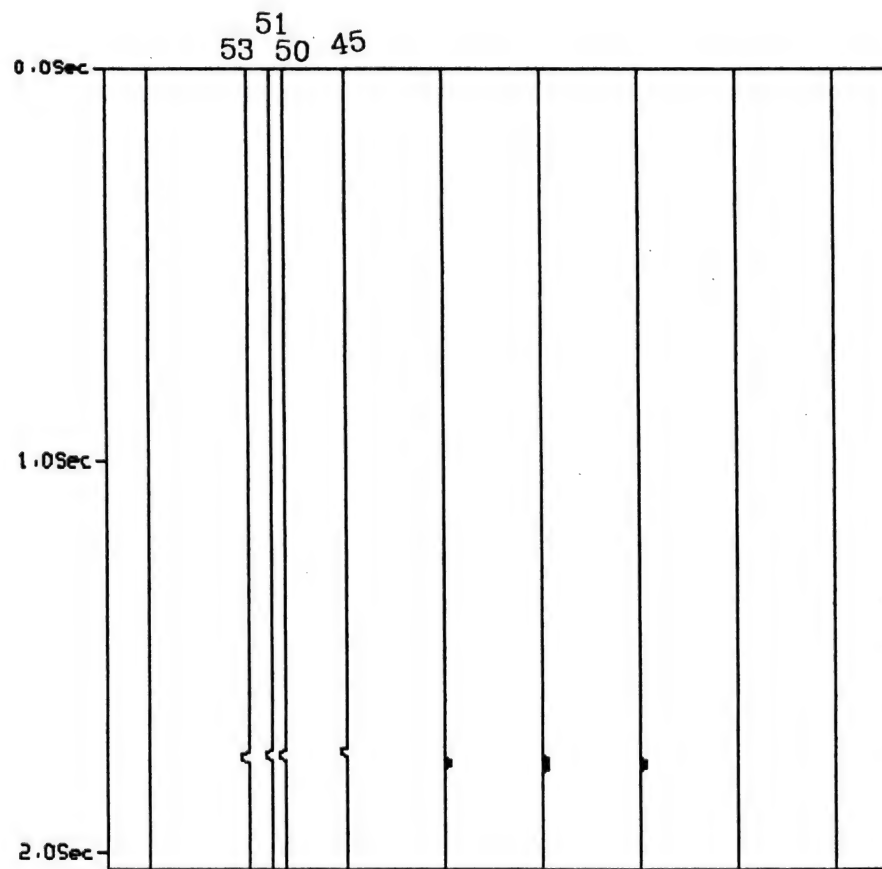


Figure 5.14B Tree classification result of bright spots

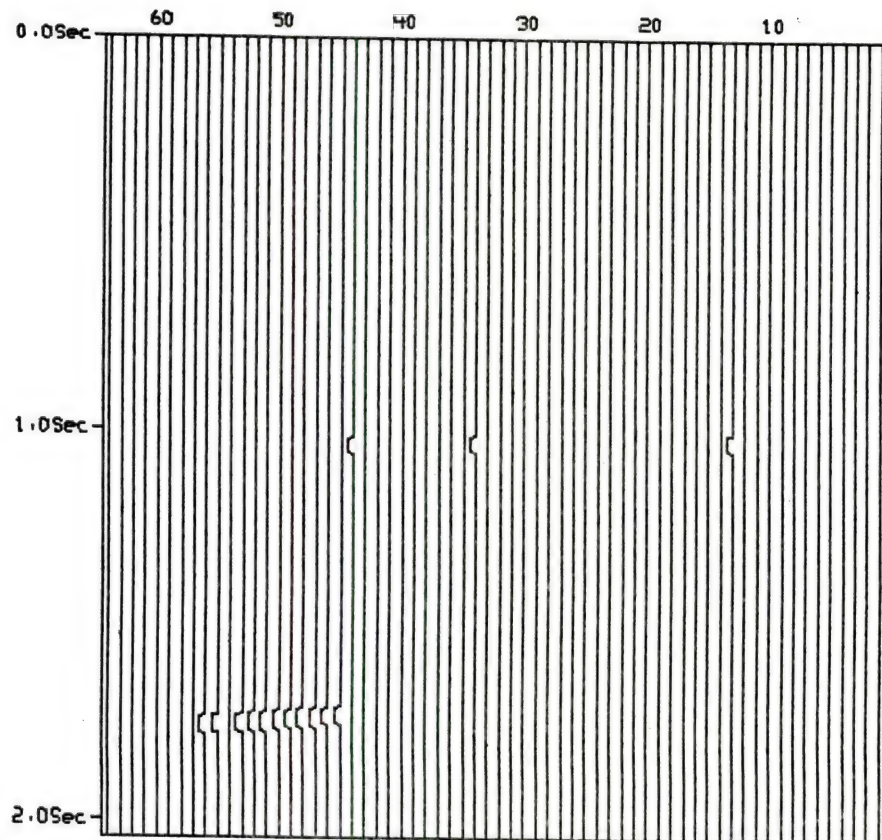


Figure 5.14C Classification result of bright spots

symbols (Table 5.2). The input seismogram is encoded also.

(1) Likelihood Ratio Test (LRT)

From the likelihood ratio test, the threshold for signal and noise is determined. Signal is present, if $\tau \geq 0.0208826$, or $\tau \leq -0.0208826$.

(2) Threshold for global detection

Comparing the 8-level optimal quantization with LRT, the closest levels to $\beta = \pm 0.0208826$ are the end points at $\pm 0.0249277 = \pm 0.5\sigma_s$. (Fig. 5.15). Then, $\pm 0.0249277 = \pm 0.5\sigma_s$ are selected as the new threshold. The areas above 0.0249277 and below -0.0249277 are the detected areas of the signal, i.e., the intervals of 'b', 'c', 'd', 'B', 'C', and 'D'. The probability of detecting 'b', 'c', 'd', 'B', 'C', and 'D' is 0.617. $10 \times 0.617 = 6.17$. Truncated 6.17 = 6. The approximated number of detected symbols at 'b', 'c', 'd', 'B', 'C', and 'D', is 6 symbols. So a threshold is set, if the number of symbol, 'b', 'c', 'd', 'B', 'C', or 'D', is equal to or larger than 6, then the possible wavelet is detected. Otherwise, input the next 10-symbol string.

(3) Threshold for the detection of candidate bright spot

The exact amplitude of the signal is not known because the signal is corrupted by noise. The probability of detection cannot be calculated as in the case of the 17 Hz Ricker wavelet described in Section 5.2.5. An alternative method is proposed. Using the 8-level optimal quantization, the d_i value is quantized to the quantized value c_i , the conditional mean of each quantization interval. Assume that Gaussian noise is added to the quantized value c_i , then the probability of detection in the quantized interval can be calculated. There are 4 extracted

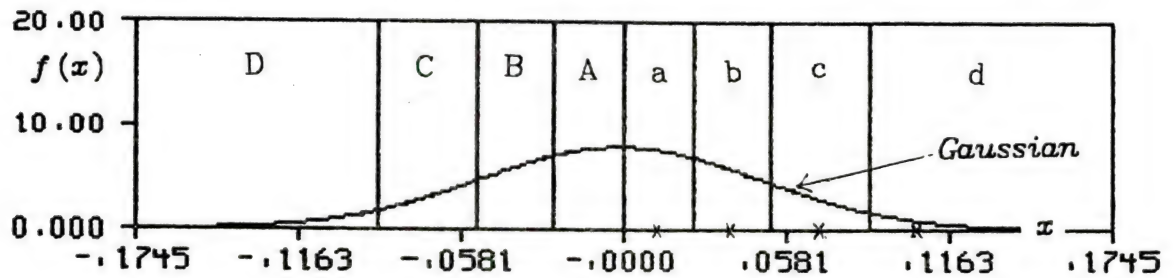


Figure 5.15A 8-level optimal quantization encoding for d_i of

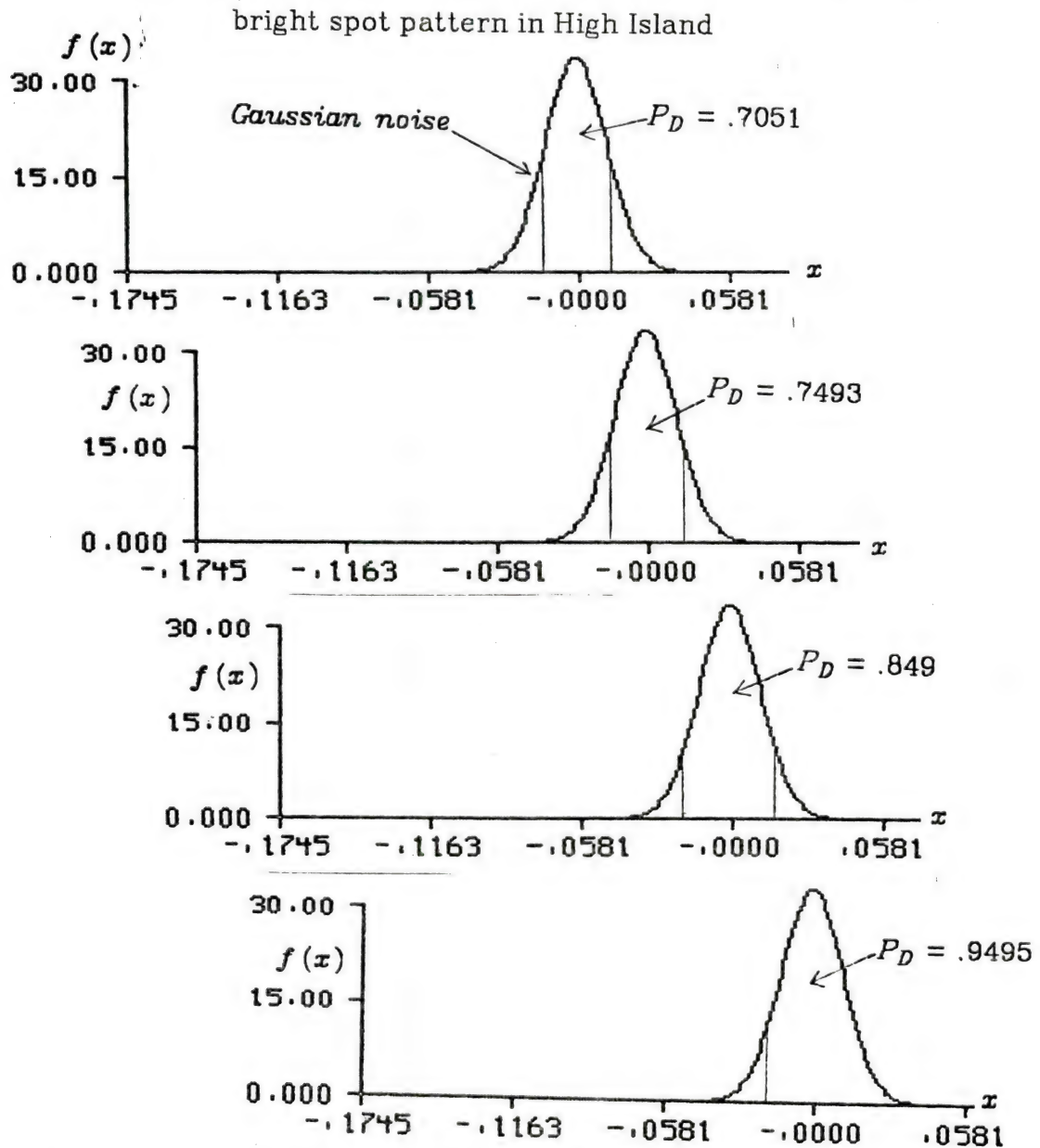


Figure 5.15B Probability of detection using the conditional mean of each interval in bright spot pattern

patterns and each pattern has 10 c_i . For 40 c_i of the quantized value of the candidate bright spot, the probability of detecting every c_i can be calculated using the statistical table of normal distribution. The sum of these 40 detection probabilities is 30.9724.

(There are 9 'a' or 'A', 20 'b' or 'B', 8 'c' or 'C', and 3 'd' or 'D'.

$$9 \cdot .7051 + 20 \cdot .7493 + 8 \cdot .849 + 3 \cdot .9495 = 30.9724)$$

For pattern string of 10 symbols of the candidate bright spot,

$$30.9724/4 = 7.7431. \text{ Truncated } 7.7431 = 7.$$

The approximated number of detected symbols is 7. The number of missing and false symbols is $10 - 7 = 3$, i.e., error or un-detected symbols. The input string belongs to the string of candidate bright spot if the Levenshtein distance is less than 3 symbols. So 3 is selected as a threshold. Suppose that x^1 , x^2 , x^3 , and x^4 are candidate bright spot strings, if $d^L(x^1, y) \leq k_1$, or $d^L(x^2, y) \leq k_2$, or $d^L(x^3, y) \leq k_3$, or $d^L(x^4, y) \leq k_4$, then y is the detected candidate bright spot string. The threshold values of k_1 , k_2 , k_3 , and k_4 are 3 in this experiment. The classification result is shown in Fig. 5.14C. Compared with the original seismogram in Fig. 5.14A, Fig. 5.14C is quite good.

5.5 Conclusions

(1) Syntactic pattern recognition uses the structural information of patterns. In a simulated seismic trace, syntactic pattern recognition technique can classify the Ricker wavelets which decision-theoretic approach is not easy to do.

(2) In the primitive recognition, there are two methods based on the optimal quantization encoding. One is the amplitude-independent encoding which can not classify the different amplitude of fHz Ricker

wavelets. The other is the amplitude-dependent encoding which can classify every kind of Ricker wavelet.

(3) In the primitive recognition, assigning the pair $y_{i+1}-y_i$ to a symbol is a quantization problem. The pairs in the Ricker wavelets are Gaussian distributed. Optimal quantization of 8 levels for the Gaussian samples is used in this study.

(4) In the simulated and real seismograms, tree classification techniques are used in the testing traces to extract the candidate bright spot patterns.

(5) The roles of likelihood ratio test, optimal quantization encoding, and probability of detecting the signal involving in the global, local detection, and threshold setting are quite important.

(6) Minimum distance and nearest-neighbor classification rules are used in the classification of Ricker wavelets. In the detection of candidate bright spot, the results using threshold setting of string distance to detect the candidate bright spot are quite satisfactory and can be used to improve seismic interpretation.

CHAPTER VI

SYNTACTIC PATTERN RECOGNITION FOR THE RECOGNITION OF BRIGHT SPOT

6.1 Introduction

In Chapter 1, bright spot is defined as the pattern having at least one of the three physical properties and a continuous reflection layer in a two-dimensional seismogram. In Chapter 3, 4, and 5, candidate bright spots are detected by using decision-theoretic and syntactic approaches. The detected bright spot patterns often scatter in a two-dimensional seismogram. The detected patterns should be continuous and represent the reflection layer. Singular patterns existing in the seismogram do not form a reflection layer. In order to remove the singular patterns and keep the continuous patterns, use of spatial relations in two-dimensional seismogram analysis is proposed. One possibility is to use a string-to-string correlation algorithm for image skeletonization to find the reflectors from one trace to the next [lu82a]. Another is to use the spatial relations in the analysis of seismogram to keep the continuous reflection coefficient and eliminate the noise.

In this study, five methods are proposed to test the continuity of the reflection layer. Local and global pattern tests are heuristic and simple, but applicable to only very limited cases. In order to test whether a continuous reflection layer is a bright spot or a non-bright

spot, syntactic pattern recognition is again proposed in the two dimensional analysis. In syntactic pattern recognition, three kinds of string distance computation are proposed to test the continuity of a bright spot pattern.

6.2 Local Pattern Testing

The classification results from the methods described in Chapters 3, 4, or 5 are used for further processing. The amplitude of the seismic data from the previous classification result is 0.0 for a non-bright spot and -0.2 for a candidate bright spot. Data with amplitude -0.2 is called negative polarity. Each detected pattern wavelet has about 10 point samples (sampling interval is 0.004 seconds). From Dobrin [dob76a], the high amplitude portion of a bright spot occupies a limited horizontal region. From real seismograms in Figs. 1.1, 1.2, and 1.3, the wavelets of a bright spot are horizontally continuous, i.e., a fairly large number of traces with wavelets appearing in the horizontal direction. So a horizontal line pattern is considered here. The procedures are discussed in the following.

At first, consider five points along the horizontal direction. The center point is a testing point. A testing point and its four horizontal neighboring points, two on each side, are considered as a horizontal line pattern and shown in the following:

o o x o o

where x is the testing point. Because only five points are considered here, we call the testing pattern a local testing pattern. The number of

points in the local testing pattern can be varied.

The local testing pattern is shifted in the seismogram from left to right and from top to bottom. If three of the five horizontal points are with negative polarity, then the five points form a reflection pattern. Then, two methods are considered below.

- (a) All five points of the testing pattern maintain their original amplitudes.
- (b) The testing point x is assigned the amplitude of negative polarity -0.2 and the original amplitudes of the four neighboring points remain unchanged.

Otherwise, assign zeros to the testing pattern as the output and test the next pattern.

Here (b) is adopted because a non-bright spot will be changed to a bright spot with the help of its neighboring bright spots.

Algorithm 6.1: Local pattern testing

Input:

(1) An array $A(i,j), i=1, \dots, M, j=1, \dots, N$ of a 2-dimensional seismogram with N traces and M points in each trace.

(2) The amplitudes of $A(i,j)$ are $c = -0.2$ for a candidate bright spot and 0.0 for a non-bright spot, where i is the index along the trace, the vertical coordinate, and j is the index along the top of each trace (station), the horizontal coordinate.

(3) Testing pattern length L and threshold $t = \text{rounding of } \frac{(L+1)}{2}$.

Output: $B(i,j), i=1, \dots, M, j=1, \dots, N$, the local reflection patterns.

Method:

- (1) Set the output amplitudes $B(i,j)=0.0$, $i=1,2,\dots,M, j=1,2,\dots,N$. Select a horizontal testing pattern of L points. Set the location of the center of the horizontal testing pattern at an integer of $\frac{(L+1)}{2}$. The center point is the testing point. At first, the pattern is at the top and left of the seismogram, i.e., $i=1, j=1$.
- (2) Let the number of negative polarities in the horizontal testing pattern of L points be tt .
- (3) If the number tt is less than the threshold t , then set the testing point to zero. Otherwise, if tt is larger than or equal to the threshold t , then the output amplitude $B(i,j)$ of the testing point is set equal to $c=-0.2$ and the original amplitudes of the $(L-1)$ neighboring points remain unchanged and are assigned to the output array $B(i,j)$.
- (4) Shift to the next right pattern position, i.e., shift the testing point to the next position. If the pattern reaches the right-most edge of the seismogram, $j=N$, then the pattern is shifted to the beginning of the next horizontal line. Then go to Step (2) and continue until the lower right corner of the 2-dimensional seismogram is reached, i.e., $i=M, j=N$.

In Algorithm 6.1, the number L , length of the testing pattern, is determined by the spatial relation of seismic traces, i.e., the distance between two traces. The amplitude of t , threshold, is determined from L .

In this study, the syntactic classification results in Chapter 5 are used as the input. Using Algorithm 6.1, the length of horizontal testing

pattern is $L=5$ and the threshold t is 3 which are selected for the analysis of three seismograms here. Three results are shown.

(1) Simulated seismogram

From the classification result in the simulated seismogram shown in Fig. 6.1 (Fig. 5.10E), there are two missing traces. Using this local line pattern testing, the result is shown in Fig. 6.2. The missing parts of bright spot, the 27th and the 38th traces, are filled with the help of the neighboring points of bright spot.

(2) High Island

From the classification result (Fig. 6.3, Fig. 5.14C), there is one missing trace at the lower left corner of the seismogram and there are three singular patterns in the middle of the seismogram. Using the local line pattern testing, the result is shown in Fig. 6.4. The missing part of bright spot, the 54th trace, is filled with the help of the neighboring points of bright spot. The singular patterns are removed.

(3) Mississippi Canyon

From the classification result (Fig. 6.5, Fig. 5.12C), there are many missing traces and many singular patterns in the seismogram. Using the local line pattern testing, the result is shown in Fig. 6.6. The missing parts of bright spot are filled with the help of the neighboring points of bright spot. The singular patterns are removed.

Although the result in Fig. 6.6 is good, many missing traces exist between four groups. The locations of the four groups of local pattern are the 7th to the 15th traces, the 20th to the 23th traces, the 28th to the 44th traces, and the 48th to the 51th traces in Fig. 6.6. The local

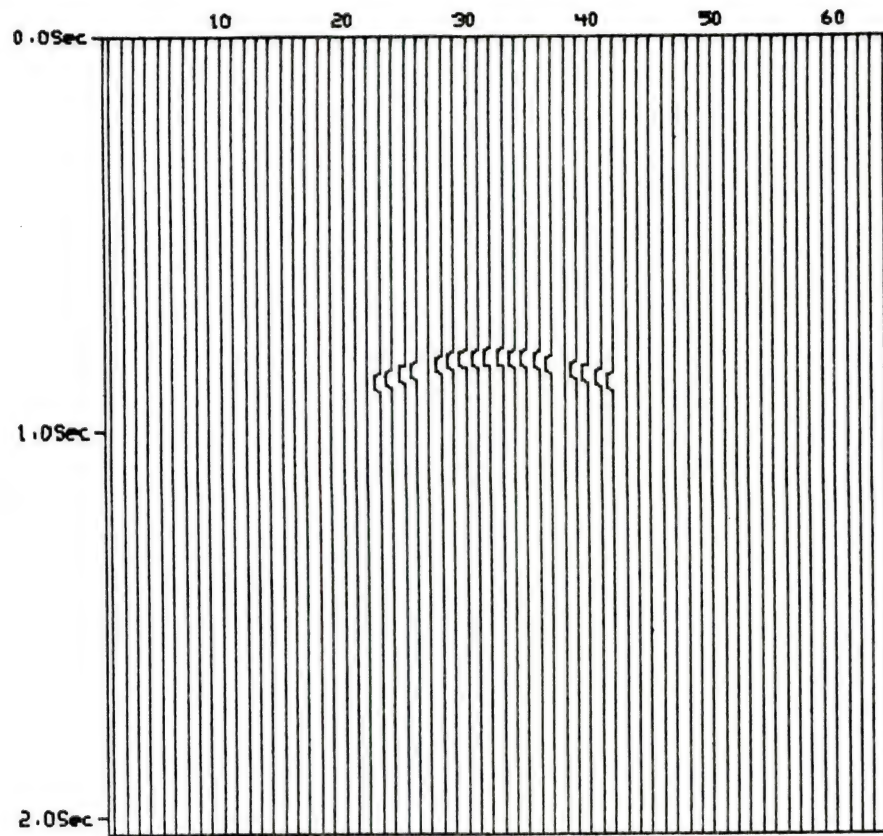


Figure 6.1 1-D Classification result of the simulated seismogram

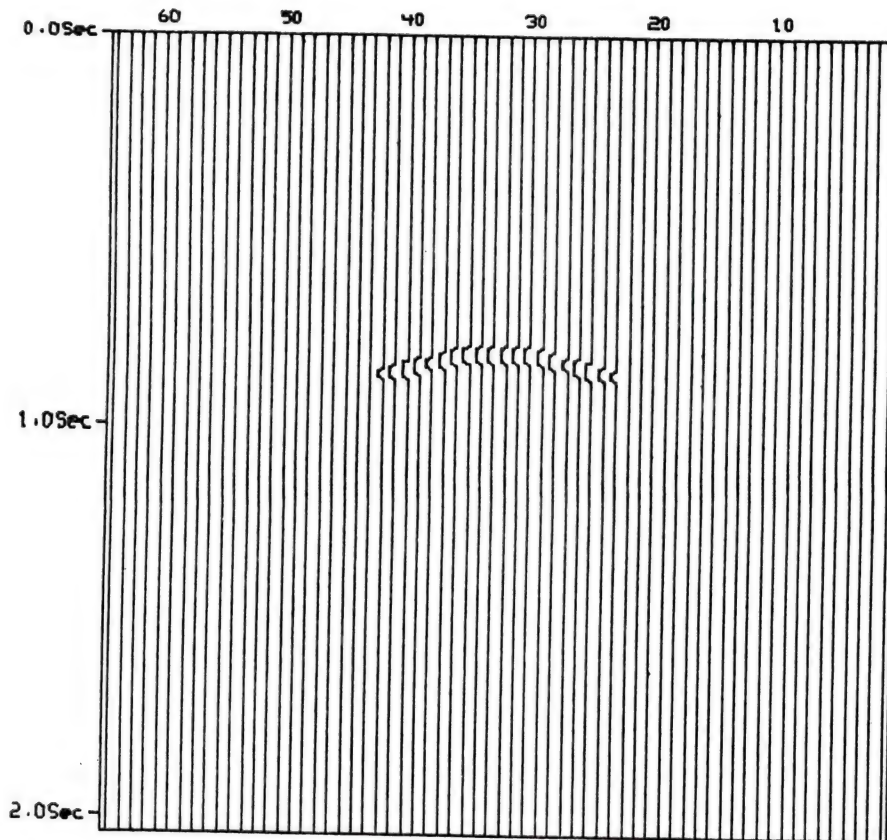


Figure 6.2 2-D Local pattern testing result of the simulated seismogram

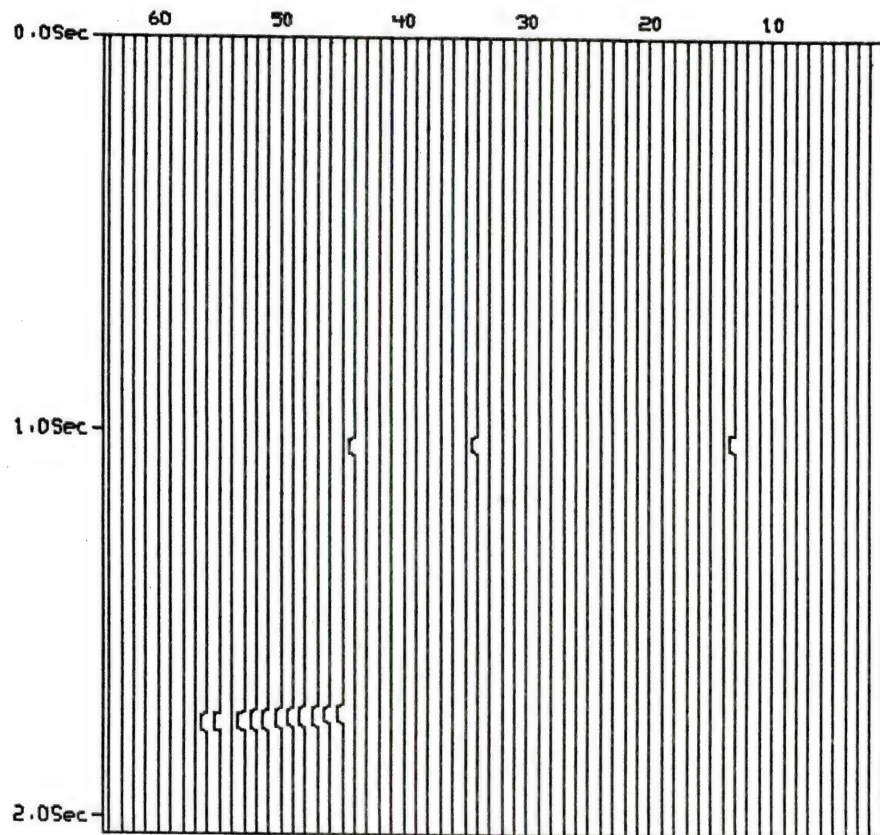


Figure 6.3 1-D Classification result at High Island

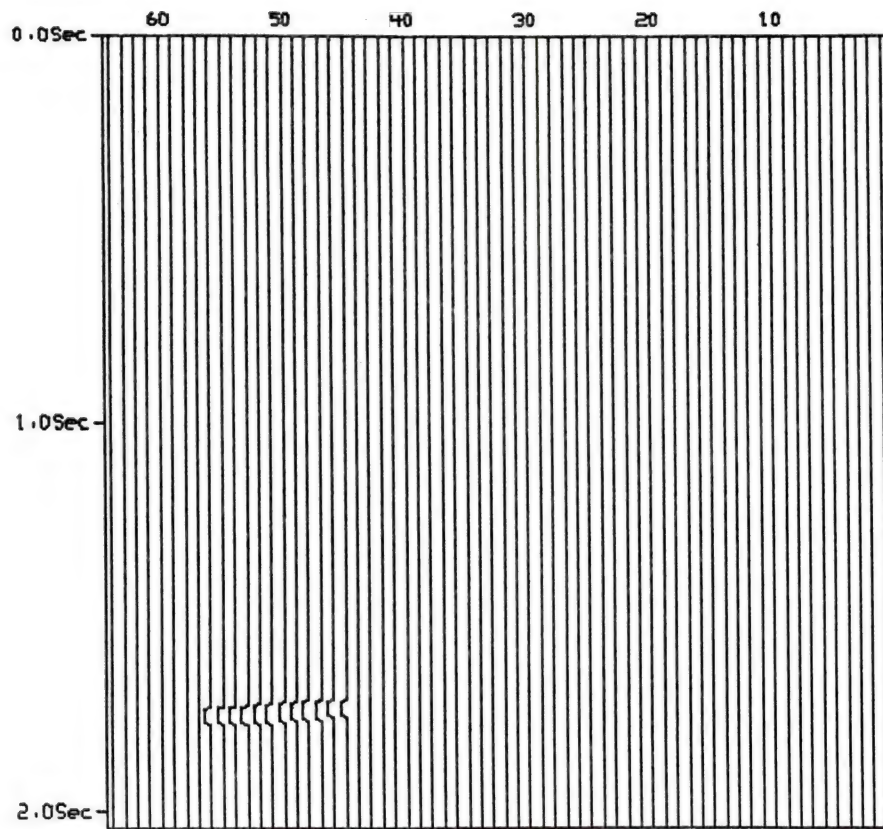


Figure 6.4 2-D Local pattern testing result at High Island

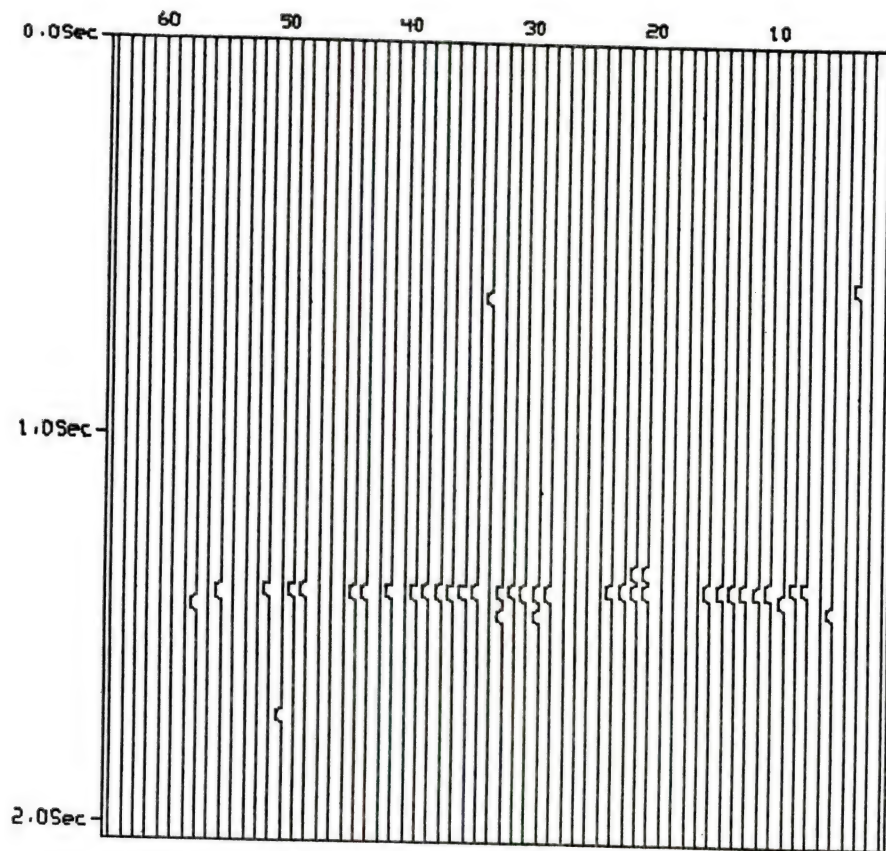


Figure 6.5 1-D Classification result at Mississippi Canyon

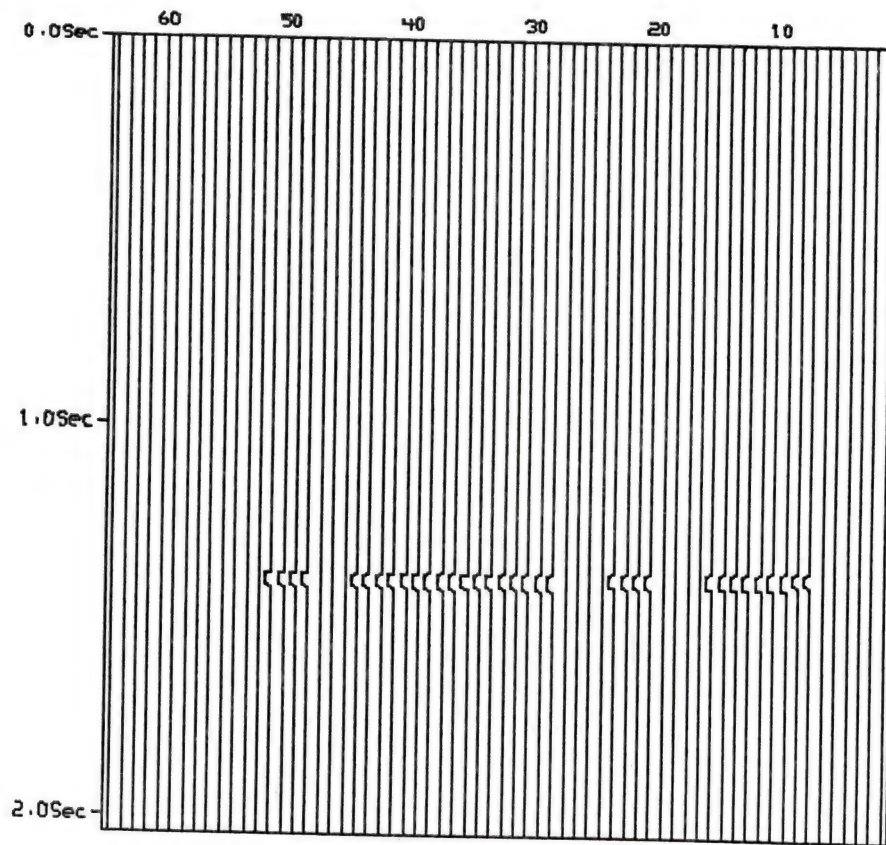


Figure 6.6 2-D Local pattern testing result at Mississippi Canyon

pattern testing can not be applied to test the continuity among the four group patterns. A global pattern testing is proposed in the following to test whether the local patterns form a continuous reflection layer.

6.3 Global Pattern Testing

After the local pattern testing, singular patterns are usually removed. Only local patterns exist in the seismogram. The local patterns may have some spatial relation between them. i.e., they may be on the same reflection layer or on different reflection layers. For example in Fig. 6.6, many missing traces exist among the four groups. The purpose of the global pattern testing is to group the patterns if they belong to the same reflection layer. The procedure is discussed in the following.

Consider a horizontal line pattern. Six horizontal points are tested. The number of points in the global pattern testing can be varied. For this case we have

$o \ x \ x \ x \ x \ o$

where x is a testing point. There are 4 testing points in the pattern.

At first, the amplitudes of the input seismogram from the previous local pattern testing are assigned to the output. The line pattern is shifted from top and left to bottom and right in the seismogram to test the four testing points. If the amplitudes of the two end points from these six points are -0.2 , then the amplitudes of the four middle testing points are assigned a negative polarity $c = -0.2$ as the output.

According to the discussion above, Algorithm 6.2 is presented as follows.

Algorithm 6.2: Test of the continuity of local patterns

Input: $B(i,j), i=1, \dots, M, j=1, \dots, N$, with the amplitudes of 0 and $c=-0.2$ from Algorithm 6.1, and a constant d . The length of the horizontal line pattern is $d+2$.

Output: $C(i,j), i=1, \dots, M, j=1, \dots, N$, the continuous reflection layer.

Method:

(1) Assign the amplitudes of $B(i,j)$ to $C(i,j), i=1, \dots, M, j=1, \dots, N$, i.e., the original amplitudes remain unchanged.

(2) The horizontal testing pattern with length $d+2$ starts at the top and left of the input seismogram, i.e., $i=1, j=1$.

(3) If the amplitudes of the two end points of the testing pattern are -0.2, then the amplitudes of the d testing points within the two end points are assigned the amplitude $c=-0.2$.

(4) Shift to the next one right position and go to Step (3), until the lower right corner of the 2-dimensional seismogram is reached, i.e., $i=M, j=N$.

In Algorithm 6.2, the length of the testing pattern ($d+2$) depends on the spatial relation of seismic traces and can be varied. In this

experiment, d equals 4. The input seismogram is the result from local pattern testing of Fig. 6.6 at Mississippi Canyon. The result of processing Fig. 6.6 using Algorithm 6.2 is shown in Fig. 6.7. Fig. 6.7 is a continuous reflection layer.

6.4 Syntactic Pattern Recognition for the Recognition of Bright Spot

In Section 6.2, the local pattern testing is useful only for very limited cases, i.e., for horizontal line patterns. So syntactic pattern recognition of bright spot is proposed to handle other situations. A block diagram of syntactic pattern recognition for the recognition of bright spot is shown in Fig. 6.8. Each candidate bright spot is an input seismogram in this section.

6.4.1 Preprocessing

(1) For an input seismogram, the midpoint of the duration of the candidate bright spot is extracted. The amplitude of the midpoint is $c = -0.2$ as the negative polarity. The output seismogram is called "peak seismogram".

(2) Extract the pattern from the peak seismogram. The technique described in [lu82a] may be used to link the reflectors from one trace to the next. Visual inspection is adopted in the experiment here. For the extracted pattern, the number of peaks in each group of $L=5$ traces are larger than or equal to $t=3$. The number L of selected traces depends on the spatial relation of seismic traces and can be

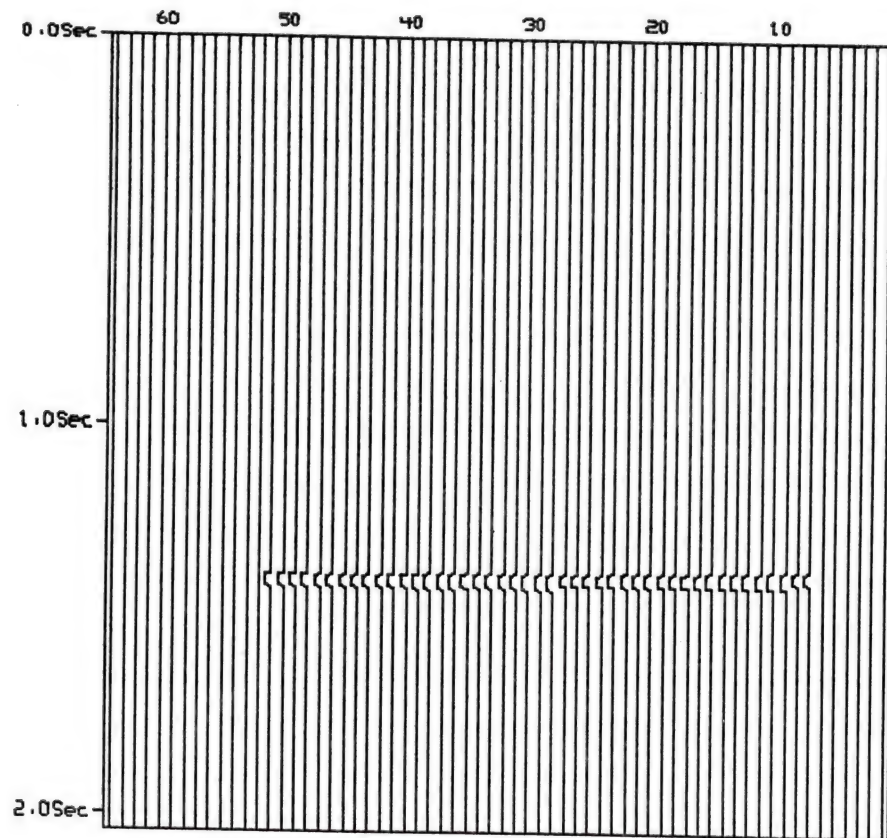


Figure 6.7 2-D Local and global pattern testing result at Mississippi Canyon

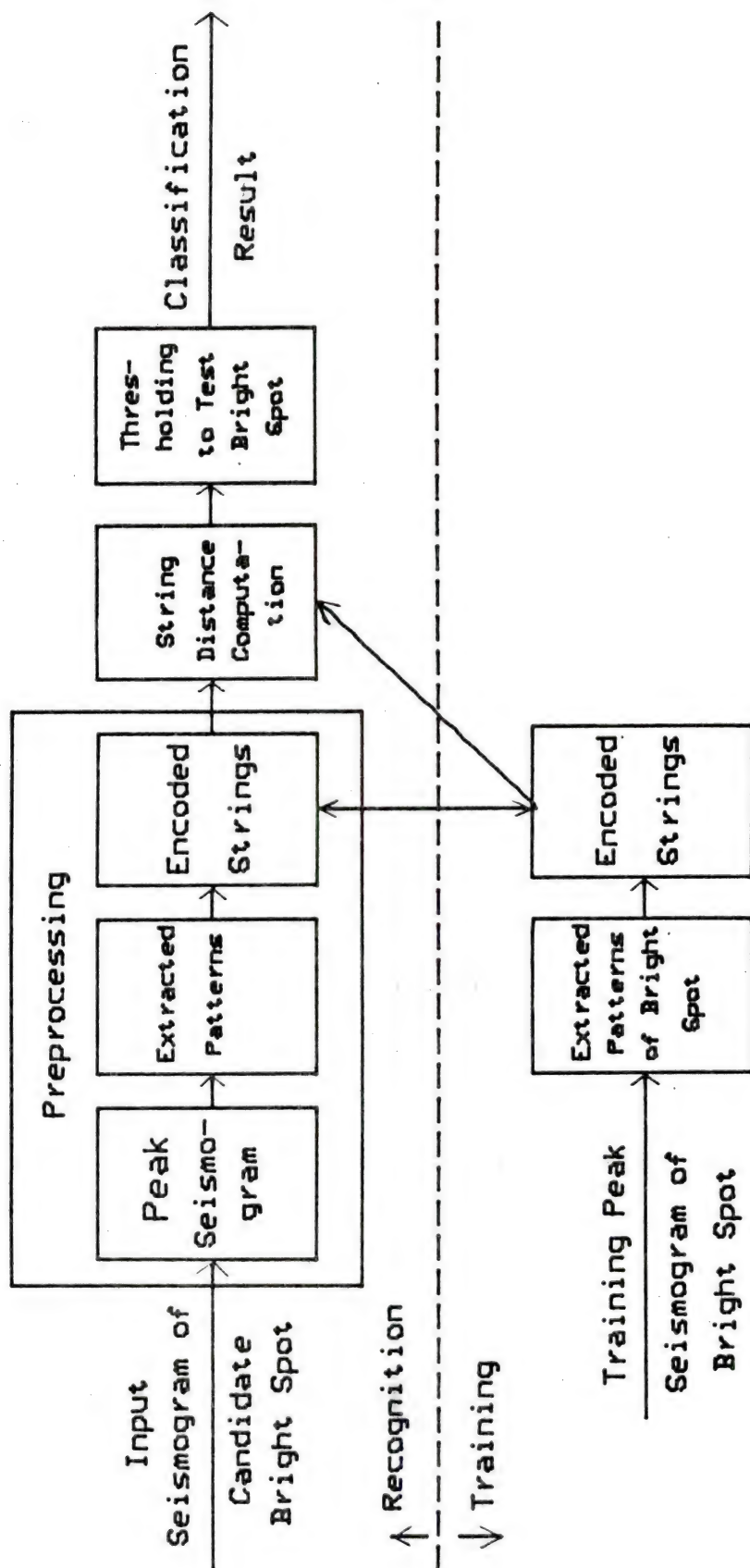


Figure 6.8 A block diagram of syntactic pattern recognition system
(For the recognition of bright spot in 2-D seismogram of candidate bright spot)

varied. The threshold t is related to the number of selected traces as in the local pattern testing described in Section 6.2. The points between two peaks are interpolated if the pattern is extracted and are called "interpolated-peaks". The vertical distance between two successive peaks is less than or equal to 7 intervals (sampling interval is 0.004 seconds). The reason for the selection of 7 intervals of vertical difference will be discussed later. Following the above procedure, the singular peak is eliminated. Edge detection technique in image processing can not handle this kind of problem because two successive peaks may not be the neighbors.

Consider the thickness of a reflection layer and the time shift between two successive peaks. The duration of 7 intervals is 7×0.004 seconds = 0.028 seconds for the two-way vertical travel time of P-wave. So one-way travel time is 0.014 seconds. Suppose that from Fig. 3.5A, the P-wave velocity at gas sand zone is 1.737 Km/sec, then the thickness of the layer corresponding to 0.014 seconds is $1.737 \text{ Km/sec} \times 0.014 = 24.318$ meters. If the distance between two adjacent traces is 25 meters, then the dipping angle is approximately 45 degrees which indicates a high dipping layer. If the vertical difference of two successive peaks is larger than 7 intervals, the pattern is discontinuous and is not considered here.

(3) The difference $d_i = y_{i+1} - y_i$ of vertical coordinates of two adjacent peaks, (x_{i+1}, y_{i+1}) and (x_i, y_i) , is assigned a symbol ω_i . The primitives are as follows.

$$\omega_i = c \text{ for } d_i = 6 \text{ or } 7.$$

$$\omega_i = b \text{ for } d_i = 4 \text{ or } 5.$$

$$\omega_i = a \text{ for } d_i = 2 \text{ or } 3.$$

$\omega_i = 0$ for $d_i = 1, 0$, or -1 .

$\omega_i = A$ for $d_i = -2$ or -3 .

$\omega_i = B$ for $d_i = -4$ or -5 .

$\omega_i = C$ for $d_i = -6$ or -7 .

From the peak to peak or the peak to interpolated-peak, the pattern is encoded. From the interpolated-peak to peak or interpolated-peak, the pattern is encoded as $\omega_i = x$.

6.4.2 Generation of Training Patterns of Bright Spot

In Figure 1.1, 1.2, and 1.3, the shape of a bright spot pattern may be arched, horizontal, or concave. The flat or concave shape of bright spots may be caused by the velocity variation above the bright spots. The mathematical equation of geological structure to generate the 19 seismic patterns are given in the following. The P-wave velocity at the gas sand zone is 1.737 Km/sec. Above the gas sand zone, a shale layer is assumed, the P-wave velocity is 2.59 Km/sec which is the same as that in Fig. 3.5A.

(1) For flat and arched patterns

$$f(i) = C \left(\sin \frac{2\pi i}{1024} \right)^2 - 2.0 \quad i = 180 - 332$$

where C is 0.0, 0.2, 0.3, 0.4, 0.5, 0.6, 0.7, 0.8, 0.9, and 1.0 for the flat and arched patterns respectively.

(2) For concave patterns

$$f(i) = c \left(\sin \frac{2\pi i}{1024} \right)^2 - 1.0 \quad i = 180 - 332$$

where C is -0.2, -0.3, -0.4, -0.5, -0.6, -0.7, -0.8, -0.9, and -1.0 for the concave patterns respectively.

The training patterns with different shapes of bright spot are simulated. The 19 simulated seismograms of reflection coefficient are generated. Only reflection coefficients are shown in the seismograms, so the seismograms are the peak seismograms. The shape of bright spot can be changed by varying the shape at the top boundary of the gas sand zone. Fig. 6.9 shows the flat shape. Fig. 6.10 - 6.18 show the arched shapes. Fig. 6.19 - 6.27 show the concave shapes. Fig. 6.18 and 6.27 have 7 intervals for the vertical difference of two successive peaks which is the maximum encoded distance in this study. There are 20 traces in each seismogram of a bright spot pattern, Training strings of 19 symbols are encoded for each seismogram. The encoded string of each bright spot pattern is given in the caption of each figure. Because the candidate bright spot of Fig. 6.1 has 20 traces, so peak seismogram of 20 traces is simulated here. In this study, the 20 traces of bright spot pattern and 19 simulated seismograms can handle those of which the number of traces is less than or equal to 20. If the number of traces of a candidate bright spot is larger than 20, then simulated seismograms with more than 20 traces can also be generated.

6.4.3 String Distance Computation

Three kinds of string distance computation are discussed in the following.

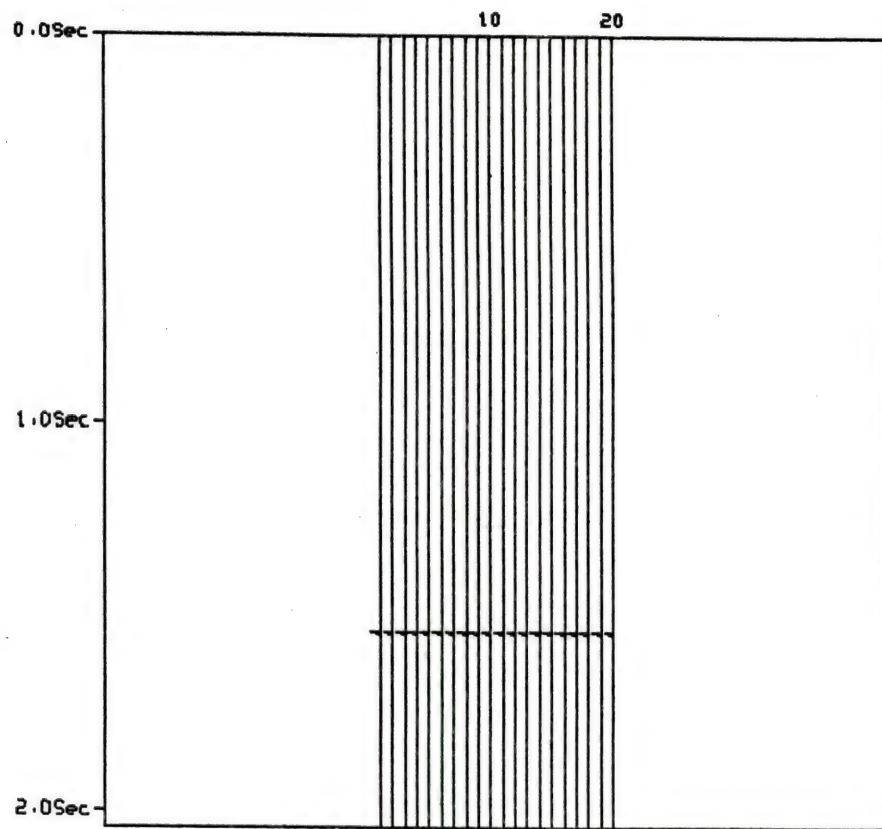


Figure 6.9 Simulated peak seismogram of bright spot
for flat shape, training string o^{19}

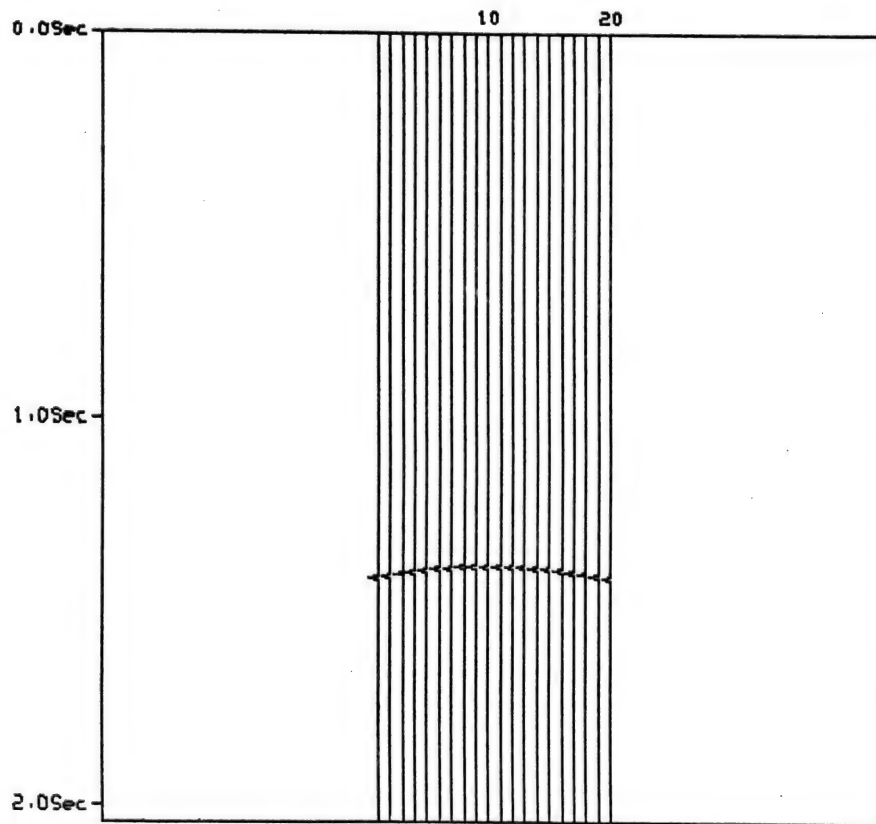


Figure 6.10 Simulated peak seismogram of bright spot
for arched shape, training string $oao^{15}Ao$

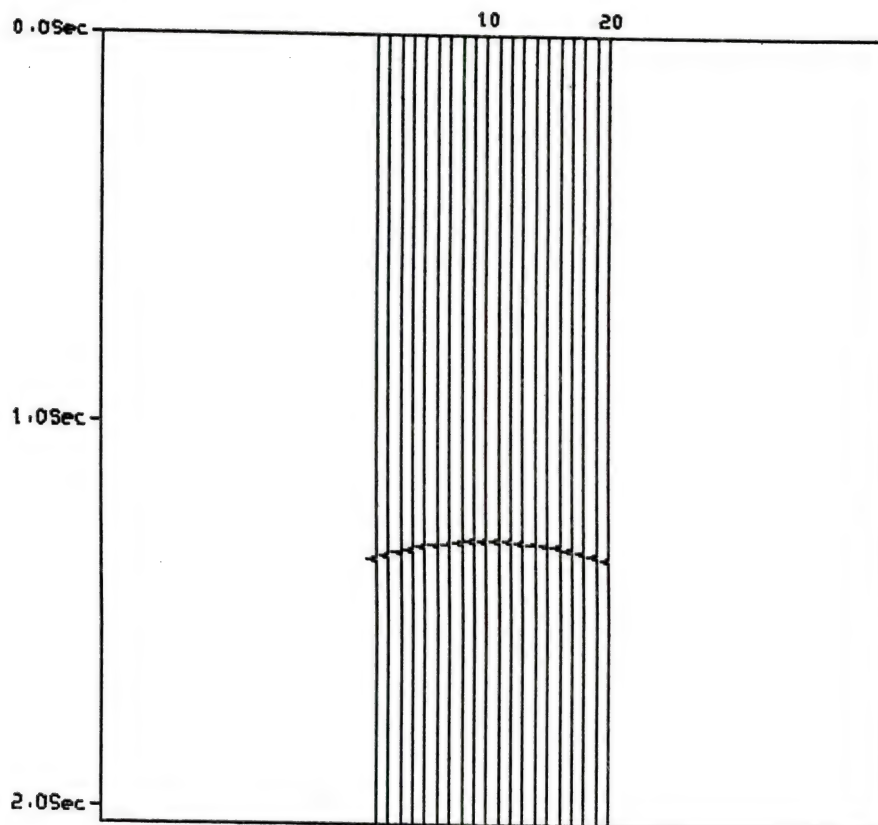


Figure 6.11 Simulated peak seismogram of bright spot
for arched shape, training string $\alpha^4_0^{11}A^4$.

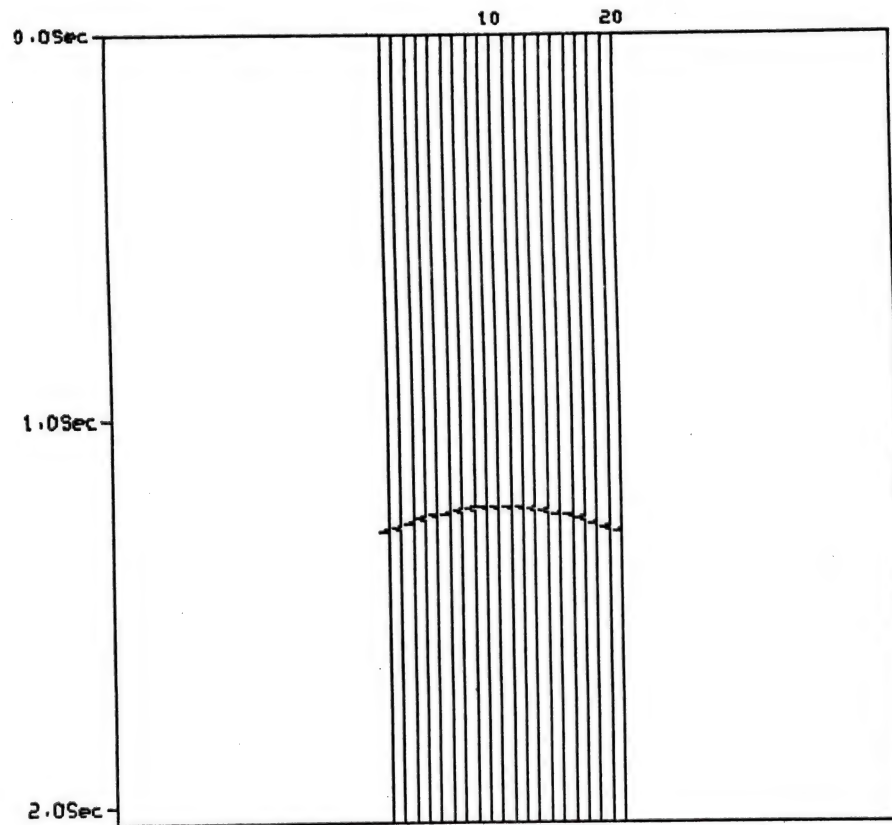


Figure 6.12 Simulated peak seismogram of bright spot
for arched shape, training string $a^4oao^7AoA^4$

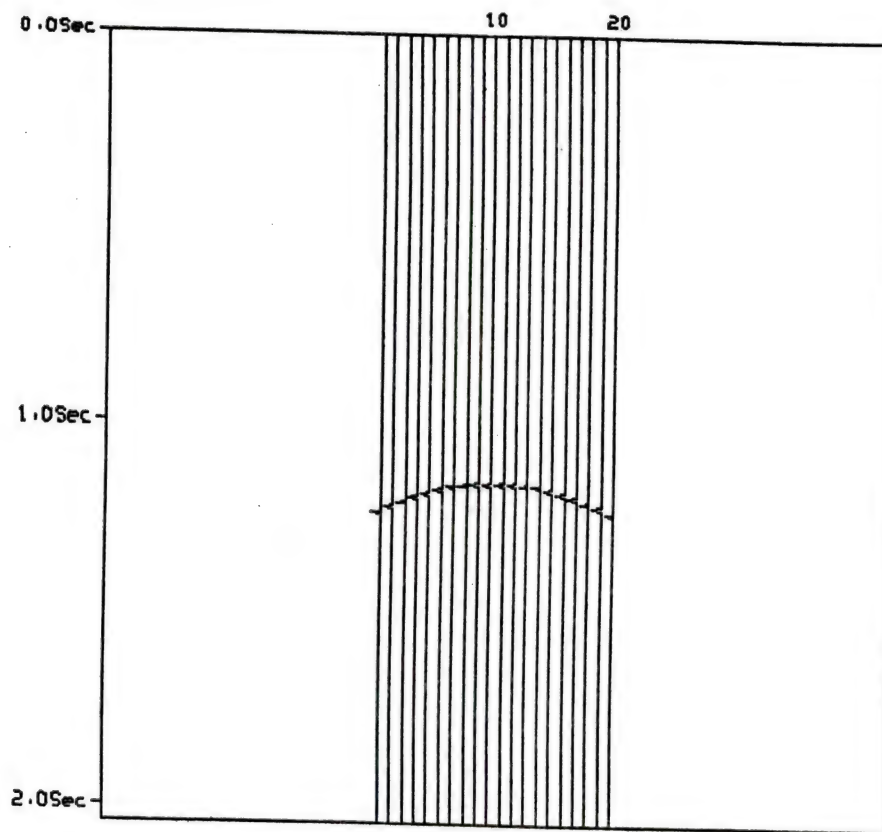


Figure 6.13 Simulated peak seismogram of bright spot
for arched shape, training string $ba^5o^7A^5B$

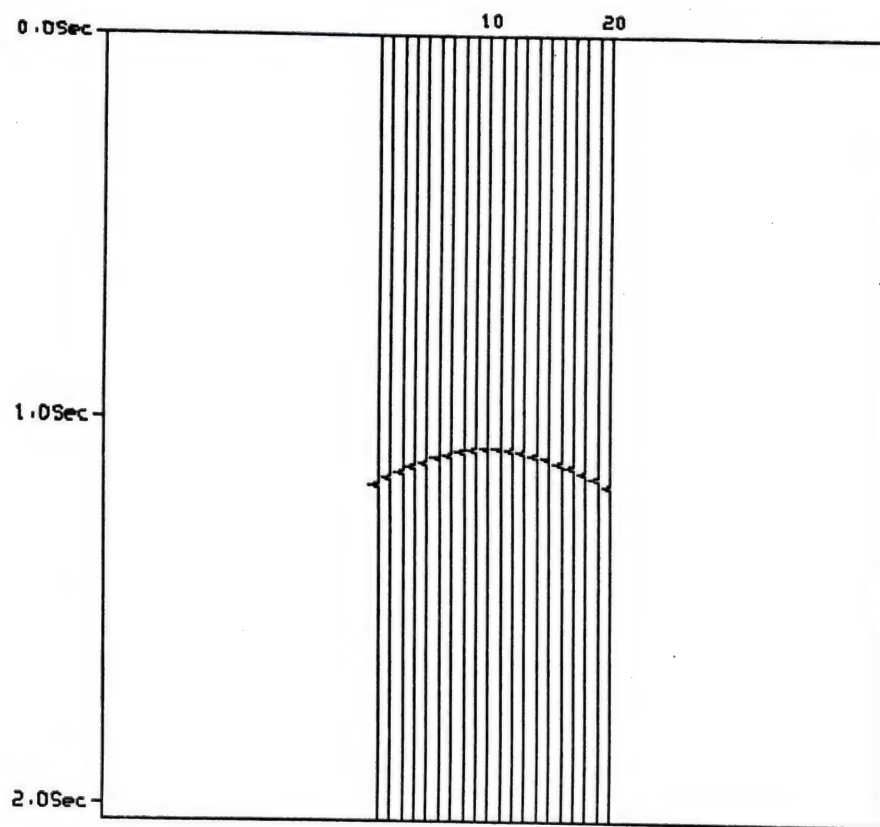


Figure 6.14 Simulated peak seismogram of bright spot
for arched shape, training string $b^2a^5o^5A^5B^2$

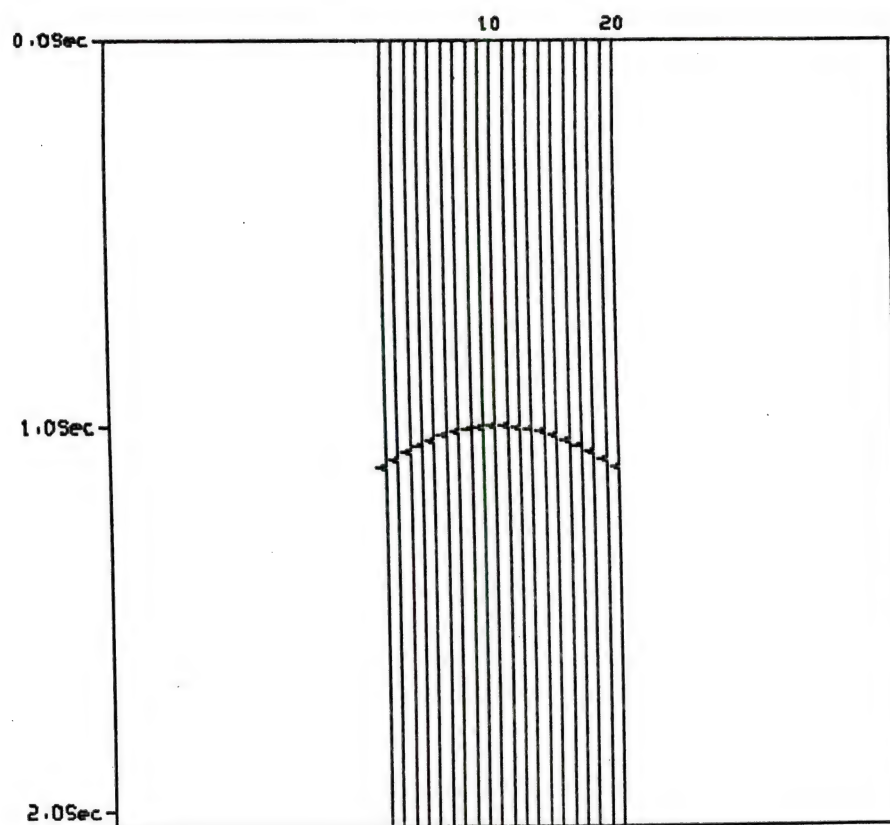


Figure 6.15 Simulated peak seismogram of bright spot
for arched shape, training string $b^3aba^2o^5A^2BAB^3$

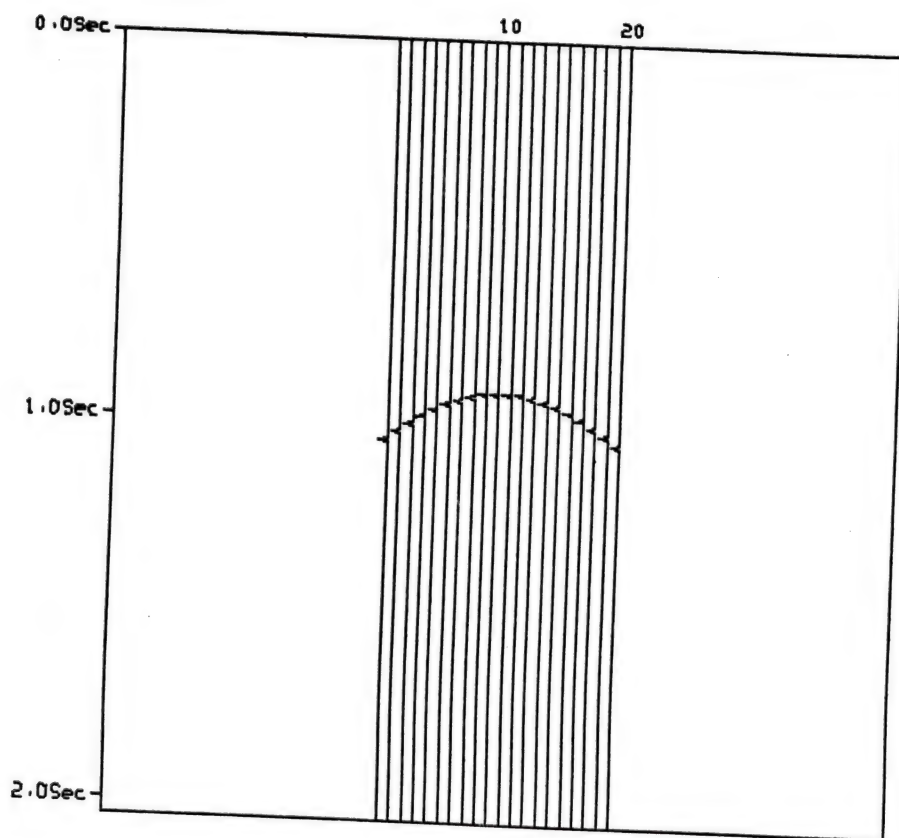


Figure 6.16 Simulated peak seismogram of bright spot
for arched shape, training string $cb^4a^3o^3A^3B^4C$

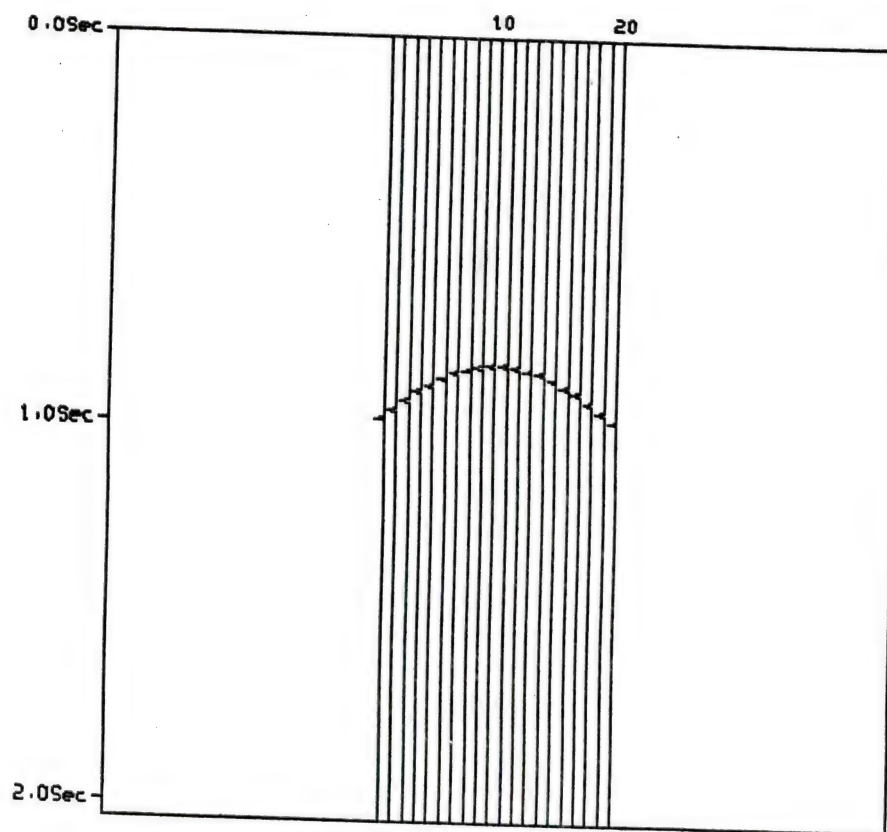


Figure 6.17 Simulated peak seismogram of bright spot
for arched shape, training string $c^3b^3a^2o^3A^2B^3C^3$

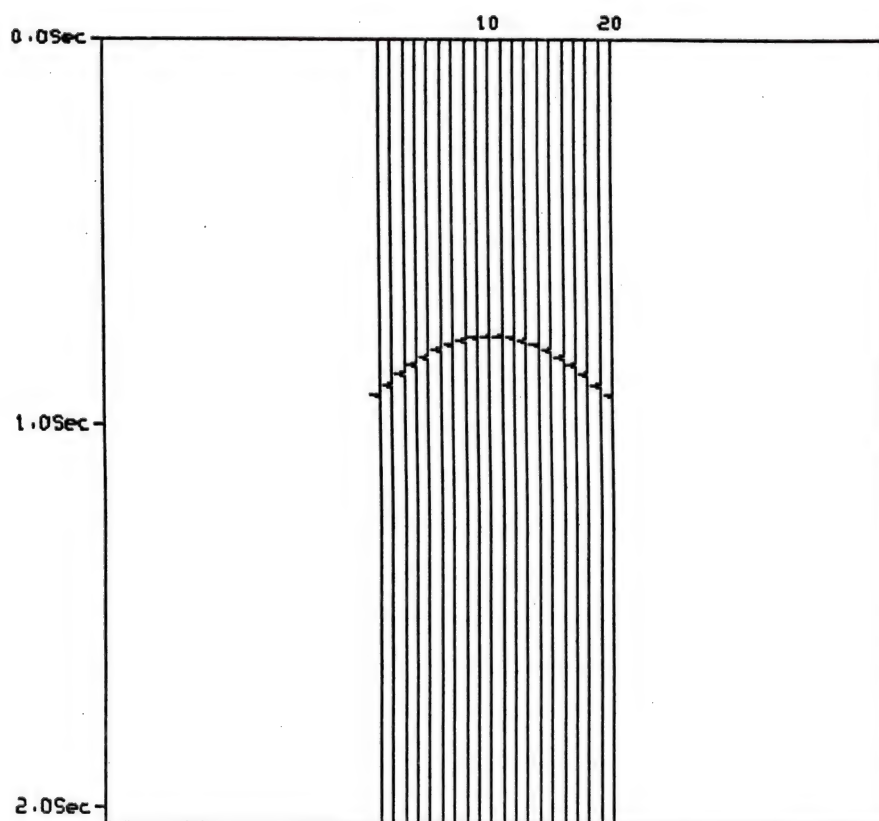


Figure 6.18 Simulated peak seismogram of bright spot
for arched shape, training string, $c^3b^2a^3o^3A^3B^2C^3$

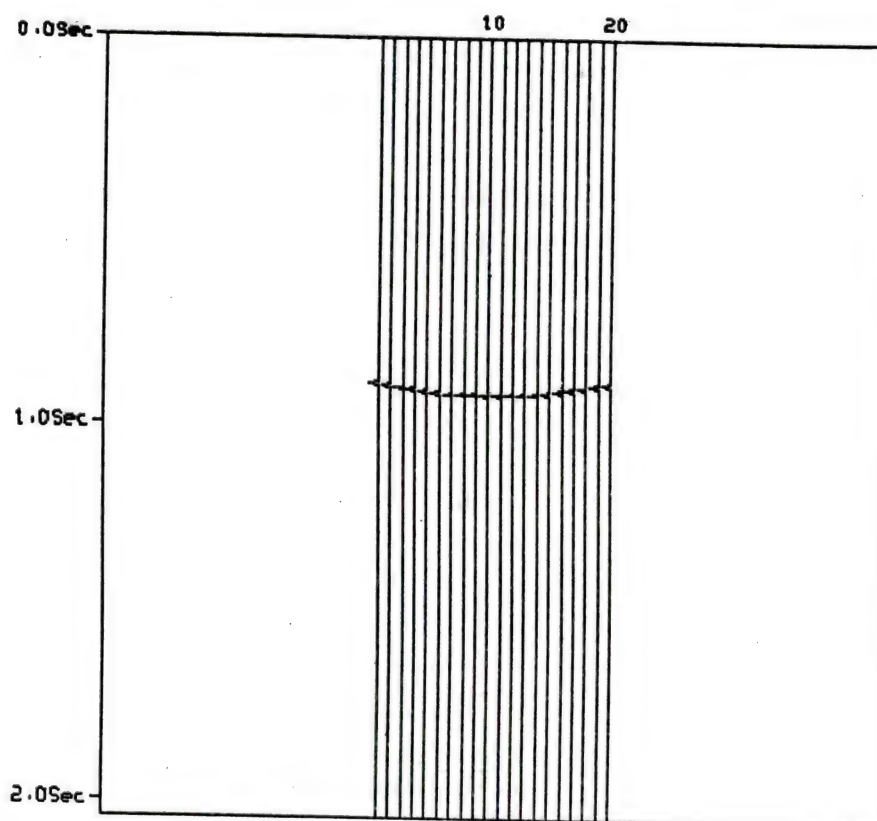


Figure 6.19 Simulated peak seismogram of bright spot
for concave shape, training string $oAo^{15}ao$

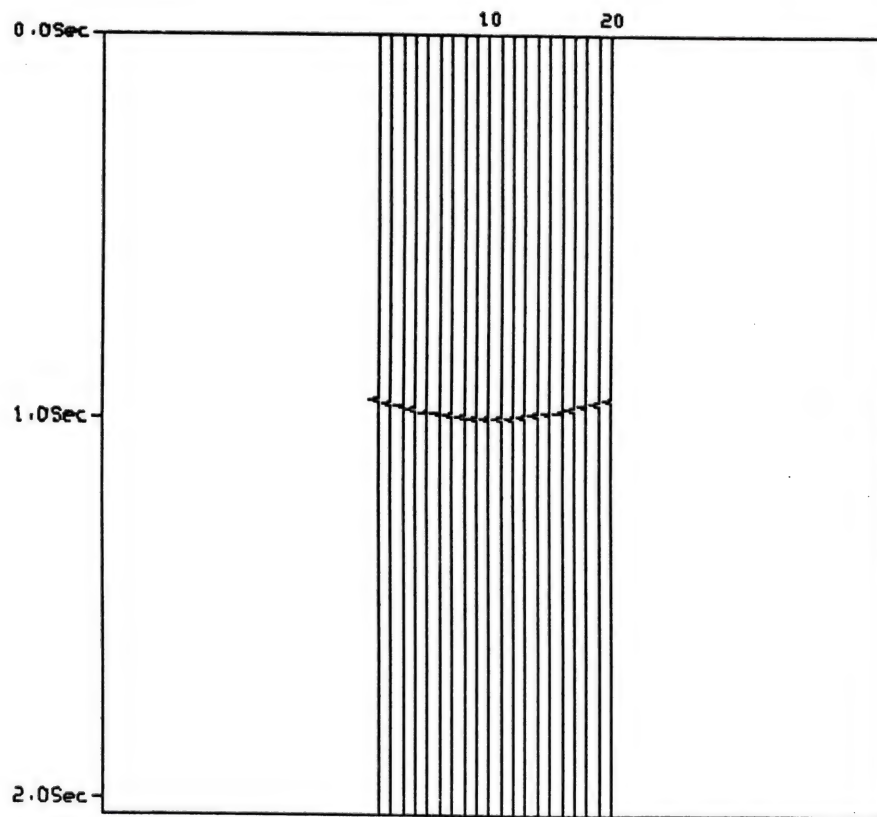


Figure 6.20 Simulated peak seismogram of bright spot
for concave shape, training string $A^4 o^{11} a^4$

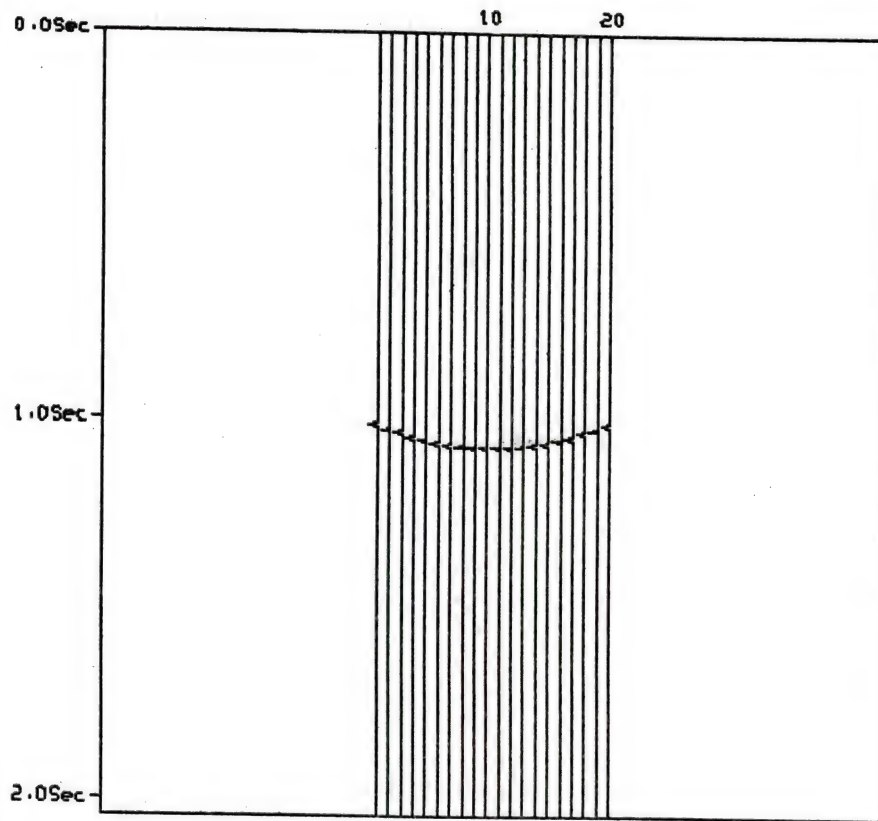


Figure 6.21 Simulated peak seismogram of bright spot
for concave shape, training string $A^5 o^9 a^5$

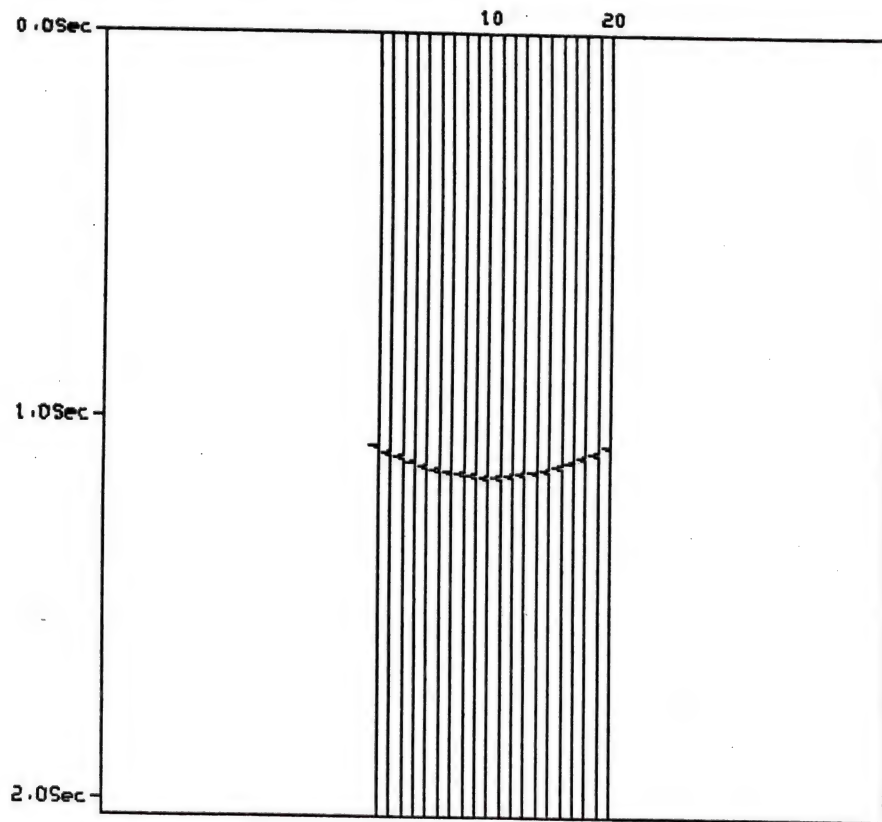


Figure 6.22 Simulated peak seismogram of bright spot
for concave shape, training string $BA^5o^7a^5b$

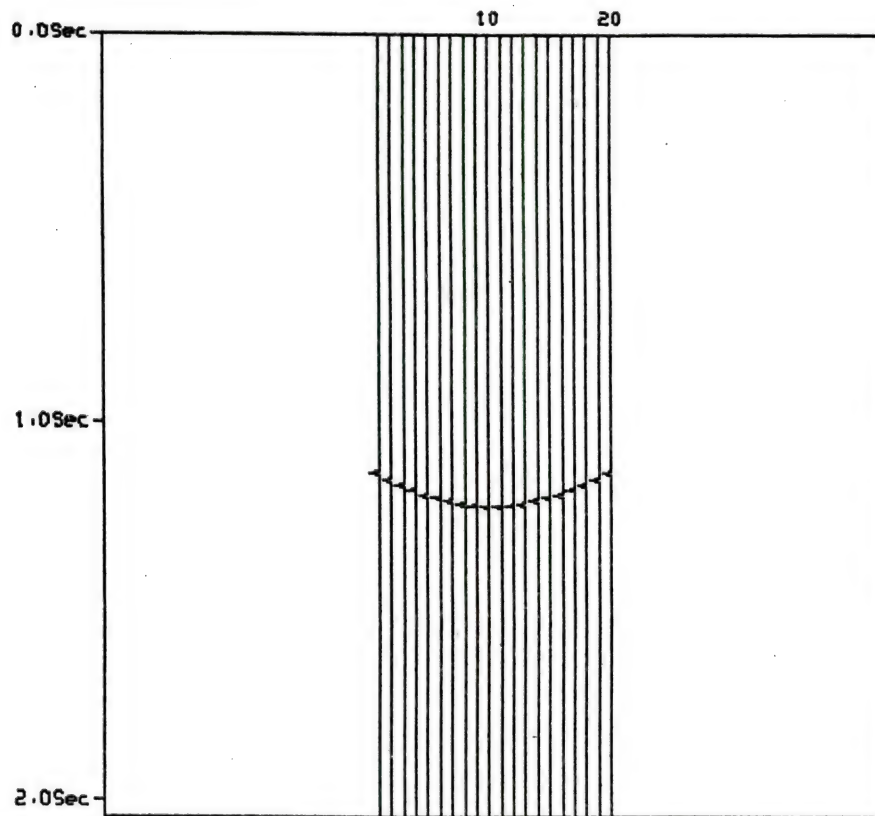


Figure 6.23 Simulated peak seismogram of bright spot
for concave shape, training string $B^2ABA^3o^5a^3bab^2$

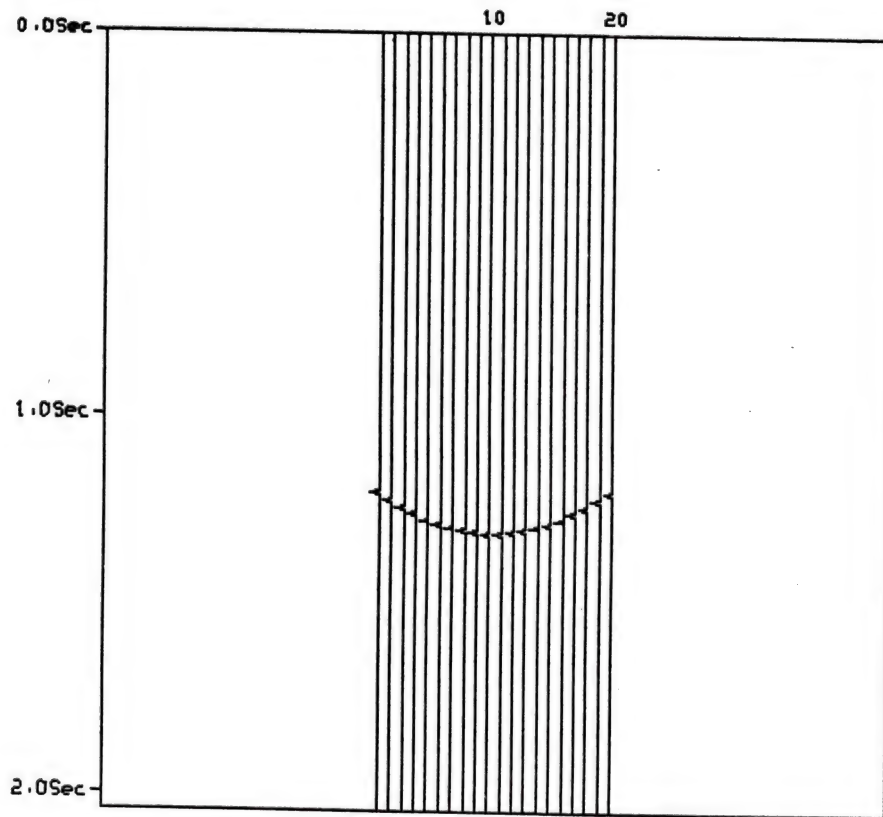


Figure 6.24 Simulated peak seismogram of bright spot
for concave shape, training string $B^4A^3o^5a^3b^4$

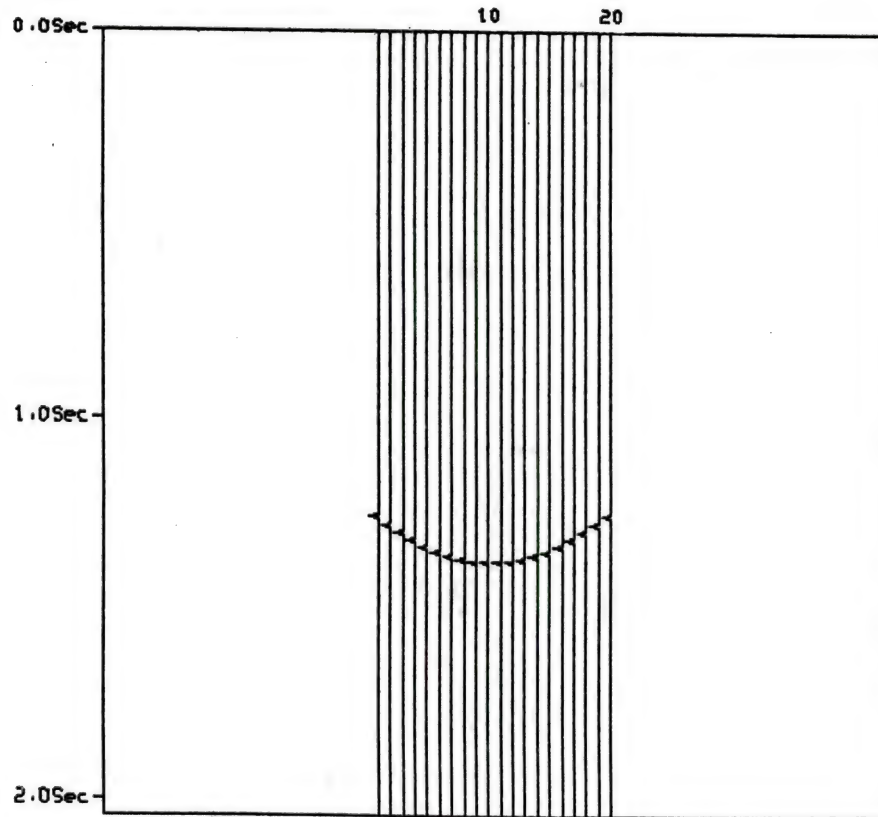


Figure 6.25 Simulated peak seismogram of bright spot
for concave shape, training string $CB^3A^4o^3a^4b^3c$

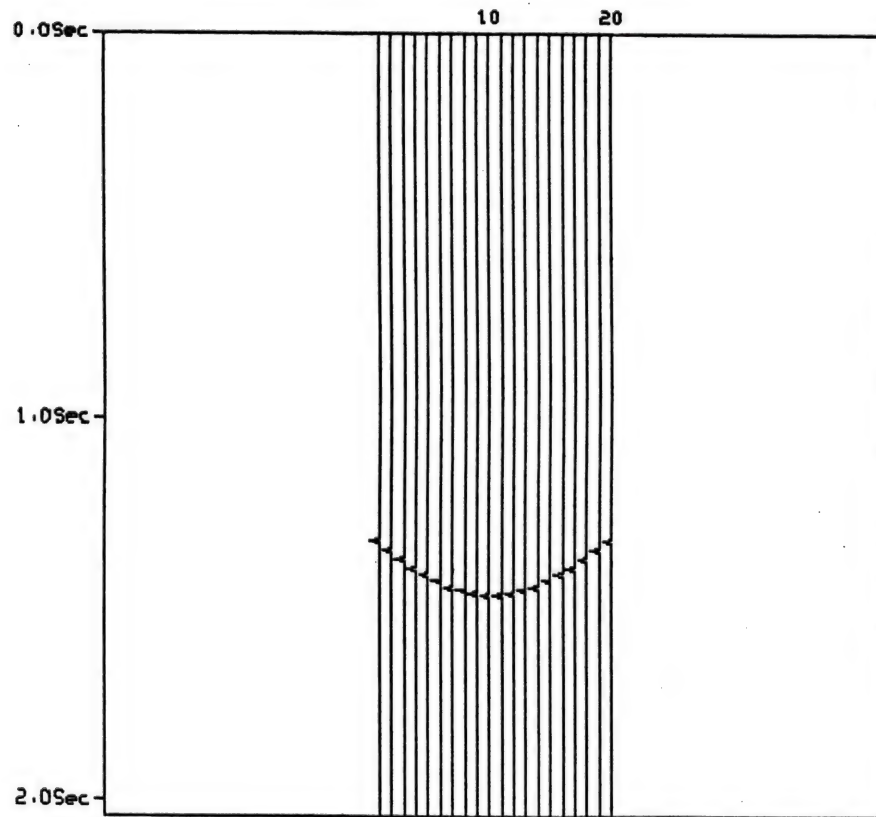


Figure 6.26 Simulated peak seismogram of bright spot
for concave shape, training string $C^3B^3A^2o^3a^2b^3c^3$

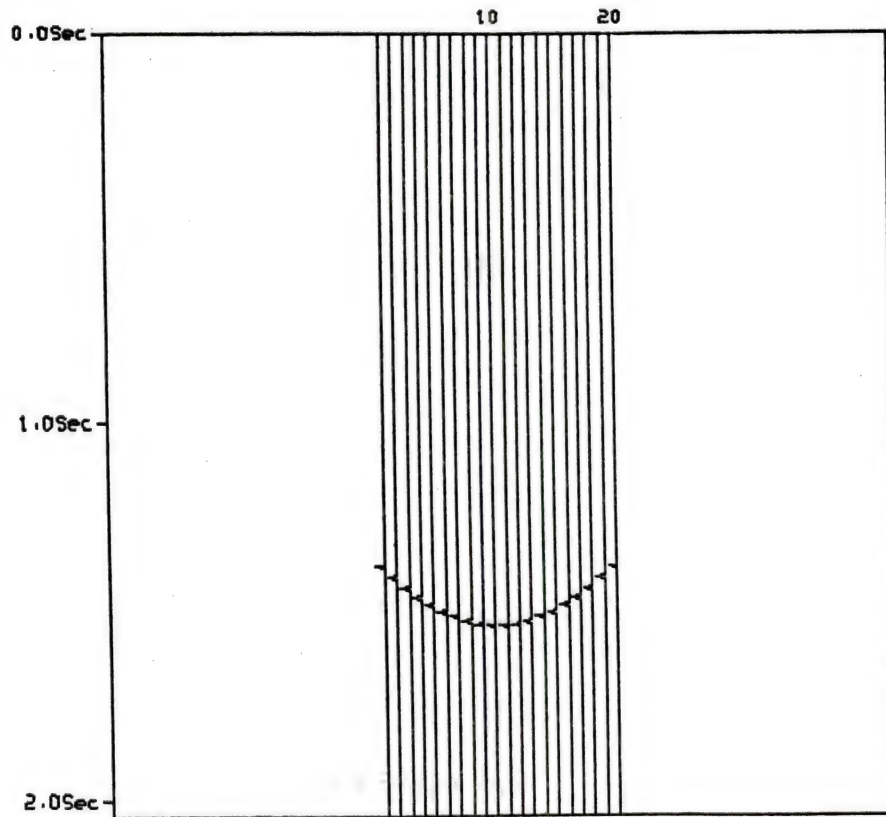


Figure 6.27 Simulated peak seismogram of bright spot
for concave shape, training string $C^3B^2A^3o^3a^2b^3c^3$

(I) Shifted string matching method

Levenshtein distances between the extracted string of candidate bright spot and the training strings of bright spot are calculated. Suppose that the length of a training string of bright spot is N and the length of an extracted string is M . N is larger than or equal to M . Initially, Levenshtein distance is computed between the extracted string of length M and the beginning M symbols of a training string. The distance is d_1 . Because the lengths of the two strings are equal, only substitution errors need to be considered. It is the disadvantage that the deletion and insertion errors are not considered in the string distance computation. Then, Levenshtein distance is computed between the extracted string of length M and the next M symbols of the training string. The distance is d_2 . The shifted interval is 1 symbol. So there are $N-M+1$ distances for the extracted string moving across one training string. Then Levenshtein distances are computed between the extracted string with the next training string until Levenshtein distances between the extracted string and all the training strings are computed. Finally, comparing the calculated Levenshtein distances, and the minimum is selected as the distance between the training strings and the extracted string.

(II) Modified distance computation

In [fu79a], the normalized distance is defined as follows.

$$d_N^L(x, y) = \frac{d(x, y)}{\max[|x|, |y|]}$$

The purpose is to take the variation of pattern size into consideration.

Here a modified distance is defined as

$$d^L(x,y) = d(x,y) - ||x| - |y||$$

where $|x|$ denotes the length or the number of terminal symbols of x . The reason for this definition is to take the difference of the lengths of x and y into consideration. In this study, y may be a substring of x and the length of y is shorter than the length of x . Deletion error due to the difference in lengths of x and y is considered. Levenshtein distance is computed between the extracted string and each training string. The minimum is determined from all the computed Levenshtein distances as the distance between the training strings and the extracted string.

(III) Substring matching computation

In [oom82a], Oommen developes an algorithm which computes the distance between a string and a substring. The string x is divided into all possible individual elements of a certain subset of the contiguous substrings, then Levenshtein distances between all possible substrings of x and substring y are computed. The minimum of the Levenshtein distances is determined as the distance between training string x and substring y .

Oommen's technique can be expanded to match a substring with several strings. Here, the strings are the training strings of bright spot patterns and the substring is the extracted string of a candidate bright spot. The minimum of the Levenshtein distances is determined as the distance between all the training strings and the substring.

6.4.4 Thresholding for the Recognition of Bright Spot String

From Section 6.4.3, the minimum distance between a set of training strings and an extracted string can be calculated. Then, set a threshold $t = \text{rounding off } \frac{N}{3}$. This threshold can be varied due to the classification results from the previous chapters. If the minimum distance is less than or equal to this threshold, then the extracted string is classified as a bright spot. Otherwise, the extracted string is a non-bright spot.

Input the next extracted string and compute the string distance described in Section 6.4.3, until all the extracted strings are tested.

Three flow charts are shown in Fig. 6.28 - Fig. 6.30. Fig. 6.28 uses the method (I), moving technique. Fig. 6.29 uses the method (II), revised distance computation. Fig. 6.30 uses the method (III), strings and substring matching computation.

6.5 Experimental Results

Three seismograms of candidate bright spot, Fig. 6.1, 6.3, and 6.5, are processed. In the real seismogram at Mississippi Canyon and High Island, the distance between two adjacent traces is 25.54 meters, i.e., 64 traces for 1 mile (1.609 Km).

(1) Experiment using simulated seismogram

From Fig. 6.1, using the midpoint of the duration of candidate bright spot, the peak seismogram is shown in Fig. 6.31. From Fig. 6.32, the extracted string is *aaaaxaooooooooAAxAAA*. The 19 training strings from Section 6.4.2 are used. The computations follow the flow charts of

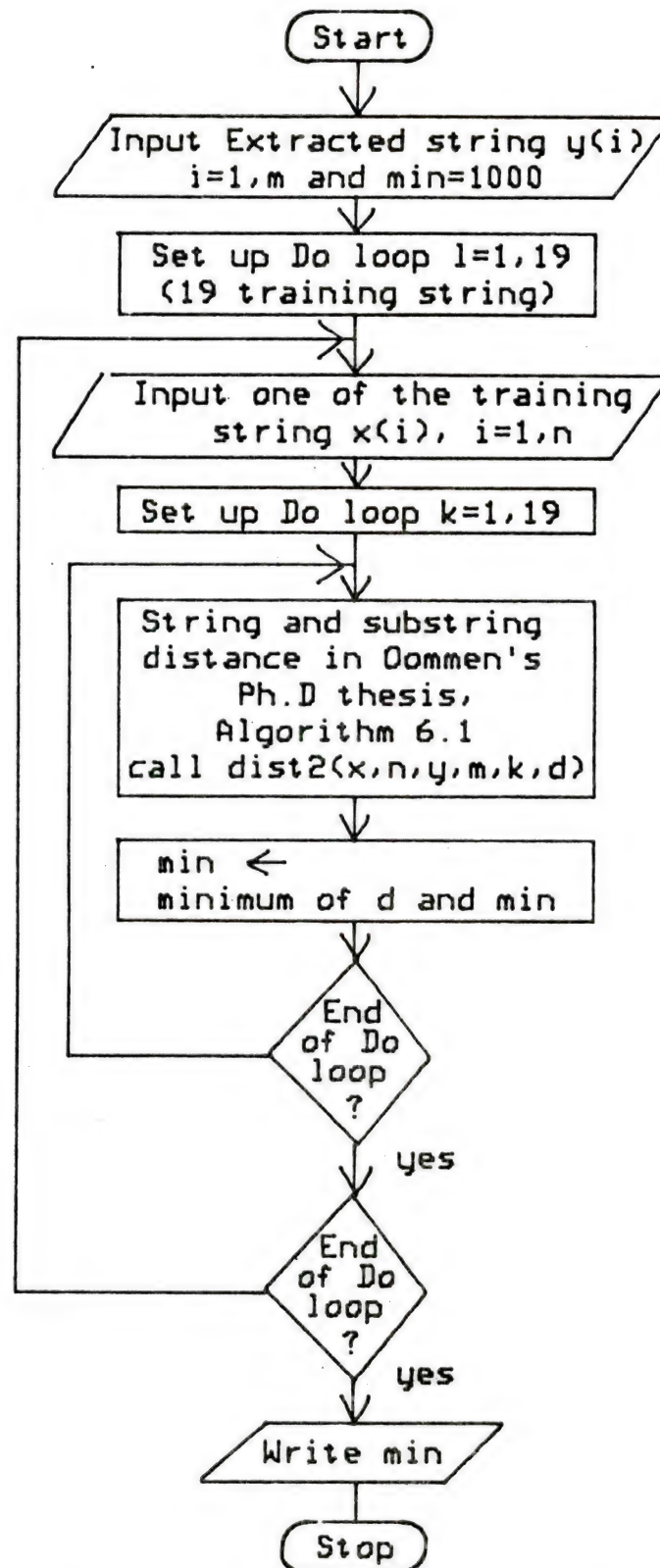


Figure 6.28 Flow chart of method (I)

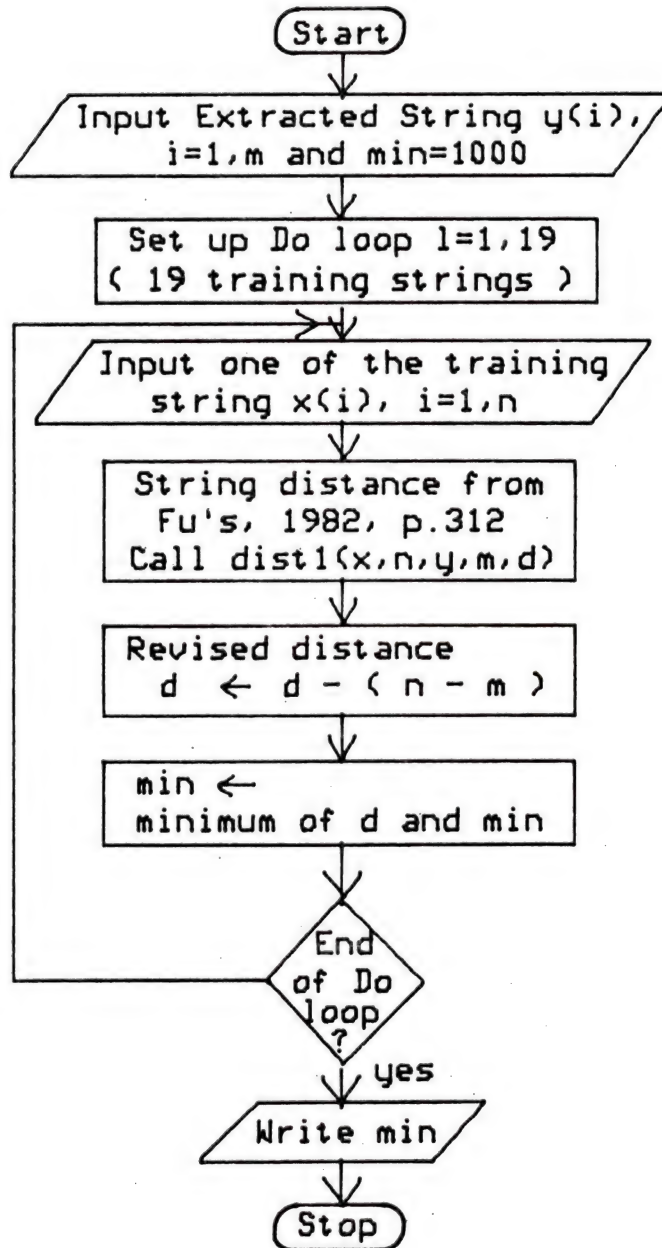


Figure 6.29 Flow chart of method (II)

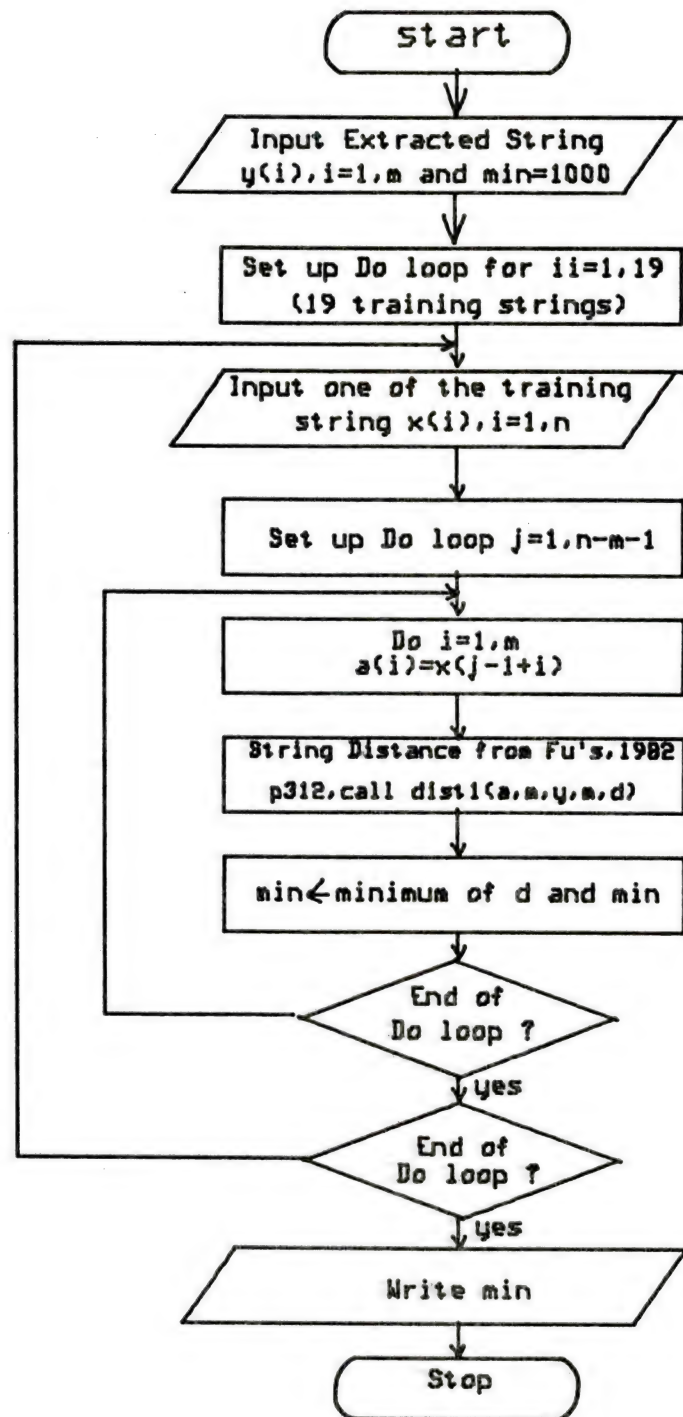


Figure 6.30 Flow chart of method (III)

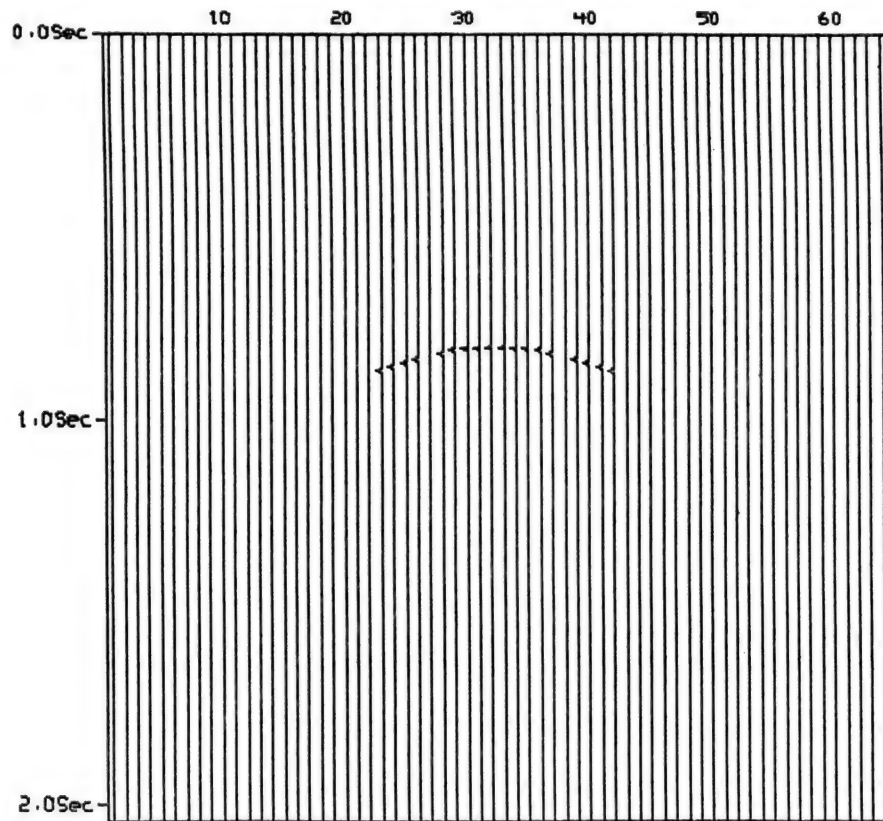


Figure 6.31 Peak seismogram of Figure 6.1

Station

21222324252627282930313233343536373839404142434445

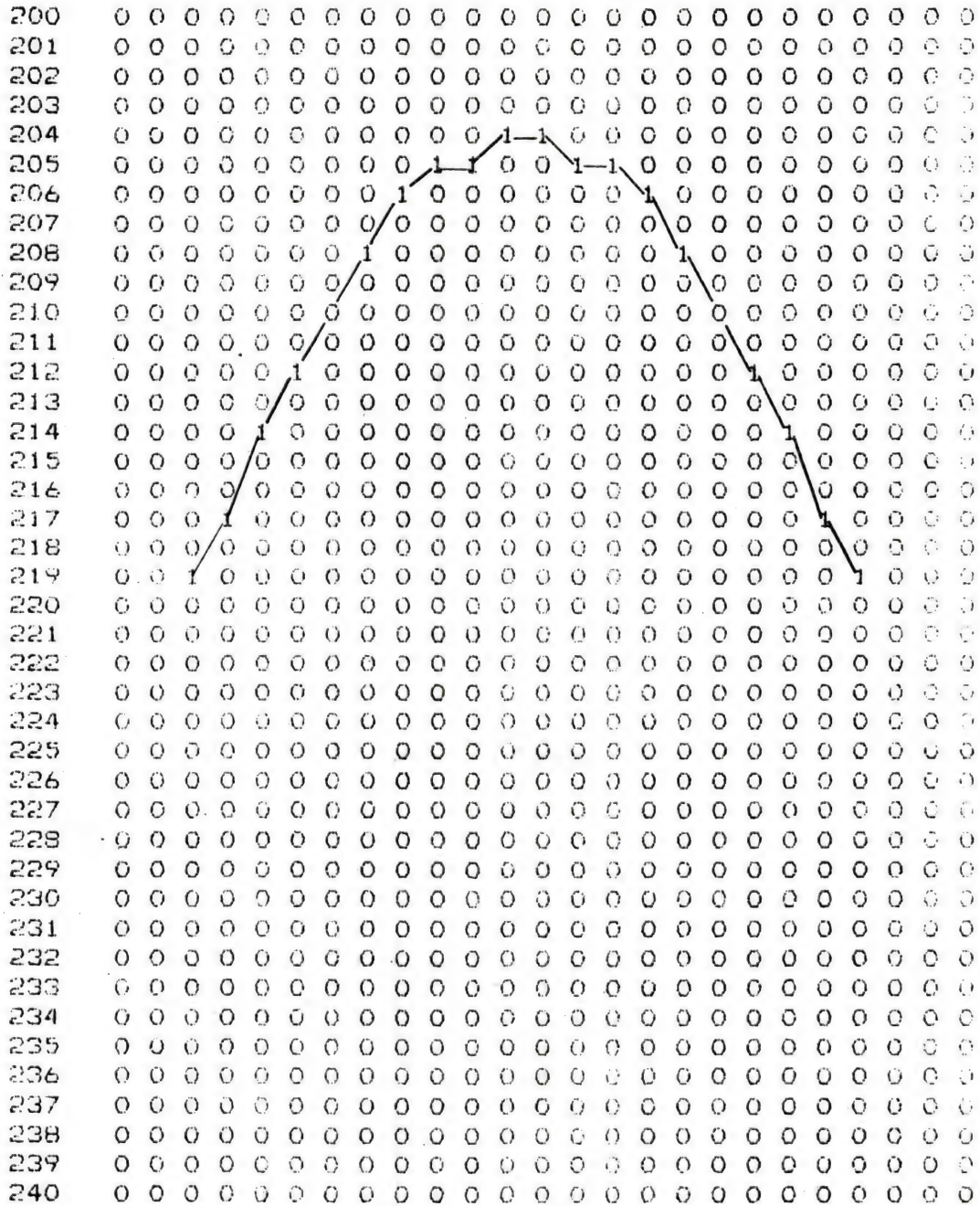


Figure 6.32 Extracted string, $a^4xao^7A^2xA^3$, from simulated seismogram

Fig. 6.28, 6.29, and 6.30. Using method (I) (Fig. 6.28) the lengths of the extracted string and the 19 training strings are equal, there is no moving for the extracted string. Levenshtein distance is computed between each training string and the extracted string. The minimum is selected from the 19 Levenshtein distances and is the distance between the training strings and the extracted string. The minimum distance is 3. Using method (II) (Fig. 6.29) the minimum distance is 3. Using method (III) (Fig. 6.30) the minimum distance is 2. Threshold is set as $t = \text{rounding off } \frac{19}{3} = 6$. Distance 2 or 3 is less than the threshold 6. So the extracted string is recognized as a bright spot. Comparing the results from the three methods, the minimum distance 2 using method (III) is the shortest.

(II) Experiment using the data from Mississippi Canyon

From Fig. 6.5, using the midpoint of the duration of candidate bright spot, the peak seismogram is shown in Fig. 6.33. From Fig. 6.34, four extracted strings are *oxo*, *ooxoxzooooooooxoooo*, *ooo*, *ooooooooxo*.

For the first string *oxo*, using method (I), the minimum distance is 1. Using method (II), the minimum distance is 1. Using method (III), the minimum distance is 1. Threshold is set as $t = \text{rounding off } \frac{3}{3} = 1$. So the first string is recognized as a bright spot.

For the second string *ooxoxzooooooooxoooo*, using method (I), the minimum distance is 4. Using method (II), the minimum distance is 4. Using method (III), the minimum distance is 4. Threshold is set as $t = \text{rounding off } \frac{16}{3} = 5$. So the second string is recognized as a bright spot.

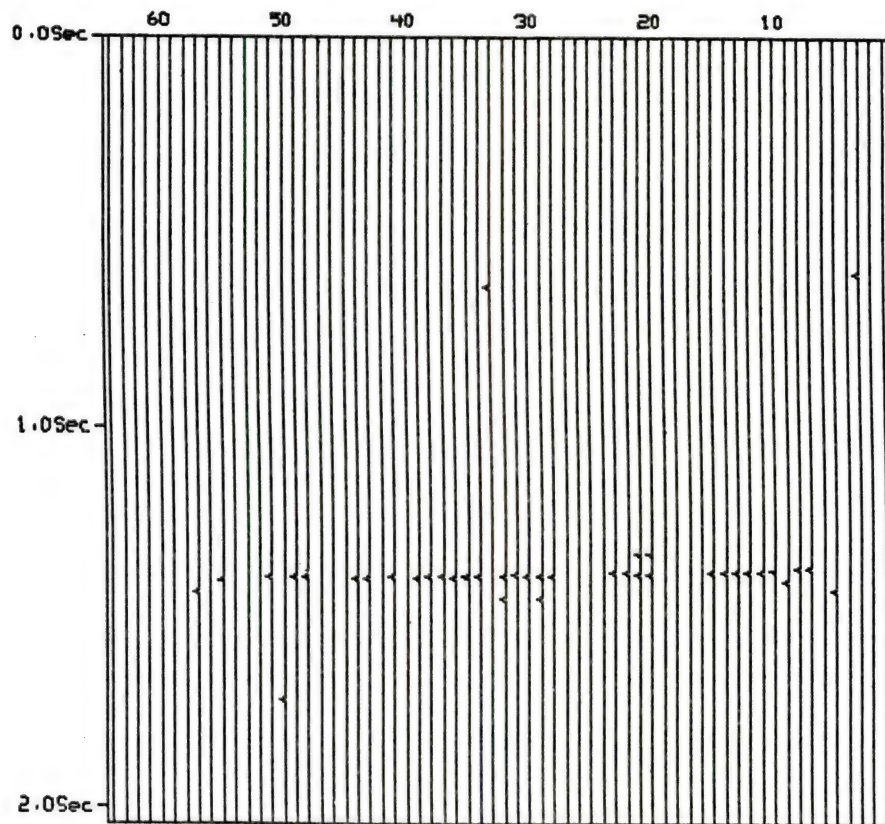


Figure 6.33 Peak seismogram of Figure 6.5

Station																	
		6	0	5	9	5	8	5	7	5	6	5	5	5	4	5	3
		5	2	5	1	5	0	4	9	4	8	4	7	4	6		
330		0	0	0	0	0	0	0	0	0	0	0	0	0	0	0	0
331		0	0	0	0	0	0	0	0	0	0	0	0	0	0	0	0
332		0	0	0	0	0	0	0	0	0	0	0	0	0	0	0	0
333		0	0	0	0	0	0	0	0	0	0	0	0	0	0	0	0
334		0	0	0	0	0	0	0	0	0	0	0	0	0	0	0	0
335		0	0	0	0	0	0	0	0	0	0	0	0	0	0	0	0
336		0	0	0	0	0	0	0	0	0	0	0	0	0	0	0	0
337		0	0	0	0	0	0	0	0	0	0	0	0	0	0	0	0
338		0	0	0	0	0	0	0	0	0	0	0	0	0	0	0	0
339		0	0	0	0	0	0	0	0	0	0	0	0	0	0	0	0
340		0	0	0	0	0	0	0	0	0	0	0	0	0	0	0	0
341		0	0	0	0	0	0	0	0	0	0	0	0	0	0	0	0
342		0	0	0	0	0	0	0	0	0	0	0	0	0	0	0	0
343		0	0	0	0	0	0	0	0	0	0	0	0	0	0	0	0
344		0	0	0	0	0	0	0	0	0	0	0	0	0	0	0	0
345		0	0	0	0	0	0	0	0	0	0	0	0	0	0	0	0
346		0	0	0	0	0	0	0	0	0	0	0	0	0	0	0	0
347		0	0	0	0	0	0	0	0	0	0	0	0	0	0	0	0
348		0	0	0	0	0	0	0	0	0	0	0	0	0	0	0	0
349		0	0	0	0	0	0	0	0	0	0	0	0	0	0	0	0
350		0	0	0	0	0	0	0	0	0	1	0	1	1	0	0	0
351		0	0	0	0	0	0	0	0	0	0	0	0	0	0	0	0
352		0	0	0	0	0	1	0	0	0	0	0	0	0	0	0	0
353		0	0	0	0	0	0	0	0	0	0	0	0	0	0	0	0
354		0	0	0	0	0	0	0	0	0	0	0	0	0	0	0	0
355		0	0	0	0	0	0	0	0	0	0	0	0	0	0	0	0
356		0	0	0	0	0	0	0	0	0	0	0	0	0	0	0	0
357		0	0	0	0	0	0	0	0	0	0	0	0	0	0	0	0
358		0	0	0	0	0	0	0	0	0	0	0	0	0	0	0	0
359		0	0	0	0	0	0	0	0	0	0	0	0	0	0	0	0
360		0	0	0	1	0	0	0	0	0	0	0	0	0	0	0	0
361		0	0	0	0	0	0	0	0	0	0	0	0	0	0	0	0
362		0	0	0	0	0	0	0	0	0	0	0	0	0	0	0	0
363		0	0	0	0	0	0	0	0	0	0	0	0	0	0	0	0
364		0	0	0	0	0	0	0	0	0	0	0	0	0	0	0	0
365		0	0	0	0	0	0	0	0	0	0	0	0	0	0	0	0
366		0	0	0	0	0	0	0	0	0	0	0	0	0	0	0	0
367		0	0	0	0	0	0	0	0	0	0	0	0	0	0	0	0
368		0	0	0	0	0	0	0	0	0	0	0	0	0	0	0	0
369		0	0	0	0	0	0	0	0	0	0	0	0	0	0	0	0
370		0	0	0	0	0	0	0	0	0	0	0	0	0	0	0	0

Figure 6.34 Four extracted strings, oxo , $o^2xor^2o^5xo^4$, o^3 , o^6xo , from the data at Mississippi Canyon

Figure 6.34 Continued

Station

	24	23	22	21	20	19	18	17	16	15	14	13	12	11	10	9	8	7	6	5	4	3	2	1
330	0	0	0	0	0	0	0	0	0	0	0	0	0	0	0	0	0	0	0	0	0	0	0	0
331	0	0	0	0	0	0	0	0	0	0	0	0	0	0	0	0	0	0	0	0	0	0	0	0
332	0	0	0	0	0	0	0	0	0	0	0	0	0	0	0	0	0	0	0	0	0	0	0	0
333	0	0	0	0	0	0	0	0	0	0	0	0	0	0	0	0	0	0	0	0	0	0	0	0
334	0	0	0	0	0	0	0	0	0	0	0	0	0	0	0	0	0	0	0	0	0	0	0	0
335	0	0	0	0	0	0	0	0	0	0	0	0	0	0	0	0	0	0	0	0	0	0	0	0
336	0	0	0	1	-1	0	0	0	0	0	0	0	0	0	0	0	0	0	0	0	0	0	0	0
337	0	0	0	0	0	0	0	0	0	0	0	0	0	0	0	0	0	0	0	0	0	0	0	0
338	0	0	0	0	0	0	0	0	0	0	0	0	0	0	0	0	0	0	0	0	0	0	0	0
339	0	0	0	0	0	0	0	0	0	0	0	0	0	0	0	0	0	0	0	0	0	0	0	0
340	0	0	0	0	0	0	0	0	0	0	0	0	0	0	0	0	0	0	0	0	0	0	0	0
341	0	0	0	0	0	0	0	0	0	0	0	0	0	0	0	0	0	0	0	0	0	0	0	0
342	0	0	0	0	0	0	0	0	0	0	0	0	0	0	0	0	0	0	0	0	0	0	0	0
343	0	0	0	0	0	0	0	0	0	0	0	0	0	0	0	0	0	0	0	0	0	0	0	0
344	0	0	0	0	0	0	0	0	0	0	0	0	0	0	0	0	0	0	0	0	0	0	0	0
345	0	0	0	0	0	0	0	0	0	0	0	0	0	0	0	0	1	-1	0	0	0	0	0	0
346	0	0	0	0	0	0	0	0	0	0	0	0	0	0	0	0	0	0	0	0	0	0	0	0
347	0	0	0	0	0	0	0	0	0	0	0	0	0	0	0	1	0	0	0	0	0	0	0	0
348	0	1	-1	0	0	0	0	0	0	1	-1	-1	-1	-1	0	0	0	0	0	0	0	0	0	0
349	0	0	0	1	-1	0	0	0	0	0	0	0	0	0	0	0	0	0	0	0	0	0	0	0
350	0	0	0	0	0	0	0	0	0	0	0	0	0	0	0	0	0	0	0	0	0	0	0	0
351	0	0	0	0	0	0	0	0	0	0	0	0	0	0	0	0	0	0	0	0	0	0	0	0
352	0	0	0	0	0	0	0	0	0	0	0	0	0	0	0	0	0	0	0	0	0	0	0	0
353	0	0	0	0	0	0	0	0	0	0	0	0	0	0	0	0	0	0	0	0	0	0	0	0
354	0	0	0	0	0	0	0	0	0	0	0	0	0	0	0	0	1	0	0	0	0	0	0	0
355	0	0	0	0	0	0	0	0	0	0	0	0	0	0	0	0	0	0	0	0	0	0	0	0
356	0	0	0	0	0	0	0	0	0	0	0	0	0	0	0	0	0	0	0	0	0	0	0	0
357	0	0	0	0	0	0	0	0	0	0	0	0	0	0	0	0	0	0	0	0	0	0	0	0
358	0	0	0	0	0	0	0	0	0	0	0	0	0	0	0	0	0	0	0	0	0	0	0	0
359	0	0	0	0	0	0	0	0	0	0	0	0	0	0	0	0	0	0	0	0	0	0	0	0
360	0	0	0	0	0	0	0	0	0	0	0	0	0	0	0	0	0	0	0	0	0	0	0	0
361	0	0	0	0	0	0	0	0	0	0	0	0	0	0	0	0	0	0	0	0	0	0	0	0
362	0	0	0	0	0	0	0	0	0	0	0	0	0	0	0	0	0	0	0	0	0	0	0	0
363	0	0	0	0	0	0	0	0	0	0	0	0	0	0	0	0	0	0	0	0	0	0	0	0
364	0	0	0	0	0	0	0	0	0	0	0	0	0	0	0	0	0	0	0	0	0	0	0	0
365	0	0	0	0	0	0	0	0	0	0	0	0	0	0	0	0	0	0	0	0	0	0	0	0
366	0	0	0	0	0	0	0	0	0	0	0	0	0	0	0	0	0	0	0	0	0	0	0	0
367	0	0	0	0	0	0	0	0	0	0	0	0	0	0	0	0	0	0	0	0	0	0	0	0
368	0	0	0	0	0	0	0	0	0	0	0	0	0	0	0	0	0	0	0	0	0	0	0	0
369	0	0	0	0	0	0	0	0	0	0	0	0	0	0	0	0	0	0	0	0	0	0	0	0
370	0	0	0	0	0	0	0	0	0	0	0	0	0	0	0	0	0	0	0	0	0	0	0	0

Figure 6.34 Continued

For the third string *ooo*, using method (I), the minimum distance is 0. Using method (II), the minimum distance is 0. Using method (III), the minimum distance is 0. Threshold is set as $t = \text{rounding off } \frac{3}{3} = 1$. So the third string is recognized as a bright spot.

For the fourth string *oooooooo*, using method (I), the minimum distance is 1. Using method (II), the minimum distance is 1. Using method (III), the minimum distance is 1. Threshold is set as $t = \text{rounding off } \frac{8}{3} = 3$. So the fourth string is recognized as a bright spot.

The four extracted strings at Mississippi Canyon are all recognized as bright spots.

(III) Experiment using the data from High Island

From Fig. 6.3, using the midpoint of the duration of candidate bright spot, the peak seismogram is shown in Fig. 6.35. From Fig. 6.36, the extracted string is *ooxoooooooo*. Using method (I), the minimum distance is 1. Using method (II), the minimum distance is 1. Using method (III), the minimum distance is 1. Threshold is set as $t = \text{rounding off } \frac{11}{3} = 4$. So the extracted string is recognized as a bright spot.

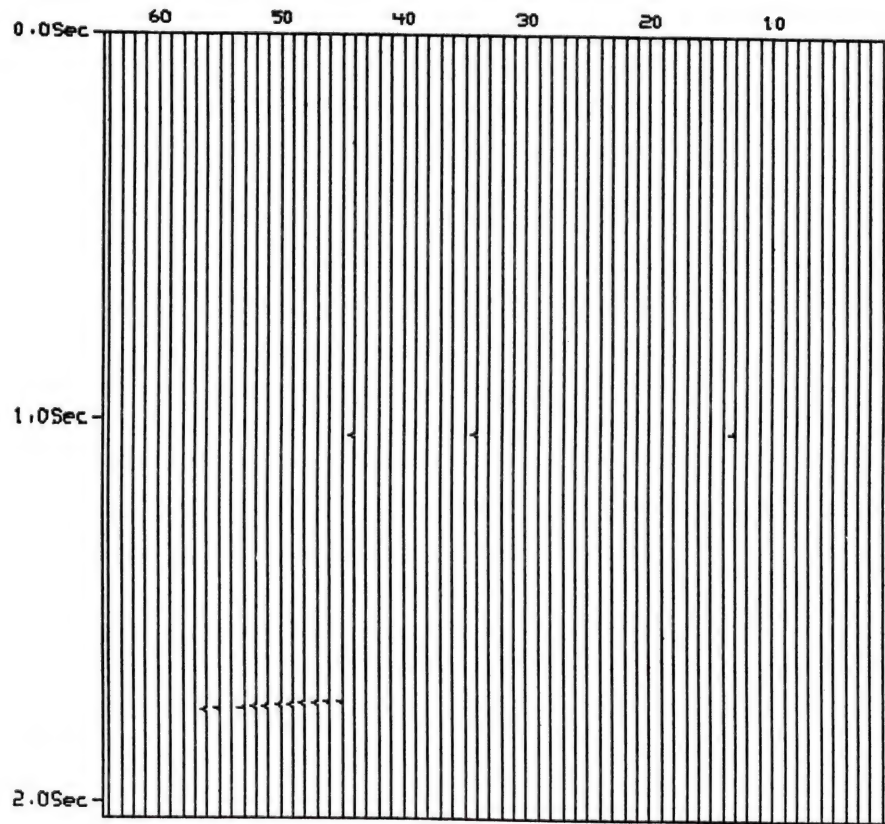


Figure 6.35 Peak seismogram of Figure 6.3

Station

6059585756555453525150494847464544434241

410	0	0	0	0	0	0	0	0	0	0	0	0	0	0	0	0	0	0	0
411	0	0	0	0	0	0	0	0	0	0	0	0	0	0	0	0	0	0	0
412	0	0	0	0	0	0	0	0	0	0	0	0	0	0	0	0	0	0	0
413	0	0	0	0	0	0	0	0	0	0	0	0	0	0	0	0	0	0	0
414	0	0	0	0	0	0	0	0	0	0	0	0	0	0	0	0	0	0	0
415	0	0	0	0	0	0	0	0	0	0	0	0	0	0	0	0	0	0	0
416	0	0	0	0	0	0	0	0	0	0	0	0	0	0	0	0	0	0	0
417	0	0	0	0	0	0	0	0	0	0	0	0	0	0	0	0	0	0	0
418	0	0	0	0	0	0	0	0	0	0	0	0	0	0	0	0	0	0	0
419	0	0	0	0	0	0	0	0	0	0	0	0	0	0	0	0	0	0	0
420	0	0	0	0	0	0	0	0	0	0	0	0	0	0	0	0	0	0	0
421	0	0	0	0	0	0	0	0	0	0	0	0	0	0	0	0	0	0	0
422	0	0	0	0	0	0	0	0	0	0	0	0	0	0	0	0	0	0	0
423	0	0	0	0	0	0	0	0	0	0	0	0	0	0	0	0	0	0	0
424	0	0	0	0	0	0	0	0	0	0	0	0	0	0	0	0	0	0	0
425	0	0	0	0	0	0	0	0	0	0	0	0	0	0	0	0	0	0	0
426	0	0	0	0	0	0	0	0	0	0	0	0	0	0	0	0	0	0	0
427	0	0	0	0	0	0	0	0	0	0	0	0	0	0	0	0	0	0	0
428	0	0	0	0	0	0	0	0	0	0	0	0	0	0	0	0	0	0	0
429	0	0	0	0	0	0	0	0	0	0	0	0	0	0	0	0	0	0	0
430	0	0	0	0	0	0	0	0	0	0	0	0	0	0	0	0	0	0	0
431	0	0	0	0	0	0	0	0	0	0	0	0	0	0	0	0	0	0	0
432	0	0	0	0	0	0	0	0	0	0	0	0	0	0	0	0	0	0	0
433	0	0	0	0	0	0	0	0	0	0	0	0	0	0	0	0	0	0	0
434	0	0	0	0	0	0	0	0	0	0	0	0	0	0	0	0	0	0	0
435	0	0	0	0	0	0	0	0	0	0	0	0	0	0	0	0	0	0	0
436	0	0	0	0	0	0	0	0	0	0	0	0	0	0	0	0	0	0	0
437	0	0	0	0	0	0	0	0	0	0	0	0	0	0	0	0	0	0	0
438	0	0	0	0	0	0	0	0	0	0	0	0	0	0	0	0	0	0	0
439	0	0	0	0	0	0	0	0	0	0	0	0	0	0	0	0	0	0	0
440	0	0	0	0	0	0	0	0	0	0	0	0	0	0	0	0	0	0	0
441	0	0	0	0	0	0	0	0	0	0	0	0	0	0	0	0	0	0	0
442	0	0	0	0	0	0	0	0	0	0	0	0	0	0	0	0	0	0	0
443	0	0	0	0	0	0	0	0	0	0	0	0	0	0	0	0	0	0	0
444	0	0	0	0	0	0	0	0	0	0	0	0	0	0	0	0	0	0	0
445	0	0	0	0	0	0	0	0	0	0	0	0	0	0	0	0	0	0	0
446	0	0	0	0	0	0	0	0	0	0	0	0	0	0	0	0	0	0	0
447	0	0	0	0	0	0	0	0	0	0	0	0	0	0	0	0	0	0	0
448	0	0	0	0	0	0	0	0	0	0	0	0	0	0	0	0	0	0	0
449	0	0	0	0	0	0	0	0	0	0	0	0	0	0	0	0	0	0	0
450	0	0	0	0	0	0	0	0	0	0	0	0	0	0	0	0	0	0	0

Figure 6.36 Extracted string, o^2zo^8 , from the data at High Island

6.6 Discussions

(1) The length and the threshold in the local and global testing patterns can be varied. The distance between two adjacent traces is considered in the determination of the length and the threshold of the pattern. Interpolation techniques may be used in the interpolation of the traces. The threshold may be changed.

(2) Each detected candidate bright spot pattern has about 10 samples. From the real seismogram in this study, the wavelets of a bright spot are horizontally continuous. So horizontal line pattern is used for local and global pattern tests. But the method is only useful for very limited cases.

(3) Syntactic pattern recognition technique can be used to recognize the reflector of a bright spot.

(4) The difference of the vertical coordinates of two successive peaks is not larger than 7 intervals (sampling interval is 0.004 seconds) in this study.

(5) The 20 traces of a bright spot pattern and the 19 simulated seismograms generated as the training patterns of bright spot can be used to handle the bright spot patterns of which the number of traces is less than or equal to 20. If the number of traces of a candidate bright spot is larger than 20, then simulated seismograms with more than 20 traces need to be generated.

(6) From the experimental results, the extracted strings from the real data at Mississippi Canyon and High Island are recognized as bright spots.

CHAPTER VII

SUMMARY AND RECOMMENDATIONS

7.1 Summary

We have studied the application of decision-theoretic and syntactic pattern recognition techniques to the detection of bright spot. The difficulty of applying pattern recognition techniques in this study lies in the feature extraction. Analytic signal analysis can extract the features from the original signal. In decision-theoretic pattern recognition, our studies concentrate on the extraction of physical properties. In syntactic pattern recognition, our studies concentrate on the structural information of waveform pattern.

We may summarize this study as follows:

(1) Decision-theoretic and syntactic pattern recognition techniques are used for the classification of Ricker wavelets and the detection of candidate bright spot.

(2) Analytic signal analysis can be used to extract envelope, instantaneous frequency, and polarity as the features.

(3) From the analysis of zero-phase Ricker wavelets, tree classification is adopted. Using the structural information of string wavelets, syntactic pattern recognition for bright spot detection is established.

(4) Three hypotheses are proposed as the constrained conditions to detect the candidate bright spot in the tree classification.

(5) In syntactic pattern recognition, the roles of likelihood ratio test, optimal quantization encoding, and the probability of detecting signal involving in the global and local detection, and the threshold setting to detect the candidate bright spot are quite important.

(6) Spatial relation in a two dimensional seismogram can be used to test the continuity of reflection layer and remove the singular patterns.

(7) Syntactic pattern recognition technique can be used to recognize the string representation of a bright spot pattern in a two dimensional seismogram. Three kinds of string distance computation are proposed.

(8) In simulation and real data experiments, the classification results can be used to improve seismic interpretation and provide a reference for the prediction of gas accumulation.

(9) In real applications, if physical properties of the waveform pattern are separable, (i.e., envelope is higher than 0.15 and the difference of the instantaneous frequencies of the two class centers for bright spot and non-bright spot is larger than 3.0 Hz) the result of tree classification is good. If the instantaneous frequency is not separable, then the result from syntactic pattern recognition is better.

It is known that the bright spot technique (predicting by the high amplitude portion of the reflection) has had 70 percent success [flo76a] in locating gas accumulations in offshore Nigeria, Indonesia, and the United States Gulf Coast. It should be interesting to use the proposed tree classification techniques and syntactic pattern recognition techniques to detect the bright spot and, hopefully, to increase the success

of future utilizations of bright spot technique.

7.2 Recommendation

The following problems are recommended for further investigation:

(1) In Chapter 3, zero-phase and minimum-phase wavelets are decided by geophysicist, an automatic method to determine the dominant wavelet is necessary. Waveform shaping filter can be used to change the wavelet to zero-phase Ricker wavelet, then a tree classifier is easy to design.

(2) In Chapter 6, an automatic method to link peaks as a string should be developed.

(3) The application of pattern recognition techniques to the recognition of other patterns in the seismogram, for example, flat spot pattern, pinchout pattern, . . . , etc [dob76a, pan70a, pay77a, she74a, she75a, she76a] should be an interesting research project.

(4) Analytic signal analysis has produced a certain number of features useful in seismic pattern recognition; by using image processing techniques, new features may be extracted that could improve the pattern recognition results.

(5) The synthetic seismogram may be generated by using sophisticated methods. When diffraction, reflection and refraction patterns are included in the synthetic seismogram, the application of pattern recognition techniques to seismic analysis should be a challenging work.

(6) The two dimensional pattern of gas reflection is affected by the velocity above the gas sand zone. Velocity effect may be considered in the syntactic approach.

LIST OF REFERENCES

- [and78a] Anderson, K.R., "Automatic analysis of microearthquake network data," *Geoexploration*, vol. 16, 1978, pp.159-175.
- [and82a] Anderson, Kenneth R., "Syntactic analysis of seismic waveforms using augmented transition network grammars," *Geoexploration*, vol.20, 1982, pp.161-182.
- [blo76a] Bloomfield, P., *Fourier Analysis of Time Series: An Introduction*, New York, Wiley, 1976, ch.5.
- [boi80a] Bois, P., "Autoregressive pattern recognition applied to the delimitation of oil and gas reservoirs," *Geophysical Prospecting*, Vol. 28, pp. 572-591, 1980.
- [boi81a] Bois, P., "Reservoir recognition in petroleum prospection considered as an application of close man-machine communication," Proceedings of the 2nd International Symposium on Computer Aided Seismic Analysis and Discrimination, 1981, pp. 42-47.
- [boi81b] Bois, P., "Determination of the nature of reservoirs by use of pattern recognition algorithm with prior learning," *Geophysical Prospecting*, vol.29, 1981, pp.687-701.
- [boi82a] Bois, P., "Some comments on the application of pattern recognition to oil and gas exploration," *Geoexploration*, vol.20, 1982, pp.147-159.
- [bra78a] Bracewell, R. N., *The Fourier Transform and Its Applications*, New York, McGraw-Hill Book Co., Inc., 1978, pp.336-337.
- [car81a] Carpenter, E.W., "Absorption of elastic waves - an operator for a constant Q mechanism," UK Atom. Ener. Auth. AWRE Rep.0-43, 1966.
- [che77a] Chen, C. H., "Seismic pattern recognition," Proc. Intl. Symp. on Computer-Aided Seismic Analysis and Discrimination, June 9-10, 1977, IEEE No. 77CH1244-3C.
- [che78a] Chen, C.H., "Seismic pattern recognition," *Geoexploration*, vol. 16, no. 1/2, 1978, pp. 133-146.
- [che82a] Chen, C.H., "A review of geophysical signal analysis and recognition," Proceedings of the 2nd International Symposium on Computer Aided Seismic Analysis and Discrimination, 1981, pp. 144-152.

- [che83a] Chen, C.H., "Pattern analysis of acoustical and seismic events," Proceedings of the Third International Symposium on Computer-Aided Seismic Analysis and Discrimination, The Catholic University of America, Washington, D.C., June 15-17, 1983, pp.114-118.
- [cra67a] Cramer, Harold, and Leadbetter, M. R., *Stationary and Related Stochastic Processes*, J. Wiley and Sons, 1967, Ch.14.
- [dob76a] Dobrin, Milton B., *Introduction to Geophysical Prospecting*, Third Edition, McGraw-Hill, Inc. 1976, Chapter 10.
- [far75a] Farnback, J. S., "The complex envelope in seismic signal analysis," Bull. Seismol. Soc. Amer., 1975, vol.65, pp.951-962.
- [flo76a] Flowers, B. S., "Overview of exploration geophysics - recent breakthrough and challenging new problems," *Bulletin of American Association of Petroleum Geologists*, Vol.60, pp. 3-11, 1976.
- [fra69a] Franks, L. E., *Signal Theory*, Prentice-Hall, Inc., Englewood Cliffs, New Jersey, 1969, ch.4.
- [fu74a] Fu, K.S., *Syntactic Methods in Pattern Recognition*, Academic Press, New York, 1974.
- [fu79a] Fu, K. S. and Lu, S. Y., "Size normalization and pattern orientation problems," *IEEE Transactions on Systems, Man, and Cybernetics*, Vol.SMC-9, No.1, January 1979, pp.55-58.
- [fu82a] Fu, K. S., *Syntactic Pattern Recognition and Applications*, Prentice-Hall, Inc., Englewood Cliffs, New Jersey, 1982.
- [fuk72a] Fukunaga, K., *Introduction to Statistical Pattern Recognition*, Academic Press, New York, 1972.
- [fut62a] Futterman, W.I., "Dispersive body waves," *Journal of Geophysical Research*, vol.67, no.13, 1962, pp.5279-5291.
- [gab46a] Gabor, D., "Theory of communication," *J. Inst. Elect. Eng.*, Vol. 93, part III, 1946, pp.429-441.
- [gab83a] Gaby, J.E. and Anderson, K.R., "Using affinity to derive the morphological structure of seismic signals," Proceedings of the Third International Symposium on Computer-Aided Seismic Analysis and Discrimination, The Catholic University of America, Washington, D.C., June 15-17, 1983, pp.20-28.
- [gag78a] Gagliardi, Robert M., *Introduction to Communications Engineering*, John Wiley & Sons, Inc., 1978, pp.485-490.
- [gar64a] Gardner, G.H.F., Wyllie, M.R.J., and Droschak, D.M., "Effects of pressure and fluid saturation on the attenuation of elastic waves in sands," *Journal of Petroleum Technology*, Feb, 1964, pp.189-198.

- [gar74a] Gardner, G.H.F., Gardner, L.W., and Gregory, A.R., "Formation velocity and density - the diagnostic basics for stratigraphic traps," *Geophysics*, vol.39, 1974, pp.770-780.
- [gol69a] Gold, B., Oppenheim, V., and Rader, C. M., "Theory and implementation of the discrete Hilbert transform," *Proc. Sym. Computer Processing in Communications*, 1969, pp.235-250.
- [hag81a] Hagen, David C., "The application of principal components analysis to seismic data sets", *Proceedings of the 2nd International Symposium on Computer Aided Seismic Analysis and Discrimination*, 1981, pp.98-109.
- [ham72a] Hamilton, Edwin L., "Compressional-wave attenuation in marine sediments," *Geophysics*, vol.37, 1972, pp.620-646.
- [hin82a] Hinich, M. J., "Detecting a hidden periodic signal when its period is unknown," *IEEE Transactions on Acoustics, Speech, and Signal Processing*, Vol. ASSP-30, NO. 5. October 1982, pp.747-750.
- [hor75a] Horowitz, Steven L., "A syntactic algorithm for peak detection in waveforms with applications to cardiograph," *Comm. ACM*, Vol.18, No.5, May 1975, pp.281-285.
- [hor77a] Horowitz, S.L., "Peak recognition in waveforms," in *Syntactic Pattern Recognition Application*, ed. by Fu, K.S., Springer-Verlag, 1977, pp.31-49.
- [hua80a] Huang, Kou-Yuan "Analytic signal representation in the synthetic seismogram of bright spots," Master Thesis, Purdue University, 1980, LARS Technical Report 081280 & TR-EE 80-36.
- [hua81a] Huang, K. Y., McGillem, C. D., and Anuta, P. E., "Analytic signal representation in the synthetic seismogram of bright spots," *Proceedings of IEEE International Conference on Acoustic, Speech and Signal Processing*, April 1, 1981, pp.1062-1065.
- [hua81b] Huang, K. Y., McGillem, C. D., and Anuta, P. E., "Detection of bright spots using pattern recognition techniques," presented at the 51st annual international SEG meeting, October 13, 1981, Los Angeles, LARS Technical Report 080982, Purdue University.
- [hua81c] Huang, Kou-Yuan, McGillem, Clare D., and Anuta, Paul E., "Structural pattern recognition in seismogram analysis," presented at the 51st annual international SEG meeting, 1981.

- [hua82a] Huang, K. Y. and Fu, K. S., "Decision-theoretic pattern recognition for the classification of Ricker wavelets and the detection of bright spots," presented at the 52nd annual international SEG (Society of Exploration Geophysicists) meeting, October 20, 1982, Dallas.
- [hua83a] Huang, Kou-Yuan and Fu, K. S., "Classification of Ricker wavelets and the detection of bright spots using a tree classifier", Proceedings of the Third International Symposium on Computer-Aided Seismic Analysis and Discrimination, The Catholic University of America, Washington, D.C., June 15-17, 1983, pp.89-97.
- [hua83b] Huang, Kou-Yuan and Fu, K. S., "Characteristics of analytic signal analysis in Gaussian bandpass noise and their use in the classification of Ricker wavelets," presented at the 53rd annual international SEG meeting, September, 1983, Las Vegas.
- [hua83c] Huang, Kou-Yuan and Fu, K. S., "Detection of bright spots in frequency attenuated seismograms using a cutting-method and tree Classification," presented at the 53rd annual international SEG meeting, September, 1983, Las Vegas.
- [hua83d] Huang, Kou-Yuan and Fu, K. S., "Syntactic pattern recognition for classification of Ricker wavelets," presented at the 53rd annual international SEG meeting, September, 1983, Las Vegas.
- [hua83e] Huang, Kou-Yuan and Fu, K. S., "Detection of bright spots using a tree classifier," *Oil & Gas Journal*, September, 1983.
- [joh81a] Johnston, David H., "Attenuation: a state-of-art summary," in *Seismic Wave Attenuation*, Toksoz, M. Nafi and Johnston David H., ed., Geophysics reprint series, Society of Exploration Geophysicists, 1981, pp.123-135.
- [kja79a] Kjartansson, E., "Constant Q-wave propagation and attenuation," *Journal of Geophysical Research*, vol.84, 1979, pp.4737-4748.
- [lev66a] Levenshtein, V. I., "Binary codes capable of correcting deletions, insertions and reversals," *Sov. Phys. Dokl.*, 10(8), pp.707-710, Feb., 1966.
- [lin80a] Lin, Yun-Kung J, *An Application of Pattern Recognition Techniques to PAP Smear Inspection*, Ph.D Thesis, Purdue University, December, 1980.

- [liu82a] Liu, H.H. and Fu, K.S., "A syntactic approach to seismic pattern recognition," *IEEE Trans. Patt. Anal. Mach. Intel.*, Vol. PAMI-4, March 1982, pp.136-140.
- [liu82b] Liu, H. H. and Fu, K.S., "A syntactic pattern recognition approach to seismic discrimination," *Geoexploration*, vol. 20, no. 1/2, Oct. 1982, pp.183-196.
- [liu83a] Liu, H. H. and Fu, K.S., "An application of syntactic pattern recognition to seismic discrimination," *IEEE Transactions on Geoscience and Remote sensing*, vol.GE-21, no.2, April, 1983, pp.125-132.
- [lu82a] Lu, S. Y., "A string-to-string correlation algorithm for image skeletonization," *Proceedings of International Conference on Pattern Recognition*, 1982, pp.178-180.
- [net82a] Neter, J., Wasserman, W. and Whitmore, G. A., *Applied Statistics*, Allyn and Bacon, Inc., Boston, 2nd edition, 1982, pp.410-417.
- [obr61a] O'Brien, P.N.S., "A discussion of the nature and magnitude of elastic absorption in seismic prospecting," *Geophysical Prospecting*, vol.9, no.2, 1961, pp.261-275.
- [oom82a] Oommen, Basantkumar John, *Pattern recognition with strings, substrings and boundaries*, Ph.D. Thesis, Purdue University, May 1982.
- [opp75a] Oppenheim, A. V. and Schafer, R. W., *Digital Signal Processing*, Prentice Hall, 1975, pp.337-375.
- [pan70a] Pan, P.H. and De Bremaecker, J.Cl., "Direct location of oil and gas by the seismic reflection method," *Geophysical Prospecting*, vol.18, 1970, pp.712-727.
- [pap65a] Papoulis, A., *Probability, Random Variables, and Stochastic Processes*, McGraw-Hill, New York, 1965, ch.7 & 10.
- [pav71a] Pavlidis, T., "Linguistic analysis of waveforms," in *Software Engineering*, ed. by Tou, J. T., vol. 2, Academic, New York, 1971, pp.203-225.
- [pav73a] Pavlidis, T., "Waveform segmentation through functional approximation," *IEEE Trans. Comput.*, vol. C-22, 1973, pp.689-697.
- [pay77a] Payton, C. E., Ed., *Seismic Stratigraphy - applications to hydrocarbon exploration*, AAPG Memoir 26, Tulsa, Am. Assn. Petroleum Geologists, 1977.

- [rab75a] Rabiner, L. R. and Gold, B., *Theory and Application of Digital Signal Processing*, Prentice Hall, 1975, pp.71-72 & 168-177.
- [ric40a] Ricker, Norman, "The form and nature of seismic wavelets and the structure of seismograms," *Geophysics*, 1940, vol.5, pp.348-366.
- [ric45a] Ricker, N., "The computation of output disturbances from amplifiers for true wavelet inputs," *Geophysics*, vol.10, 1945, pp.207-220.
- [ric53a] Ricker, Norman, "The form and laws of propagation of seismic wavelets," *Geophysics*, 1953, Vol.18, pp.10-40.
- [rob81a] Robertson, James D. and Nogami, Henry H., "Thin bed stratigraphy from complex trace attributes," presented at the 51st Annual International Meeting of SEG, October, 1981, Los Angeles.
- [rob67a] Robinson, E. A., *Multichannel Time Series Analysis with Digital Computer Program*, Holden-Day, 1967, San Francisco.
- [san79a] Sankar, P.V. and Rosenfeld, A., "Hierarchical representation of waveforms," *IEEE Trans. Patt. Analy. and Mach. Intel.*, vol. PAMI-1, no.1, 1979, pp73-79.
- [sar80a] Sarna C.S. and Stark H., "Pattern recognition of waveforms using modern spectral estimation techniques and its application to earthquake/explosion data," Proc. 5th Intl. Conf. on Pattern Recognition, Dec. 1-4, Miami Beach, FL. 1980.
- [sar82a] Sarna C.S. and Stark H., "Pattern recognition of waveforms using autoregressive modeling with applications to earthquake/explosion data," Proceedings of the Second International Symposium on Computer-Aided Seismic Analysis and Discrimination, 1983, pp.138-143.
- [sch78a] Schoenberger, M. and Levin, F.K., "Apparent attenuation due to intrabed multiples," *Geophysics*, vol.43, 1978, pp.730-737.
- [she74a] Sheriff, Robert E., "Seismic detection of hydrocarbons - the underlying physical principles," Offshore Technology Conference, Page No. OTC 2001, 1974.
- [she75a] Sheriff, R.E., "Factors affecting seismic amplitudes," *Geophysical Prospecting*, vol.23, 1975, pp.125-138.
- [she76a] Sheriff, R.E., "Inferring stratigraphy from seismic data," *Bulletin of Am. Assn. Petroleum Geologists*, vol.60, 1976, pp.528-542.

- [shl82a] Shlien, Seymour, "Segmentation of digital curves using linguistic techniques," *Computer Vision, Graphics, and Image Processing*, vol.22, 1983, pp.277-286.
- [sic78a] Sicking, Charles J., "Modeling with the complex trace," presented at the 48th annual international SEG meeting, October 29, 1978 in San Francisco.
- [str70a] Strick, E., "A predicted pedestal effect for pulse propagation in constant - Q solids," *Geophysics*, vol.35, 1970, pp.387-403.
- [swa77a] Swain, P.H. and Hauska, H., "The decision tree classifier: design and potential," *IEEE Trans. Geosci. Electron.*, vol. GE-15, pp.142-147, July 1977.
- [swa78a] Swain, Philip H. and Davis, Shirley M., *Remote Sensing: The Quantitative Approach*, McGraw-Hill, Inc., 1978
- [tan77a] Taner, M. T. and Sheriff, R. E., "Application of amplitude, frequency, and other attributes to stratigraphic and hydrocarbon determination," *Seismic Stratigraphy - applications to hydrocarbon exploration*, C. E. Payton, Ed., AAPG Memoir 26, Tulsa, Am. Assn. Petroleum Geologists, 1977, pp.301-327.
- [tan79a] Taner, M. T., Koehler, F. and Sheriff, R. E., "Complex seismic trace analysis," *Geophysics*, Vol.44, 1979, pp.1041-1063.
- [tan80a] Discussion "On: "Complex seismic trace analysis"(M. T. Taner, F. Koehler, and R. E. Sheriff)," by J. G. Saha, N. D. J. Rao, and M. C. Agrawal, with reply by author, *Geophysics*, Vol.45, 1980, pp.1877-1878.
- [tho69a] Thomas, J., *An Introduction to Statistical Communication Theory*, Wiley, New York, 1969, pp.154-160.
- [tjo75a] Tjostheim, D., "Autoregressive representation of seismic P-wave signals with an application to the problem of short-period discriminants," *Geophys. J. R. Astr. Soc.*, vol.43, 1975, pp.269-291.
- [tjo77a] Tjostheim, D., "Recognition of waveforms using autoregressive feature extraction," *IEEE Trans. Comput.*, vol.C-26, 1977, pp.268-270.
- [tjo78a] Tjostheim, D., "Improved seismic discrimination using pattern recognition," *Phys. Earth Planet. Inter.*, vol.16, 1978, pp.85-103.
- [tjo79a] Tjostheim, D. and Sandvin, O., "Multivariate autoregressive feature extraction and the recognition of multichannel waveforms," *IEEE Trans. Patt. Analys. and Mach. Intell.*, vol.PAMI-1, no.1, 1979, pp.80-86.

- [tok81a] Toksoz, M. Nafi and Johnston, David H., *Seismic Wave Attenuation*, Society of Exploration Geophysicists, 1981.
- [tou74a] Tou, J.T. and Gonzalez, R.C., *Pattern Recognition Principles*, Addison-Wesley, New York, 1974.
- [tro62a] Trorey, A.W., "Theoretical seismograms with frequency and depth dependent absorption," *Geophysics*, vol.27, 1962, pp.766-785.
- [van68a] Van Trees, H.L., "*Detection, Estimation, and Modulation Theory*," vol.I, Wiley, New York, 1968.
- [vog78a] Vogel, M.A. and Wong, A.K.C., "PFS clustering method," *IEEE Trans. Patt. Anal. Mach. Intel.*, vol. PAMI-1, no.3, pp.237-245, 1978.
- [wag74a] Wagner, R.A. and Fischer, M.J., "The string-to-string correction problem," *J. ACM*, vol.21, no.1, 1974, pp.168-173.
- [wu75a] Wu, C., Landgrebe, D., and Swain P., "The decision tree approach to classification", TR-EE 75-17, Purdue University, May 1975.
- [wyl62a] Wyllie, M.R.J., Gardner, G.H.F., and Gregory, A.R., "Studies of elastic wave attenuation in porous media," *Geophysics*, vol.27, 1962, pp.569-589.
- [you76a] You, K.C. and Fu, K.S., "An Approach to the design of a linear binary tree classifier", Proc. Symposium of Machine processing of Remotely Sensed Data, Purdue University, pp.3A-1 to 3A-10, 1976.
- [zie76a] Ziemer, R. and Tranter, E., *Principles of Communications*, Houghton Mifflin Co., 1976, ch.2 & 5.